UNIVERSITÉ DE SHERBROOKE
Faculté de génie
Département de génie mécanique

ÉLÉMENTS SPECTRAUX POUR LES ONDES ULTRASONORES GUIDÉES

Formulation, analyse de la dispersion et résultats de simulation

SPECTRAL ELEMENTS FOR GUIDED WAVES

Formulation, Dispersion Analysis and Simulation Results

Thèse de doctorat
Specialité : génie mécanique

Ramy MOHAMED

Jury: Patrice MASSON (directeur)
Alain BERRY
Luc FRÉCHETTE
Mohammad Reza MOFAKHAMI

Sherbrooke (Québec) Canada Septembre 2014

لِسُمَيَّةَ و رَنَا
المَرفَأُ
و المَرتَعُ
و المَلَاذ
عَينَاكُمَا ... جَنَّتِي

لذِكرَى أبى

To Somaia and Rana
my haven and sanctuary
your eyes ... is my Heaven

To the memory of my father

RÉSUMÉ

La surveillance de l'intégrité des structures (*Structural Health Monitoring* - SHM) est une nouvelle technologie, et comme toute nouvelle avancée technologique, elle n'a pas encore pas réalisé son plein potentiel. Le SHM s'appuie sur des avancées dans plusieurs disciplines, dont l'évaluation non-desctructive, les matériaux intelligents, et les capteurs et actionneurs intégrés. Une des disciplines qui permet son déploiement est la simulation numérique. Le SHM englobe une variété de techniques basées sur la génération d'ondes vibratoires et d'ondes ultrasonores guidées. L'utilisation d'ondes guidées offre en particulier une vaste gamme d'avantages.

Le défi majeur associé à la pleine utilisation de la simulation numérique dans la conception d'un système SHM basé sur l'utilisation d'ondes guidées réside dans les ressources de calcul requises pour une simulation précise. La principale raison pour ces exigences est la dispersion induite par la discrétisation numérique, tel qu'indiqué dans la littérature. La méthodes des éléments spectraux (SEM) est une variante de la *p*-version de la méthode des éléments finis (FEM) qui offre certains outils pour solutionner le problème des erreurs de dispersion, mais la littérature souffre toujours d'une lacune dans l'étude systématique des erreurs de dispersion numérique et de sa dépendance sur les paramètres de simulation.

Le présent ouvrage tente de combler cette lacune pour les théories d'ingénierie en vibrations. Il présente d'abord le développement de la formulation des éléments spectraux pour différentes théories d'ingénierie pertinentes pour la propagation des ondes vibratoires dans différents types de structures, comme des tiges et des plaques. Puis, une nouvelle technique pour le calcul des erreurs de dispersion numériques est présentée et appliquée systématiquement dans le but d'évaluer la dispersion numérique induite en termes d'erreurs dans les vitesses de propagation. Cette technique est utilisable pour les différentes formes de propagation des ondes vibratoires dans les éléments structuraux visés dans la présente thèse afin d'évaluer quantitativement les exigences de précision en termes de paramètres de maillage. Les ondes de Lamb constituent un cas particulier de la déformation plane des ondes élastiques, en raison de la présence des doubles frontières à traction libre qui couplent les ondes longitudinales et de cisaillement et qui conduisent à une infinité de modes propagatifs qui sont dispersifs par nature. La simulation des ondes de Lamb n'a pas fait l'objet d'analyse systématique de la dispersion numérique dans la littérature autant pour la SEM que la FEM. **Nous rapportons ici pour la première fois les résultats de l'analyse de dispersion numérique pour la propagation des ondes Lamb**. Pour toutes les analyses de dispersion numérique présentées ici, l'analyse a été effectuée àăla fois dans le domaine fréquentiel et dans le domaine temporel.

En se basant sur la nouvelle compréhension des effets de discrétisation numérique de la propagation des ondes guidées, nous étudions l'application de la SEM à la simulation numérique pour des applications de conception en SHM. Pour ce faire, l'excitation piézoélectrique est développée, et **une nouvelle technique de condensation statique est développée et mise en oeuvre pour les équations de la matrice semi-discrète, qui élimine le besoin de solution itérative**, ainsi surnommée *fortement couplée* ou *entièrement couplée*. Cet élément piézoélectrique précis est ensuite utilisé pour étudier en détails les subtilités de la conception d'un système SHM en mettant

l'accent sur la propagation des ondes de Lamb. Afin d'éviter la contamination des résultats par les réflexions sur les bords **une nouvelle forme particulière d'élément absorbant a été développée et mise en oeuvre**. Les résultats de simulation dans le domaine fréquentiel jettent un éclairage nouveau sur les limites des modèles théoriques actuels pour l'excitation des ondes de Lamb par piézoélectriques. L'excitation par un élément piézoélectrique couplé est ensuite entièrement simulée dans le domaine temporel, et les résultats de simulation sont validés par deux cas de mesures expérimentales ainsi que par la simulation classique avec des éléments finis en utilisant le logiciel commercial ANSYS.

Mots-clés : ondes de Lamb, SHM, éléments spectraux, dispersion numÃl'rique

ABSTRACT

Structural health monitoring (SHM) is a novel technology, and like any new technological advancement it has yet not realized its full potential. It builds on advancements in several disciplines including nondestructive evaluation, smart materials, and embedded sensors and actuators. One of the enabling disciplines is the numerical simulation. SHM encompasses a variety of techniques, vibration based, impedance and guided ultrasonic waves. Guided waves offers a wide repertoire of advantages.

The major challenge facing the full utilization of the numerical simulation in designing a viable guided waves based SHM System is the formidable computational requirements for accurate simulation. The main reason for these requirements is the dispersion induced by numerical discretization as explained in the literature review. The spectral element (SEM) is a variant of the *p*-version finite element (FEM) that offers certain remedies to the numerical dispersion errors problem, yet it lacks a systematic study of the numerical dispersion errors and its dependence on the meshing parameters.

The present work attempts to fill that gap for engineering theories. It starts by developing the formulation of the spectral element for different relevant engineering theories for guided waves propagation in various structural elements, like rods and plates. Then, extending the utility of a novel technique for computing the numerical dispersion errors, we systematically apply it in order to evaluate the numerically induced dispersion in terms of errors in the propagation speeds. This technique is employed for the various forms of guided waves propagation in structural elements covered in the present thesis in order to quantitatively assess the accuracy requirements in terms of the meshing parameters. The Lamb guided waves constitute a special case of the plane strain elastic waves, that is due to the presence of the double traction free boundaries, couple in the section plane and this coupling leads to an infinitude of propagating modes that are dispersive in nature. Lamb waves simulation have not been a subject of numerical dispersion analysis in the open literature neither for SEM nor FEM for that matter. **We report here for the first time the numerical dispersion analysis results for Lamb waves propagation**. For all the numerical dispersion analysis presented here, the analysis was done for both the frequency domain and time domain analysis.

Based on the established understanding of the numerical discretization effects on the guided waves propagation, we utilize this knowledge to study the application of SEM to SHM simulations. In order to do so the piezoelectric excitation is developed, and **a new static condensation technique is developed for the semidiscrete matrix equations, that eliminate the need for iterative solution**, thus dubbed *strongly coupled* or *fully coupled* implementation. This accurate piezoelectric element are then used to study in details the intricacies of the design of an SHM system with specific emphasis on the Lamb waves propagation. In order to avoid the contamination of the results by the reflections from the edges **a new special form of absorbing boundary was developed and implemented**. The Simulation results in the frequency domain illuminated the limitations of the current theoretical models for piezoelectric excitation of Lamb waves. The piezoelectric excitation of a fully coupled element is then simulated in the time domain, and the

the results of simulation was verified against two cases of experimental measurements as well as conventional finite element simulation using the commercial software ANSYS.

Keywords: Lamb Waves, Structural Health Monitoring, Spectral Element, Numerical Dispersion

ACKNOWLEDGEMENTS

To express my debt and gratitude to Prof. Patrice Masson is an attempt condemned a priori to be a failure. I learned from him a lot that I am still discovering every passing day, and a part of what resulted from his patient guidance, I hope, is manifested in this work.

The author also wishes to thank his colleagues in the SHM group for many stimulating discussions and help. In particular, the many fruitful discussions with Nicolas Quaegebeur and Pierre-Claude Ostiguy as well as their help with the experimental work are much appreciated.

From all my friends I wish to especially thank Abdellah Ousegui and a friend who insisted to remain anonymous for being true friends.

As to my wife/life Somaia Ahmed, words is not enough -and will never be- to express exactly what I feel. The language -any human language- is inherently limited when it comes to describing how much I am indebted to you.

Much of the funding for the research which led to this thesis was provided by NSERC. This support is gratefully acknowledged.

CONTENTS

LIST OF FIGURES

LIST OF TABLES

LIST OF SYMBOLS

Greek symbols

α	Arbitrary multiplier, expansion coefficient in Taylor expansion, or $\sqrt{\omega^2/c_L^2 - k^2}$
β	$\sqrt{\omega^2/c_T^2 - k^2}$
Γ	Shear lag coefficient
ϵ	Mechanical strain tensor
ε^S	Dielectric permittivity 2nd order tensor
η	Reference coordinate
Λ	Standard one dimensional element $[-1\ 1]$
λ	Wavelength, or Lamé's constant
μ	Lamé's material constant
ν	Poisson's ratio for isotropic elastic material
ξ	Reference coordinate
Π	Standard two dimensional element $[-1\ 1]^2$
ρ	Material Density
σ	Mechanical Stress Tensor
$\mathbf{e}^\sigma$	Dielectric permittivity tensor
τ_a	Interfacial shear stress amplitude
ϕ	Scalar potential field
$\phi(t)$	Electric potential
φ	shear-lag parameter
$\mathbf{\Psi}$	Vector potential field
Ω	Physical domain or exact eigenvalue
Ω_n	Numerical eigenvalue of the discrete generalized eigenvalue problem
ω	Circular frequency of the discrete generalized eigenvalue problem

Mathematical Operator

$[\dot{\ }]$	First time derivative
$[\ddot{\ }]$	Second derivative with respect to time
$\partial_x^n[\ ]$	The n^{th} partial derivative with respect to x
∇	The divergence operator
∂	Physical Boundary

Alphabetical Symbols

$\bar{\mathbf{t}}$	Surface traction
$\mathbf{I}$	Identity matrix
$\mathbf{u}$	Particle displacement vector
c_f	CFL Number
c_g	Group velocity
c_l	Longitudinal wave velocity

c_o	Rod velocity
c_p	Phase velocity
c_R	Rayleigh wave velocity
c_t	Transverse wave velocity
h_e	Representative element size
k_l	Lamb wavenumber
A_n	n^{th} asymmetric Lamb's mode
S_n	n^{th} symmetric Lamb's mode
M_n	n^{th} SH mode
$\mathbf{d}$	Piezoelectric coupling tensor
$\mathbf{D}$	Electrical displacement vector
$\mathbf{s}^E$	Elastic compliance tensor
$\mathbf{E}$	Electric field vector
J^e	one dimensional Jacobian
$\mathbf{J}^e$	Jacobian matrix
J_n	Bessel function of first kind of order n
$\mathbf{T}$	Cauchy stress 2nd order tensor elements
$\mathbf{S}$	infinitesimal strain 2nd order tensor elements
$\mathbf{D}$	electrical displacement vector
$\mathbf{c}^E$	Elastic 4th order tensor of piezoelectric material
$\mathbf{e}$	3rd order tensor of piezoelectric stress constants
$\mathbf{E}$	electric field vector.
G_b	shear modulus of the adhesive material

LIST OF ACRONYMS

AE	Acoustic Emission
CAD	Computer Aided Design
CFL	Courant-Friedrichs-Lewy condition
CPU	Central Processing Unit
DTI	Direct Time Integration
EUSR	Embedded Ultrasonic Structural Radar
FD	Finite Difference
FDTD	Finite Difference Time Domain
FEM	Finite Element Method
FFT	Fast Fourier Transform
FFT-SEM	Frequency Domain Spectral Element Method
FSDT	First order Shear Deformation Theory
GW	Guided Wave
GLL	Gauss-Lobatto-Legendre
IFFT	Inverse Fast Fourier Transform
LISA	Local Interaction Simulation Approach
LW	Lamb Waves
MS	Mode Superposition
NDE	Nondestructive Evaluation
NDT	Nondestructive Testing
NME	Normal Mode Expansion
ODE	Ordinary Differential Equation
PDE	Partial Differential Equation
PS	Pseudo-Spectral
PZT	Piezoelectric Lead Zirconate Titanate
SEM	Spectral Element Method
TD-SEM	Time Domain Spectral Element Method
SHM	Structural Health Monitoring
PML	Perfectly Matched Layer

CHAPTER 1

Introduction

> The purpose of computing is insight, not number.
>
> RICHARD HAMMING (1915-88)

AN elastic waveguide is a physical structure that supports the propagation of elastic waves along its elongated direction, and dictates the behavior of such waves with respect to wave propagation in the bulk material. There are two fundamental peculiarities of guided waves propagation. The first is the *quantization* of waves into discrete propagating modes, of which only a finite number are possible for a given frequency, and whose properties are determined by the shape of the cross section and boundary conditions of the waveguide. The second is the existence of *dispersion*, which is a nonlinear dependence of phase velocity on the frequency. As a consequence, signals with a spectral bandwidth are distorted as they propagate along the waveguide, because their spectral components propagate with different phase velocities.

The use of guided waves (GW) for damage detection is an active research area since Worlton first recognized the benefits of using Lamb waves in non-destructive testing of plates [Worlton, 1957]. Guided waves generation using conventional hand held transducers is now well understood and used in some non-destructive evaluation (NDE) systems, where the transducers operate by *tapping* the surface thus generating normal stresses on the surface. On the other hand guided waves generation using surface bonded/embedded piezoceramic transducers (piezos) for structural health monitoring (SHM) is a relatively nascent field. Piezoceramic elements are inexpensive devices that can be surface bonded to an already functioning structure for SHM purposes or embedded between the layers of lap joints, or inside composite materials during the manufacturing process.

1.1 Background and motivation

Being a multidisciplinary field, SHM technology requires a thorough understanding of materials, sensors and electronics, along with the ability to perform sophisticated numerical and analytical modeling and signal processing. Modeling forms an indispensable component in developing SHM technology. Simulated data are used to support the development of new algorithms for damage detection, or for an improved understanding of the effects of damage on the wave propagation.

Two major concerns are pertinent to GW based SHM techniques. The first is the fact that different modes have varying sensitivity to geometrical location of the damage, necessitating time consuming experimentation, as well as utilizing some modes that are only accessible at high frequency. The second is the fact that the size of detectable damage is limited by the smallest wavelength of the propagating modes, which again may require a high frequency excitation. As mentioned earlier, a key characteristic of guided waves is that more than one mode can be excited at any given frequency. This poses a difficulty in interpreting the complicated GW signals which are usually found in NDE/SHM applications. The modal discretization plus the inherent dispersion, when applied to the real world structures, limits the utility of analytical methods in analyzing the real-world configurations. This makes numerical simulation an indispensable tool especially at the design phase of a NDE/SHM system.

To allow such a numerical simulation, the finite element (FE) method has been the tool of choice for structural dynamics analysis for almost half a century now. The method remains under continuous development to improve its accuracy, efficiency, and reliability. The FE method, although very versatile, is confronted by serious limitations when the high frequency response of structures needs to be evaluated, or when configurations with very small features need to be accurately represented (*i.e.* damages). Both of these situations arise abundantly in the simulation of SHM problems. The numerical solution by the usual linear and quadratic (h-type) finite elements gives rise to substantial amounts of numerical dispersion due to the discretization and element characteristics. These *dispersive* errors exist for both lumped and consistent mass matrices. As a consequence, the solutions can be significantly in error, even when unusually fine meshes are used. For the explicit time integration case, this is particularly true when the time increment used is less than the maximum permitted by stability considerations (Courant-Friedrichs-Lewy CFL Condition).

Research on the p-version FE analysis, in which the error is reduced not by refining the mesh but by increasing the order of interpolating polynomials, dates back to the late 1960's. Many important advances occurred in the 1970's. The theoretical basis was established in 1981 and optimal meshing strategies appropriate for the p-version were developed in the period 1984-1985 [Babuška and Suri, 1994]. The main advantage of the p-version is that errors of approximation are reduced at an exponential rate when the number of degrees of freedom are increased, provided that the finite element mesh is properly constructed. The h-version can provide algebraic convergence rates only. This makes error control much more effective in the p-version. Furthermore, a converging sequence of solutions is much more naturally and conveniently obtained with the p-version than with the h-version. This makes it feasible to employ quality control procedures in the setting of practical engineering decision-making processes [Babuška *et al.*, 1981].

A specific variant of the *p*-version finite element method is increasingly gaining acceptance and recognition in the field of high frequency wave propagation simulation: the spectral element in time domain. This approach mainly addresses the issues of degraded accuracy for the elastic wave propagation. Though in the literature it has been observed that this method suffers less from the numerical dispersion errors, there is very few detailed and systematic analyses of the numerical dispersion, and the work been done is mainly done for non-engineering applications, *i.e.* generic 1D classical wave propagation and generic 2D elastodynamic equations. The present work attempts to fill that gap, focusing on the main challenges facing the use of numerical simulation as a development tool for SHM.

1.2 Research goals, scopes and objectives

Engineering decisions are increasingly based on computed information with the expectation that those computed quantities will provide a reliable quantitative estimate of some attributes of a physical system or process. SHM systems is not an exception. The question of how much reliance on computed information can be justified is being asked with increasing frequency and urgency. Assurance of the reliability of computed information has two key aspects: (a) selection of a suitable mathematical model and (b) approximation of the solution of the corresponding mathematical problem. The process by which it is assessed that a mathematical model meets necessary criteria for acceptance (*i.e.*, it is suitable for purposes of analysis) is called *validation*. The process by which it is assured that the approximate solution, as well as the data computed from the approximate solution, meet necessary conditions for acceptance, given the goals of computation, is called *verification*.

Over the past decades numerical analysts and applied mathematicians have developed and ascertained different measures of accuracy (see App. A). For the purpose of validation and verification of guided waves based SHM systems design and simulation -as the author wishes to demonstrate convincingly in the upcoming chapters- these conventional error measures are more general and less pertinent to the errors of concern to the prediction accuracy of a certain mathematical model and its numerical implementation in GWs propagation.

The main proposition that constitutes the underlying and unifying thread of the present thesis, is the suggestion that *dispersion* is the major concern in the GWs simulation. For that purpose, not only the analysis of the numerical dispersion of the approximate solution is valuable but also the dispersion that is predicted by the mathematical model underlying the implementation.

1.3 Thesis outline

The second chapter reviews the literature with main emphasis on the guided waves based SHM system design requirements. The peculiarities of such systems from the point of view of numerical simulation are used as the main points for evaluating the numerical methods typically used in the numerical simulation of wave propagation phenomena. At the second half of the chapter a review of the major issues that SHM design poses on numerical simulation using the present methods is reviewed. In an attempt to justify the need for a more robust and efficient alternatives to the available numerical methods, the focus is put in understanding why ultrasound guided waves propagation is too computationally demanding. The main reason in the final analysis is the induced numerical dispersion which emanates from the discretization and the nature of interpolation used.

This lead to the emphasis on the concept of dispersion as an error measure both in the validation and verification phases. The dispersion entailed by the mathematical model is analytically determined, for different families of approximate engineering theories. These dispersion relations are determined by the assumptions and simplifications of the mathematical model. Then spectral element implementation of those theories are developed, and viewed from the point of verification phase, *i.e.* the numerical dispersion are analyzed and quantified as dependent on the approximate solution parameters.

The present thesis first develops the spectral element formulation for different approximate engineering theories, for both rods and plates. As such the presentation is made as independent of the specific shape functions used, or quadrature rule as possible, postponing the embodiment in the spectral element framework to the last step. This unified approach of the representation makes the comparison between different implementation of approximate theories more concise as well as clear. Another benefit of this representation, especially with the rapid development in symbolic mathematics software, is the possibility of the automatic production of numerical codes from symbolic premises.

The third chapter deals with the one dimensional guided wave propagation in rods. An important line of demarcation is drawn, between the exact solution, and the engineering approximate theories, some of those theories are explained and their dispersion characteristics are studied (validation phase). The spectral element formulation for the different theories have been developed in detail, followed by a detailed numerical dispersion analysis of those developed formulations (verification phase).

The fourth chapter is devoted to the GW in two dimensional structures, *i.e.* plane strain elastic waves in unbounded media and in plates, with a similar emphasis on the distinction between the

exact solution, and the approximate theories, and the difference in their dispersion relations. The developed formulations are then analyzed from the perspective of numerical dispersion extending the dispersion analysis method presented in chapter 3. The traction free boundary condition for Lamb waves is incorporated in the analysis and the results illustrate the superiority of the spectral element method in simulating the Lamb waves propagation. The chapter ends with a detailed analysis of the numerical dispersion characteristics of the first order shear deformation theory.

Besides the formulation and implementation of the spectral elements for approximate engineering theories, the added contribution of the present work is the consistent application of a novel numerical dispersion analysis technique to all the developed formulations. This leads to a more detailed understanding and appreciation of the major problematic error responsible for deteriorating the accuracy of numerical simulation of guided waves propagation. To the knowledge of the author, ***it is the first time that the numerical dispersion analysis incorporates the boundary conditions, and it is reported here in the numerical dispersion analysis applied to the Lamb waves in the plane strain 2D settings***.

Having the knowledge established in the forth chapter of the meshing parameters needed for accurate simulation of Lamb waves propagation, the spectral element formulation of the coupled piezoelectric element with an elastic plate is developed in the fifth chapter, followed by using this formulation in performing a detailed analysis of the effects of strong coupling of ideally bonded PZT, as well as the adhesive layer and the effect of the thickness changes of the actuator, and material properties of the adhesive layer on the amplitudes of the fundamental modes propagating. In order to eliminate the reflections from the boundaries, ***a new absorbing boundary is developed and implemented in the frequency domain, the proposed absorbing boundary formulation is equally applicable to the time domain simulation***.

Lastly, concluding remarks are presented in the final chapter.

CHAPTER 2

Literature review

> When you can measure what you are talking about and express it in numbers, you know something about it.
>
> LORD KELVIN (1824-1907)

ALL civil, mechanical and aerospace structures are subject to damage as a result of fatigue, overloading conditions, and degradation through environmental effects, which compromises the structure's performance of its intended functions. Assessment of the in-service structures' health on a continuous basis is a very important objective for manufacturers, end-users and maintenance teams.

2.1 Structural health monitoring (SHM)

Structural health monitoring (SHM) refers to the process of implementing a damage identification strategy for aerospace, civil and mechanical engineering infrastructure [Farrar and Worden, 2007]. The increasing demand on SHM techniques is driven by economical and safety requirements. SHM marks a transition in maintenance philosophy from preventive to predictive phase. The drastic consequences in the work organization of maintenance services include: replacement of scheduled and periodic maintenance inspection with performance-based (or condition-based) maintenance (long term) or at least (short term) by reducing the required labour, in particular by avoiding dismounting parts where there is no hidden defect; second by minimizing the human involvement, and consequently reducing downtime and human errors, thus improving safety and reliability. The adoption of SHM allows an optimal use of the structure, and gives an additional advantage for design improvement [Balageas, 2006].

A primary application of SHM is to facilitate decision making regarding where and when to apply maintenance remedies. A second application is to utilize SHM information to provide appropriate estimates of future loads in order to feed a prognosis prediction system by relevant information as to the mechanisms according to which the damage might progress and how long the structure may survive without failing or requiring maintenance. The multitude of possible structural behaviours and interactions often limit the utility of simple quantitative health assessments. Easy-to-measure

quantities, such as geometry, provides only limited indicators as to the structural health state. Other bits of information, such as incipient failure modes, which are more valuable, may be more difficult to determine quantitatively.

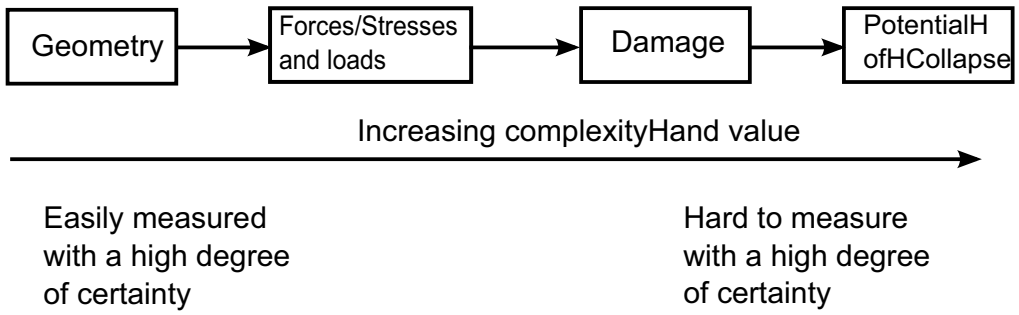

Figure 2.1 Complexity and certainty over a range of structural health measurements [Huston, 2011].

Figure 2.1 shows the relations between ease of measurement, complexity, information value, and uncertainty. Structural health could be identified in terms of load, damage state, and estimated life characteristics:

Usage Monitoring: Identification of the operational and environmental loads acting on the structure mainly in the undamaged state [Adams, 2007; Farrar and Worden, 2007].

Structural Health Monitoring: Detection of the mechanical damage that is caused by loading and monitoring the growth of damage as the structure operates; damage is defined as changes to the material and/or geometric properties of the monitored structures, including changes to the boundary conditions and components connectivity, which adversely affect the current or future performance of these structures [Sohn *et al.*, 2004].

Damage Prognosis: Estimating the future performance of the structure as damage accumulates [Farrar and Lieven, 2007].

The ultimate purpose of the SHM system [Huston, 2011] is to:

— Provide early enough warning of collapse or catastrophic failure.
— Provide information for planning maintenance activities on-demand, rather than on a usage or post-event basis.
— Determine if the structure meets predetermined performance criteria.
— Identify the presence of fault conditions.
— Provide structural condition assessment information for use in maintenance, operational, and rehabilitation activities.

— Evaluate the condition of the structure upon discovery of a problem, such as incipient cracks.
— Assess the integrity of the structure following catastrophic events.
— Provide data to estimate the remaining lifetime of the structure.
— Provide information that aids in the development of new design codes and procedures.
— Assist in construction processes by increasing safety and/or productivity.
— Establish the viability and performance of novel sensor or SHM systems.
— Certify the safety of prototype and production designs.
— Provide a maintenance history and state assessment as part of an economic assessment of a structure.

2.2 Advantages and design requirements of SHM systems

Boller suggests a unifying definition of SHM as [Boller, 2012]

> *the integration of sensing and possibly also actuation devices to allow the loading and damaging conditions of a structure to be recorded, analysed, localized, and predicted in a way that non-destructive testing (NDT) becomes an integral part of the structure and a material.*

This definition emphasizes on the similarities between the SHM, and NDT/NDE systems. It is not arguable that non-destructive evaluation (NDE) is a generic name that encompasses numerous techniques that can be used both in schedule-based inspection, on-site or in a maintenance facility, or in SHM with permanently installed sensors for continuous or on-demand inspection [Achenbach, 2009]. But as Kroening *et al.* [Kroening *et al.*, 2005] noted, the requirements for the design of SHM systems are somewhat different from the requirements of NDE systems. Table 2.1 lists some of the principal design requirements and the differences between the two.

A typical SHM system consists of an embedded network of sensors for data acquisition and some central processor employing an algorithm to evaluate structural health. The schemes available for SHM can be categorized into passive and active schemes. Passive schemes normally require high sensor density per structure. Unlike passive methods, active schemes are capable of *checks-on-demand*, and require less sensor density per structure [Raghavan and Cesnik, 2005b].

Another less emphasized feature is that whether the SHM system is going to be implemented into an already functioning structure, or in a new in-design structure. For the first case, the most important design requirement is that SHM system must not impact or alter the structural performance, which could be called *non-intrusiveness* requirement. This requirement is more

Table 2.1 Design requirements of NDE *vs* SHM systems [Kroening *et al.*, 2005]

Requirement	NDE System	SHM System
Measurement interval	Periodic	Periodic or continuous
Transducer location	Coupling or non-contact	Structure integrated
Measurement location and modality	Scanning or imaging	Local (hot spots) or averaging (fibers, plate waves), imaging.
Performance versus cost	High performance High cost	Moderate performance Low cost
Signal processing	Signal preprocessing on board	Intelligent (processor + interface)
Replacement versus reliability	Easy to replace	Extremely high reliability
Energy supply and consumption	Energy not critical	Stand-alone energy management

important in the case of already functioning structures. In the second case, the SHM system is being incorporated during the design of the new structure, the impact of the SHM implementation on the structure performance could be assessed during the design phase, leaving a larger repertoire of choices as to which SHM scheme and technology could be used. For the *non-intrusive SHM system*, some aspects such as accessible configuration with respect to the structure, the weight, sensitivity of the SHM technology to the working conditions limits the design choices considerably. Ideally, a non-intrusive SHM system would have the minimum impact on the structure performance as well as high durability, *i.e.* it must not constitute a new maintenance burden, reliability, *i.e.* for an aircraft it must be isolated against possible interferences, and have a low energy requirements.

In Table 2.2, a summary of the different techniques available for SHM with their main characteristics is presented. The main characteristics definitions are:

Network Density: The density of the network of sensors and/or actuators that is needed to achieve a full coverage of the structure. This is strongly connected with the Detection Range. This is very important characteristic for the non-intrusiveness requirement, since

Table 2.2 Available techniques for typical SHM systems

Approach	Network Density	Frequency Range	Reliability	Accuracy of localization	Detection Range	Cost	Mode of Operation
Modal data	Low	< 10 kHz	Low	Low	Full Coverage	Low	Passive
Electromechanical impedance	High	> 30 kHz	Medium	Sensor Size	Low	Very Low	Active or passive
Static parameter (displacement strain, etc.)	High	0 kHz	High	Sensor Size	Low	Very Low	Passive
Acoustic emission	High	> 1 MHz	Very Low	Very High	Wide Coverage	High	Passive
Guided Waves Based Systems	Low	< 1 MHz	Very High	Very High	Wide Coverage	Medium	Active

a large network density will mainly affect the inertia of the system, increase its weight, and most likely will impact the function performance of the structure.

Detection Range: The range the single sensor can cover, as well as the ability to cover both surface and hidden damages.

Frequency Range: The range of the frequency that the technique are most effective at. This is normally connected with the cost and energy requirements for active mode of operation, and for passive mode it is more suitable to consider it as sensitivity parameter.

Reliability: The sensitivity to the changes of the boundary conditions, environmental effects, as well as the ease with which a *single* measurement could be affected with noise.

Accuracy of Localization: The accuracy with which the damage could be located. This is largely dependent on the post-acquisition signal processing, but it is also related to the ability of the technique to yield reliable information about the location of the damage.

Mode of Operation: The ability to operate the SHM system in either passive or active mode, this is directly related to the *checks-on-demand* requirement.

In comparison with other NDE approaches, those using GW can offer faster and more cost-effective evaluation of various types of damage. For example, rather than using a single ultrasonic probe to inspect a long insulated pipe point by point, one can employ a wave transmitter and receiver pair at one location on the pipe, using the pulse-echo configuration to check the entire pipe instantaneously by examining the reflected wave signals without removing the insulating layer. Types of damage to which ultrasonic guided waves are particularly sensitive include voids, porosity, debonding, corrosion, cracking, hole, delamination, resin variation, broken fibre, fibre misalignment, resin crack, cure variation, inclusions and moisture [Su and Ye, 2009].

Smaller sizes of damage reaching a few millimetres can be detected using guided waves in the frequency range from 100 kHz to 1 MHz, as seen in Fig. 2.2 for the case of Lamb waves, this gives GW based damage detection techniques advantage over established NDE techniques. The main reason for the limited damage size sensitivity is that the small wavelength waves could interact with the micro-structural details of the material, such as grain size of rolled sheets, thus contaminating the signal with multiple reflections to the degree that it yields no useful information. Furthermore, less power is required by a Lamb wave transmitter for identifying damage than by other methods since it offers a full coverage of the structure, as seen in Fig. 2.3, the energy required per damage of LW technique is more economical.

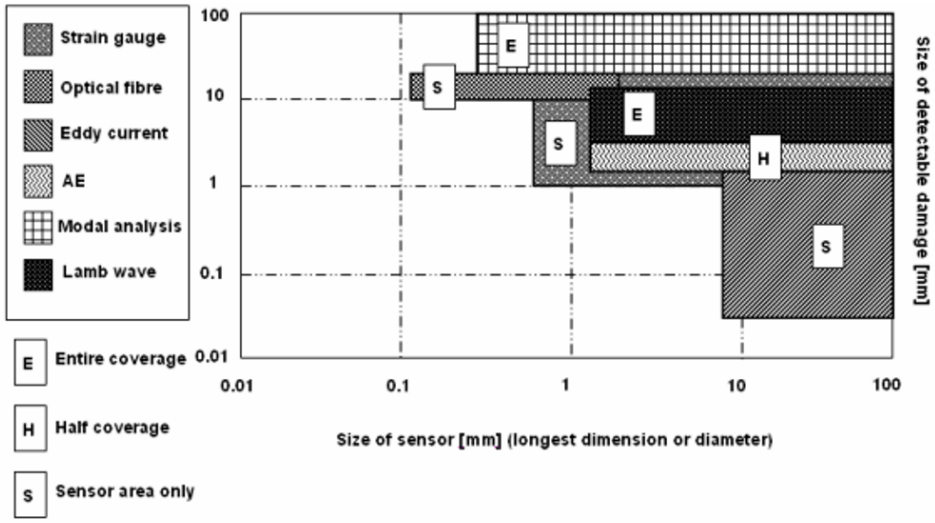

Figure 2.2 Comparison of Lamb-wave-based damage identification with other methods: minimum size of detectable damage *vs* size of sensor [Kessler, 2002].

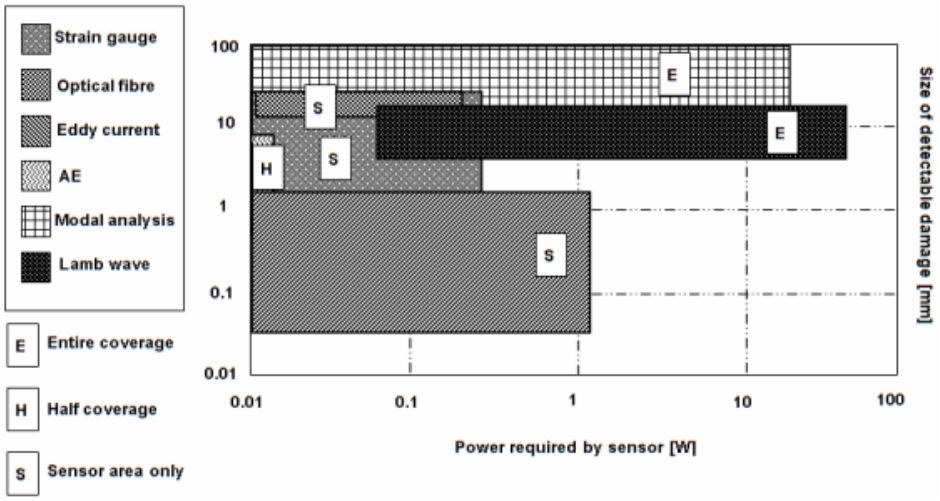

Figure 2.3 Comparison of Lamb-wave-based damage identification with other methods: minimum size of detectable damage vs. power required by sensor (excluding the power required for data acquisition) [Kessler, 2002].

2.3 Guided waves: its nature and generation

This section starts by a short description of the nature of elastic waveguides, and follows by the most typical methods of exciting them in plate-like structures.

2.3.1 Nature of guided waves

The only two modes of wave propagation on elastic waves in solid infinite isotropic medium are the pressure waves and shear waves. Once a free surface in introduced to the medium the incident wave experience a mode conversion as depicted in Fig 2.4. The ratio between the angles of reflection are governed by Snell's Law for elastic waves reflection $\frac{\sin\theta_1}{\sin\theta_2} = r$ where $r^2 = \frac{c_l^2}{c_s^2} = \frac{2-2\nu}{1-2\nu}$.

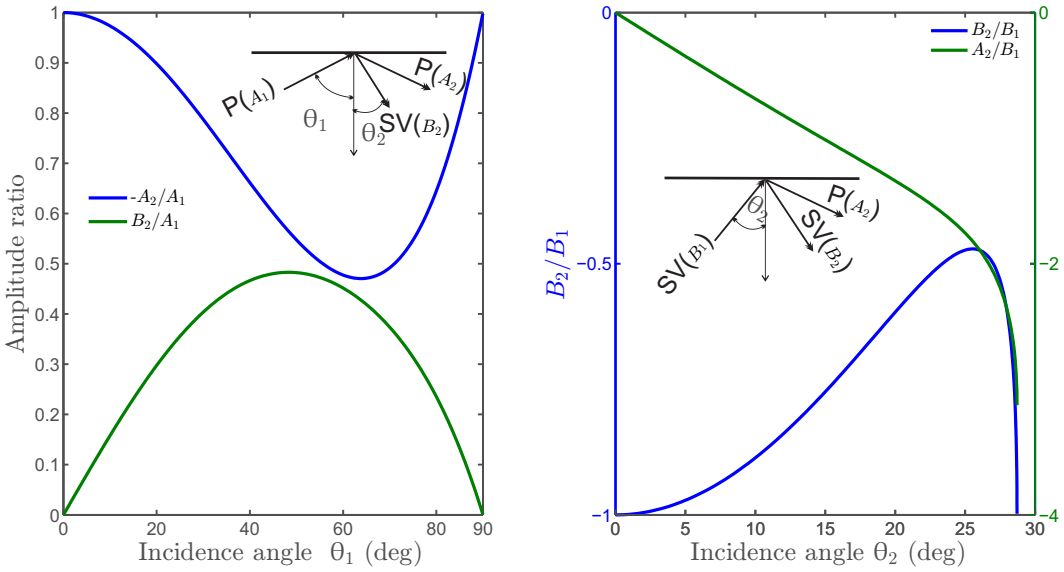

Figure 2.4 The reflection coefficients for incident pressure (left) and shear vertical SV (right), showing the mode conversion due to the presence of the free surface.

So, in the case of existence of two parallel surfaces plate-like structure, there will be multiple reflections with the associated mode conversion from the upper and lower surfaces. After few of these reflections (see Fig. 2.5), the reflected and converted modes (SV and P) start coupling together, generating a standing wave in the thickness direction. Due to the finiteness of the thickness, their are possible multiple vibration modes in the thickness direction.

Hence the mutimodal nature of Lamb waves. The second important feature that needs emphasis is the dispersion, which is nonlinear dependence of the phase velocity on the frequency. This comes from the fact that the propagation in elongated direction is determined by the material properties, the thickness vibration modes available at a specific frequency and the thickness. The relation between the phase velocity and the frequency of vibration is captured in the Rayleigh-Lamb dispersion equations (see sec. 4.1 for a detailed derivation).

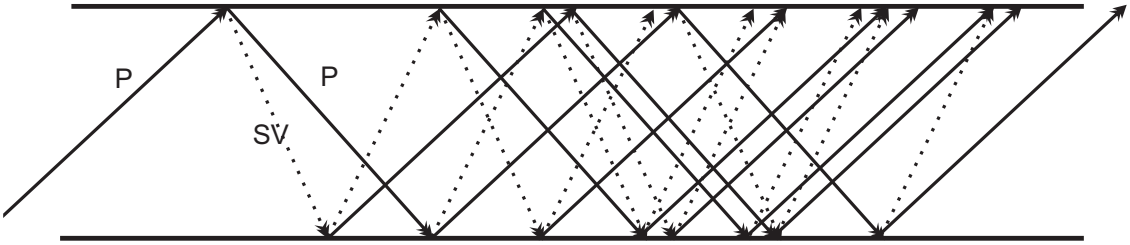

(a) Partial waves from an incident pressure wave for two parallel surfaces of a plate

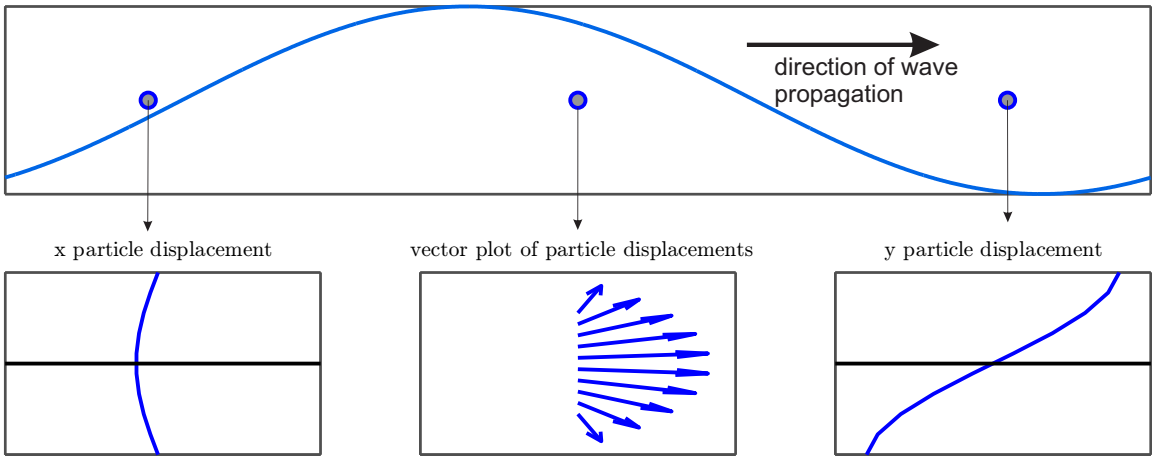

(b) Thickness modes carried by a propagating harmonic wave in the elongated direction

Figure 2.5 The thickness vibrations carried by a travelling harmonic wave in the x_1 direction for the fundamental symmetric Lamb wave.

Waves in elastic structures can be excited using different methods. For NDT purposes the excitation devices that can be used are not necessarily coupled or weakly coupled with the structure, for SHM the wave actuators need to be integrated into the structure or mounted on its surface.

2.3.2 Conventional wedge transducer

Piezoelectricity was discovered by Jacques and Pierre Curie in 1880, when they found that some kinds of crystals were able to generate positive or negative electric charges when pressurized [Katzir, 2006]. A charge is generated when molecular electrical dipoles are caused by a mechanical loading: that is, the direct effect. Conversely, when an electric charge is applied, a slight change occurs in the shape of the structure: that is, the inverse effect. Piezoelectric materials

can be used at the same time as actuators and sensors, obtaining the self-sensing piezoelectric actuator [Dosh *et al.*, 1992].

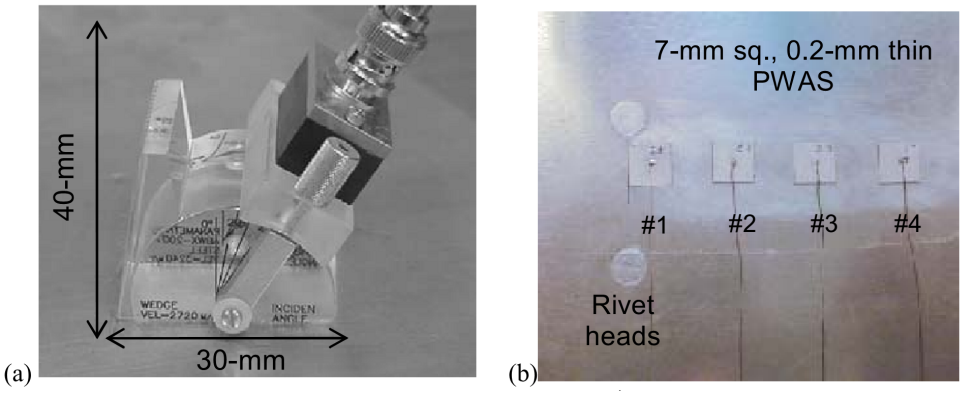

(a) (b)

Figure 2.6 conventional Lamb wave ultrasonic transducer, 25 grams, $400, 40-mm tall (a); PZT element: 0.08 grams, $15, 0.2 mm thin (b) [Giurgiutiu, 2005].

Producing guided waves via a conventional piezoelectric transducer can be done by both contact, and non-contact methods. Contact methods either place the transducer in direct contact with the material using a small layer of coupling agent (such as water, glycerine, or ultrasonic gel) to ensure the best transmission of the acoustic waves into the sample. Or, more typically, an indirect contact arrangement is used, where the transducer is placed in contact with a wedge of a known material (see Fig. 2.6), which, in turn, is in contact with the sample. The wedge material is chosen to aid in transmission of acoustic waves and to obtain better resolution of the incidence of acoustic waves within the substructure. Although it is widely used in NDE applications, the conventional transducers being composed of a piezoelectric resonator disc, a protective layer and a damping block are too bulky and expensive to be used for SHM purposes. For example, the perspex wedge coupled angle-adjustable ultrasonic probes (ultrasonic transducers) frequently used in NDT are normally non-negligible due to their weight and sizes because the properties of the structure can be affected by the transducers considerably. Hence, they are less suitable for using in SHM techniques.

2.3.3 Piezoceramic element

An alternative excitation method is available by piezoelectric lead zirconate titanate (PZT) thin elements, which excite Lamb waves directly through the electromechanical coupling effect in a piezoceramic material. If the applied voltage is oscillating, it produces propagating oscillatory waves due to the in-plane strain coupling between PZT element and the structure. PZT elements deliver excellent performance in guided wave generation and acquisition for SHM purposes, since

it is particularly suitable for integration into a host structure as an in-situ actuator-sensor, as well as for their negligible mass to volume ratio, easy integration, excellent mechanical strength, wide frequency responses, low power consumption and acoustic impedance, as well as low cost [Su *et al.*, 2006].

The PZT actuator action as ultrasonic transducer is fundamentally different from that of conventional wedge transducers. The main differences between the conventional wedge transducer and the PZT element can be summarized in the following points [Giurgiutiu, 2005]:

1. Conventional wedge transducers are weakly coupled with the investigated structure through gel, water, or air. In contrast, PZT element are strongly coupled with the structure through an adhesive bond, as shown in Fig. 2.7.
2. Conventional wedge transducers are resonant narrowband devices, they function only at certain frequencies, the resonance frequencies. In contrast, PZT element is a broadband device not restricted to resonant frequencies.
3. Conventional wedge transducers excite and sense the GWs in the structure indirectly through acoustic waves impinging on the structural surface and the associated mode conversion. In contrast, PZT element excite and sense the guided waves in the structure directly through in-plane strain coupling. In contrast to PZT elements, the ultrasonic wedge transducers are characterized by the displacement coupling. Due to the electromechanical coupling in PZT elements, the PZT elements can also be used as sensors for measuring of propagating waves.

Adding to that the large difference in price and size as depicted in Fig. 2.6, the increasing tendency toward utilizing the PZT elements for LW and in general GW generation in the industry as well as the research is justifiable.

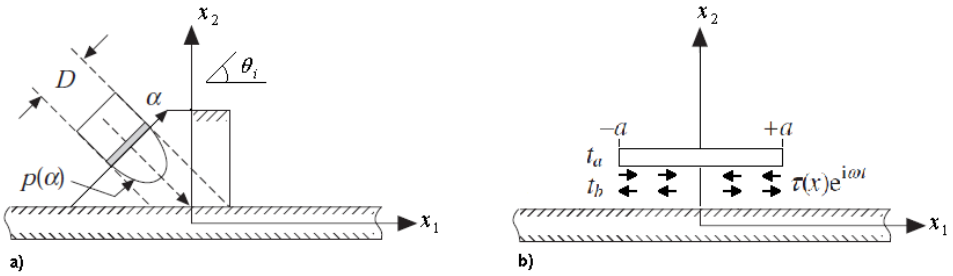

Figure 2.7 An illustration of the wedge-transducer setup for oblique incidence LW generation (a) [Ditri and Rajana, 1997]. and an illustration of the PZT element principle for Lamb wave generation (b).

For efficient use of Lamb waves for damage identification by piezoeceramic elements, the appropriate mode, excitation form, wave magnitude and wavelength should be chosen. These

parameters can be manipulated by selecting the appropriate actuator shape and dimensions and by choosing the driving electric voltage signal. Another important factor which influences heavily the wave propagation characteristics is the adhesive layer (glue) [Crawley and de Luis, 1987; Giurgiutiu, 2005] as explained in Sec. 2.3.5.

2.3.4 Excitation signals and modes of operation

In order to avoid excessive dispersion, enhance the sensitivity of waves to damages and simplify subsequent signal processing and interpretation, it is an adopted practice to use excitation signals with a frequency spectrum that is concentrated near a single frequency.

As a first type of finite excitation pulses the n-cycles sine tone bursts are considered in [Glushkov *et al.*, 2010]:

$$v_n(t) = \begin{cases} \sin \omega_c t, & 0 \leq t \leq nT \\ 0, & t \leq 0 \parallel t \geq nT \end{cases} \tag{2.1}$$

where the period of the oscillations $T = 2\pi/\omega_c$ is defined using a central circular frequency ω_c. Such an excitation signal with 3.5 sine cycles with a central frequency $f_c = \omega_c/2\pi = 100$ kHz is presented in Fig. 2.8(a) with its frequency spectrum plotted in Fig. 2.8(b).

A concentration of the signal spectrum near to its central frequency $f_c = 100$ kHz is clearly observed here, so the wave dispersion can be considerably reduced [Su and Ye, 2009]. The main disadvantage in using such driving signals lies in a possible significant contribution of waves actuated at high frequencies, so that in spite of using relatively low central frequency also high frequency effects should be taken into account.

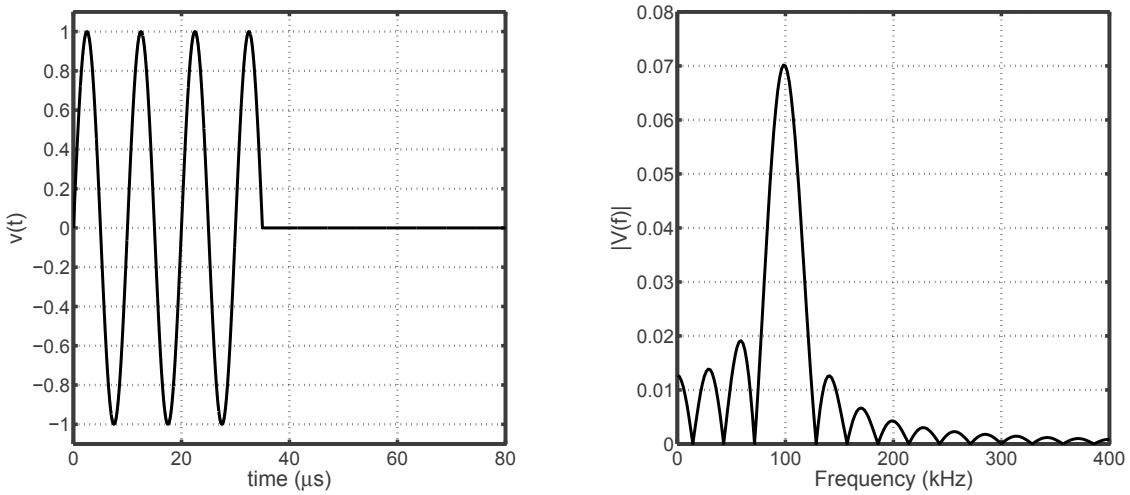

(a) (b)

Figure 2.8 Three and half cycles sine excitation signal (a) with central frequency $f_c = 100$ kHz and its frequency spectrum (b).

Another frequently used pulse is an n cycles sine-windowed sine excitation [Glushkov *et al.*, 2011]:

$$v_n(t) = \begin{cases} \sin \omega_c t \sin \frac{\omega_c t}{2n}, & 0 \leq t \leq nT \\ 0, & t \leq 0 \parallel t \geq nT \end{cases} \tag{2.2}$$

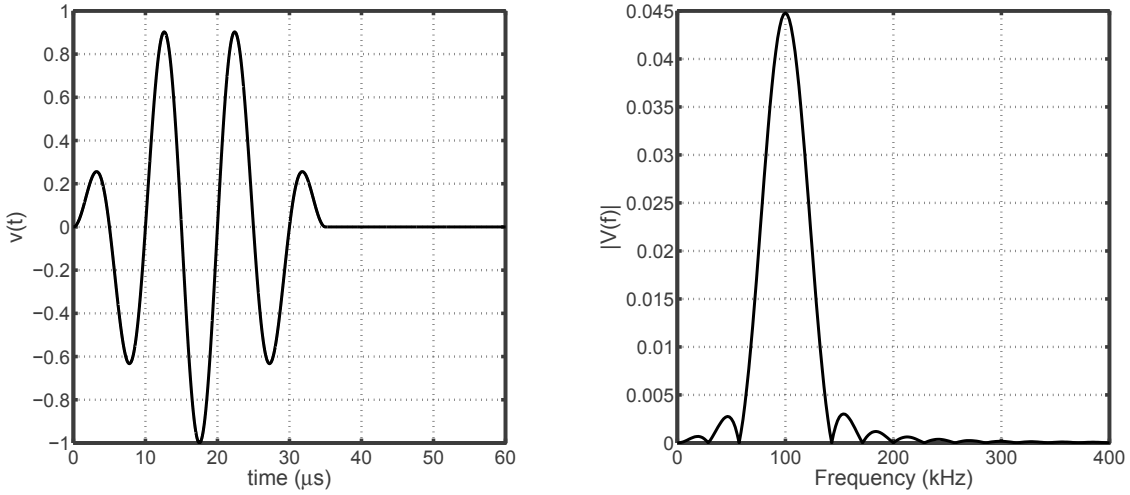

(a) (b)

Figure 2.9 Three and half cycles sine windowed excitation signal (a) with central frequency $f_c = 100$ kHz and its frequency spectrum (b).

As for an n-cycles sine tone burst, the corresponding frequency spectrum of the sin windowed n cycles is also concentrated near the excitation frequency as depicted in Fig. 2.9(b). Comparing this spectrum with the previous one for n-cycles sine tone burst (Fig. 2.8(b)) it can be concluded that amplitudes of high and low frequency waves are much smaller than for the main frequency band. As a result only this main frequency band is needed to be analyzed.

A better yet localization of power around a single central frequency can be achieved in the case of Hann-modulated toneburst [Salas and Cesnik, 2010]:

$$v_n(t) = \begin{cases} \left(1 - \cos\frac{\omega_c t}{n}\right)\cos\omega_c t, & 0 \le t \le nT \\ 0, & t \le 0 \,||\, t \ge nT \end{cases} \tag{2.3}$$

This excitation pulse with central frequency 100 kHz and corresponding frequency spectrum are plotted in Fig. 2.10(a). It seems to be a more suitable for practical applications since the concentration of the power near a central frequency as seen in Fig. 2.10(b) is better, and the contribution of low and high frequency side lobes is almost negligible.

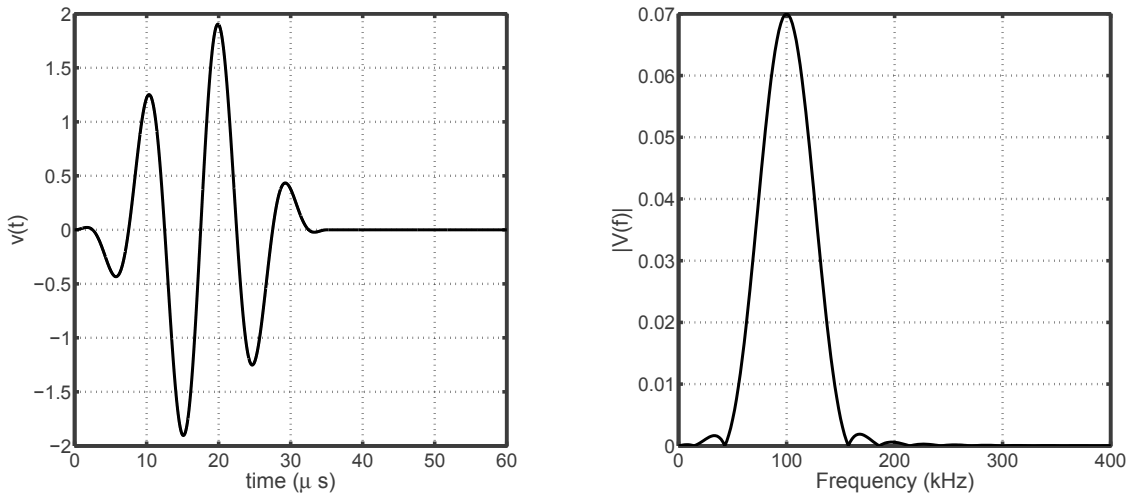

(a) (b)

Figure 2.10 Three and half cycles Hann windowed excitation signal (a) with central frequency f_c = 100 kHz and its frequency spectrum (b).

With increasing number of cycles the signal becomes more and more concentrated near the central frequency allowing the consideration of the excitation as nearly steady state harmonic. A compromise between the required concentration and the spread in the time domain with the increasing number of cycles is needed, since in the time domain this may induce excessive

overlap between the different modes when reflected and converted which complicates the signal processing.

The multi-point excitation concept is considered as a more versatile means to manipulate the generation of Lamb waves [Moulin *et al.*, 2000a]. In these cases, multiple PZT elements are bonded normal to the surface in a straight line to produce a linear array of transducers. Different operational modes of the linear array have been suggested, a linear phased array is operating by adding a time delay to the signal sent to the individual elements of the array, or by interleaving multiple arrays of elements and giving each array a signal with a different time delay. A common mode of operation for linear array of transducers or elements is as a comb transducer [Rose *et al.*, 1998], where each element of the comb (each single transducer or PZT element) vibrates in phase with each other. As can be seen form Fig. 2.11 the beam pattern is symmetric with respect to the array axis, which is a source of ambiguity in imaging. Furthermore, it can be also seen that the array has a considerable side lobe level. Another undesired feature of linear arrays is their azimuth dependent angular resolution, the main lobe width of a steered array increases with azimuth and achieves its maximum at the array's fire ends.

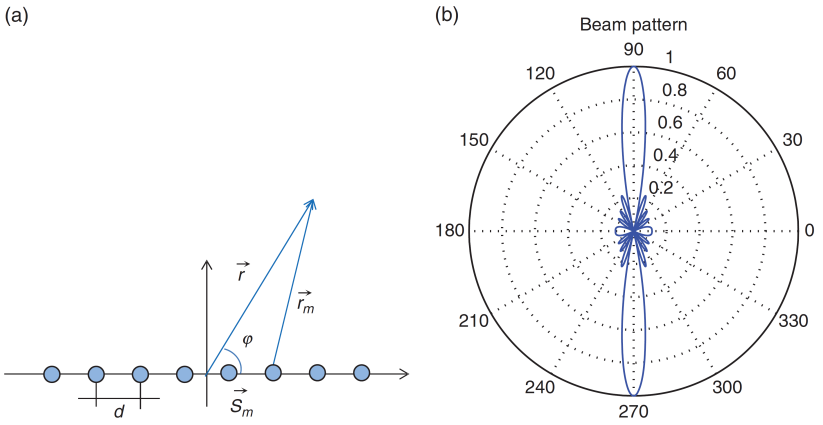

Figure 2.11 (a) Linear uniform array operating in a comb mode (all the elements are excited in phase). (b) A normalized beam pattern of a linear uniform array with 9 elements and $d = \lambda/2$, plotted in polar coordinates as a function of azimuth [Ambroziński, 2013].

A second typical operational mode is the inter-digital mode [Sadler and Maev, 2007], where each element is excited at an inverted phase to its neighbour, so that even elements are excited with wave form $V(t)$, while odd elements are excited with wave form $-V(t)$. Equivalently, an inter-digital array can be created with two interleaved linear arrays, one of which operates with a signal $V(t)$, and the second with signal $-V(t)$ (see Fig. 2.12).

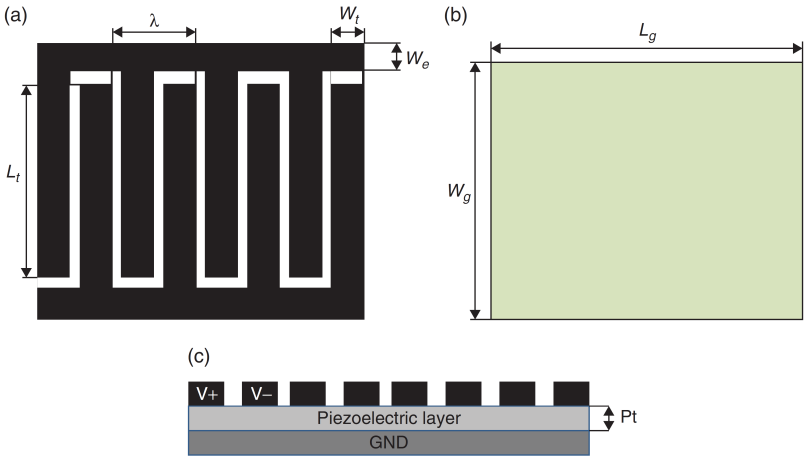

Figure 2.12 Structure of the single-sided interdigital transducer: (a) top electrode; (b) bottom electrode; and (c) cross section [Mańka *et al.*, 2013].

Both the comb configuration, and inter-digital configuration have the common feature that they are linear arrays made of ordinary PZT elements and excite modes dependent on the inter-element spacing. The modes produced by these linear arrays are indicated by the intersection of the line of constant wavelength with the modes on the dispersion curves. A major shortcoming with the different versions of the linear array is the inability to differentiate between echoes coming from either side of the actuators line.

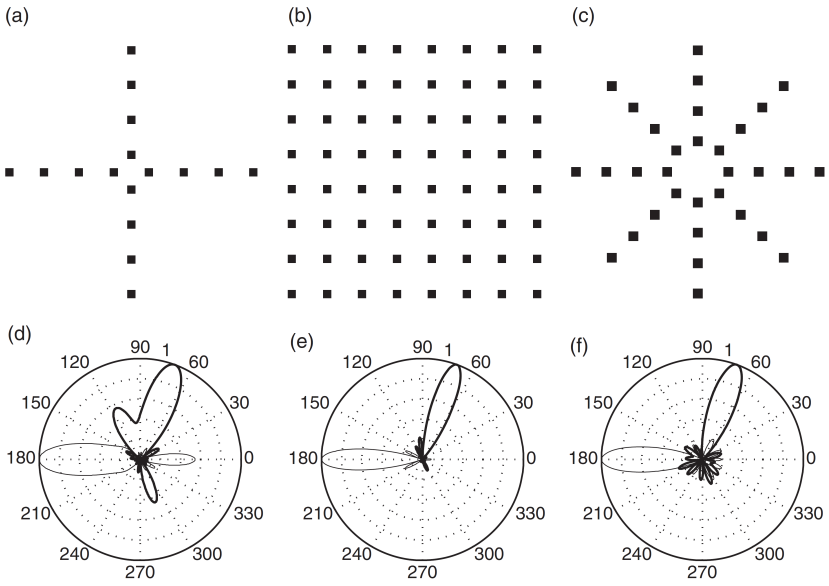

Figure 2.13 Comparison of three 2D array configurations with their beam patterns obtained for steering angles of 70 deg and 180 deg: cross-shaped, 16 elements (a and d); square matrix, 64 elements (b and e); and star-shaped, 32 elements (c and f) [Ambroziński, 2013].

To avoid the shortcomings of linear arrays different researchers considered a number of 2D array topologies characterized by uniform element distribution with high degree of symmetry [Ambroziński, 2013]. A 2D generalized variant of the linear array is the 2D phased array configuration, which alleviates the problem of symmetry indifferentiability. It was initially developed for radar applications where it operates with single-mode electromagnetic waves. The phased array concept was adapted to Lamb waves by Giurgiutiu and Bao [Giurgiutiu and Bao, 2002] under the name *embedded ultrasonics structural radar* (EUSR). The generation of guided Lamb wave by 2D phased array utilizes an array of several closely spaced actuators that are attached to the substructure, with a variety of spatial configurations, as circular, box, and rectangular grid to mention a few. The wave pattern generated by the phased array is the result of the superposition (with destructive/constructive interference) of the waves generated by each individual element.

By sequentially firing the individual elements of an array transducer at slightly different time delays, the ultrasonic wave front can be focused or steered in a specific direction (see Fig. 2.13). Thus, scanning and/or refocusing of the beam is achieved electronically without physically manipulating the transducers, making the phased array concept more versatile to interrogate different regions, specially inaccessible ones, from the same location. The main challenge in all of the above applications is still the fact that Lamb waves are basically multi-modal and generally dispersive.

2.3.5 Piezoelectric actuator coupling effects

Due to the presence of material discontinuity between the actuators and the host medium, complicated stress fields will be generated when external electric fields are applied to the actuators, which are usually difficult to deal with analytically. The interaction between the piezoelectric element and the host structure is a complex process that is affected by the dynamics of the actuators, the dynamics of adhesive layers and the dynamics of the plate itself, *i.e.* this is a *coupled problem*.

The dynamic coupled contact problem of Lamb wave excitation by PZT thin elements was considered by Glushkov *et al.* and Seemann *et al.* in [Glushkov *et al.*, 2007; Seemann *et al.*, 2007] for actuators bonded on one side of the host structure. However, the effect of the bonding layer was not considered, *i.e.* ideal bonding was assumed. The problem was reduced to a system of differential integral equations obtained using the equations of motion of the piezoelectric element, the elastodynamic equations of motion of the host structure, the conditions of ideal bonding between the plate and the piezoelectric element, and boundary conditions. The dynamic coupled contact problem of Lamb wave excitation by PZT was solved by Seemann [Seemann *et al.*, 2007] only for a plane strain case assuming sole dependence of the load and host structure properties on

one of the in-plane coordinates, namely the propagation direction. Wang and Meguid [Wang and Meguid, 2000] studied the static behavior of a thin-sheet piezoelectric actuator attached to an infinite elastic medium using a one-dimensional model to investigate the load transfer between the actuator and the host medium and the stress concentration near the ends of the actuator. The static electromechanical field of a piezoelectric layer bonded to an elastic medium with both interfacial and normal stresses being considered has also been studied in [Zhang *et al.*, 2003a,b]. Due to the several complicating effects, the problem statement in coupled form is not suitable for a real industrial application at the moment due to its complexity.

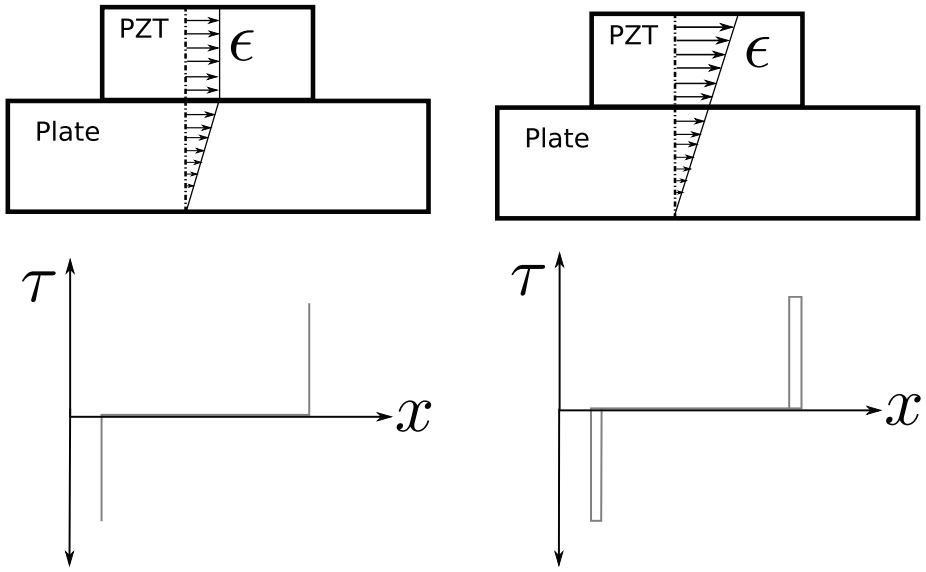

(a) strain distribution of the Bernoulli-Euler model and the induced shear stress in the plate

(b) strain distribution of the Kirchhoff plate model and the induced shear stress in the plate

Figure 2.14 An illustration of the strain distribution and the induced shear stresses in the plate according to different assumptions used in the simplified actuation models.

Different simplified actuator models have been developed over the years to simulate the actuation process. Crawley and de Luis [Crawley and de Luis, 1987] analyzed a beam-like structure with surface-bonded and embedded thin-sheet piezoelectric actuators to study the load transfer from the actuators to the host structure. In this analysis, the axial stress in the actuator was assumed to be uniform across its thickness (see Fig. 2.14(a)). Crawley and Anderson [Crawley and Anderson, 1990] developed a Bernoulli-Euler model of a piezoelectric actuator by considering the linear stress distribution across the thickness (see Fig. 2.14(b)). A refined actuator model based on the plane stress condition was further studied to investigate the electromechanical behavior of a beam with symmetrically surface-bonded actuator patches [Lin and Rogers, 1993]. Plate and shell

models have been extensively used in modeling the electromechanical behavior of piezoelectric structures [Banks *et al.*, 1996; Dimitriadis *et al.*, 1991].

A common methodology for calculating the waves generated by a specific traction applied to the surface of the plate is based on the solution of the wave equation in the spatial Fourier domain [Viktorov, 1967]. This technique has been applied to the analysis of waves generated by several actuator configurations in isotropic structures in [Giurgiutiu, 2005, 2008], where they demonstrated the effect of the size of the actuator as a very important parameter for tuning the excitation to a specific frequency and wave mode.

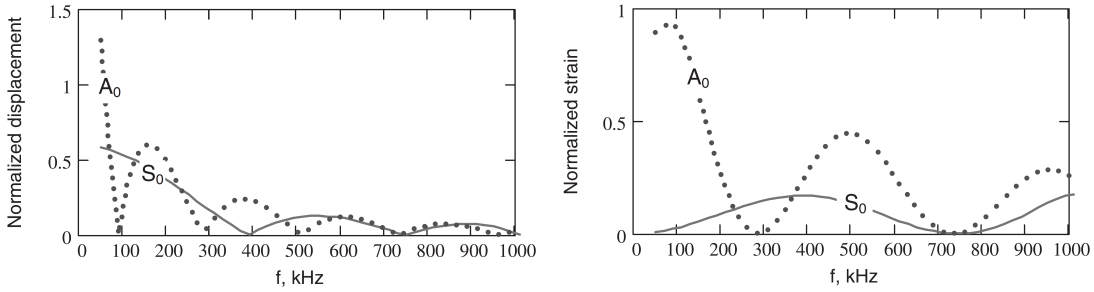

(a) Displacement response for a 14 mm piezoelectric element

(b) Strain response for a 7 mm piezoelectric element

Figure 2.15 Predicted Lamb wave response of a 1.6 mm aluminum plate under piezoelectric element excitation based on the ideal bonding assumption of a one dimensional model developed by Giurgiutiu [Giurgiutiu, 2005].

They concluded as shown in Fig. 2.15(a) and 2.15(b) that maximum amplitude will occur when the piezoelectric element length equals an odd multiple of the half wavelength. In the same time, minima will occur when the piezoelectric element length is integer multiple of the wavelength. These results, which were limited to one-dimensional wave propagation, are extended to the 2D analysis of crested waves propagation in plates in [Raghavan and Cesnik, 2005a] where an analytical model allows the investigation of the effects of the in-plane shape of the piezo-patch. The formulation relies on the solution of the 3D equations of elasticity with the stress field generated by the surface bonded piezoceramic element as a boundary condition. But again, all this FFT based calculations were based on an equivalent loading of the piezo mainly using the idealization put forward in [Crawley and de Luis, 1987], to obtain an analytical description of the stress induced by a thin layer of piezoelectric material. These commonly used assumptions treat the piezoelectric element as a Love-Kirkchoff layered system characterized by linear variations of displacements through its thickness a shown in Fig. 2.14(b). Furthermore, the induced interface shear stress computation assumes that no reacting forces are applied to the piezo element. In addition, electro-mechanical coupling effects are largely simplified by considering a constant

electrostatic field within the piezoelectric layer. This standard assumption allows removing the electrical degrees of freedom from the fully coupled electro-mechanical formulation.

In case of ideal bonding, the forces is typically assumed to be transfered over an infinitesimal region at the edges of the PZT-plate interface, and the induced strain is assumed to be fully equivalent to that will be induced by two concentrated forces applied at its ends (pin force model) as shown in Fig. 2.14. The pin force idealization has several limitations, The model is a good approximation only if Young's modulus and thickness of the actuator are small compared to those of the host structure or the bonding layer is very thin and stiff. Gopalakrishnan *et al.* [Gopalakrishnan *et al.*, 2011] in an attempt to avoid these limiting assumptions, they performed the analysis of the fully coupled electro-mechanical behavior of the layered structure. By discretized the three-dimensional FE formulation, whose generality can be exploited to investigate complex geometries and bonding conditions between the layers. The fully coupled model is used specifically to estimate the interface stresses through the numerical estimation of the excitation functions entering into the wave number solution. So they essentially extracted the shear stress distribution under which the plate is subjected via FE fully coupled analysis for the part of the PZT and the plate bonded into its, and substituted that numerical stress functions into the wavenumber transform method to extract the propagated modal amplitudes. *i.e.* they included the effect of the complicated changes in the actuation mode, but ignored the mechanical coupling between the plate and the acutator. The results they obtained for a circular PZT element are shown in Fig. 2.16. Their results corroborate what have been observed and reported earlier by the author in [Mohamed and Masson, 2010a].

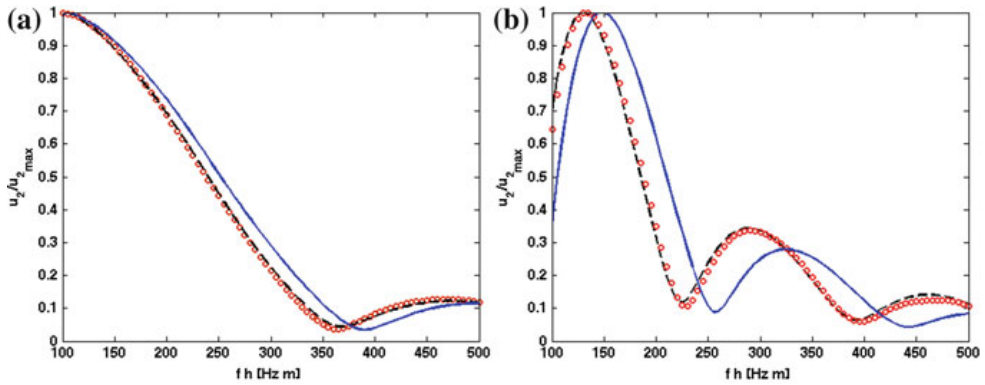

Figure 2.16 Variation of amplitude of the plate in-plane displacement versus excitation frequency at 5 cm from the source. Comparison of analytical (circle), semi-analytical with Dirac applied stress (dashed line) and semi-analytical results with FE-evaluated interface stresses (solid line) for the S0 (a) and A0 mode (b) [Gopalakrishnan *et al.*, 2011].

The PZT element when subjected to an electric voltage produces an interfacial stress between the actuator and the structure. The corresponding stresses are usually unknown and depend on the electric field applied on the electrode surface, its shape, shape of the actuator, the excitation frequency (for the case of harmonic excitation), and on the properties and boundary conditions of the plate under excitation. The assumption of ideal bonding between PZT element and the plate are only one step into a more realistic simulation, the actual coupling between the PZT element and the plate is achieved via a bonding material. Usually the actuators and sensors are bonded onto the host structure using a thin adhesive layer (glue).

The first attempt for modeling of interaction between the PZT element and an isotropic plate through the adhesive layer was proposed firstly by Crawley and de Luis [Crawley and de Luis, 1987] for a plane strain problem. It is based on the quasistatic modeling, taking into account the effect of adhesive layer, considered classically using what is known as *shear lag effect* in the adhesive layer analysis or Volkersen's shear lag analysis [Crocombe and Ashcroft, 2008], and relying on the independence of interfacial stresses on the excitation frequency, *i.e.* the model is static. The configuration studied was of two piezoelectric elements bonded symmetrically on both sides of an elastic thin structure. The in-plane induced strain in the PZT was calculated as:

$$\epsilon_{ISA} = d_{31}\frac{v(t)}{h_a} \tag{2.4}$$

where $v(t)$ is the transient applied voltage, d_{31} the piezoelectric strain coefficient in m/V capturing the coupling between the vertically polarized field and the in-plane induced strain and h_a is the thickness of the actuator. The interfacial stress in the adhesive layer under quasistatic conditions then becomes

$$\tau_{xz} = \frac{h_a\varphi}{a(\varphi+\alpha)}E_a\epsilon_{ISA}\left(\Gamma a\frac{\sinh\Gamma x}{\cosh\Gamma a}\right) \tag{2.5}$$

for $|x| \leq a$, where

$$\Gamma^2 = \frac{G_b(\varphi+\alpha)}{E_a h_a h_b \varphi} \tag{2.6}$$

with $\varphi = \frac{Eh}{E_a h_a}$, where G_b is the shear modulus of the adhesive material, h_b the thickness of the adhesive layer, E, h, E_a, h_a are Young's modulus and thickness of the plate and the actuator respectively. The parameter α is called the modal repartition number, and it depends on the stress, strain, and displacements across the plate thickness. The shear lag parameter Γ was found to depend on modal repartition number α which took the value $\alpha = 1$ for symmetric (i.e., axial) excitation and $\alpha = 3$ for antisymmetric (i.e., out of phase) excitation. This initial analysis was further detailed by Crawley and Anderson [Crawley and Anderson, 1990]. Giurgiutiu in [Giurgiutiu, 2005] extended Crawley's theory [Crawley and Anderson, 1990; Crawley and de Luis, 1987] to the case of only one piezoelectric element bonded to the thin-wall structure by

calculating the total effect as a superposition of symmetric and antisymmetric contributions and found the value for a single-sided piezoelectric excitation to be $\alpha = 4$.

The piezo-plate interaction through the bonding layer is schematically represented in Fig. 2.17(a). The classical shear lag solution described previously can be simplified in case of a very thin bonding layer. Assuming $h_b \ll 1$, one obtains $\Gamma \gg 1$, namely the shear transfer process becomes very rapid and concentrates over some infinitesimal distances at the ends of the PZT element. So the pin force model covered earlier is a limiting case for the classical shear lag analysis.

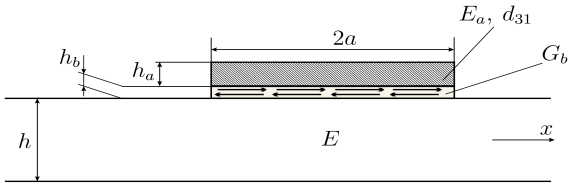

(a) Transmission of mechanical stresses from the PZT element to the host structure through the adhesive layer [Giurgiutiu, 2008].

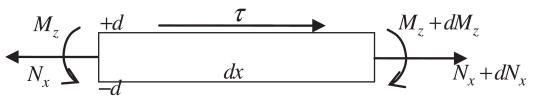

(b) Equilibrium of a differential element of the structure where it is excited only by shear stress transmitted into it through the adhesive layer [Yu *et al.*, 2010].

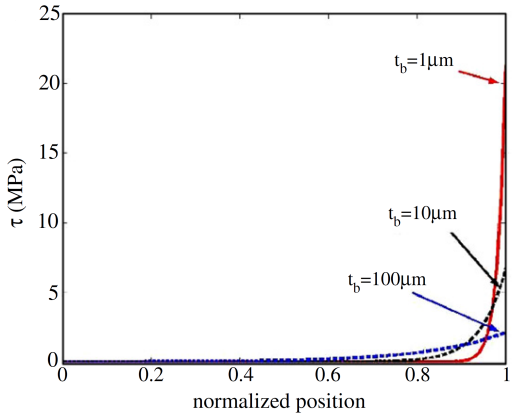

(c) variation of shear-lag transfer mechanism with bond thickness for a PZT element with $E_a = 63$ GPa, $t_a = 0.2$ mm, $l_a = 7$ mm, $d_{31} = 175$ mm/kV attached to a thin-wall aluminum structure $E = 70$ GPa and $t = 1$ mm, through a bond layer of $G_b = 2$ GPa [Yu and Giurgiutiu, 2008].

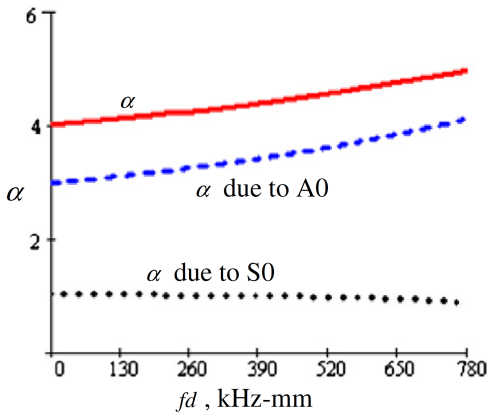

(d) Effect of non-linear stress distribution on the repartition parameter as frequency changes for an Aluminum 2024 plate [Yu *et al.*, 2010].

Figure 2.17 Transmission of mechanical stresses from the PZT wafer to the host structure through the adhesive layer, and the equivalent shear lag model solution.

In an attempt to relax the quasistatic assumption underlying the classical shear lag solution, Yu *et al.* [Yu *et al.*, 2010] have developed a closed form solution for the case of the nonlinear strain

distribution in the plate cross section, which is the case for the mode shapes at higher frequencies. Fig. 2.17(d) shows the variation of α when including this nonlinear distribution into the analysis. It is apparent that, at low frequencies, the previously calculated values from the classical solution $\alpha = 4$ applies. As fd increases, α also increases, from $\alpha = 4$ at low frequencies to $\alpha \approx 5$ at high frequencies. It is also noticeable that, at high frequencies, the relative contribution of S0 and A0 changes, with S0 contribution decreasing while A0 contribution increases. There results demonstrated a shift to higher frequency with the inclusion of the variable repartition parameter with respect to the constant repartition parameter.

In a similar vein, attempting to remedy the observed discrepancy between the theoretically predicted mode tuning curves and the experimentally observed measurements; Sohn and Lee [Sohn and Lee, 2010] developed an adjustment method of relative amplitudes between Lamb wave modes considering the strain distribution across the thickness of the structure in order to reduce the amplitude discrepancy between the experimental and theoretical Lamb waves tuning curves. Moreover, they introduced a PZT size calibration methods using a 3D shear lag model and PZT admittance measurement to estimate the effective PZT size and to minimize the discrepancy between the experimental and theoretical Lamb waves tuning curves where there is a shift to higher frequency of maxima and minima of experimental results compared to theoretical mode tuning curves. They attributed the observed frequency shift effect solely to the presence of the adhesive layer.

2.4 Numerical methods for guided waves simulation

The goal of numerical simulation is to make predictions concerning the response of physical systems to various kinds of excitation and, based on those predictions, make informed decisions. To achieve this goal, mathematical models are defined and the corresponding numerical solutions are computed.

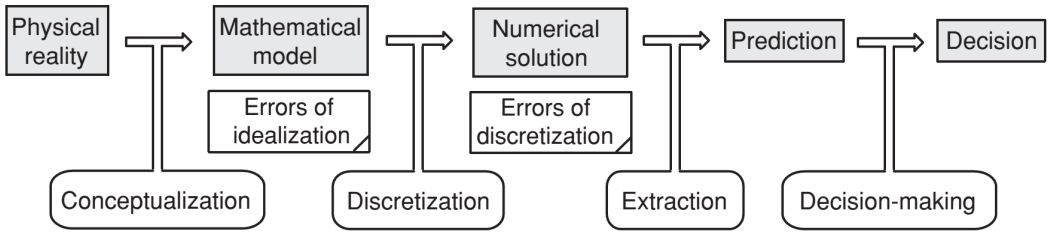

Figure 2.18 The main steps of numerical simulation and the associated errors [Szabó and Babŭska, 2011].

Mathematical models are idealized representations of reality and should never be confused with the physical reality that they are supposed to represent. The choice of a mathematical model depends on its intended use: What aspects of physical reality are of interest? What data must be predicted? What accuracy is required? The main elements of numerical simulation and the associated errors are indicated schematically in Fig. 2.18.

Some errors are associated with the mathematical model and some errors are associated with its numerical implementation. These are called errors of idealization and errors of discretization respectively. For the predictions to be reliable both kinds of errors have to be sufficiently small. The errors of idealization are also called modeling errors, the assessment of its relevance to the problem at hand is commonly referred to as *validation*. Conceptualization is a process by which a mathematical model is formulated. Discretization is a process by which the exact solution of the mathematical model is approximated, the evaluation of its accuracy is commonly referred to as *verification*. Extraction is a process by which the response quantities of interest are computed from the approximate solution.

In this section a review of the most relevant numerical methods to elastic wave undamped propagation are presented with special emphasis on the guided waves simulation. Since the damping in isotropic media, in general, attenuate the wave amplitude either as a geometric spread or in the form of material losses and typically is assumed to have no effect on the wave propagation speed. The mathematical model that will be used as a concrete example is the scalar wave equation without damping, or the one dimensional classical wave equation:

$$\rho\ddot{u} - E\partial_x^2 u = 0 \tag{2.7}$$

which when combined with the specification of the boundary conditions,

$$\text{Free} : \partial_x u(x,t) \mid_{x=0 \text{ or } l} = 0 \tag{2.8}$$

$$\text{Fixed} : u(x,t) \mid_{x=l \text{ or } 0} = 0 \tag{2.9}$$

and the initial conditions

$$u(x,0) = 0 \quad ; \quad \dot{u}(x,0) = 0 \tag{2.10}$$

provides the mathematical model of a constant speed elastic wave propagating in a one dimensional media. This form of description of the mathematical model (*i.e.* partial differential equation with BCs and ICs) is called *strong form* due to the strict requirements it imposes on the approximating function continuity.

2.4.1 Finite difference

Finite difference (FD) method is a collocation method based on the strong form, seeking an approximate solution (based on local interpolation), and requiring that the residual at the specific points of interpolation is exactly zero. In approximating an exact solution numerically, an infinite expansion is typically replaced with a finite representation. $\mathbf{u}(\mathbf{x}) = \sum_{j=0}^{N} \mathbf{u}(\mathbf{x}_j) l_j(\mathbf{x}) + O(N+1)$ where $l_j(\mathbf{x})$ are the characteristic Lagrange polynomials, associated with a set of optimal nodes, and the unknowns are the nodal values of the function $\mathbf{u}(\mathbf{x}_j)$.

We illustrate the development of the centered difference FD scheme in the following steps:
Q1: Given a set of grid points $\{x_j\}$ and a corresponding function values $\{u(x_j)\}$ how can we use this data to approximate the derivative of u?. To be specific, consider a uniform grid $\{x_1, \ldots, x_n\}$ with step size $h = x_{j+1} - x_j$ for each j, and a set of corresponding data values $\{u_1, \ldots, u_n\}$. Let g_j denote the approximation to $u'(x_j)$ the derivative of u at x_j. In order to construct an approximation of the derivative we start by interpolating the known points.
For $j = 1, 2, \ldots, N$

1. Let p_j be the unique polynomial of degree ≤ 2 with $p_j(x_{j-1}) = u_{j-1}$, $p_j(x_j) = u_j$, and $p_j(x_{j+1}) = u_{j+1}$.
2. Set $g_j = p_j'(x_j)$

This algorithmic description could be extended to higher orders as well be demonstrated further. So, if we construct the interpolant based on the existing data using the Lagrange characteristic polynomials $p_j(x) = u_{j-1} l_{j-1}(x) + u_j l_j(x) + u_{j+1} l_{j+1}(x)$, we have for the derivative to differentiate the Lagrange polynomials, and evaluate it at x_j. Thus $g_j = u_{j-1} l'_{j-1}(x_j) + u_j l'_j(x_j) + u_{j+1} l'_{j+1}(x_j)$.

Q2: Knowing the relation between the function values at the uniform grid and its derivative, can we obtain the values of the function from its derivative values? The solution starts by constructing the derivative in matrix equation:

$$\begin{pmatrix} g_1 \\ g_2 \\ \vdots \\ g_N \end{pmatrix} = \begin{pmatrix} l'_1(x_1) & l'_2(x_1) & l'_3(x_1) & 0 & \cdots \\ 0 & l'_2(x_2) & l'_3(x_2) & l'_4(x_2) & 0 \\ \ddots & \ddots & \ddots & \ddots & \ddots \\ 0 & 0 & l'_{N-2}(x_2) & l'_{N-1}(x_2) & l'_N(x_2) \end{pmatrix} \begin{pmatrix} u_1 \\ u_2 \\ \vdots \\ u_n \end{pmatrix} \tag{2.11}$$

If we know the values of the derivative $\mathbf{g}$ but not the function $\mathbf{u}$, we can approximate the function values by inverting the tridiagonal *derivative matrix*. Since the interpolant p_j is unique, this means that the residual are exactly zero at the specific grid points of the approximation and hence the term *collocation*.

In FD methods, the number of interpolation points N is usually small and controls the accuracy of the method. The approximating function is locally interpolated based on a mesh of N points, not necessarily uniform. After substituting this approximation (which for the case of third order unique interpolating polynomial $g_j = \frac{u_{j+1}-u_{j-1}}{2h}$), the governing PDE is converted to a difference equation in terms of the values of the dependent variable over a domain of local support (FD cell). The essential and natural boundary conditions as well as the compatibility requirements at the cell interface with the other cells are enforced, which gives a set of algebraic equations, then solving these equations for the unknown nodal values. For the model equation, the finite difference approximation needs to be constructed for second order derivative by repeated application of the previous process.

The method has two sub categories, namely explicit and implicit methods. In explicit method, the size of cell (also called the step size) is very critical for the solution accuracy. That is, the explicit methods such as central difference scheme, have a constraint placed on the step size. When the step sizes are larger than the critical value, the solution diverges. However, the solution process mandates that the value at the present step is dependent only on the values preceding the current step and hence at every step, we need to solve only an algebraic equation (*conditionally stable*). For the wave propagation problem, this critical step size is determined by the well known Courant-Friedrichs-Lewy (CFL) condition. In the implicit method, the value of an unknown dependent variable also depends on the value preceding the current step and also values ahead of the current step. Hence, we need to solve matrix system of equations at every step. The main advantage is that this method does not constraint the step size (*unconditionally stable*).

In the context of high frequency wave propagation, cell size is very critical. If the size of the damage is very small, then for the purpose of SHM, for the wavelength to be sensitive to damage size this might require a signal having very high frequency content to be applied to the system. At these high frequencies, the wavelengths are very small and hence the cell sizes need to be compatible with the wavelength of the response of the structure. Typically 8 to 20 cells should span each wavelength [Gopalakrishnan *et al.*, 2011].

Several FD schemes have been utilized to model elastic wave propagation. The most important is the staggered finite difference time domain (FDTD) or Yee scheme which was used in modelling electromagnetic waves propagation in wave-guides, and has been used successfully in modelling elastic waves propagation in the computational seismology, based on the velocity-stress formulation [Virieux, 1986]. Higher order FD also have been used for elastic waves propagation simulation [Balasubramanyamy *et al.*, 1996; Zingg, 2000].

2.4.2 Local interaction simulation approach

The local interaction simulation approach (LISA) was originally devised as FD similar scheme that utilizes the computational parallel structure offered by the connection machine, and to avoid the severe errors encountered in conventional FD schemes when modelling sharp change in properties or discontinuities in the propagation medium. Strictly speaking LISA is not purely a finite difference scheme [Delsanto *et al.*, 1994, 1997, 1992]. It is different from the conventional FD schemes in two respects. The first fundamental difference is that LISA starts with a discrete form of the elastodynamic equations to be solved exactly, which avoids the problems associated with the smoothing of any discontinuity in the FD schemes. The second difference is in the handling of the boundary conditions, where in LISA the boundary is integrated directly into the simulation without any need for a specific redefinition at the boundary as compared to FD schemes [Sundararaman and Adams, 2008] . The LISA can be used for wave propagation in any heterogeneous material of arbitrary shape and complexity. The method discretizes the structure under investigation into a grid of cells. The material properties are assumed to be constant within each cell but may differ between cells. A standard explicit time discretization is employed for time marching. The algorithm can be derived from the elastodynamic wave equation for elastic, isotropic and homogenous media given as:

$$(\lambda + \mu)\nabla(\nabla \cdot \mathbf{u}) + \mu\nabla^2\mathbf{u} = \rho\ddot{\mathbf{u}} \tag{2.12}$$

where λ and μ are Lamé constants, ρ is the material density and $\mathbf{u}$ is the vector of particle displacements. For the 2D plane strain case Eq. (2.12) simplifies to:

$$\rho\ddot{u}_i = (\lambda + \mu)\partial_{li}u_i + \mu\partial_{ll}u_i \text{ and } i = 1, 2; l = 1, 2 \tag{2.13}$$

This equation can be rewritten in matrix form as:

$$\overbrace{\begin{pmatrix} \lambda+\mu & 0 \\ 0 & \mu \end{pmatrix}}^{A}\begin{pmatrix} \partial_{11}u_1 \\ \partial_{11}u_2 \end{pmatrix} + \overbrace{\begin{pmatrix} \mu & 0 \\ 0 & \lambda+2\mu \end{pmatrix}}^{B}\begin{pmatrix} \partial_{22}u_1 \\ \partial_{22}u_2 \end{pmatrix} + \overbrace{\begin{pmatrix} 0 & \lambda+\mu \\ \lambda+\mu & 0 \end{pmatrix}}^{C}\begin{pmatrix} \partial_{12}u_1 \\ \partial_{12}u_2 \end{pmatrix} = \rho\begin{pmatrix} \ddot{u}_1 \\ \ddot{u}_2 \end{pmatrix} \tag{2.14}$$

The structure is discretized into cells, as shown in Fig. 2.19. Consider A, B, C, are matrices containing material data, D and F are the vectors of nodal displacements and forces respectively, and τ is the 2D stress tensor. The junction of the four cells defines the nodal point P. The second time derivatives across the four cells are required to converge towards a common value at point P. This ensures that if the cell displacements are continuous at P for the two initial times t = 0 and t = 1, they will remain continuous for all later times. A finite difference scheme is used to

calculate spatial derivatives in the four surrounding cells to P. This results in four equations in eight unknown quantities, thus the remaining four equations are needed. Imposing continuity of the stress tensor τ at the point P and using further finite difference formulae gives four additional equations in the unknown quantities, thus allowing these unknown spatial first derivatives to be solved.

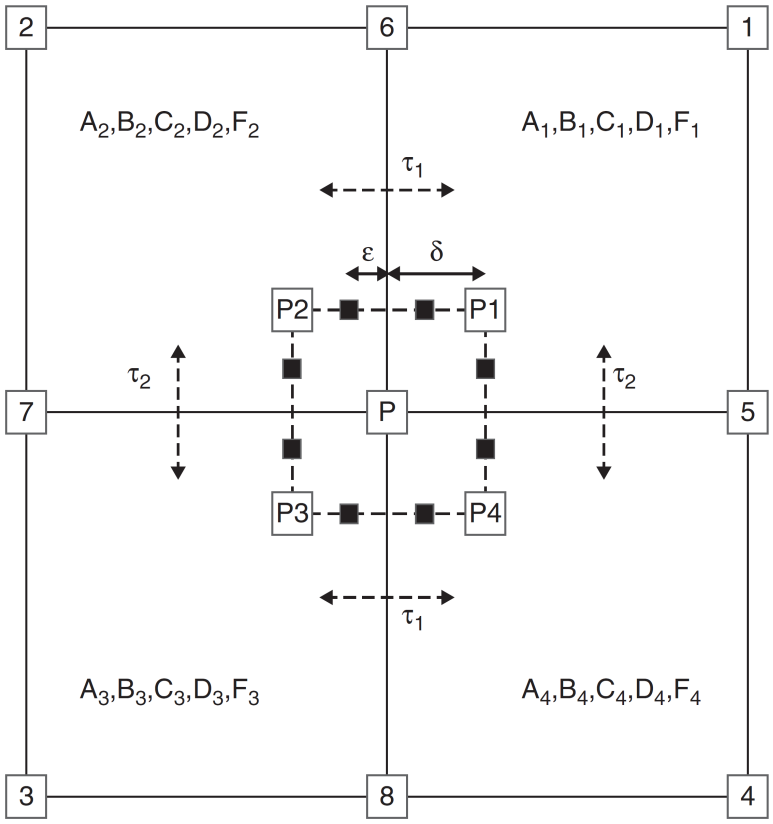

Figure 2.19 Intersection of four LISA cells for the 2D case. Each cell contributes to the common node P, thus the equilibrium conditions are considered separately and matched by using stress continuity relations [Paćko, 2013].

This reveals the main advantage of LISA over FD; the fact that the local interaction nature of boundaries in the model is enforced at each cell interface. The sharp interface model (SIM) is used to average physical properties at the interface grid points which represent intersections of the four elementary cells. In other words, cells are treated as discontinuous and displacements and stresses are matched at interface grid points. The SIM allows for a more physical and unambiguous treatment of interface discontinuities for different layers of material than the typical FD schemes. The classical FD algorithms require parameters smoothing across material interfaces, which depends on the applied scheme, therefore are not very accurate for sharp interfaces of high

impedance mismatch. The SIM leads to more accurate results when wave propagation problems in complex media with complex boundaries are studied [Packo *et al.*, 2012].

Agostini *et al.* [Agostini *et al.*, 2003] used the LISA to model the Lamb waves propagation in a glass fibre reinforced plate considered as transversely isotropic in four cases, a through hole, and notch and subsurface cracks, as well as delaminations, their results agreed well with experimental measurements.

In a series of papers Lee and Staszewski [Lee and Staszewski, 2003a,b, 2007a,b] implemented LISA for modelling GW propagation, and interaction with defects. An interesting feature is that they implemented the LISA on a serial PC, as did Sundararaman and Adams in [Sundararaman and Adams, 2008]. This reflects the versatility of the method, the high computational speed is an advantage in using the LISA on parallel structures, but it is not restricted to the parallel computers. Common to all the previously mentioned papers modelling GW with LISA is that they simulated only the fundamental modes A0 and S0, to avoid the complexity associated with the multi-mode propagation.

Lee and Staszewski [Lee and Staszewski, 2007a] applied the 1D model for the diffusion bond model, with five different layers, a piezoelectric medium representing the excitation layer, a copper layer, a coupling layer and again a copper layer and a piezoelectric layer representing the sensor. The total of five layers were surrounded by vacuum, the excitation signal was Hanning modulated five cycle sine wave. For the 2D case they simulated the excitation from a piezoelectric piston, inducing normal stresses (8 mm diameter, and 0.5 mm thickness) distributed spatially as a Gaussian distribution.

2.4.3 Pseudo-spectral method

Pseudo-spectral (PS) method could be seen as extending the FD collocation points to the limit of all the collocation points, *i.e.* the value of the local derivative is dependent on all the values of the function at the collocation points. The mesh of points is uniform only in the case of periodic boundary conditions and the approximating function is expanded in terms of Fourier series.

In the case of non-periodic boundary conditions, the mesh that will achieve spectral accuracy is the zeros of any of the Jacobi polynomials, usually Chebyshev or Legendre is used [Trefethen, 2001]. The convergence rate is spectral *i.e.* the approximation error decays in an exponential rate $O(\Lambda^N)$, where Λ is Lebesgue constant. This rate distinguishes spectral methods from FD methods, where the rate for the pth order method would be $O(1/N^p)$, reflecting polynomial rather than exponential convergence.

The solution is highly accurate provided that the sought solution is smooth enough [Fornberg, 1996]. Pseudo-spectral methods handle nonlinearities in material properties as well as material interfaces more robustly than FD. Although, for hyperbolic systems, to which the elastodynamic problem belongs, the boundary conditions needs special treatment [Carcione, 1991, 1994, 1996], mainly as first order in velocity-stress formulation. The excitation signal is prescribed as a source force term or as an initial condition.

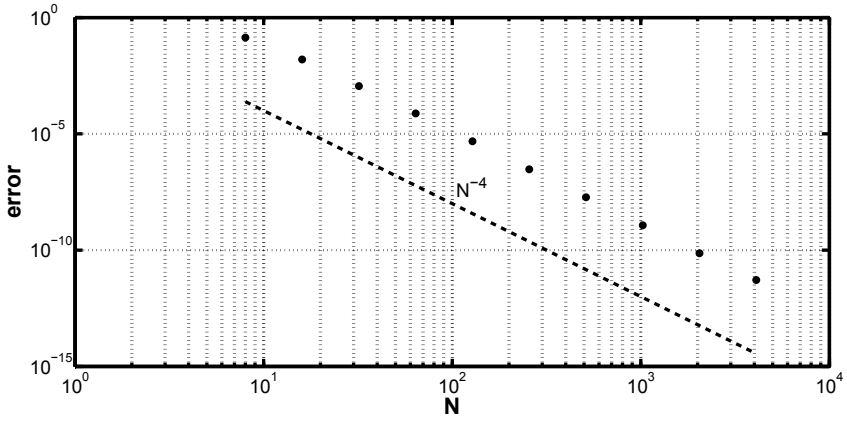

(a) Fourth-order convergence of the finite difference differentiation process. The use of sparse matrices permits high values of N.

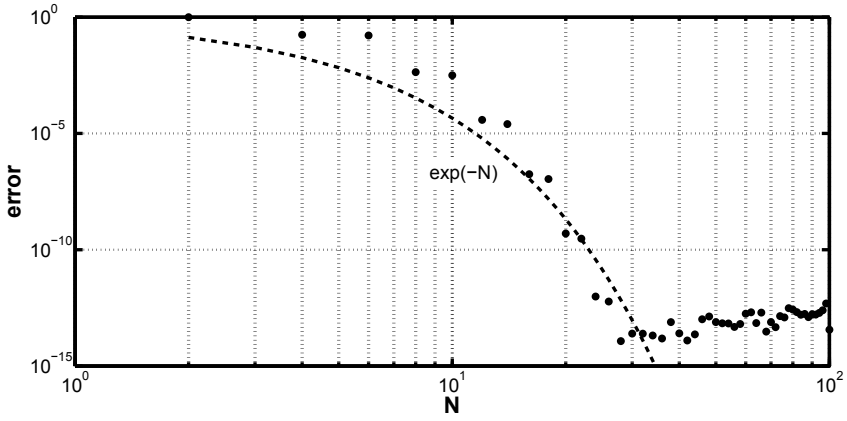

(b) Spectral accuracy of the pseudospectral differentiation, until the rounding errors take over around 10^{-14}. The matrices are dense, but the values of N are much smaller than in FD case.

Figure 2.20 A comparison between the fourth order FD differentiation of a smooth function $f(x) = \exp(\sin(x))$, and the spectral differentiation of the same function, the error estimate was the max norm.

For the *same accuracy*, the PS method, with its accurate spatial differentiation as shown in Fig. 2.20(b) compared to the algebraic convergence rate of the FD differentiation shown

Fig. 2.20(a), requires several orders of magnitude less computer memory and computation time compared to other numerical modelling schemes. For example, for 2-D and 3-D modelling, the memory requirements for the PS method are about 1/8 and 1/64 of that for the fourth-order finite-difference scheme, respectively [Furumural and Takenaka, 1996].

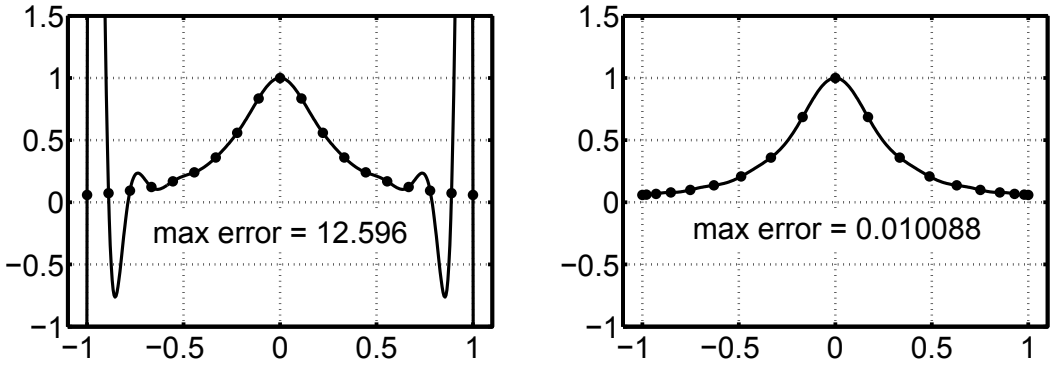

(a) Equispaced points (b) Legendre points

Figure 2.21 Degree N interpolation of $u(x) = \frac{1}{1+16x^2}$ in $N+1$ equispaced and Legendre points for $N = 18$. With increasing N, the errors increase exponentially in the equispaced case *i.e. the Runge phenomenon* whereas in the Legendre case they decrease exponentially, the error estimate was the max norm.

This spectral accuracy in the differentiation is related to the so called *Runge Phenomenon*. Runge phenomenon was discovered independently more than a century ago by Carl Runge, C. Meray and Emilie Borel: Their discovery was that polynomial interpolation on an equispaced grid was unreliable. Borel gave an example of non-convergent interpolation at the Heidelberg Mathematical Congress in 1904, but apparently did not publish it [Boyd and Ong, 2009]. Even if $f(x)$ is analytic for all real x, its interpolants $f_N(x)$ will diverge as $N \to \infty$ near the endpoints $x = \pm 1$ if $f(x)$ has singularities within the "Runge Zone" in the complex x-plane [Epperson, 1987]. When smooth functions are interpolated by polynomials in N equally spaced points, the approximations not only fail to converge in general as $N \to \infty$, but they get worse at a rate that may be as great as $2N$ [Trefethen, 2001]. If one were to differentiate such interpolants to compute derivatives, the results would be in error by a similar factor. This phenomenon is illustrated in Fig. 2.21(a), where the same example of Runge was used. The effect of using the clustered points at the edges of the interval on the accuracy of the polynomial interpolant is dramatic as shown in Fig. 2.21(b), where the interpolation points are the zeros of the Legendre polynomial.

2.4.4 Boundary element method

In the Boundary Element method (BEM), the governing PDEs over the domain of interest are converted into two components, one containing the integral over the domain surface and the second component is a volume integral over the domain. The solution of the second component comprised of the volume integral is obtained with the aid of special Green's functions for a point load on an infinite space, the so called *Fundamental Solutions*. The first component of the PDE, namely the boundary integral on the surface of the domain are solved via standard FEM. This process reduces the dimensionality of the problem by one, that is a 2D problem become 1D and a 3D problem becomes a 2D problem. However, the main disadvantage of this method is that the fundamental solutions are available only to small subset of problems. Analyzing non-linear problems are very difficult. There is a great advantage of using BEM to SHM problems. This is because, the internal part of the domain of interest need not be modeled. However, if a crack or some damage is present in the structure, they form the part of the boundary. As in the other two methods, the mesh sizes for the boundary should be small enough to be comparable to the wavelength of the input signal.

Rokhlin [Rokhlin, 1980, 1981] started using the BEM to study the diffraction and resonance phenomena of Lamb waves by a finite parallel crack in a plate using Wiener-Hopf technique and multiple diffraction methods.

Cho and Rose [Cho and Rose, 1996] developed a hybrid BEM combined with the normal mode expansion technique to study Lamb wave mode conversion from the edge of a plate and its interaction with surface breaking defects. Later Zho and Rose [Zhu and Rose, 1999] used the same hybrid BEM technique to simulate the wave generation procedure with time delay linear periodic actuator arrays. Experimental results also were presented for two typical time-delay periodic arrays to qualitatively validate the theoretical designs. The effects of the array parameters on the array performance, such as the selectivity of Lamb modes and effectiveness of Lamb wave generation, were investigated through the 2-D phase velocity-frequency spectrum analyses as well as Lamb mode wave structure calculations. Their work have been further advanced in [Rose *et al.*, 2000] [Cho and Rose, 2000]. Rose and Zhao [Rose and Zhao, 2001] extended the same technique to demonstrate the potential of SH wave for defect sizing. They studied the interaction of the $N0$ mode SH wave with various crack and corrosion boundaries in a structure. Zhao and Rose [Zhao and Rose, 2003] used the hybrid BEM normal mode expansion technique to the study of both Lamb and SH waves of any mode of incidence onto a half-elliptical shaped surface breaking defect.

Ballandras *et al.* [Ballandras *et al.*, 2009] developed a model combining periodic FEA and a BEM to study the problem of elastic guided waves and surface waves generation using surface acoustic wave transducers arranged in periodic structures in the saggital plane with general geometry. Mazzotti *et al.* [Mazzotti *et al.*, 2013] used a 2.5D boundary element technique to extract the dispersion curves for waveguides with material attenuation. They analyzed waveguides of complicated cross-section by discretizing its contour only with monodimensional elements. Their method was based on a regularized boundary integral formulation leading to a nonlinear eigenvalue problem in the complex axial wavenumber for any fixed frequency. The eigenvalue problem is solved in the complex wavenumber domain by using a contour integration method to extract the dispersion relations.

2.4.5 Finite element method

Either FD or PS methods are based on the strong form of governing partial differential equations, making the method geometrically inflexible, and also pose problems in implementing boundary conditions. The finite element method (FEM), and more generally numerical methods based on Bubnov-Galerkin approximation, which rely on the variational formulation of the governing equations, offer more flexibility in both of these respects.

The general approach of the FE method is as follows. Starting from the PDE with given boundary conditions, multiplying it by appropriate test functions and integrating over the whole simulation domain. Then performing a partial integration arrives at the variational formulation, also called the weak formulation. Applying Galerkin's approximation method using finite elements (FE) results in the algebraic system of equations.

In the FEM, the solution for an elastodynamic problem is based on an assumed polynomial approximation for displacements. These assumed displacement polynomials are required to satisfy the weak form of the governing differential equation, which yields the stiffness and the mass matrices.

These elemental matrices are assembled to obtain global stiffness and mass matrices. The assembly process ensures equilibrium of forces between connected elements. This procedure will give the discretized form $\mathbf{M}\ddot{\mathbf{u}} + \mathbf{C}\dot{\mathbf{u}} + \mathbf{K}\mathbf{u} = \mathbf{F}(t)$ where $\mathbf{M}$ and $\mathbf{K}$ are the global mass and stiffness matrix and $\ddot{\mathbf{u}}$, $\dot{\mathbf{u}}$ and $\mathbf{u}$ are the acceleration, the velocity and the displacement nodal vectors, respectively. The damping matrix $\mathbf{C}$ is typically obtained from a proportional damping scheme as a linear combination of stiffness and mass matrix [Zienkiewicz and Taylor, 2005; Zienkiewicz *et al.*, 2005].

There are two methods of solving the obtained system of ordinary differential equations, the Direct Time Integration (DTI) and the Mode Superposition (MS) Method. The MS method of solution is not practical for wave propagation analysis, because the solution requires extraction of all the higher order eigenmodes, which is computationally prohibitive. The preferred solution method is the time marching scheme, which is essentially a finite difference scheme applied to a system of 2nd order ODEs, thus two different strategies are available, the explicit methods which are conditionally stable and the unconditionally stable implicit methods [Liu and Quek, 2003b].

For wave propagation and highly transient dynamic problems, explicit methods are normally preferred [Hughes, 1987]. In the time marching scheme, the solution process takes place over a small time step Δt. The solution of the dynamic equations will give displacement, velocity and acceleration histories. The solution process is repeated for n time steps until the total time $T_{total} = n\Delta t$ is reached. The solution computation time is directly proportional to the number of degrees of freedom in the model, which is usually very high for wave propagation problems.

For sufficiently smooth problems on regular domains, h-type FE exhibit an algebraic convergence to the exact solution, *i.e.* the approximation error is proportional to $1/N^{p+1}$, where N is the number of degrees of freedom (DOFs) of the problem, and p is the polynomial order of the element shape functions. Low-order ($p = 2$ or 3) h-type elements, which are preferred in structural dynamics for their computational efficiency, have a serious deficiency in that they propagate elastic waves poorly [Sprague and Geers, 2007].

Alternatively, one may employ p-type FE where the spatial domain is discretized as with h-type elements, but solution accuracy is improved by increasing the polynomial order p of element shape functions, thereby increasing the number of DOFs in an invariant mesh of elements. For sufficiently smooth problems on regular domains, p-type elements may exhibit exponential convergence, *i.e.* the error is proportional to $\exp(\beta N)$ for some constant β that depends on the polynomial degree [Babuška and Suri, 1994].

Utilizing its inherent versatility for modeling complex geometries, simulation studies of Lamb waves (LW) interaction with defects almost exclusively were based on FEM. Alleyne and Cawley [Alleyne and Cawley, 1992] used a 2D, uniform square mesh of 4-noded quadrilateral with more than 10 elements per wavelength to model the interaction of the fundamental Lamb modes with surface breaking straight sided notches. The excitation of each individual mode was achieved by imposing the appropriate mode shape as a time dependent displacement boundary condition. The transmission ratio is evaluated based on a 2D FFT. Lowe *et al.* [Lowe *et al.*, 2002; Lowe and Diligent, 2002] used a similar FEM approach, but with lumped mass formulation, to study the reflection characteristics of the two fundamental modes, they have included the case of

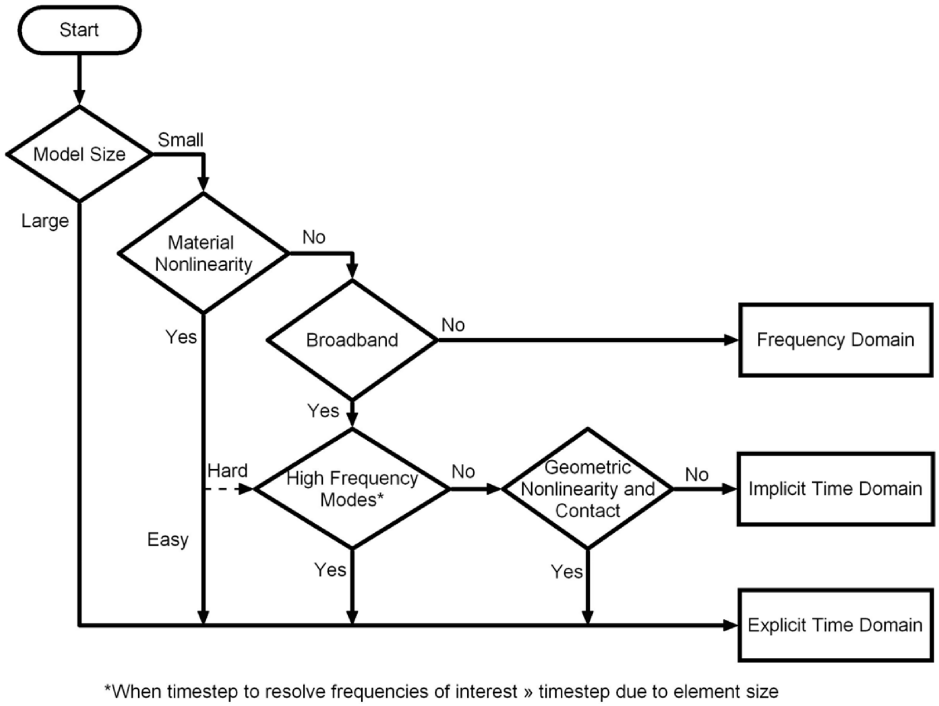

Figure 2.22 FEM road map for efficient simulation [pzflex, 2005].

zero width crack, by eliminating the connectivity between the neighboring nodes. There results were compared with experimental results obtained using water wedge excitation by a conventional pressure transducer for the A0 mode, and edge mounted transducer for exciting S0 mode. Lua *et al.* [Lua *et al.*, 2008] implemented a three dimensional FEM to study the interaction of oblique incident Lamb waves at a varying range of frequencies (0.2-0.6 MHz) with a through-thickness crack of different lengths in aluminium plates. They used the Hilbert transform to extract the reflections and transmission coefficients. Nieuwenhuis *et al.* [Nieuwenhuis *et al.*, 2005a,b] used FE to model Lamb wave generation and reception by a PZT surface bonded element, and compared their results with an equivalent force model, the agreement with the experimental results were better than the pin-force model, although for the reception, they implemented a coupled piezoelectric elastodynamic analysis using COMSOL multiphysics.

The semi-analytical finite element (SAFE) method was also applied for the study of Lamb waves propagation in both isotropic homogeneous plates and anisotropic composite laminated plates [Ahmad *et al.*, 2013]. Dispersion curves for these complex materials were calculated using SAFE. The effect of obstacles on the reflection and transmission of Lamb waves was also considered. SAFE was also used for 2D point force response analysis. By applying the 2D point response analysis for perfectly bonded strip actuators, mode tuning behavior is calculated. Consideration for the edge reflections were also implemented by applying the ratio of Lamb

mode reflections at plate edges, and representing the reflection at plate edges using infinite plate solutions, the semi-analytical finite element method can be applied for transient response simulation [Ahmad and Gabbert, 2012].

[Benmeddour *et al.*, 2011] A three dimensional (3D) hybrid method combining the classical finite element (FE) method with the semi-analytical finite element (SAFE) technique is developed. This hybrid method was employed to study the interaction of guided waves with non-axisymmetric damages in cylinders. The near field surrounding the damage is analysed with the 3D FE method. The solution is expanded into sums of guided modes on both inlet and outlet cross-sections. Such eigenmode expansions enabled the separation into ingoing and outgoing waves, i.e., incident, reflected and transmitted waves. Using the SAFE method, elastic guided modes are then computed at the cross-sections thus reducing the analysis to two dimensions (2D). The amplitudes of the incident modes are imposed, whereas those of the scattered modes are determined by solving the global system of the 3D hybrid FE-SAFE model.

Moulin *et al.* [Moulin *et al.*, 2000a,b] used a coupled finite element-normal expansion method to study the in-phase and phase-delayed excitation of Lamb wave using multiple transducers integrated with composite laminates, by considering surface bonded or embedded transducers. Due to the complexity of the problem, the input, *i.e.*, the acoustic field related to each eigenmode and the surface forcing function, was derived through the FEM. Grondel *et al.* [Grondel *et al.*, 2002] used the same approach for optimizing the spacing between double surface bonded piezoelectric elements with in-phase excitation. Another benefit for using the normal mode expansion, is minimizing the computational cost by treating the PZT actuator with the bonded part of the structure by the FE, and applying the normal mode expansion for the wave propagation. A similar economy was targeted by several FEM based studies [Kim *et al.*, 1997; Sze and Pan, 1999], where Kim *et al.* [Kim *et al.*, 1997], developed a transition element between the PZT actuator modeled by a 3D 8 nodes brick element, and the plate modeled using a 2D plate element, to minimize the computational cost. [Mori *et al.*, 2013] studied the reflection and transmission of Lamb waves at an imperfect joint of plates numerically by the modal decomposition method and the finite element method. The joint was modeled as a spring-type interface characterized by distributed normal and tangential stiffnesses. The analysis focused on two fundamental symmetric and antisymmetric Lamb modes. The frequency-dependent reflection and transmission characteristics of these Lamb modes are computed for different interfacial stiffnesses, together with the generation behavior of localized, non-propagating higher-order Lamb modes.

In [Casadei *et al.*, 2014] Casadei *et al.* used a new development in the FEM, the multiscale FEM, to investigate the interaction between elastic waves and defects of different nature. The Geometric Multiscale FEM,formulates multi-node elements which can model small geometrical

features without resorting to excessive mesh refinements and without compromising the quality of the discretization in the uniform portion of the domain.

2.4.6 Spectral element method

It is important to distinguish between two different spectral (SEM) element approaches reported in the literature. The first one in the frequency domain and is based on the fast Fourier transform (FFT-SEM) [Doyle, 1989; Gopalakrishnan *et al.*, 2008], whereas the second one is the time domain spectral element method (TD-SEM). TD-SEM refers to a spectral spatial approach. In his first work on this subject, Patera [Patera, 1984] proposed a subparametric approach for standard FEM. This means that the high-order polynomials are used for field variable approximation while the geometry is described by a low order polynomial. He introduced high-order Lagrange interpolants along with the Chebyshev-Gauss-Lobatto integration rule. This leads to an exactly diagonal mass matrix which naturally allows for efficient explicit time integration.

Frequency domain spectral element

The frequency domain spectral element method based on fast Fourier transformation (FFT-SEM) was initially proposed by Beskos and Narayan [Beskos and Narayanan, 1983]. But the main impetus have been given to it by Doyle and co-workers [Doyle, 1989]. Among many frequency domain methods based on FFT, the FFT-SEM is potentially the most effective numerical tool for wave propagation modelling [Lee, 2009]. The FFT spectral element method is essentially a finite element method formulated in the frequency domain. However, its method of implementation are quite different from the conventional FEM. In the FEM the solution for an elastodynamic problem is based on an assumed polynomial approximation for displacements. These assumed displacement polynomials are required to satisfy the weak form of the governing differential equation, which yields the stiffness and the mass matrices.

FFT-SEM on the other hand uses in most cases the exact solution to the wave equation in the frequency domain as its interpolating function. Unlike the polynomials in the case of FEM, a need to deal with complex exponentials as the interpolating functions arises. The exact solution will have wave coefficients corresponding to the incident and reflected wave components. If one wants to model an infinite domain, then the reflected components have to be dropped from the interpolating functions. This gives what is called the throw-off elements formulation. Using the complex interpolating functions for the displacement, the dynamic elemental stiffness matrix is formulated. One can formulate this stiffness matrix as in the case of conventional FEM, using the weak form of the governing equations. This approach will involve complex integration. Alternatively, one can formulate the dynamic stiffness matrix using stress or force resultant

expressions. This method is more suitable for structural dynamics simulation as it does not involve complex integration.

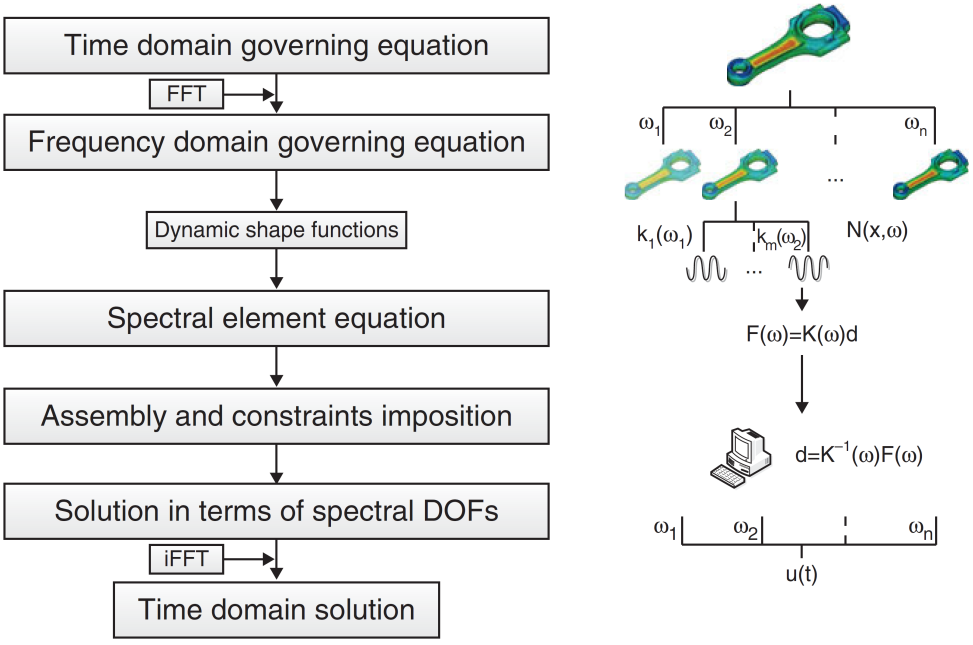

Figure 2.23 The FFT-SEM workflow. The main ideas are the Fourier transform and the dynamic shape functions [Paćko, 2013].

The basic steps involved in the analysis using FFT-SEM are as follows. First, the given forcing function is transformed to the frequency domain using the forward Fast Fourier Transform (FFT). In doing so, it is necessary to choose the time sampling rate and number of FFT points to decide on the analysis time window. Care should be taken to ensure that the chosen window is good enough to avoid what is called *wraparound* problems which arises from the periodic nature of FFT [Gopalakrishnan *et al.*, 2008, 2011]. The FFT output will yield the frequency, the real and imaginary part of the forcing function, which are stored separately. Over a big frequency loop, the element dynamic stiffness matrix is generated, assembled and solved as in the case of conventional FEM. Then, the dynamic shape functions are built for each frequency. These are derived, directly from the governing equation, which means that the functions are exact and as accurate as the governing equation [Banerjee, 1997]. The exact solutions have pair components representing incident and reflected waves. This is of particular importance for the artificial boundary conditions that may be formulated at this level by influencing each part independently, e.g. throw-off elements. This constitutes a frequency dependent dynamic stiffness matrix. However, assembly and solution steps have to be performed at each sampled frequency. This does not pose a major computational hurdle since the problem sizes are many orders smaller

than conventional FEM. The solution process is first performed for a unit impulse, which directly yields the frequency response function (FRF). The FRF is then multiplied with the load to get the required output in the frequency domain. This output is then transformed to the time domain using the inverse Fourier transform (IFFT). The workflow and employed numerical tools are presented in Fig. 2.23.

The key advantages of the FFT-SEM over the conventional FEM include: high accuracy due to the exact form of the shape functions, minimization of the number of degrees of freedom (DOFs) since one element provides a very accurate solution for a regular part of the domain, relatively low computational cost (to the resolution offered), effective for frequency-dependent problems, since it is formulated in the frequency domain, easy formulation of absorbing boundary conditions and the explicit availability of the system transfer functions.

This technique is well suited to simple problems, but becomes difficult to use for complex geometries. Some difficulties also arise with the periodic nature of FFT when 2D or 3D problems must be analysed. The FFT-based SEM demands additional throw-off elements due to the periodic nature of the FFT. Because of that Doyle solves only problems of infinite or semi-infinite rods and beams [Doyle, 1989]. To overcome the problem of the periodic nature of the FFT the Laplace transform can be applied instead of the FFT [Igawa *et al.*, 2004]. Another limitation of the FFT-SEM method is the difficulty of solving coupled problems such as piezoelectric element bonded to an elastic structure.

The FFT-SEM also has serious drawbacks that limit its application to certain classes of problems. The most salient of those are: the nonavailability of exact shape functions, in general, except only for relatively simple systems (this usually poses a problem for multidimensional systems). Approximate methods may be used but the accuracy decreases. The method cannot be applied directly to time-variant, nonlinear systems. The solution involves inverse time frequency transformation which may cause numerical problems (e.g. inverse Laplace transform) and deteriorates the solution quality [Paćko, 2013].

Time domain spectral element

The spectral element method was derived from two previously developed numerical approaches, which are the pseudo-spectral methods and the Finite Element Method. The former one is known to be very accurate (it is exact up to the Nyquist frequency), whereas the latter has the advantage of being highly flexible when dealing with complex geometries.

The spectral element method in time domain (TD-SEM) could be considered a special case of the *p*-version FEM except for the specific approximation functions it uses. Elemental interpolation nodes are located at points corresponding to zeros of an appropriate family of Jacobi polyno-

mials (usually Legendre or Chebyshev). A set of local shape functions consisting of Lagrange polynomials, which are defined at these points, are built and used. SEM differs from both PS and conventional FE methods in two ways: first; pure spectral methods employ high degree approximating functions with support over the entire domain, and second; finite element methods use low degree approximating functions with compact support (piecewise polynomials) . Spectral element methods exploit the advantage of high degree functions inherent in pure spectral methods, along with the flexibility finite element methods provide in representing geometrically complex domains. Henceforth, SEM will be used as acronym only for spectral element method in the time domain.

The SEM was first conceived by Patera [Patera, 1984] in the context of computational fluid dynamics. The idea was to combine the advantages of the global spectral methods with those of the finite element method. That is, the accuracy and rapid convergence of the former and the geometrical flexibility of the latter. The name was deduced from the fact that the SEM has the same spectral convergence behaviour as the PS when the order of interpolating polynomials N tends to infinity. Patera originally used Chebychev system as a basis. The main fields of application of SEM currently include: fluid dynamics [Canuto *et al.*, 2007; Karniadakis and Sherwin, 2005], acoustics [Dauksher and Emery, 1996], seismology [Komatitsch *et al.*, 2000; Komatitsch and Tromp, 1999; Komatitsch and Vilotte, 1998; Komatitsch *et al.*, 1999; Tromp *et al.*, 2008].

However, it appears that the use of SEM for problems of propagation of elastic waves in structural elements is receiving an increasing attention more recently. Kudela *et al.* [Kudela *et al.*, 2007a] applied SEM in the time domain for detection of waves scattered by a lumped mass in 1D structures based on simplified rod and Timoshenko beam theories. Numerical results have been compared to those obtained from the classical finite element approach as well as experimental results. The same approach have been extended for the analysis of the propagation of transverse (SV) elastic waves in a 2D composite plate, using the first-order shear deformation theory for plates in [Kudela *et al.*, 2007b]. Peng *et al.* [Peng *et al.*, 2009] implemented a 3D Lamb wave model for damage detection in an Al plate, with a rectangular through thickness cut, they used nodal forces for excitation of the two fundamental Lamb modes.

Desceliers *et al.* [Desceliers *et al.*, 2008] introduced a numerical hybrid method to simulate wave propagation in a multilayer semi-infinite medium subjected to given transient loads. The method has a low numerical cost and is relatively straightforward to implement. It is based on a time-domain formulation associated with a 2D-space Fourier transform for the variables associated with the two infinite dimensions and uses a finite element approximation in the direction perpendicular to the layers.

Zak *et al.* [Zak *et al.*, 2006] used spectral element method in the analysis of in-plane elastic wave propagation in a composite panel. The composite panel is modelled by a 36-node spectral membrane finite elements with nodes defined at Gauss-Lobatto-Legendre points. As approximation polynomials they used fifth order Lagrange polynomials. In order to calculate the element stiffness and mass matrices the Gauss-Lobatto quadrature has been applied. Numerical calculations were carried out for various orientations of reinforcing fibres within the panel as well as for various volume fractions of the fibers.

Zak [Zak, 2009] presented a novel formulation of a spectral plate finite element for analysis of propagation of elastic waves in isotropic structures. In his formulation, the spectral plate finite element shape functions are approximated by Chebyshev polynomials of the first kind. The element makes use of on an extended form of the displacement field that enabled him to investigate selectively or simultaneously both symmetric and anti-symmetric modes of Lamb waves propagating in plate structures.

Schulte *et al.* [Schulte *et al.*, 2010] presents what they call a flat shell spectral element approach, which is an implementation of the Mindlin plate theory. They included the effect of the piezoceramic excitation, via equivalent loading, to simulate the effect of piezoceramic element bonded to the plate, which ignores the presence of the piezoceramic and substitute a mechanical load generated by the piezoceramic.

Zak and Krawczuk [Zak and Krawczuk, 2011] discusses various numerical issues associated with the spectral element formulation for longitudinal waves in rods, they conclude that out of three nodal distributions considered, the Lobatto node distributions offer the best properties of the elemental shape functions and characteristic matrices. In a similar vein, Witkowski *et al.* [Witkowski *et al.*, 2012] studied the 2D spectral elements in both static and dynamic formulations. They verified the absence of *Locking effect* and spurious zero-energy modes as opposed to the low order conventional finite elements for the same case. Another advantage of the spectral element demonstrated in their work that the solution accuracy is less sensitive to element distortions than the conventional finite elements.

Peng *et al.* [Peng *et al.*, 2010] presents a two-dimensional spectral element method for characterizing wave propagation in composite beam structures for the purpose of damage detection. The interaction of Lamb waves with delamination in an 8-ply carbon fiber/epoxy (CF/EP) laminate is investigated, and some mechanisms of interaction between Lamb wave modes and delamination are revealed in detail. They demonstrated that the reflection at the far end of the delamination is much stronger in magnitude than that from the near end, and when the delamination length is comparable to the wavelength of the wave mode, the reflections from both ends of the de-

lamination merge into one. They concluded that the fundamental antisymmetric (A0) mode is more suitable for identification of delamination in multi layered composite structures than the fundamental symmetric (S0) mode, especially when the delamination is in the symmetric plane.

Kim *et al.* [Kim *et al.*, 2008] developed a full 3D SEM-based method for modelling the outputs of a built-in piezoelectric sensor in response to an excitation induced by a built-in piezoelectric transducer in ultrasound range in isotropic metallic structure integrated with a network of piezoelectric transducers and sensors. They are the only ones in the literature to include a coupled electromechanical field equations and employs an explicit time-integration scheme for the elastodynamic solver and Gauss elimination for static electric fields, which makes their approach a *weak coupling* approach.

Ha and Chang [Ha and Chang, 2010] in an attempt to develop an efficient spectral element for modelling piezoelectric actuator-induced high-frequency wave propagation in thin plates. They proposed a hybrid spectral element that supposedly take advantage of both a high-order spectral element in the in-plane direction and a linear finite element in the thickness direction in order to efficiently analyse Lamb wave propagation in thin plates. Their claims about the computational efficiency may be valid, but the approach to use reduced integration in the thickness directions raises serious limitations regarding the range of frequency that could be simulated accurately.

Mulder [Mulder, 1999] analyzed the accuracy of the 1D acoustic SEM scheme. He concluded that the error introduced by the spurious, or nonphysical, modes can be neglected and that SEM using Gauss-Lobatto nodes and quadrature rules was more accurate than Chebyshev-SEM or classical FEM. He also analyzed the asymptotic behavior of the grid dispersion.

Cohen [Cohen, 2002] analyzed the grid dispersion of the 1D, 2D, and 3D acoustic SEM schemes analytically using Gauss-Lobatto nodes and quadrature rules. In his approach, he used an eigenvalue formulation and Taylor-series to get the asymptotic behavior of the grid dispersion. In his results, he showed dispersion curves for the 1D case using second or third-order methods and various time-stepping schemes.

As for the elastic FEM or SEM, there seems to be fewer grid-dispersion or stability-analysis results available in the literature. This has led to set the order of the elements and the grid spacing according to the results available for the acoustic case [Chaljub *et al.*, 2007; Komatitsch *et al.*, 2005].

Babase and Sen [Basabe and Sen, 2007] extended the approach introduced by Cohen [Cohen, 2002] to analyze the acoustic FEM and SEM schemes of any order and developed a similar approach to analyze the elastic FEM and SEM schemes of any order. For the lowest order elements, they use this approach to develop numerical dispersion formulas in closed form, and

for the higher-order elements the numerical dispersion curves were calculated numerically. They also demonstrated that the numerical dispersion curves of some classical acoustic and elastic FD compare well with those corresponding FEM schemes. As a result, they confirm the assumption in [Chaljub *et al.*, 2007; Komatitsch *et al.*, 2005] on the applicability of grid dispersion and stability criteria of the acoustic case to the elastic case.

Seriani and Oliveira [Seriani and Oliveira, 2008] studied the numerical dispersion of spectral element methods of arbitrary order for the isotropic elastic wave equation in two and three dimensions by a simplified modal analysis of the discrete wave operators. This analysis is based on a Rayleigh quotient approximation of the eigenvalue problem that characterizes the dispersion relation. This approximation takes full advantage of the tensor product representation of the spectral element matrices. They computed dispersion graphs that show the dependence of the phase/group velocity, the polarization error, and the numerical anisotropy on the grid resolution as well as the polynomial degree with both Gauss-Lobatto-Chebyshev and Gauss-Lobatto-Legendre collocation points.

Overall, the time domain spectral element have the following advantages that makes it more suitable for the simulation purpose of relatively high frequency guided waves propagation:

- Almost free from the shear locking effects and zero-energy modes,
- less sensitive to element distortions, due to the well conditioning of the elemental matrices,
- free from the Runge oscillations, which might contaminate the accuracy even of similar p version of finite element, with equidistant nodal distribution,
- have less numerical dispersion for wave propagation.

2.4.7 Comparison of numerical methods for guided waves simulation

As a visual cue for the main differences between the different methods used, Fig. 2.24 illustrates the type of dependence of the derivative approximation for each of the discussed methods. Table 2.3, attempts to quantify the major differences between the numerical methods mentioned.

The estimated CPU time expenses are roughly based on the fact that a significant portion of computational cost (often more than 50-90 % of the total running time) goes in solving the linear system of equations, The CPU time for solving a symmetric positive-definite system of equations is given by; CPU = Cn^{α}, where n is the number of unknowns or the number of degrees of freedom in the FE or SE model. The values of C and α depend on the choice of linear solver, as well as sparsity and conditioning of matrix [1] [Fish and Belytschko, 2007].

1. This matrix could be the differentiation matrix corresponding to FD of PS methods, or the stiffness matrix in either FE or SE.

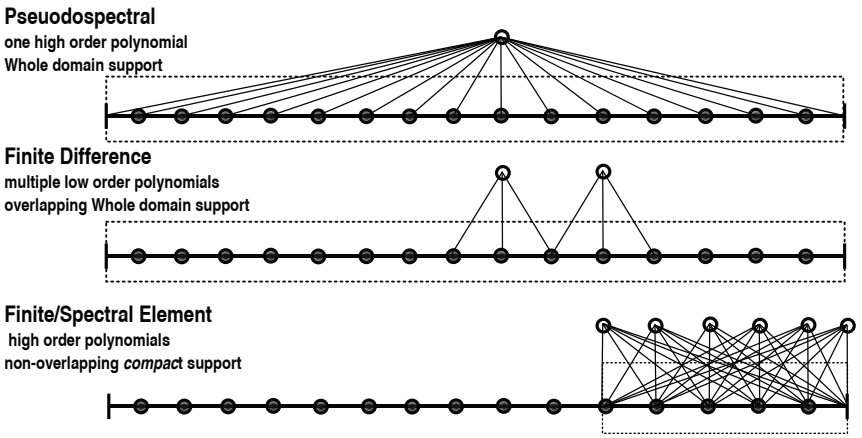

Figure 2.24 A schematic of the computational dependence of the derivative approximation for the different numerical methods. The thin, slanting lines illustrate all the grid points (black circles) that directly affect the estimates of derivatives at the points shown above the lines by open circles. The thick black vertical lines in the bottom grid are the subdomain (element) walls.

Table 2.3 Comparison of numerical methods

Method	**Geometrical Flexibility**	**Convergence** [a]	**Computational Time** (α)	P/λ_{min} [b]
FD pth order	poor	$O(1/N^p)$	$nCp^{\alpha-1}$ (1-2)	6
PS Fourier	poor	$O(\Lambda^N)$	Cn^α (3)	2
PS Chebyshev	poor	$O(\Lambda^N)$	Cn^α (3)	π
FEM pth order [c]	Excellent	$O(1/N^p)$	$Cn^{3\alpha}$ (1-2)	20
FEM pth order [d]	Excellent	$O(1/N^p)$	Cn^α (1-2)	20
TD-SEM Jacobi	Excellent	$O(\Lambda^N)$	$Cn^{2\alpha}$ (3)	5
TD-SEM Legendre	Excellent	$O(\Lambda^N)$	Cn^α (3)	5

a. N is the total number of the grid points

b. The minimum number of points per wavelength needed to resolve a wave, the memory requirements is assumed to be $\propto P/\lambda_{min}{}^d$ where d is the dimensionality.

c. Consistent mass matrix

d. Lumped mass matrix

If the matrix is dense, the value of the exponent α is 3 for most commonly used direct solvers. For sparse matrix it is in the range of 1-2. Another factor that would make the comparison difficult, is that in FE or SE based on any Jacobi polynomial except Legendre's, there is the added cost of inverting the mass matrix, which could increase considerably the amount of time, so it is assumed that it will increase the CPU time [2] by multiples of α. Although, in the case of FD (pth order), the

2. The Jacobi SEM would take the same value of α for the mass matrix inversion and solution of the linear system, but for FEM with consistent mass matrix (dense) it will take a value of 3, while for the sparse stiffness matrix it will take the value 1-2.

CPU time for solving the linear system is $O(p^{\alpha})$, but C in this case is approximately multiplied by n/p, for each time step. The comparison is based on one time step CPU. Another important fact, n the number of the unknowns are dependent on p, polynomial degree used in approximation for both the FEM-p version and TD-SEM. This demonstrates the major advantage in adopting the SEM as a CAD tool for SHM actuators and sensors pattern design.

2.5 SHM challenges to numerical simulation

In this section the main challenges facing the use of numerical simulation as a CAD tool for SHM systems are reviewed.

2.5.1 Computational efficiency or errors

The classical error estimates of FEM such as the convergence rate which is based mainly on the local truncation error are typically used to assess the accuracy, and consequently the efficiency of the different algorithms. Though there are certain peculiarities of the wave propagation problem that pose an extra need for a more representative error measures. As put by Bathe [Bathe, 1996]:

> *The major difference between a structural dynamics problem and a wave propagation problem can be understood to be that in a wave propagation problem a large number of frequencies are excited in the system. It follows that the one way to analyse a wave propagation problem is to use a sufficiently high cut-off frequency to obtain enough solution accuracy. The difficulties are in identifying the cut-off frequency to be used and in establishing a corresponding finite element model.*

The computational efficiency is not merely a time issue, as put elegantly by Lloyd N. Trefthen [Trefethen, 2011], it is the main goal of the numerical analysis and engineering discipline:

> *Numerical analysis is the study of efficient algorithms for mathematical problems not the study of rounding errors on computers. If computers had infinite precision numerical analysis would still be here; if they had infinite speed, most of it would not.*

Another aspect of computational efficiency is that it reflects certain accuracy requirements. So, the main reason behind the huge computational requirements is the existence of certain conditions to ensure the accuracy of the solution. In this section, the main type of error introduced by numerical discretization, and how it constitutes the main reason for the computational efficiency problems facing the SHM simulation are explored. Since the FEM is the most dominant in the field of simulation of the elastic wave propagation, it seems appropriate to confine the present

discussion to FEM. Although the original ideas for this analysis originated mainly in the FD analysis, the ideas are applicable to all the previously covered methods.

Typically the wave propagation problem are tackled using explicit time integration scheme, as shown in Fig. 2.22. Generally the highest frequency of interest is determined first, then the representative element size h_e is determined based on the wavelength resolution required. The size of the elements are chosen in a manner so that the propagating waves are spatially resolved. Alleyne and Crawley [Alleyne and Cawley, 1991] recommends that more than 10 nodes per wavelength be used, while in [Ansys Inc., 2011], the recommendation is much higher of the order of 20 nodes per minimum wavelength $h_e = \lambda_{min}/20$. These recommendations can be considered as a rule of thumb, but it again requires reconsideration when trying to model guided waves in thin structures. The mode shapes that a rod or a plate could experience vary with the frequency, and in that case a need to consider whether the mesh chosen is capable of representing the mode shapes accurately enough even after considering the wavelength in the propagation direction.

The numerical models for SHM must be able to accurately represent ultrasonic waves with frequencies in the MHz range. These high frequencies require an extremely high resolution in time (the time increments between calculated solution points), even for very short real times (μs range). Since these MHz frequencies have very short wavelengths, so as the numerical model must have small element size to accurately resolve these spatial features; this high spatial resolution requires very small elements, in the range of mm or even fractions of it, this refining directly leads to very small time steps in explicit conditionally stable schemes for time integration. An additional complication of this small element size is that a large number of elements (and thus a large system of equations) is needed to model a realistic component. As a result, the solution generally requires the inversion of a large stiffness matrix, leading to formidable computational demands [Moser *et al.*, 1999; Mulder, 1999].

Choosing an adequate integration time step, Δt, is very important for the accuracy of the solution. In *general*, the accuracy of the model can be increased with increasingly smaller integration time steps but this depends on the time integration scheme employed. With time steps that are too long, the high frequency components are not resolved accurately enough. On the other hand, too small time steps are considered a waste of computational resources. Therefore, a compromise must be found. For the implicit time integration schemes, this compromise is 20 points per cycle of the highest frequency of interest $\Delta t = 1/20 f_{max}$; this gives accurate solutions in an efficient manner [Moser *et al.*, 1999]. If the excitation gets closer to a step function, the ratio 20 might not provide sufficient temporal resolution. In some cases, this ratio has to be increased up to $\Delta t = 1/180 f_{max}$ [Ansys Inc., 2011]. Also, the time step can alternatively be related to the time the fastest possible wave needs to propagate between successive nodes in the mesh. This means

that the fastest mode in the case of guided waves propagation controls the choice of the time step, which is normally the interpretation that is adopted in the literature for the CFL condition for explicit time schemes.

The view of CFL number as a ratio between the numerical speed with which the information is propagating to the real speed of wave is more suitable for the analysis of numerical dispersion for wave propagation problems. What Courant, Friedrichs, and Lewy in their seminal work in 1928 [Courant *et al.*, 1967] [3] pointed out was that a great deal can be learned by considering the domains of dependence of a partial differential equation and of its discrete approximation. Consider an initial-value problem, the mathematical domain of dependence of the solution, is defined as the set of all points in space where the initial data at $t = 0$ may have some effect on the solution in time t. For hyperbolic equation either linear or nonlinear, the domain of dependence is finite and bounded. The reason is that in hyperbolic problems, energy or information travels at a finite speed. This is a characteristic of the hyperbolic partial differential equations. For elastic waves, this is normally exemplified by the *characteristic curves* of the wave propagation, which is only straight for the linear elastic media. A numerical approximation also has a domain of dependence. With an implicit time integration scheme, since each value of the variables depends on all the values at one or earlier steps, the domain of dependence is unbounded. On the other hand, with an explicit formula, the value depends on only a finite range of values at previous time steps. The CFL condition states that for a numerical scheme to be convergent (*i.e.* stable and consistent), the mathematical domain of dependence should be contained in the numerical domain of dependence. It is a necessary but not sufficient condition for stability. So, for example, for a one dimensional wave, the numerical value of the mesh spatial distance between two nodes divided by the time step, define a speed with which the information is numerically propagated in time and this speed must be less than or equal to the physical speed of propagation in the equation.

The stability of a numerical integration in time is a measure of how fast the perturbations in initial conditions will decay when $t \to \infty$, an unstable scheme will amplify the perturbations, which comes mainly from the truncation errors of the spatial approximation, and possibly from the round-off errors of the machine. So, if the stability requirements are satisfied, the question becomes: are the truncation errors a good enough measure for the accuracy of the numerical approximation of propagating waves? In other words, having satisfied the stability requirements, and established convergent scheme based on the local truncation errors of the spatial approximation is that enough to ensure the accuracy of the solution? The general answer to this question is NO as has been

3. In German: "Über die partiellen Differenzengleichungen der mathematischen Physik" Math. Ann.100 (1928), 32-74. An English translation appeared much later in IBM Journal 11 (1967), 215-234.

demonstrated by Trefethen [Trefethen, 1982]. There is more to the inaccuracy of a numerical scheme than truncation error. The convergence norms based on truncation errors such as energy norms are satisfied stepwise, but in the normal error analysis, the errors are considered random either emanating from truncation or random perturbations coming from round-off errors, but if we base our estimate of the accuracy of the numerical wave propagation on the accumulation of such errors which are assumed random in nature, the estimate will not provide a good measure for the accuracy of the solution. This is due to the fact that errors caused by time integration differencing are not random perturbations, but a *systematic superposition* of dispersions and possibly dissipations of various orders. Understanding behavioral features such as phase and group velocity of numerical errors can yield various benefits.

In designing a numerical approximation technique for a time dependent partial differential equation, it is often useful to divide the process into two steps: first, discretize the problem with respect to space, thereby generating a system of ordinary differential equations in time; next, solve this system by some discrete method in time. A system of ordinary differential equations of this kind is known as a *semidiscrete* approximation to a partial differential equation. The idea of constructing a semi-discrete approximation and then solving it by a numerical method for ordinary differential equations is known as the *method of lines*. In the spirit of the method of lines, we shall discuss the effect of the time integration on the propagation of elastic waves numerically, as well as the spatial discretization. This division between the spatial and temporal discretization, stems from the fact that we need to distinguish between the dispersion errors emanating from each.

The classical numerical dispersion analysis typically starts by assuming an unbounded mesh, which means that all the system's equations are of the same form. This assumption, for the linear FE with equally spaced nodes, is typically followed by a reduction of the system to a single degree of freedom. A wave with a prescribed wavenumber and amplitude is assumed and substituted and the corresponding frequency is then determined.

If we substitute directly the harmonic displacements into the semi-discrete equations:

$$\mathbf{M\ddot{u}} + \mathbf{Ku} = \mathbf{0} \tag{2.15}$$

we have an estimate of the dispersion error due to the spatial discretization alone. The order of the method in this case is inherited from the classical convergence orders mentioned in § 2.4. If we substitute the harmonic solutions, in the time integration scheme, we then are estimating the dispersion error coming from both spatial and temporal discretization, thus including both the

accumulative superposition as well as possible cancellation of the temporal and spatial errors, each has its own order.

In order to motivate the discussion for the numerical dispersion errors, it is better to start with explicit central difference scheme since it is the most suitable for the wave propagation simulation. The explicit time central difference integration scheme is conditionally stable, *i.e.* have a restriction on the maximum time step permitted. The semi-discrete system of equations is solved iteratively via:

$$\mathbf{M}\mathbf{u}^{t+\Delta t} - (2\mathbf{M} - \Delta t^2\mathbf{K})\mathbf{u}^t + \mathbf{M}\mathbf{u}^{t-\Delta t} = \Delta t^2\mathbf{f} \tag{2.16}$$

where the mass matrix $\mathbf{M}$ is assumed to be diagonal, either by a special diagonalising technique or by construction. The numerical error arising from both the temporal and spatial discretization could be formulated as a dispersion relation. Both phase and group velocity of the numerically propagated wave is dependent on the spatial Δx and temporal Δt discretization parameters. For example, considering a wave propagation in a one dimensional mesh of linear finite element of length Δx with the mass matrix given as $\rho\Delta x\mathbf{I}$ and stiffness matrix row at a node, given as $(E/\Delta x)[-1 \;\; 2 \;\; -1]$. For each node, Eq. (2.16) becomes, with no forces:

$$\rho\Delta x(u_n^{t+\Delta t} - 2u_n^t + u_n^{t-\Delta t}) - E\frac{\Delta t^2}{\Delta x}(u_{n+1}^t - 2u_n^t + u_{n-1}^t) = 0 \tag{2.17}$$

which after plugging a harmonic solution gives the frequency equation of the central difference scheme, for the one dimensional classical wave equation:

$$\frac{E}{\rho}\left(\frac{\Delta t}{\Delta x}\right)^2(1 - \cos(k\Delta x)) + (\cos(\omega\Delta t) - 1) = 0 \tag{2.18}$$

where $\sqrt{\frac{E}{\rho}}\frac{\Delta t}{\Delta x} = c_f$ is the CFL number for this specific case, (*i.e.* the ratio of the physical wave phase velocity to the numerical wave phase velocity). So, solving for ω, gives the frequency equation of this specific numerical scheme.

$$\omega = \frac{\cos^{-1}\left(1 - c_f^2 + c_f^2\cos(k\Delta x)\right)}{\Delta t} \tag{2.19}$$

which is non-dispersive (*i.e.* $\omega/k = \Delta x/\Delta t$) and solves the problem exactly only if the $c_f = 1$ (see Fig. 2.25). Although it is believed that the smaller the time step the more accurate the solution and that the only sacrifice is in the computational efficiency, this mainly depends on the choice of the time integration scheme as shown by this analysis. Eq. (2.19) reveals that using CFL numbers smaller than one, though still preserving the stability, it will lead to a dispersive phase

and group velocity of the numerically propagated waves, even for the non-dispersive physical wave propagation.

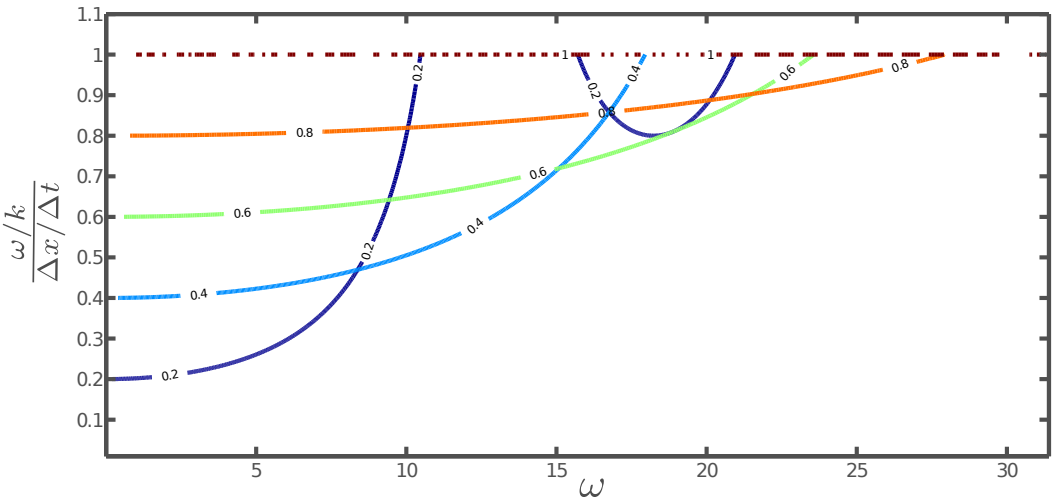

Figure 2.25 The variation of the numerical wave speed with the changes in CFL number at different values of circular frequency. The numbers on the contour is the values of c_f.

In general, the spatial and temporal discretizations may interact and their total dispersive errors may not be a linear summation of the dispersive errors due to the two individual discretizations. A dispersion analysis indicated that the explicit linear spatial discretization alone, in the absence of a temporal discretization, is highly dispersive [Jensen, 1996; Trefethen, 1982]. A similar evaluation demonstrates that the central difference in time discretization is also highly dispersive [Dablain, 1986; Dauksher and Emery, 2000].

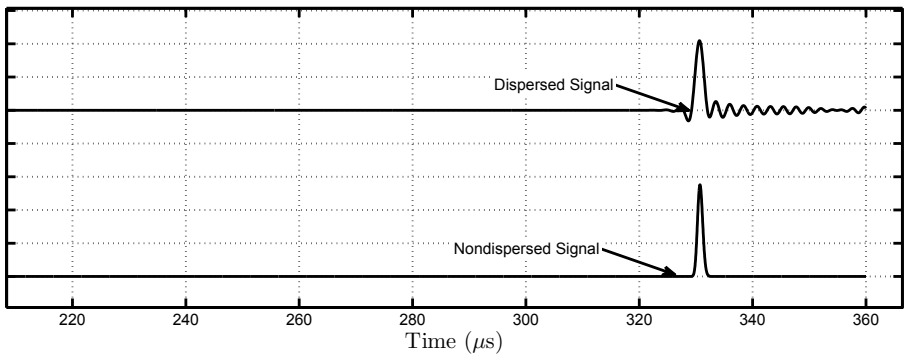

Figure 2.26 Phase velocity dispersion, for wide band one dimensional elastic wave.

Figure 2.26, demonstrate the effect of numerical dispersion with a Gaussian pulse, for a constant phase velocity one dimensional elastic wave, integrated with CFL number = 0.8. Figure 2.27,

shows a 5.5 tone burst modulated by a Hanning window, time marched with the same CFL number as for the Gaussian pulse.

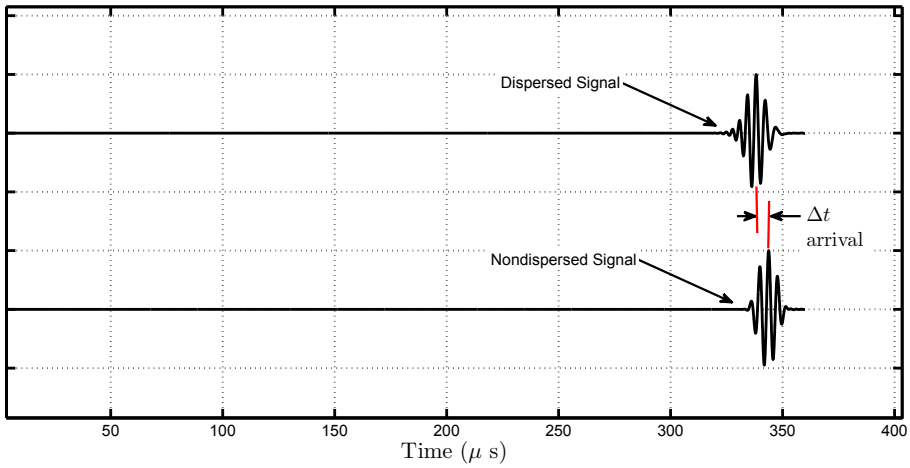

Figure 2.27 Group velocity error in a one dimensional elastic wave a 5.5 tone burst.

The main observation is that although the packet in Fig. 2.27 has moved 20% too slowly, it has broadened very little 5%. A packet is distorted with time only to the extent that its frequency content is broad enough to include wave numbers whose speeds differ significantly, and in the case of 5.5 the tone burst case the frequency band is fairly narrow, while the dispersion is more pronounced in the Gaussian pulse, because its frequency content is wide enough for the dispersion to be manifested as time distortion of the signal. Thus the absence of conspicuous dispersion in a wave packet is not a guarantee that it has traveled at the right speed.

In order to estimate the ramification of this 20% delay in arrival time on a typical Time of Flight (ToF) analysis, assume that the bar was 1 m long, and the speed of the propagation was that of the rod of aluminum i.e. 5000 m/s. If the defect reflecting the wave was in the middle of the rod, the incident wave packet would arrive in the numerical simulation 20% slower and the reflection and transmission would suffer from a similar delay. If the distance of propagation was 0.5 m this means that the signal would take in the physical rod $1\text{x}10^{-4}$ s, while in the numerical simulation it will take $1.2\text{x}10^{-4}$ in the simulation. This will lead for the localization to errors of the order of 0.2 m. So, if the numerical simulation was used, for example, to determine the optimum sensor placement, this will lead to erroneous design decisions.

For a more realistic example, in Fig. 2.28, there is an illustration of the effect of delay in the ToF that could be caused by numerical dispersion of the simulated signal. Beside the complete mis-localization there is also an added uncertainty in the determination of the damage location emanating from the shrinking in the ellipses.

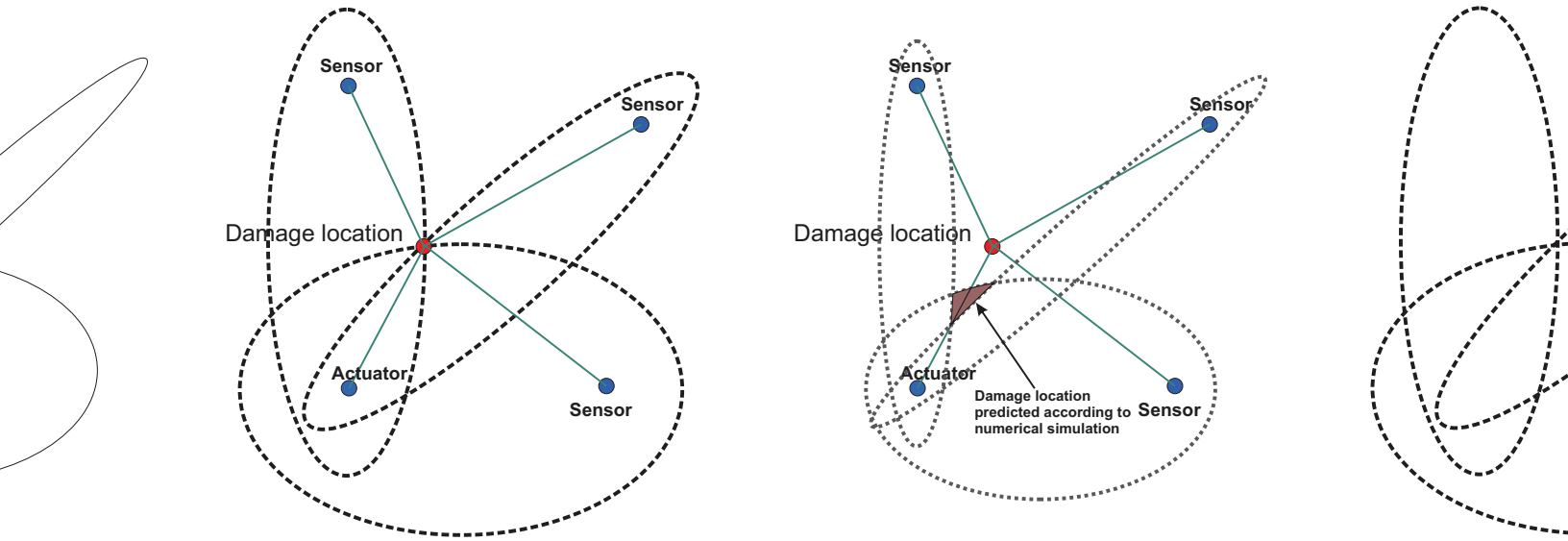

(a) The accurate localization

(b) The effect of the delay in ToF caused by numerical dispersion

Figure 2.28 Damage localization using the ToF-based ellipse method. (a) Without numerical dispersion errors and (b) with numerical dispersion errors.

While it is possible in one dimensional case which contains regions of different, but constant, material properties to adjust the spacing in each region to maintain a constant CFL number of one everywhere for a given value of the time step, this is clearly not possible for higher dimensional cases where the waves travel in arbitrary directions. Likewise it is impossible to avoid the numerical dispersion errors in 2D and 3D elastic systems, which contain both transverse and longitudinal waves, since it is inevitable that we treat each wave with the same CFL number.

Figure 2.29 The unit cell of one dimensional element for numerical dispersion analysis, for a 6 nodes Legendre spectral element

The extension of the classical dispersion analysis to higher order elements involves the following steps:

1. Determine a set of characteristic nodes that represent the element behavior in an infinite mesh as shown in Fig. 2.29, for a 6 node Legendre polynomial.

2. Substitute harmonic waves with arbitrary amplitudes into the displacements,
3. Solve for the characteristic equations of the linear system.

For higher order elements, there are several characteristic equations (as many as the characteristic nodes chosen in step 1), these nodes define a unique *Unit cell* for the mesh such that a repetition of the unit cell will produce the unbounded mesh [Dauksher and Emery A. F., 1997; Seriani and Oliveira, 2008; Zyserman and Gauzellino, 2005; Zyserman *et al.*, 2003]. By examining the dispersive behavior of the characteristic equations, the numerical dispersion of the mesh can be quantified.

In order to include the effect of the temporal discretization, after a slight rearrangement of Eq. (2.16) with zero forces, and considering only the matrix elements corresponding to the characteristic nodes (the superscript c) we obtain:

$$\mathbf{M}^c\mathbf{u}^{t+\Delta t} - (2\mathbf{M}^c + \Delta t^2\mathbf{K}^c)\mathbf{u}^t + \mathbf{M}^c\mathbf{u}^{t-\Delta t} = 0 \tag{2.20}$$

for $\mathbf{u}$, we assume a harmonic solution of the form,

$$\mathbf{u}^t = \mathbf{A}e^{-ik\mathbf{x}}e^{i\omega t} \tag{2.21a}$$

$$\mathbf{u}^{t+\Delta t} = \mathbf{A}e^{-ik\mathbf{x}}e^{i\omega(t+\Delta t)} \tag{2.21b}$$

$$\mathbf{u}^{t-\Delta t} = \mathbf{A}e^{-ik\mathbf{x}}e^{i\omega(t-\Delta t)} \tag{2.21c}$$

where $\mathbf{x}$ is the vector of nodal locations. For $t = 0$ this leads to

$$\left[2\cos(\omega\Delta t)\mathbf{M}^c e^{-ik\mathbf{x}} - 2\mathbf{M}^c e^{-ik\mathbf{x}} + \Delta t^2\mathbf{K}^c e^{-ik\mathbf{x}}\right]\mathbf{A} = 0 \tag{2.22}$$

So, for a specific choice of Δt, Eq. (2.22) determines the relation between ω and k, in the form of a generalized eigenvalue problem. The resulting eigenvalues correspond to values of $\cos(\omega\Delta t)$. One of the eigenvalues will be for the so called "acoustical branch", and the remaining typically called optical branches. The acoustic radial frequency ω is the one with physical meaning, and is obtained from the largest of the eigenvalues [Brillouin, 1946, 1960; Thompson and Pinsky, 1994]. Phase and group velocities follow from $c_p = \omega/k$ and $c_g = c_p + k\frac{dc_p}{dk}$. Since both spatial and temporal components are included, the previous method of numerical dispersion analysis predicts the total dispersion due to the finite/spectral element discretization.

It is generally accepted paradigm to think of the spatial discretization as the more constraining factor, and as such, a decrease in the space discretization error by mesh refinement may reduce the dispersion error as it is the starting step in the meshing procedure; but this remedy increases considerably the computational costs. Therefore, several techniques have been proposed for the

reduction in the numerical dispersion error which is also related to the pollution effect [Babuška *et al.*, 1995]. One simple approach for acoustic and elastic wave propagation problems is based on the use of the averaged mass matrix instead of the consistent or lumped mass matrix with Newmark scheme [Krenk, 2001; Mullen and Belytschko, 1982]. For linear finite elements, this technique reduces the relative error in the wave velocity for harmonic waves from the second order to fourth order in the 1D case, by the order of error we mean the proportionality constant p in the error decay rate $\mathcal{O}(1/N^p)$. However, this approach suffers from the same problem, like the explicit time integration scheme namely the impossibility of eliminating the numerical dispersion completely due to the presence of at least two wave velocities, nevertheless, in the case of harmonic wave propagation for 2D and 3D problems, the averaged mass matrix gives more accurate results compared with the lumped mass matrix [Idesman *et al.*, 2010].

Since the dispersion errors are mainly dependent on the time integration scheme used because it is typically of less order, this motivated the search for controlling the numerical dispersion error through developing new time integration schemes that target specifically minimizing the dispersion errors [Idesman *et al.*, 2010, 2008; Semblat and Brioist, 2000].

2.5.2 Infinite and absorbing boundaries

Unwanted reflections from the boundaries of the system have been and still one of the major challenges that limits the applicability of FE simulation of waves. In time domain, this leads to a large increase in the model geometric size (and therefore a large increase in the number of degrees of freedom to be solved) as it is needed to separate the interaction of the waves with defects from unwanted boundary reflections. As illustrated in Fig. 2.30 where the plate had to be extended to achieve appropriate separation of the signal of interest and the unwanted reflections in the time signal. Moreover, in frequency domain, removal of unwanted reflections is a requirement in order to correctly represent wave propagation in the system.

Very often the need arise to analyze a specific region of an engineering structure in detail, without the need to consider the complications and the associated costs of simulating a fully blown CAD model. This need arises in different aspects of the simulation of wave phenomena, such as seismic wave simulation, electromagnetic waves propagation. The main four types of methods that have emerged in order to achieve this objective are: boundary integral methods, infinite element, absorbing layer and non-reflecting or absorbing boundary condition methods. The later three methods are based on the FD or FE technique.

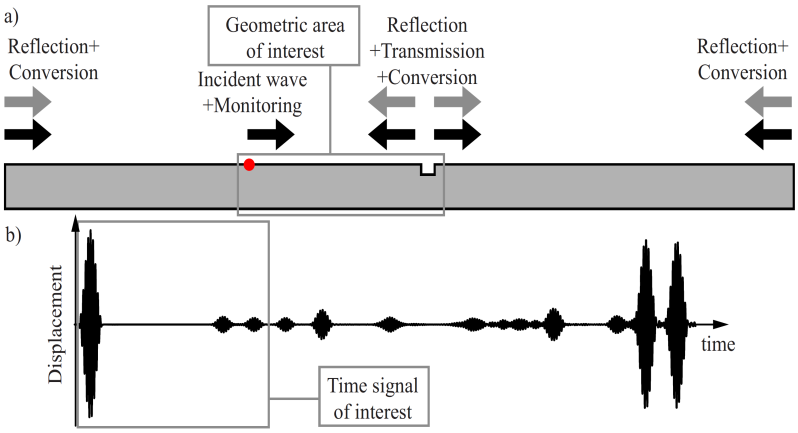

Figure 2.30 2D plane strain model of a plate including a defect (a), and time signal at the monitoring point (b) [Drozdz, 2008].

Infinite elements are a special type of element with modified properties which is used in conjunction with standard finite elements to simulate an infinite extension in the domain. A single row of infinite elements is typically positioned outside the boundaries of the area of study [Bettess, 1992]. Infinite elements is known to perform relatively well for static cases as well as in certain applications of wave propagation: electromagnetism, acoustics and elastic bulk waves with incidence angles that almost normal. For guided waves simulation, the non-normal incidence of the different modes, as shown by Liu and Quek [Liu and Quek, 2003a] limits the applicability of the infinite elements as an appropriate radiation boundary condition.

Absorbing or non-reflecting boundary conditions are special boundary conditions used in FE or FD methods to model wave propagation in unbounded media. The dimensions of the model are the same as the area of study; only the boundary conditions are changed. The first conditions for absorbing boundaries in elastic wave equations were introduced by Clayton and Engquist [Clayton and Engquist, 1977], which is considered a first order absorbing boundary condition. Second order absorbing boundary condition were developed later by Bayliss and Turkel [Bayliss and Turkel, 1980] and Engquist and Madja [Engquist and Madja, 1979].

Absorbing layers differs than the absorbing boundary conditions, they are finite regions attached at the boundaries of a model. The objective is to approximate the case of an unbounded problem by absorbing waves entering them. Lysmer and Kuhlemeyer [Lysmer and Kuhlemeyer, 1969] were the first to propose a non-reflecting boundary for elastic waves. They suggested that introducing damping at the plane of the finite boundary and by choosing appropriate damping constants, minimize the reflected wave energy. The conditions are applied by considering separately

longitudinal wave, transverse wave and surface wave. Therefore, a general propagation problem with a combination of waves will require an approximation. This approximation may not prove effective for a guided waves whereby the wave propagates in a more complex manner in the form of dispersive multiple modes.

The perfectly matched layer (PML) technique was created in 1994 by Berenger [Berenger, 1994] for electromagnetism and has been extended to other fields such as acoustics [Qi and Geers, 1994]. As its name indicates, a PML matches perfectly the impedance of the area of study. This means that, in theory, a wave enters a PML without reflection. Once inside it, the wave decays exponentially. A PML can therefore be used to achieve total radiation of a wave out of the area of study. The PML seem to be very efficient and may be sufficient for most of the problems in elastic wave propagation. The PML were in the first part introduced for FD simulations of wave propagation in heterogeneous media using the differential form of the wave equation in the velocity-stress formulation by Collino and Tsogka [Collino and Tsogka, 2001]. Komatitsch and Tromp [Komatitsch and Tromp, 2003] used a first order approximation based on a formulation by Stacey [Stacey, 1988] for the absorbing boundaries.

Another variant of the damping layer is the absorbing layer with increased Damping (ALID), The ALID is an absorbing layer which is made of a material with the same properties as those of the area of study apart from having a gradually increasing damping. The general concept was mentioned in 1980 by Israeli and Orszag [Israeli and Orszag, 1981] and was recently revisited [Liu and Quek, 2003a] and [Drozdz *et al.*, 2007].

2.5.3 Damage modeling

Reliable damage modelling is a key issue when considering numerical simulations as a means to predict structures performance and lifetime, and provide a way to simulate and improve the SHM and NDT/NDE systems. According to the level of consideration, damage modelling methods can be classified analogously to multiscale modelling methods [Packo and Uhl, 2011] as single and multiscale models (meso, micro and nano).

Different approaches have been proposed to model damages for the SHM simulation applications. Among the different failure modes, delamination, and fibre breakages are important modes of failure in composites. These failure modes correspond to horizontal and vertical cracks in metallic structures. This section outlines some of the approaches adopted to model these failure modes in metallic structures in the context of FE simulation.

It is quite well known that the presence of damage causes a reduction of stiffness in a structure. A simple way of modeling damages is to incorporate the stiffness loss in the region of the damage

by modifying the materials properties. The benefits of this approach is its ease of implementation, and the preservation of continuity between the adjacent elements. So, no need for specific algorithmic handling of singularities that normally arise in the fracture mechanics simulation. Though it lacks the ability to feed a prognostic system with relevant data such as the direction and the patterns of damage progression, since the reduction in stiffness is mainly arbitrary. It provide a general qualitative understanding of the behavior of the structure. If the damage is a crack, delamination, void, inclusion or other type of the material's discontinuity then it may be modeled by direct, local change of material properties. However, since a sharp discontinuity is considered, the accuracy of the damage model relies on the numerical model's ability to simulate the wave interaction with the interface of high impedance mismatch. Since the vast majority of elastic waves based monitoring strategies analyze the reflection from defects, this is the most important phenomenon that must be simulated accurately, and SEM excels in that respect since it could assign a different material to each node separately, and the ability to represent the continuous function sharp variations at the sudden interfaces is superior to that of classical FEM [Fornberg, 1996]. What is more, nonlinear effects may arise during wave propagation and interaction with damage, such as friction on the crack faces, temperature-related wavefield changes, e.g. inhomogeneous temperature field or thermoelasticity, plasticity at the crack tip, etc. These may be simulated by using contact algorithms [Martowicz *et al.*, 2012], coupled thermomechanical analysis considering the influence of temperature field on the material properties, thermoelastic coupling based on strain calculations [P *et al.*, 2010], nonlinear material models, etc. The broad range of phenomena that should be taken into account, especially nonlinear effects, requires significantly larger computational resources. However, these complex structure's responses are frequently confined to the damage region that is relatively small compared with the structure dimensions and thus may be efficiently analysed by hybrid and multiscale approaches.

A better way of modeling cracks in FE is to completely model the entire crack front through the so called "Duplicate Node Method". Modeling can be done using finite elements using the concept of duplicate nodes. The modeling of a damage such as a delamination is done by keeping the two nodes in same place, one for the elements above the damage and other below it. The damage is modeled through proper nodal connectivity of the elements containing the crack or the damage, this approach is creating an interior free surface [Gopalakrishnan *et al.*, 2011].

2.6 Conclusion

The goal of this chapter was to review the advancements in the numerical simulation of GWs with a specific focus on SHM requirements, and constraints on the numerical simulation. It is the author's hope that by now the reader is convinced that dispersion is an important if not the

most important accuracy estimate in GW simulation. If so, it should be considered persistently in both the validation and verification phases of the numerical simulation. Considering it in the validation step means mainly; evaluating the dispersion as dictated by the mathematical model. Fortunately, for the majority of the engineering theories the dispersion relations could be determined analytically. On the side of verification, numerical dispersion is an important error measure by its own right and as such it depends mainly on the numerical approximation parameters.

The spectral element offers certain advantages with respect to the GWs simulation, as discussed in the present chapter. This explains the growing adoption by the wave propagation community of SEM, both for low frequency (mainly seismological applications that utilize SEM for its strengths in representing material nonlinearities and interfaces) and high frequency applications for the low numerical dispersion behavior. However, very few detailed studies aimed at an accurate quantifications of the numerical dispersion and its dependence on the meshing parameters, and those studies were more of a mathematical orientation than an engineering focus, and were more focused on simple generic cases. In the present work an attempt to fill that gap, by focusing on the mathematical models of engineering origin, analyzing its dispersion behavior and implementing the SEM approximation of the solution, and analyzing the numerical dispersion.

In the next chapter, the dispersion relations of different approximate models of guided waves in rods are deduced as well as compared with the exact solution. Next the spectral elements for those approximate mathematical models are formulated in detail. The numerical dispersion are analyzed for each model by applying a systematic novel numerical dispersion approach.

CHAPTER 3

Formulation and numerical dispersion analysis of spectral element for guided waves propagation in rods

Numbers as realities *do* misbehave.

DOUGLAS HOFSTADTER (1945-)

LONGITUDINAL waves are broadly used for the purposes of non-destructive evaluation of materials and for generation and sensing of acoustic vibration of surrounding medium by means of transducers. Many mathematical models describing longitudinal wave propagation in solids have been developed in order to analyze the effects of different materials and geometries on wave propagation characteristics without the need for costly experimental studies.

Beside this, the main purpose of considering the rod elements in this chapter is to deploy the numerical dispersion analysis as well as to explain clearly the details of the formulation of the spectral element method without the need to tackle the complexity of multiple dimensionality. In the rest of the chapter we follow a unified approach to derive three different families of differential equations describing the longitudinal waves propagating in cylindrical waveguides based on the Hamilton variational principle. Dispersion curves, representing the dependence of phase velocity on the frequency of these theories are obtained in closed form then evaluated numerically and compared with the exact solution as a reference. Those theoretical dispersion curves represent the inherent accuracy in the approximate engineering theory (validation phase), and it could also be considered as an upper limit on the accuracy of any numerical method adopting the theory.

Having knowledge of the upper limit on the accuracy does not necessarily mean that the numerical solution implementing the respective theory is accurate to that limit. Following a detailed explanation of the formulation of the spectral element, the main numerical error relevant to elastic wave propagation simulation *i.e. numerical dispersion* caused by discretization is analyzed in detail.

In the rest of this chapter, a review of the exact solution of longitudinal and flexural waves in rods is presented, followed by a review of some of the approximate theories that are typically used in

engineering approximations for longitudinal waves in rods. The following section solves for the analytical dispersion relations in order to asses the adequacy of the approximation in terms of the verification phase. The rest of chapter develops in detail the spectral element formulation of the approximate theories covered with its implementation details, and this formulated elements are then analyzed for numerical dispersion. The chapter ends with a set of relevant conclusions.

3.1 Exact solution: Pochhammer-Chree frequency equation

Propagation of elastic waves in cylindrical structural elements is described by the linear theory of elasticity. In the case of isotropic materials, the equation of motion governing propagation of elastic waves, in the absence of body forces, can be expressed in a vector form as:

$$(\lambda + 2\mu)\nabla(\nabla \cdot \mathbf{u}) - \mu\nabla \times \nabla \times \mathbf{u} = \rho\ddot{\mathbf{u}} \tag{3.1}$$

where $\mathbf{u}$ is the displacement vector, λ and μ are Lamé material elastic constants, ρ denotes material density and $\ddot{\mathbf{u}}$ is the acceleration vector. It is more convenient to analyze this problem in the cylindrical (r, θ, x) rather than the Cartesian (x, y, z) coordinates (Fig. 3.1). In the cylindrical coordinate system the components u_r, u_θ, and u_x of the displacement vector $\mathbf{u}$ are scalar functions of the space coordinates as well as time t. The solutions of the wave equation in a cylindrical

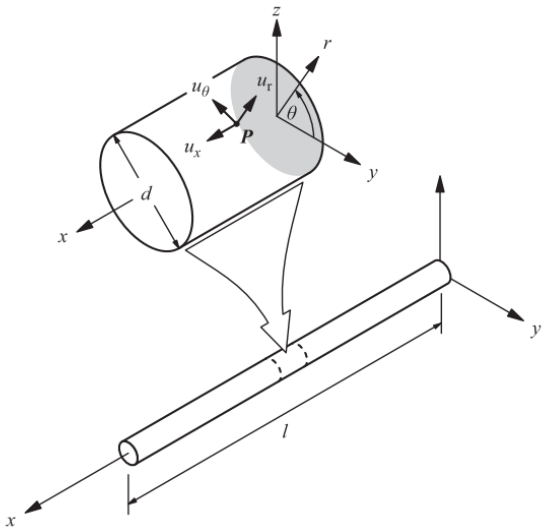

Figure 3.1 Cylindrical coordinate system for the rod system

waveguide are found by the use of potentials (*Stokes Helmholtz decomposition theorem*) [Rose, 2004] arriving at the following general form for the displacement vector ($\mathbf{u}$) and stress tensor ($\boldsymbol{\sigma}$),

where only the radial component of the field is relevant:

$$\mathbf{u}(r,\theta,x) = \mathbf{u}(r)e^{in\theta}e^{i(kz-\omega t)} \tag{3.2a}$$

$$\mathbf{u}(r) = [u_r(r) \;\; u_\theta(r) \;\; u_x(r)]^{\mathrm{T}} \tag{3.2b}$$

$$\boldsymbol{\sigma}(r,\theta,z) = \boldsymbol{\sigma}(r)e^{in\theta}e^{i(kz-\omega t)} \tag{3.2c}$$

$$\boldsymbol{\sigma}(r) = [\sigma_{rr}(r) \;\; \sigma_{\theta\theta}(r) \;\; \sigma_{xx}(r) \;\; \sigma_{\theta x}(r) \;\; \sigma_{rx}(r) \;\; \sigma_{r\theta}(r)]^{\mathrm{T}} \tag{3.2d}$$

where ω is the angular frequency, k the wavenumber, and n is an integer separation constant called the *circumferential order*, which determines the symmetry of the solutions in the θ direction.

The solution for three dimensional wave propagation in solids was derived independently by L. Pochhammer in 1876 and by C. Chree in 1889 [Graff, 1991]. The solution describes torsional, longitudinal and flexural wave propagation in cylindrical rods of infinite length and is known as the Pochhammer-Chree solution [Achenbach, 1973; Graff, 1991]. The solutions of the wave equation are classified in two classes of modes according to their axisymmetry, which depend on the circumferential index n. Modes for which $n = 0$ have no dependence on the θ, thus they only propagate symmetrically. They are further divided into torsional modes (which only involve the u_θ component), and longitudinal modes (with both radial and axial components). Antisymmetric modes ($n \geq 1$) are called flexural waves, and involve all three components of the displacement vector.

Two forms of graphical representation are typically used to analyse the dispersion relation governing wave propagation for mathematical models. The first is the *frequency spectrum* and the other is *phase velocity dispersion* curves and are obtained from the frequency equation, which shows the relation between circular frequency ω, wavenumber k and phase velocity c_p for a particular model. Although the frequency spectrum offers certain advantages, the dispersion curves have been the more abundant in engineering literature, and this convention has been adopted in this thesis.

3.1.1 Longitudinal waves ($n = 0$)

The strain field within the rod due to symmetry, have the following non vanishing components:

$$\epsilon_{xx} = \partial_x u_x, \quad \epsilon_{rr} = \partial_r u_r, \quad \epsilon_{\theta\theta} = u_r/r, \quad \gamma_{xr} = \partial_x u_r + \partial_r u_x \tag{3.3}$$

while the stress field can be calculated from Hooke's law

$$\sigma_{xx} = 2\mu\epsilon_{xx} + \lambda(\epsilon_{xx} + \epsilon_{rr} + \epsilon_{\theta\theta}), \qquad \sigma_{rr} = 2\mu\epsilon_{rr} + \lambda(\epsilon_{xx} + \epsilon_{rr} + \epsilon_{\theta\theta})$$
$$\sigma_{\theta\theta} = 2\mu\epsilon_{\theta\theta} + \lambda(\epsilon_{xx} + \epsilon_{rr} + \epsilon_{\theta\theta}), \qquad \sigma_{xr} = \mu\gamma_{xr}$$

After applying the Helmholtz decomposition, we reach two decoupled ordinary differential equations with arbitrary constants, then substituting the traction free boundary conditions ($\sigma_{rr} = \sigma_{rx} = 0$ at $r = R$) and the harmonic solution this leads to two simultaneous algebraic equations, the determinant of which must vanish leading to the well known Pochhammer-Chree frequency equation for longitudinal waves [Rose, 2004].

$$\frac{2\alpha}{R}(\beta^2 + k^2)J_1(R\alpha)J_1(R\beta) - (\beta^2 - k^2)^2(R\alpha)J_1(R\alpha)J_0(R\beta) - 4k^2\alpha\beta J_1(R\alpha)J_0(R\beta) = 0 \tag{3.5}$$

where $\alpha^2 = \omega^2/c_L^2 - k^2$, $\beta^2 = \omega^2/c_T^2 - k^2$, $J_n(x)$ is the Bessel function of first kind of order n, while c_L, and c_T are the pressure and shear bulk wave velocities in the rod material, respectively.

Figure 3.2(a) shows the phase velocities of longitudinal modes in terms of fR, the frequency radius product. As $fR \to \infty$ the first mode velocity approaches the surface wave velocity c_R, while the velocities of the higher modes tend to the bulk shear wave velocity c_T.

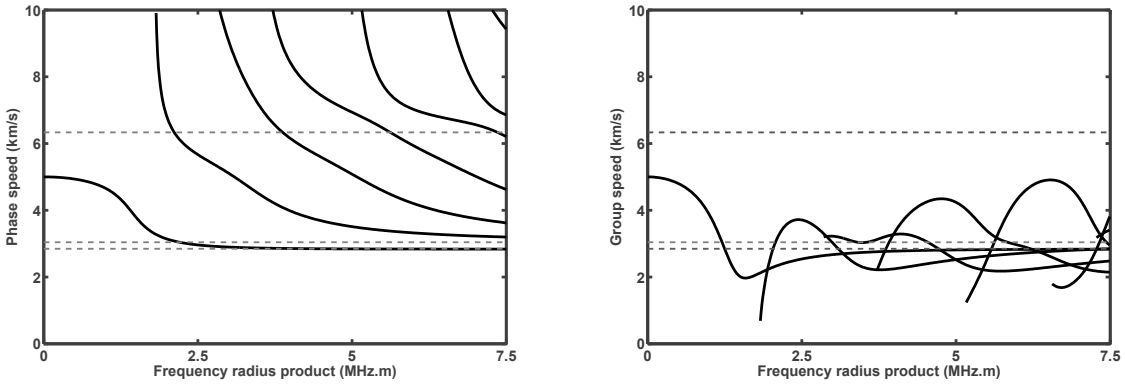

(a) Phase velocity (b) Group velocity

Figure 3.2 Pochhammer dispersion curves for longitudinal waves in an aluminum rod, ($c_L = 6.334$ km/s, $c_T = 3.042$ km/s, $c_o = 5$ km/s, and $\nu = 0.35$) [Seco and Jiménez, 2012]

3.1.2 Flexural waves ($n = 1$)

Flexural waves depend on the circumferential coordinate θ, which for $n = 1$ given as:

$$u_r(r) = u(r)\cos(\theta)e^{i(kz-\omega t)} \tag{3.6a}$$

$$u_\theta(r) = v(r)\sin(\theta)e^{i(kz-\omega t)} \tag{3.6b}$$

$$u_x(r) = w(r)\cos(\theta)e^{i(kz-\omega t)} \tag{3.6c}$$

substituting these equations in Eq. (3.1), we reach a system of three ODEs with arbitrary constants, after satisfying the traction free boundary conditions we reach an algebraic system of equations, the determinant of the system must vanish in order to have a solution. leading to the following form of Pochhammer-Chree frequency equations for the flexural waves for $n = 1$ [Pao and Mindlin, 1960]. Similar procedures could be followed for $n > 1$.

$$J_1(R\alpha)J_2(R\beta)\left(f_1\mathcal{J}_\beta^2 + f_2\mathcal{J}_\alpha\mathcal{J}_\beta + f_3\mathcal{J}_\beta + f_4\mathcal{J}_\alpha + f_5)\right) = 0 \tag{3.7}$$

$$\mathcal{J}_\alpha = \alpha\frac{J_0(\alpha)}{J_1(\alpha)} \quad , \quad \mathcal{J}_\beta = \beta\frac{J_0(\beta)}{J_1(\beta)} \tag{3.8}$$

where f_i are polynomials in α, β and k that could be found in [Graff, 1991; Pao and Mindlin, 1960].

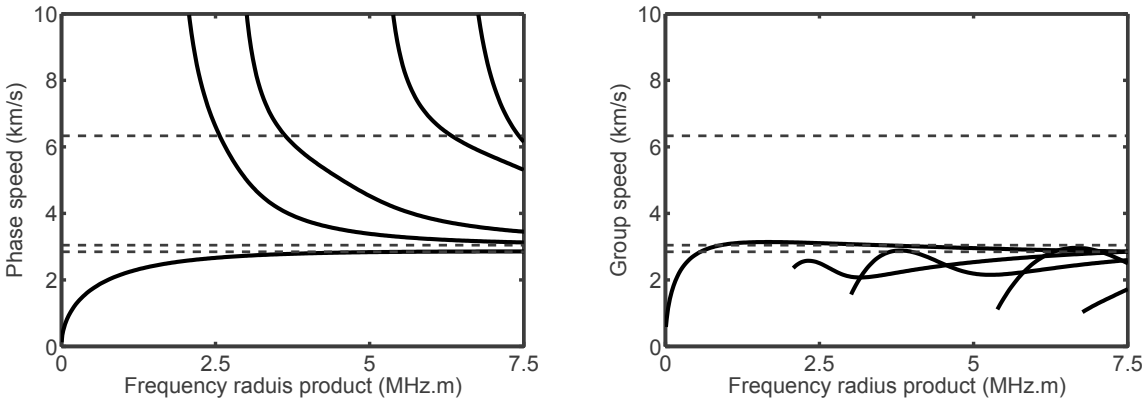

(a) Phase velocity (b) Group velocity

Figure 3.3 Pochhammer dispersion curves for flexural waves in an aluminum rod, ($c_L = 6.334$ km/s, $c_T = 3.042$ km/s, $c_o = 5$ km/s, and $\nu = 0.35$)[Seco and Jiménez, 2012].

Figure 3.3(a) shows the phase velocities of flexural modes in terms of fR, the frequency radius product. as $fR \to \infty$ the lowest mode velocity approaches the surface waves velocity c_R, while the velocities of the higher modes tend to the bulk shear velocity c_T.

3.2 Approximate longitudinal waves theories

The Pochhammer-Chree solution is valid for an infinite rod with simple cylindrical geometry only. For slightly more complex geometries, such as conical or exponential, no exact analytical solution exists. The need for useful analytical results for rods with more complex geometries motivated the development of one dimensional approximate theories. The exact Pochhammer-Chree solution typically has been used as a reference in order to assess the accuracy of the approximate theories and the limits of their application.

The classical approximate theory of longitudinal vibration of rods was developed during the 18th century by J. D'Alembert, D. Bernoulli, L. Euler and J. Lagrange. This theory is based on the analysis of the one dimensional wave equation and is applicable for long and relatively thin rods vibrating at low frequencies (*i.e.* the rod radius $R \ll 2\pi/k$). The classical theory completely ignores lateral effects with the corresponding lateral and axial shear modes.

J. Rayleigh was the first to recognize the importance of the lateral effects and analysed the influence of the *lateral inertia* on longitudinal vibration of rods. A. Love further developed this theory, which is now referred to as the Rayleigh-Love theory. The lateral inertia effects are important in the case of non-thin cross sections with respect to the wavelength. From the view point of engineering application the Rayleigh-Love theory substantially improves the accuracy of the frequency spectrum predictions in comparison with results based on the classical theory. R. Bishop further modified the Rayleigh-Love theory by taking into consideration the *lateral shear* effects. This widened the scope of applicability of the theory in terms of the frequency spectrum.

Consider a solid cylindrical bar with radius R and length l which experiences longitudinal vibration along the x-axis and lateral shear vibrations, transverse to the x-axis in the direction of the r-axis and in the tangential direction. Considering the wave propagation as a symmetrical problem the axial and lateral wave displacements can be written as a power series expansion in the radial coordinate r of the form:

$$u_x(x,r,t) = u_x(x,0,t) + +\tfrac{r^2}{2!}\partial_r^2 u_x(x,0,t) + \cdots + \tfrac{r^{2m}}{(2m)!}\partial_r^{2m} u_x(x,0,t) \tag{3.9a}$$

$$u_r(x,r,t) = r\partial_r u_r(x,0,t) + \tfrac{r^3}{3!}\partial_r^3 u_r(x,0,t) + \cdots + \tfrac{r^{2n+1}}{(2n+1)!}\partial_r^{2n+1} u_r(x,0,t) \tag{3.9b}$$

The displacements in the tangential direction are assumed to be negligible ($u_\theta(x,r,\theta,t) = 0$). That is, no torsional vibrations are present. According to choice of m and n in Eq. (3.9), different models of longitudinal vibration of bars can be obtained, including the well-known models such as those of Rayleigh-Love, Rayleigh-Bishop, Mindlin-Hermann and a three-mode model analogous to the Mindlin-McNiven *second order approximation*. Eqs. (3.9) are rewritten for the

sake of simplicity in the following form, that will be adopted hereafter to discuss the approximate theories:

$$u_x(x,r,t) = u(x,t) = u_0(x,t) + r^2 u_2(x,t) + \cdots + r^{2m} u_{2m}(x,t) \tag{3.10a}$$

$$u_r(x,r,t) = w(x,t) = r w_1(x,t) + r^3 w_3(x,t) + \cdots + r^{2n+1} w_{2n+1}(x,t) \tag{3.10b}$$

The classical, Rayleigh-Love and Rayleigh-Bishop theories are based on the fundamental assumption of *single mode* propagation, which means that the dynamics of the rod is described by a single unknown and hence, a single partial differential equation. Another fundamental assumption is that the above mentioned theories are *plane cross-sectional* theories, *i.e.* displacements in the longitudinal direction preserve their plane and are not functions of distance from the neutral axis of the rod.

The boundary conditions on the outer cylindrical surface of the rod are ignored in the classical theory. In the Rayleigh-Love theory these boundary conditions are implicitly taken into consideration because the radial component of the surface stress is zero and moreover it is always zero inside the rod while the shear stress is neglected. In the Rayleigh-Bishop theory the radial component of the surface stress is zero inside and on the outer surface of the rod but the shear stress is taken into consideration inside the rod and hence, it is non-zero on the outer surface of the rod.

3.2.1 Classical theory

The classical theory is the simplest of the models discussed here. The longitudinal displacement is represented by

$$u(x,t) = u_0(x,t) \tag{3.11a}$$

$$w(x,t) = 0 \tag{3.11b}$$

The equations of motion (and the associated boundary conditions) is derivable from the application of Hamilton's variational principle. The Lagrangian defined as $L = T - P$, where T is the kinetic energy, $T = \rho/2 \int_0^l \int_A (\dot{u}^2 + \dot{w}^2)\, dA\, dx$, and P is the potential energy $P = 1/2 \int_0^l \int_A \sigma_{ii}\epsilon_{ii}\, dA\, dx$ [1]. The Lagrangian density of the system is:

$$\mathcal{L} = \frac{1}{2}\left(\rho A \dot{u}_0^2 - EA(\partial_x u_0)^2\right) \tag{3.12}$$

1. The repeated summation convention is employed

which after substitution in the Euler-Lagrange differential equation yields the classical wave equation:

$$\rho A\ddot{u} - EA\partial_x^2 u = 0 \tag{3.13}$$

with the associated natural boundary condition $\partial_x u_0(0,t) = 0$ or $\partial_x u_0(l,t) = 0$, or essential boundary condition $u_0(0,t) = 0$ or $u_0(l,t) = 0$, we complete the mathematical description of the problem. It is worth emphasizing that the traction free boundary conditions on the outer cylindrical surface of the rod are fully ignored in the classical theory.

3.2.2 Rayleigh Love theory

In Rayleigh Love theory, the longitudinal and lateral displacements are defined by:

$$u(x,t) = u_0(x,t) \tag{3.14a}$$

$$w(x,t) = rw_1(x,t) \tag{3.14b}$$

Rayleigh and Love theory made the additional assumption that only the inertial effect of the lateral displacements are taken into consideration and the effect of stiffness on shear stress is neglected, $\gamma_{xr} = \partial_x w \neq 0$ and $\sigma_{xr} \approx 0$. Leading to the equation of motion:

$$\overbrace{\rho A\ddot{u} - EA\partial_x^2 u}^{\text{2nd order wave equation}} - \overbrace{\rho\nu^2 I_p \partial_x^2 \ddot{u}}^{\text{Rayleigh Love correction}} = 0 \tag{3.15}$$

where I_p is the polar second moment of area ($I_p = I_2 = \int_A r^2 dA = \pi R^4/2$ for circular cross-section).

3.2.3 Rayleigh Bishop theory

In the Rayleigh Bishop theory, the longitudinal and lateral displacements are represented by the two term expansion

$$u(x,t) = u_0(x,t) \tag{3.16a}$$

$$w(x,t) = rw_1(x,t) \tag{3.16b}$$

Substituting Eqs. (3.16) into the equation for the radial stress component σ_{rr} and equating all terms at R to zero yields $w_1(x,t) = -\nu\partial_x u_0(x,t)$. That is, the lateral displacement of a particle

distant from the neutral axis is assumed to be linearly dependent on the longitudinal strain:

$$w(x, r, t) = -\nu\partial_x u(x, t) = r\nu\partial_x u_0(x, t) \tag{3.17}$$

Applying this constraint to the lateral displacement means that $\sigma_{rr} = 0$ throughout the entire thickness of the bar. The Rayleigh-Bishop model is a single mode, plane cross-section theory, since both longitudinal and lateral displacements are defined in terms of a single mode of displacement, u_0, and the term $r\nu\partial_x u_0(x, t)$ in Eq. (3.17) means that lateral deformation occurs in plane and hence all plane cross sections remain plane during deformation. The equation of motion for this theory is:

$$\overbrace{\rho A\ddot{u} - EA\partial_x^2 u}^{\text{2nd order wave equation}} - \overbrace{\rho\nu^2 I_p\partial_x^2\ddot{u}}^{\text{Rayleigh Love correction}} + \overbrace{\mu\nu^2 I_p\partial_x^4 u}^{\text{Bishop correction}} = 0 \tag{3.18}$$

3.2.4 Mindlin Herrmann theory

At higher excitation frequencies, the high order modes can be activated and waves with the same frequencies but different wave number will propagate through the rod. The single mode assumption cannot be used to describe the dynamics at such frequencies, which motivated the development of the first multi-mode approximation theory by R. Mindlin and G. Herrmann, now referred to as the Mindlin Herrmann theory [Graff, 1991].

The Mindlin Herrmann theory is a two mode plane cross-sectional theory, where the lateral displacement mode is defined as an additional independent function.

$$u(x, t) = u_0(x, t) \tag{3.19a}$$

$$w(x, t) = rw_1(x, t) \tag{3.19b}$$

The dynamics of a rod modeled by the Mindlin-Herrmann theory is therefore described by a system of two coupled partial differential equation.

$$\rho A\ddot{u}_0 - (\lambda + 2\mu)A\partial_x^2 u_0 - 2\lambda A\partial_x w_1 = 0 \tag{3.20a}$$

$$\rho I_p\ddot{w}_1 + 2\lambda A\partial_x u_0 - \mu I_p\partial_x^2 w_1 + 4A(\lambda + \mu)w_1 = 0 \tag{3.20b}$$

3.3 Dispersion analysis of approximate theories

In general, the frequency equation has multiple real roots, representing the number of modes that coexist at a certain frequency. These roots yield a number of continuous curves in the $k-\omega$ plane called branches. The number of branches corresponds to the number of independent variables chosen to represent $u(x,t)$ and $w(x,t)$ in the relevant theory, and in turn corresponds to a specific mode of propagation. Each branch shows the relationship between frequency ω and wavenumber k for that particular mode of propagation. The collection of branches plotted in the $k-\omega$ plane is the frequency spectrum of the system. Dispersion curves represent phase velocity c_p versus frequency ω for each mode (branch) and can be obtained from the frequency equation by using the relation $\omega = c_p k$.

In order to find the frequency equation of a certain theory, it is assumed that each independent function can be represented as harmonic function $u_j(x,t) = C_j e^{i(kx-\omega t)}$ where j is the expansion index ($2n+1$ or $2m$) in Eq. (3.10). These harmonic assumptions for $u_j(x,t)$ are substituted into the equation(s) of motion of the relevant theory, yielding the frequency equation. A similar assumption applies for the multiple degrees of freedom, the frequency equation is then the characteristic equation of the determinant of arbitrary coefficients C_j.

The different approximate models of longitudinal vibrations of rods mentioned here will be analysed in this section and assessment of their accuracy by comparing their dispersion curves with the dispersion curve of the exact Pochhammer-Chree frequency equation are shown.

Classical theory: The dispersion equation of the Classical theory is:

$$\omega^2 = c_o^2 k^2 \tag{3.21}$$

where $c_o = \sqrt{E/\rho}$ is the rod speed. This dispersion equation implies a non dispersive phase velocity, *i.e.* the rod velocity.

Rayleigh Love theory: The dispersion equation of the Rayleigh Love theory is:

$$\omega^2 = \frac{k^2 c_o^2}{1 + \nu^2 I_n k^2} \tag{3.22}$$

where $I_n = I_p/A$

Rayleigh Bishop theory: The dispersion equation of the Rayleigh Bishop theory is:

$$\omega^2 = \frac{c_T^2 I_n k^4 \nu^2 + k^2 c_0^2}{1 + I_n k^2 \nu^2} \tag{3.23}$$

Mindlin Herrmann theory: The dispersion equation of the Mindlin Herrmann theory is:

$$\omega^2 = \frac{c_L^2 k^2 + c_T^2 k^2}{2} + \frac{2c_L^2 - 2c_T^2}{I_n} \pm \frac{\sqrt{\left(-4Ac_L^2 + 4Ac_T^2 - c_L^2 k^2 I_p - c_T^2 k^2 I_p\right)^2 - 4I_p\left(4Ac_L^2 c_o^2 k^2 - 4Ac_o^2 c_T^2 k^2 + c_L^2 c_T^2 k^4 I_p\right)}}{2I_p} \tag{3.24}$$

where the two modes are entailed by the plus and minus of the root.

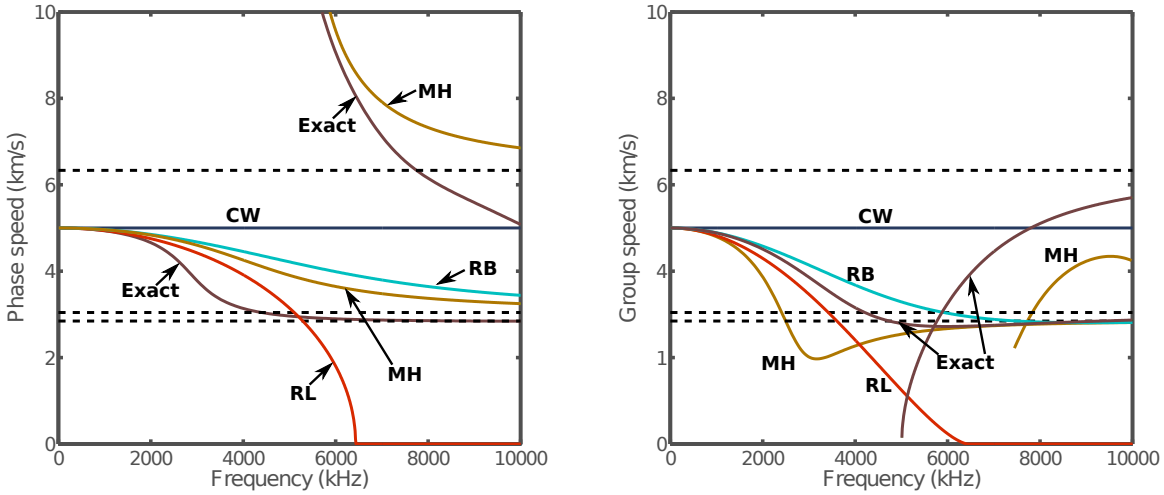

(a) Phase velocity

(b) Group velocity

Figure 3.4 A comparison between phase and group velocities as predicted by different approximate theories: Classical, Rayleigh Love (RL), Rayleigh Bishop (RB), Mindlin Hermann two mode theory (MH) and exact solution. Longitudinal waves in a one millimetre diameter aluminum rod, (c_L = 6.334 km/s, c_T = 3.042 km/s, c_o = 5 km/s, and ν = 0.35)

Figure 3.4(a) shows the phase velocity dispersion curves of the approximate longitudinal waves theories. Comparing Fig. 3.4(a) with Fig. 3.4(b) shows that relying on the group velocity to determine the limits of accuracy of the respective theories provides a more conservative estimate of the accuracy of the theories. Another observation is that RL theory is in better match with the exact theory for the low frequency range. It is noticeable that the second mode of Mindlin-Herrmann theory is adequately approximating the third exact mode but not the second, this stems

from the fact that this second mode is dependent on the value of Poisson's ratio. So, for some values of Piosson's ratio it could match the second longitudinal mode [Graff, 1991].

3.4 Numerical approximation of approximate theories

As mentioned in the introduction the second phase of ascertaining the adequacy of the simulation results as a component of successful engineering decision cycle, is the validation phase. In the validation phase the numerical approximation of a *mathematical model* is studied with focus on the errors introduced by the numerical approximation assumptions.

In this section, the spectral element approximation for the four previously studied mathematical models of the guided waves propagation is rods are developed in detail. The presentation adopted here has certain advantages, by developing the semidiscrete equations in matrix form from the weak form derived in detail in App. B, the element shape functions and quadrature rules are not specified a priori. Even the development can proceed to the fully discrete equations through an explicit time-integration scheme without reference to the specific shape functions used in the approximation. Finally, shape functions and quadrature rules are introduced to complete the formulation making this approach more appropriate to compare the differences between the classical FEM *h*-type, and Legendre spectral element. This presentation will emphasize the particular differences in using certain shape functions, and will easily clarify the origin of the merits of the spectral element in time domain method.

3.4.1 Galerkin method

Galerkin method assumes that both the test function and shape functions are approximated by the same approximating function, and that the essential boundary condition is satisfied by the shape function while the test function at the essential boundary are equal to zero.

Consider a rod of length l, that is divided into n_e elements, Each physical element domain $x \in \Omega_e = [x_1^e, x_2^e]$ is mapped onto the domain $\xi \in \Lambda = [-1, 1]$, where ξ is the non dimensional element coordinate. In the general case, where the elements have different lengths, the linear mapping function has to be computed separately for every element. It has the following form

$$\mathcal{F}_e : \Omega^e \to \Lambda, \quad \xi(x) = \frac{2(x - x_1^e)}{x_2^e - x_1^e} - 1 \tag{3.25a}$$

$$\mathcal{F}_e^{-1} : \Lambda \to \Omega^e, \quad x(\xi) = \frac{(x_2^e - x_1^e)(\xi + 1)}{2} + x_1^e \tag{3.25b}$$

with the Jacobian $J^e = \partial_\xi x = (x_2^e - x_1^e)/2$.

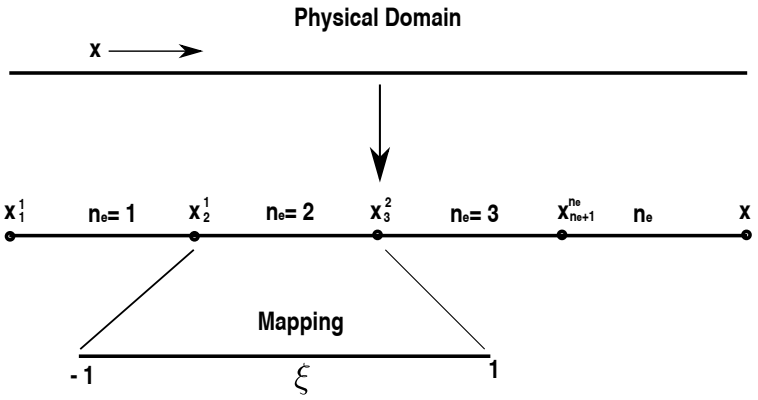

Figure 3.5 Simple domain decomposition and mapping. The rod is divided into n_e elements.

The dependent variable(s) are approximated over the element domain Ω^e by

$$u_i(x(\xi), t) = \phi_i{}^{\mathrm{T}}(\xi)\mathbf{u}_i(t) \tag{3.26}$$

where ϕ_i is a column vector of $p+1$ shape functions, and p is the degree of polynomial used to approximate the dependent variable u_i over the element. $[\,]^{\mathrm{T}}$ denotes the transpose, and $\mathbf{u}_i(t)$ is $p+1$ column vector of time dependent unknown coefficients representing the nodal approximate solution. The specific choice of the shape functions is particular to each type of element, h-type, p-type finite or spectral element, as shown in Fig. 3.6(a), Fig. 3.6(c), and Fig. 3.6(d).

Thus the semidiscrete equations are then obtained from the weak form (see App. B for detailed derivation of the weak forms of the different theories studied in the present work), based on Galerkin method by assuming that both the shape functions and the test functions are the same polynomial and of the same degree i.e. ϕ. The matrix form for each element $\mathbf{M}^e\ddot{\mathbf{u}} + \mathbf{K}^e\mathbf{u} = \mathbf{f}$ have the following components:

Classical theory: Substituting the approximation Eq. (3.26), in the weak form (see App. B)

$$\rho \int_0^l \ddot{u} v \, dx + E \int_0^l \partial_x v \partial_x u \, dx = 0 \tag{3.27}$$

and since $v(x)$ is approximated similarly, the semidiscrete form becomes

$$\begin{aligned}\mathbf{M}^e &= \rho \int_{-1}^{1} \phi\phi^{\mathrm{T}} J^e \, d\xi \\ \mathbf{K}^e &= E \int_{-1}^{1} \partial_\xi \phi \partial_\xi \phi^{\mathrm{T}} (J^e)^{-1} \, d\xi \end{aligned} \tag{3.28}$$

Rayleigh Love theory: Substituting the approximation Eq. (3.26), in the weak form (see App. B)

$$\rho \int_0^l \ddot{u} v \, dx + \rho \nu^2 I_n \int_0^l \partial_x \ddot{u} \partial_x v \, dx + E \int_0^l \partial_x u \partial_x v \, dx = 0 \tag{3.29}$$

and since $v(x)$ is approximated similarly, the semidiscrete form becomes

$$\begin{aligned}\mathbf{M}^e &= \rho \int_{-1}^{1} \phi\phi^{\mathrm{T}} J^e \, d\xi + \rho \nu^2 I_p / A \int_{-1}^{1} \partial_\xi \phi \partial_\xi \phi^{\mathrm{T}} (J^e)^{-1} \, d\xi \\ \mathbf{K}^e &= E \int_{-1}^{1} \partial_\xi \phi \partial_\xi \phi^{\mathrm{T}} (J^e)^{-1} \, d\xi \end{aligned} \tag{3.30}$$

Rayleigh Bishop theory: Substituting the approximation Eq. (3.26), in the weak form (see App. B)

$$\rho \int_0^l \ddot{u} v \, dx + \rho \nu^2 I_n \int_0^l \partial_x \ddot{u} \partial_x v \, dx + E \int_0^l \partial_x u \partial_x v \, dx + \mu \nu^2 I_n \int_0^l \partial_x^2 u \partial_x^2 v \, dx = 0 \tag{3.31}$$

and since $v(x)$ is approximated similarly, the semidiscrete form becomes

$$\begin{aligned}\mathbf{M}^e &= \rho \int_{-1}^{1} \phi\phi^{\mathrm{T}} J^e \, d\xi + \rho \nu^2 I_p / A \int_{-1}^{1} \partial_\xi \phi \partial_\xi \phi^{\mathrm{T}} (J^e)^{-1} \, d\xi \\ \mathbf{K}^e &= E \int_{-1}^{1} \partial_\xi \phi \partial_\xi \phi^{\mathrm{T}} (J^e)^{-1} \, d\xi + \mu \nu^2 I_p / A \int_{-1}^{1} \partial_\xi^2 \phi \partial_\xi^2 \phi^{\mathrm{T}} (J^e)^{-3} \, d\xi \end{aligned} \tag{3.32}$$

Mindlin Herrmann theory: Since we have two degrees of freedom, the matrices are arranged as follows:

$$\begin{pmatrix} {}_u\mathbf{M}^e & \mathbf{0} \\ \mathbf{0} & {}_w\mathbf{M}^e \end{pmatrix} \begin{pmatrix} \ddot{\mathbf{u}}_0 \\ \ddot{\mathbf{w}}_1 \end{pmatrix} + \begin{pmatrix} {}_1\mathbf{K}^e & {}_2\mathbf{K}^e \\ {}_2\mathbf{K}^{e\mathrm{T}} & {}_3\mathbf{K}^e \end{pmatrix} \begin{pmatrix} \mathbf{u}_0 \\ \mathbf{w}_1 \end{pmatrix} = \mathbf{f} \tag{3.33}$$

Substituting the approximation Eq. (3.26), in the weak form (see App. B)

$$\rho \int_0^l \ddot{u} \mathrm{v}_1 \, dx + (\lambda + 2\mu) \int_0^l \partial_x u_0 \partial_x \mathrm{v}_1 \, dx + 2\lambda \int_0^l w_1 \partial_x \mathrm{v}_1 \, dx = 0 \tag{3.34a}$$

$$\rho \mathrm{R}^2 \int_0^l \ddot{w}_1 \mathrm{v}_2 \, dx + 4\lambda \int_0^l \mathrm{v}_2 \partial_x u_0 \, dx + 8(\lambda + \mu) \int_0^l \mathrm{v}_2 w_1 \, dx + \mathrm{R}^2 \mu \int_0^l \partial_x w_1 \partial_x \mathrm{v}_2 \, dx = 0 \tag{3.34b}$$

In order to preserve the symmetry of stiffness matrix we divide Eq. (3.34) by two, yielding the following components of the matrix equation (3.33)

$$\begin{gathered} {}_u\mathbf{M}^e = \rho \int_{-1}^{1} \boldsymbol{\phi} \boldsymbol{\phi}^{\mathrm{T}} J^e \, d\xi, \quad \text{and} \quad {}_w\mathbf{M}^e = \tfrac{\rho \mathrm{R}^2}{2} \int_{-1}^{1} \boldsymbol{\phi} \boldsymbol{\phi}^{\mathrm{T}} J^e \, d\xi \\ {}_1\mathbf{K}^e = (\lambda + 2\mu) \int_{-1}^{1} \partial_\xi \boldsymbol{\phi} \partial_\xi \boldsymbol{\phi}^{\mathrm{T}} (J^e)^{-1} \, d\xi, \\ {}_2\mathbf{K}^e = 2\lambda \int_{-1}^{1} \boldsymbol{\phi} \partial_\xi \boldsymbol{\phi}^{\mathrm{T}} \, d\xi \\ {}_3\mathbf{K}^e = 4(\lambda + \mu) \int_{-1}^{1} \boldsymbol{\phi} \boldsymbol{\phi}^{\mathrm{T}} J^e \, d\xi + \tfrac{\mathrm{R}^2 \mu}{2} \int_{-1}^{1} \partial_\xi \boldsymbol{\phi} \partial_\xi \boldsymbol{\phi}^{\mathrm{T}} (J^e)^{-1} \, d\xi \end{gathered} \tag{3.35}$$

3.4.2 Centered difference explicit time integration

Time discretization of the semidiscrete equations may be accomplished with a number of standard techniques. Here, an explicit time integration FD scheme is used. A FD scheme is explicit if it contains only one nonzero term at time level $t + \Delta t$, and implicit if it contains several. Implicit formulas are typically more stable than explicit ones, but harder to implement. Another point to be taken into consideration, for an unbounded time $t \geq 0$, an implicit formula would seem to require the solution of an infinite system of equations! This is essentially true, and in practice, the system is usually developed to represent a problem with bounded time, where a finite system of equations must be solved. But for the numerical dispersion analysis, we assume, merely as a theoretical device, that the time is unbounded. So, explicit time integration is adopted for this specific reason for the numerical dispersion analysis purpose.

The time domain $0 \leq t \leq T$ is discretized into equal increments Δt, such that the time at the beginning of interval j is $t = (j-1)\Delta t$. The solution for the displacement at the next time step

$j+1$ corresponds to $t+\Delta t$ is obtained by inverting the mass matrix, which gives:

$$\mathbf{u}^{t+\Delta t} = (\Delta t)^2 \left[(\mathbf{M}^e)^{-1} (\mathbf{f} - \mathbf{K}^e \mathbf{u}^t) \right] + 2\mathbf{u}^t - \mathbf{u}^{t-\Delta t} \tag{3.36}$$

3.5 One dimensional spectral element

Until this point the semidiscrete formulation presented is independent of the specific assumption on the type of shape function (the interpolant of nodal variables ϕ), and the quadrature rules used to evaluate the various integrals of the matrices. What distinguishes the different methods, is the specific choice of these two main substitutions.

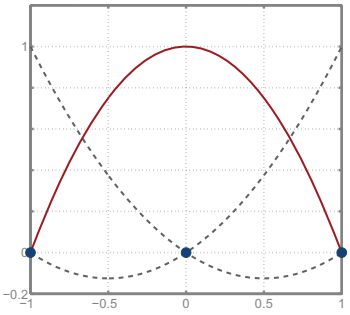

(a) Shape functions for h-type FE quadratic three node element.

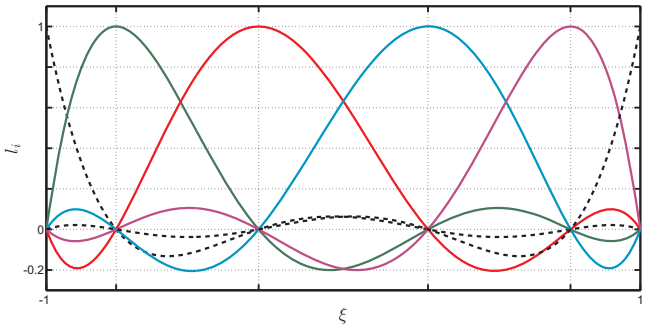

(b) Characteristic Lagrange interpolation polynomials for $p = 5$ based on Legendre nodes.

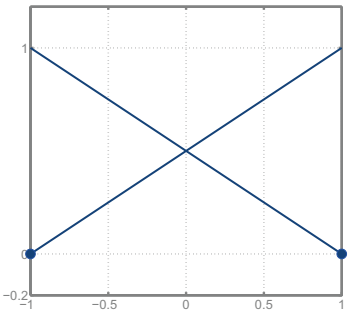

(c) Shape functions for h-type FE linear two node element.

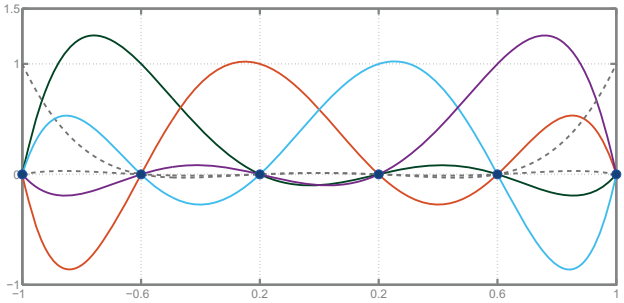

(d) Shape functions for p-type FE high order element with 6 equally spaced nodes.

Figure 3.6 An illustration of the different shape functions used in h-type, p-type FEM, and spectral element used in the present study.

3.5.1 Shape functions

Typically, a spectral element uses Lagrange polynomials of degree 4 to 10 for the interpolation of functions. The $p+1$ Lagrange polynomials (Fig. 3.6(b)) of degree p are defined in terms of $p+1$ nodes $-1 \leq \xi_j \leq 1$, $j = 0, \ldots, p$, by

$$l_j^p(\xi) = \frac{q_p(\xi)}{(\xi - \xi_j) q_p'(\xi_j)}, \qquad q_p(\xi) = \prod_{j=0}^{p} (\xi - \xi_j) \tag{3.37}$$

The interpolation nodes ξ_j are chosen to be the $p+1$ Legendre-Gauss-Lobatto (LGL) nodes which are the roots of $(1-\xi^2)P_p'(\xi) = 0$, where $P_p'(\xi)$ is the 1st derivative of Legendre polynomial of degree p.

Since the interpolating functions satisfy the orthogonality condition *i.e.* $l_i(\xi_j) = \delta_{ij}$, where δ_{ij} is the well known Kronecker-delta. This makes the $\phi = \mathbf{I}_{p+1}$ where $\mathbf{I}_{p+1}$ is the unity $p+1$ matrix, and $\partial_x \phi = \left[l_1' \cdots l_{p+1}' \right]^{\mathrm{T}}$, where the nth row $l_n' = \left[l_n'(\xi_1) \cdots l_n'(\xi_{p+1}) \right]$. This is known as the differentiation matrix.

3.5.2 Quadrature rules

The next step on the way to the matrix formulation, is the evaluation of the integrals over the natural domain. This is done using the so-called LGL quadrature of integration, i.e. transferring the integral into a finite weighted sum:

$$\int_\Lambda g(\xi)\, d\xi \approx \sum_{i=0}^{p} \omega_i g(\xi_i) \tag{3.38}$$

ω_i is the weights of the LGL quadrature, $g(\xi_i)$ is the integrand evaluated at the LGL nodes. The LGL quadrature is a special case of the Gauss quadrature, only the choice of collocation points is different. In the Gauss quadrature the boundary points -1 and 1 of the standard interval are not included. This leads to a numerical integration which is exact for polynomials up to degree $2p+1$. In contrast to that the GLL quadrature is exact only for polynomials up to degree $2p-1$. This may seem very disadvantageous, because we have to integrate polynomials of degree $2p$ (resulting from the product of the test function and the shape function). But only the LGL quadrature allows for a diagonal mass matrix as the Lagrange polynomials for the interpolation can then be defined on the same points.

Classical wave equation: Starting with the integrals we obtain for a single element, the mass and stiffness matrices:

$$\begin{aligned}\mathbf{M}^e &= \rho \int_{-1}^{1} \phi\phi^{\mathrm{T}} J^e(\xi)\, d\xi = \rho \int_{-1}^{1} \sum_{i=0}^{p} l_i(\xi) \sum_{i=0}^{p} l_j(\xi) J^e(\xi)\, d\xi \\ &= \rho \sum_{k=0}^{p} \omega_k \sum_{i=0}^{p} l_i(\xi_k) \sum_{j=0}^{p} l_j(\xi_k) J^e(\xi_k) = \rho \sum_{k=0}^{p} \omega_k \sum_{i=0}^{p} \delta_{ik} \sum_{j=0}^{p} \delta_{jk} J^e(\xi_k) \\ &= \rho \sum_{k=0}^{p} \sum_{i=0}^{p} \sum_{j=0}^{p} \omega_k J_k^e \delta_{ik} \delta_{jk} = \rho \omega_i J_i^e \delta_{ij} = M_{ij}^e \end{aligned} \tag{3.39}$$

where in $\mathbf{K}^e$ we will abbreviate $l_i(\xi_k)$, $l_i'(\xi_k)$ and $J^e(\xi_k)$ by l_{ik}, l'_{jk} and J_k^e respectively.

$$\begin{aligned}\mathbf{K}^e &= E \int_{-1}^{1} \partial_\xi \phi \partial_\xi \phi^{\mathrm{T}} (J^e(\xi))^{-1}\, d\xi = E \int_{-1}^{1} \sum_{i=0}^{p} l_i'(\xi) \sum_{i=0}^{p} l_j'(\xi) (J^e(\xi))^{-1}\, d\xi \\ &= E \sum_{k=0}^{p} \omega_k \sum_{i=0}^{p} l_i'(\xi_k) \sum_{j=0}^{p} l_j'(\xi_k) (J^e(\xi_k))^{-1} = E \sum_{i=0}^{p} \sum_{k=0}^{p} \omega_k l'_{ik} l'_{jk} (J_k^e)^{-1} = K_{ij}^e \end{aligned} \tag{3.40}$$

Rayleigh Love theory: For the sake of brevity we will list the final results of the substitution of the Legendre shape functions, and the application of the LGL quadrature rule.

$$M_{ij}^e = \rho \omega_i J_i^e \delta_{ij} + \rho \nu^2 I_p / A \sum_{i=0}^{p} \sum_{k=0}^{p} \omega_k l'_{ik} l'_{jk} (J_k^e)^{-1} \tag{3.41}$$

$$K_{ij}^e = E \sum_{i=0}^{p} \sum_{k=0}^{p} \omega_k l'_{ik} l'_{jk} (J_k^e)^{-1} \tag{3.42}$$

Rayleigh Bishop theory: One of the advantages of the spectral element formulation is the ease with which a higher order derivative could be approximated, since the interpolant are p^{th} order polynomial, it automatically satisfy $p-1$ continuity requirements on the variables.

$$M_{ij}^e = \rho \omega_i J_i^e \delta_{ij} + \rho \nu^2 I_p / A \sum_{i=0}^{p} \sum_{k=0}^{p} \omega_k l'_{ik} l'_{jk} (J_k^e)^{-1} \tag{3.43}$$

$$K_{ij}^e = E \sum_{i=0}^{p} \sum_{k=0}^{p} \omega_k l'_{ik} l'_{jk} (J_k^e)^{-1} + \mu \nu^2 I_p / A \sum_{i=0}^{p} \sum_{k=0}^{p} \omega_k l''_{ik} l''_{jk} (J_k^e)^{-3} \tag{3.44}$$

The second order differentiation matrix is obtained by the matrix multiplication of the first order differentiation matrix twice [Fornberg, 1996; Funaro, 1992].

Mindlin Herrmann theory: We list directly the results of the substitution of the shape functions in Eq. (3.35).

$$
\begin{aligned}
{}_uM^e_{ij} &= \rho\omega_i J^e_i \delta_{ij}, & {}_wM^e_{ij} &= \frac{\rho \mathrm{R}^2}{2}\omega_i J^e_i \delta_{ij},\\
{}_1K^e_{ij} &= (\lambda+2\mu)\sum_{i=0}^{p}\sum_{k=0}^{p}\omega_k l'_{ik} l'_{jk}(J^e_k)^{-1}, & {}_2K^e_{ij} &= \lambda\sum_{i=0}^{p}\sum_{k=0}^{p}\omega_k l_{ik} l'_{jk}(J^e_k)^{-1}\\
{}_3K^e_{ij} &= 4(\lambda+\mu)\omega_i J^e_i \delta_{ij} + \frac{\mathrm{R}^2\mu}{2}\sum_{i=0}^{p}\sum_{k=0}^{p}\omega_k l'_{ik} l'_{jk}(J^e_k)^{-1}
\end{aligned}
\tag{3.45}
$$

3.6 Dispersion analysis of numerical implementations

For higher-order methods like p-FEM and SEM, the numerical dispersion relation found by the classical numerical dispersion analysis is expressed as an eigenvalue problem where the eigenvalues and eigenvectors represent the approximate angular frequencies and the amplitudes within an element, respectively. Most of these eigenvalues poorly approximate the exact angular frequencies for each wavenumber and these are normally referred to as parasitic modes [Mulder, 1999]. In general, these eigenvalues do not represent eigenvalues that are entailed by the mathematical model but are artifacts of the discrete approximation. We follow [Seriani and Oliveira, 2008] where an estimate of the maximum eigenvalue by its best approximation is used, which is the Rayleigh quotient. The Rayleigh quotient is unique, so parasitic modes are not an issue.

In order to analyze the *spatial discretization* errors only. The harmonic displacement field is written as:

$$\mathbf{u} = \mathbf{A}e^{ik\mathbf{x}}e^{-i\omega t} \tag{3.46}$$

where $\mathbf{x}$ is the vector of nodal coordinates, and $\mathbf{A}$ is the vector of amplitudes associated with those nodes, not necessarily equal. Note that Eq. (3.46) is a vector equation *i.e.* the exponentiation is carried for each element in the $\mathbf{x}$ and the multiplication of the amplitudes vector is carried on an element by element basis. Substituting in the semidiscrete form, we have

$$\Omega_n^2\mathbf{M}\mathbf{y} = \mathbf{K}\mathbf{y} \tag{3.47}$$

$$\mathbf{y} = \mathbf{A}e^{ik\mathbf{x}} \tag{3.48}$$

The solution Ω^2 exists only if $\mathbf{y}$ is an eigenvector of the generalized eigenvalue problem (3.47). This is not true in general because the wave sampled by the mesh nodes is not necessarily a solution of the spectral element equation. However, we choose Ω_n that best approximates

the eigenvalue in the sense that the residual $(\mathbf{K} - \Omega_n^2\mathbf{M})\mathbf{y}$ is orthogonal to $\mathbf{y}$ [Bathe, 1996; Hochstenbach and van der Vorst, 2003]. This generalized eigenvalue problem for the spatial discretization only, has as best approximation for the maximum eigenvalue, the Rayleigh quotient as:

$$\Omega_n^2 = \frac{\overline{\mathbf{y}}^{\mathrm{T}}\mathbf{K}\mathbf{y}}{\overline{\mathbf{y}}^{\mathrm{T}}\mathbf{M}\mathbf{y}} \tag{3.49}$$

where $\overline{\mathbf{y}}^{\mathrm{T}}$ is the conjugate transpose of $\mathbf{y}$.

The *temporal discretization* errors, which only exist in interaction with the spatial discretization errors, is computed by substituting Eq. (3.46) evaluated at $t = t_n$; thus giving the displacement vector at the current t_n, the backward $t_n - \Delta t$ and the forward $t_n + \Delta t$ time steps as:

$$\mathbf{u}^{t} = \mathbf{A}e^{-ik\mathbf{x}}e^{i\omega t_n} \tag{3.50a}$$

$$\mathbf{u}^{t+\Delta t} = \mathbf{A}e^{-ik\mathbf{x}}e^{i\omega(t_n+\Delta t)} \tag{3.50b}$$

$$\mathbf{u}^{t-\Delta t} = \mathbf{A}e^{-ik\mathbf{x}}e^{i\omega(t_n-\Delta t)} \tag{3.50c}$$

into:

$$\mathbf{M}\mathbf{u}^{t+\Delta t} - (2\mathbf{M} + \Delta t^2\mathbf{K})\mathbf{u}^{t} + \mathbf{M}\mathbf{u}^{t-\Delta t} = 0 \tag{3.51}$$

and dividing by $e^{-i\omega t_n}$, we have

$$\Omega_n^2\mathbf{M}\mathbf{y} = \mathbf{K}\mathbf{y} \tag{3.52}$$

$$\Omega_n\Delta t = 2\sin^{-1}\left(\frac{\Omega\Delta t}{2}\right) \tag{3.53}$$

For the choice of Δt, we refer to the CFL condition:

$$c_p\frac{\Delta t}{\Delta x_{min}} \leq 1 \tag{3.54}$$

where Δx_{min} is minimum distance between any consecutive nodes regardless it is an interior node or belong to the element boundary, this is function of the ratio between the element size to the wavelength h/λ and polynomial order p. Since we are evaluating spectral element implementation of different approximate theories, the numerical deviation of the velocity should be measured from the exact phase velocity predicted by each theory. Δt_{max} is the maximum allowable time step, and is determined by the CFL number.

$$\Delta t_{max} = \mathrm{CFL}\frac{\Delta x_{min}}{c_p} \tag{3.55}$$

where $c_p = f(\omega)$ according to the specific approximate theory. Numerical phase and group velocities follow from $c_p^n = \Omega^n/k$ and $c_g^n = c_p^n + k\frac{dc_p^n}{dk}$.

3.6.1 Classical wave equation

For the numerical values of material parameters, although the graphs below comprise dimensionless variables, we take the values of an aluminum rod to generate the stiffness and mass matrices, $c_L = 6.334$ km/s, $c_T = 3.042$ km/s, $c_o = 5$ km/s, and $\nu = 0.35$. The measure of the grid resolution is taken to be the amount of the wavelength covered by a single element, h/λ. The error due to numerical dispersion is measured as the relative deviation $\epsilon(c)$, where c could be the group velocity or phase velocity. The difference between the numerically propagated wave c_p^n and the phase velocity c_p, which in the case of the classical wave equation is the constant rod velocity c_o:

$$\epsilon(c_p) = \frac{c_p^n}{c_p} - 1 = \frac{c_p^n}{c_o} - 1 \tag{3.56}$$

similarly for the group velocity relative error

$$\epsilon(c_g) = \frac{c_g^n}{c_g} - 1 = \frac{c_g^n}{c_o} - 1 \tag{3.57}$$

Figure 3.7(a) shows the dispersion error on phase velocity due to spatial discretization alone, obtained via the substitution of the harmonic displacements in the semi discrete equations directly. The different polynomial orders for the Legendre spectral element are shown in the curves. The general trend of the curves reveals a similar pattern, for the different polynomials, the numerical speed is underestimated by the spatial discretization. Figure 3.7(b) shows the dispersion error on group velocity of the harmonic case, *i.e.* due spatial discretization alone, as a function of the element to wavelength ratio for different polynomial degrees.

The overall behavior demonstrates the following:

1. An increase in the element order decreases the dispersion.
2. The group velocity error is larger than the phase velocity error for the same polynomial order at the same h/λ. Since the wavenumber is increasing linearly with the frequency the change in group velocity follows the slope of the numerical phase velocity change with respect to the wavenumber, and since the slope is always negative, it is normal that the numerical group velocity decreases more steeply.
3. Increasing the mesh density decreases the overall error.

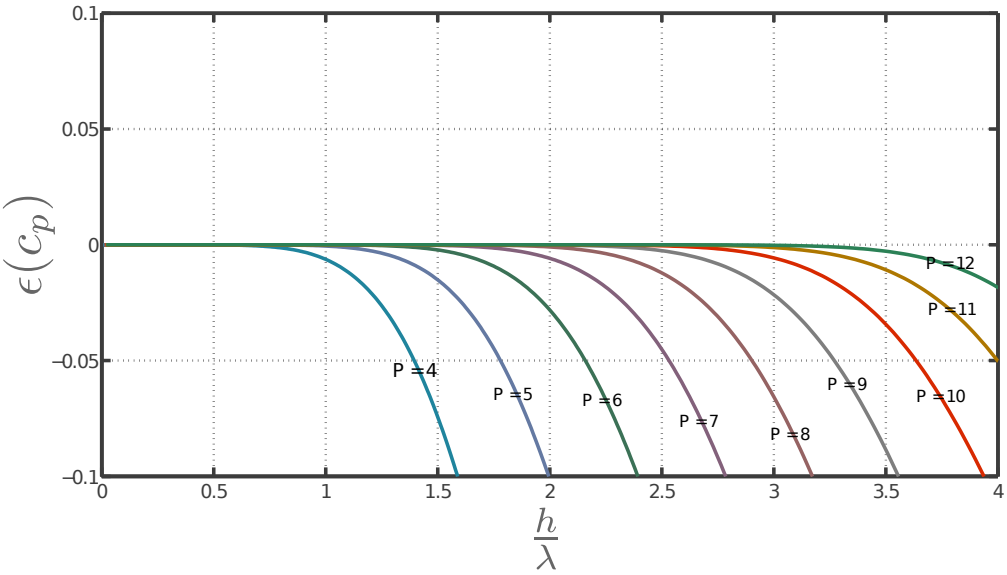

(a) The phase dispersion error due to spatial discretization

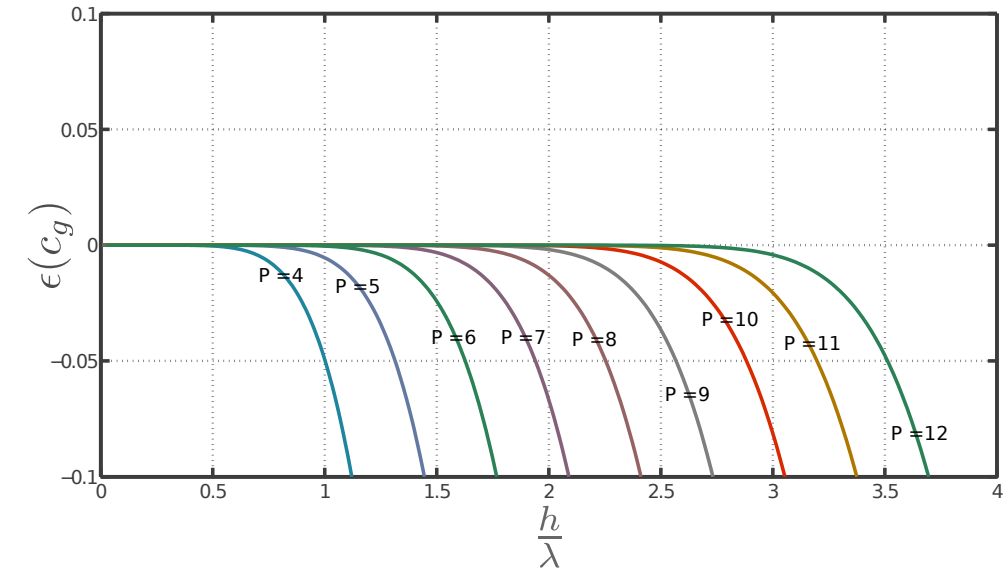

(b) The group dispersion error due to spatial discretization

Figure 3.7 Numerical dispersion errors according to the classical wave theory, for different orders of polynomials used in Legendre one dimensional spectral element.

Figure 3.8 shows the effect of the time integration for the 5th order polynomial, with different CFL numbers, on the phase dispersion errors. As low order method, the errors induced by the centered time difference (time discretization errors) are larger, at the low frequency regime, and tends to overestimate the wave velocity, this effect remains till certain ratio h/λ, which depends

on the polynomial order used, after which the spatial discretization dominates the dispersion and drags the numerical speed of wave propagation down with it.

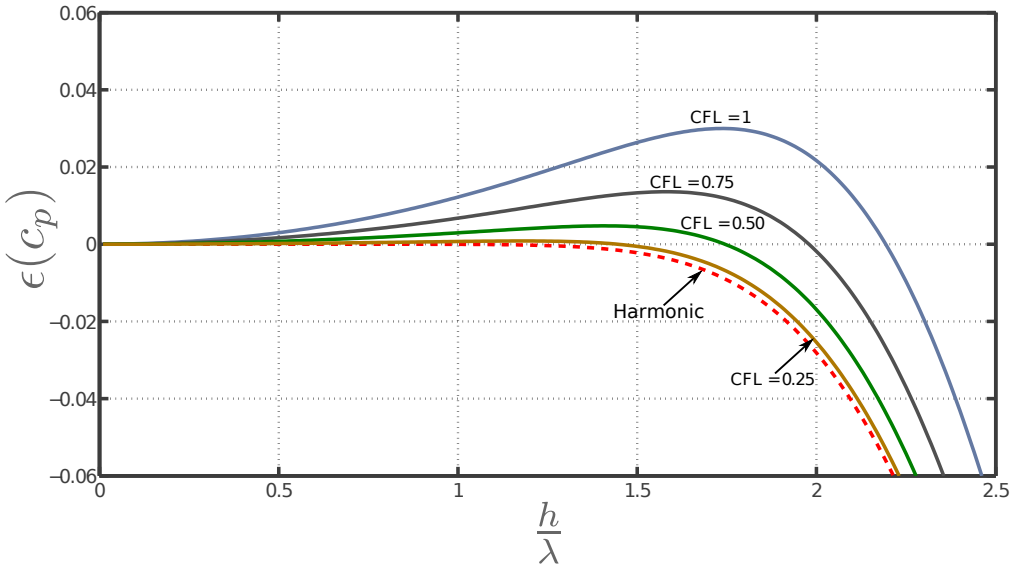

Figure 3.8 Dispersion of classical wave equation, for 5th order polynomial, for different CFL numbers

Although the 2nd order time integration, might be sought of as deteriorating the accuracy, the conflicting trends between the spatial dispersion underestimating the phase velocity, and the overestimation of the phase velocity by the 2nd order centered difference, leads to another accurate numerical phase velocity far beyond the typically accepted grid resolution of 5 points per wavelength. As shown in Fig. 3.8, the error goes to zero again at much smaller grid resolution of 2 points per wavelength for CFL = 0.75.

Figures 3.9(a) and 3.10(b) show the effect of two different CFL numbers, on the phase velocity dispersion. Figures 3.10(a) and 3.10(b) show the effect the same two CFL numbers, on the group velocity dispersion. The same observation made earlier in the harmonic case could be made here. Namely the errors in the group velocity are larger by an order of magnitude than the errors in the phase velocity. Increasing the polynomial order or decreasing the time step reduces markedly the dispersive errors.

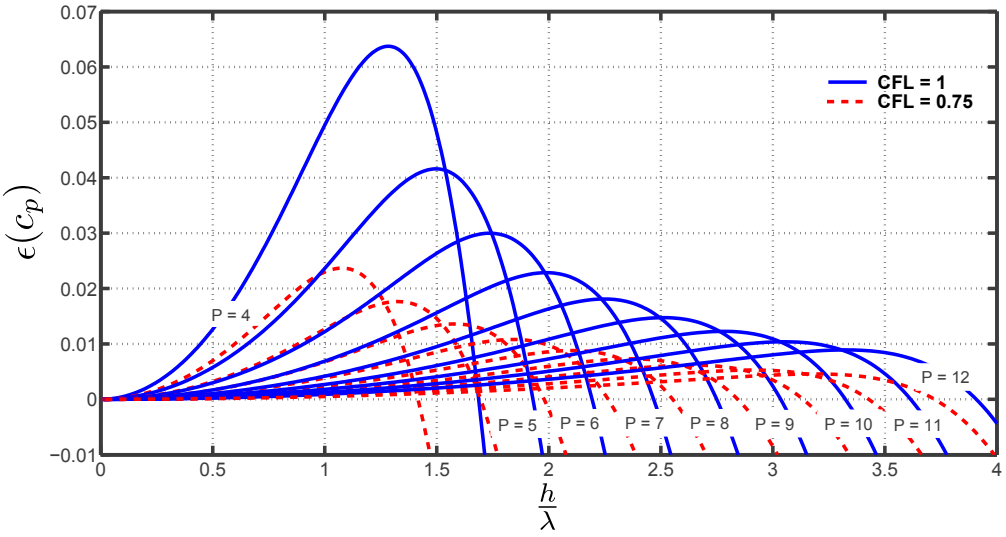

(a) CFL = 1, CFL = 0.75

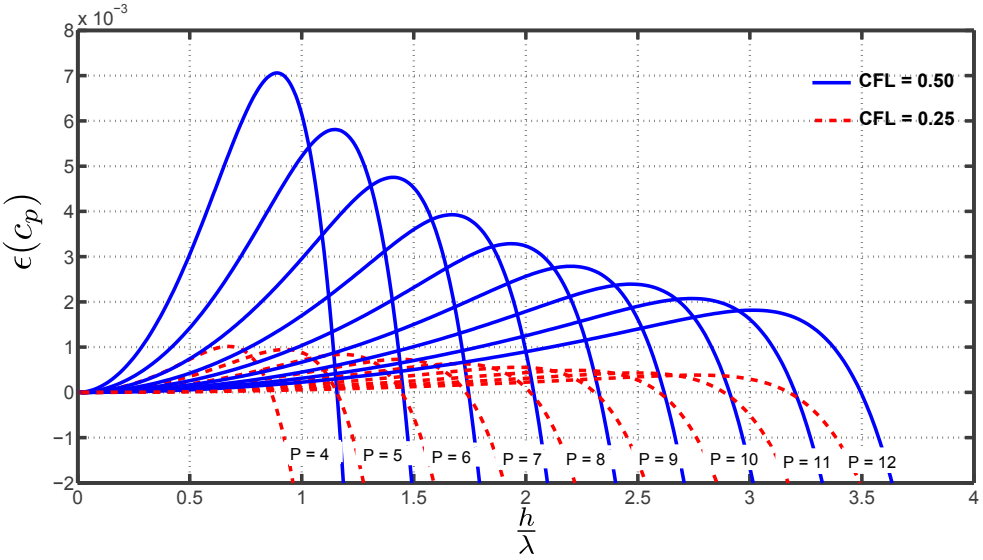

(b) CFL = 0.50, CFL = 0.25

Figure 3.9 Phase dispersion errors for classical wave theory for different CFL numbers, for polynomial orders from 4 to 12

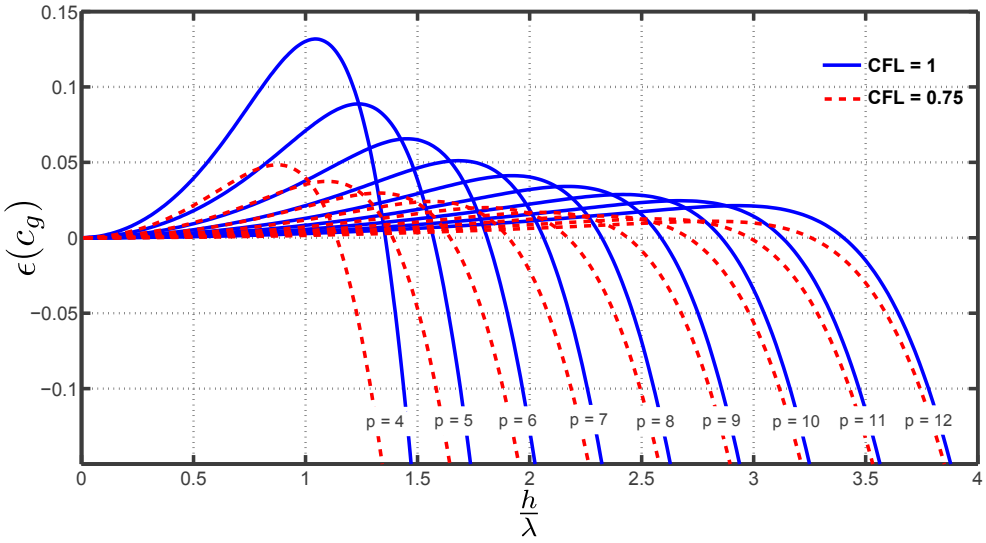

(a) CFL = 1, CFL = 0.75

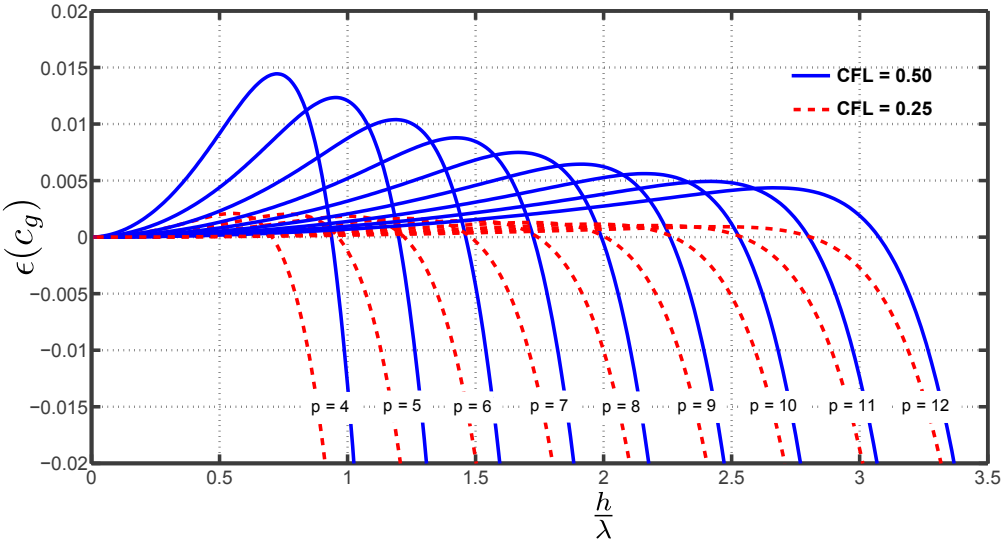

(b) CFL =0.50, CFL = 0.25

Figure 3.10 Group velocity dispersion errors for the classical wave theory due to both spatial and temporal discretization for polynomial orders from 4 to 12 for different CFL numbers

3.6.2 Rayleigh Love theory

Again, for the numerical values of material parameters, the values of an aluminum rod taken to generate the stiffness and mass matrices, are $c_L = 6.334$ km/s, $c_T = 3.042$ km/s, $c_o = 5$ km/s, and $\nu = 0.35$.

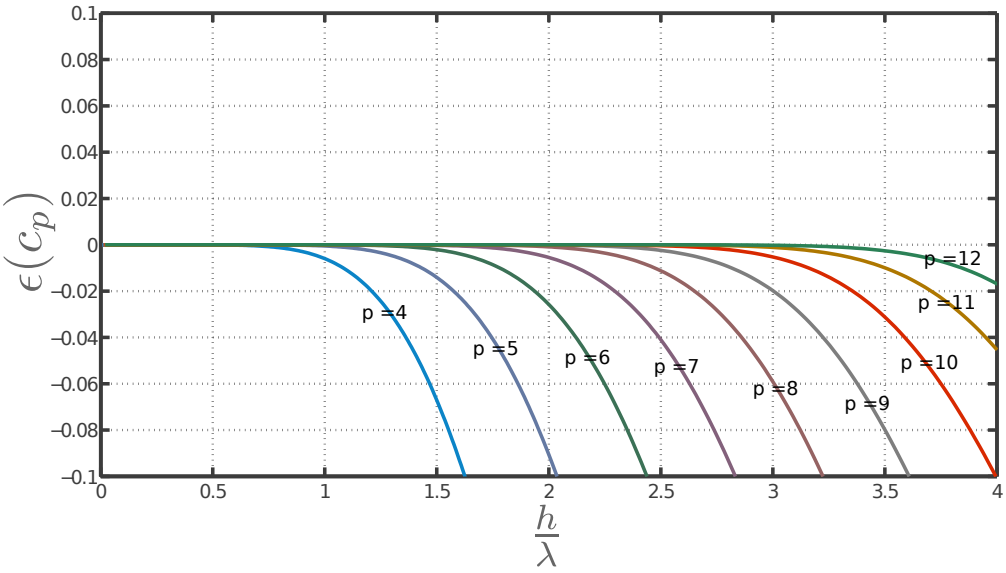

(a) The phase dispersion error due to spatial discretization

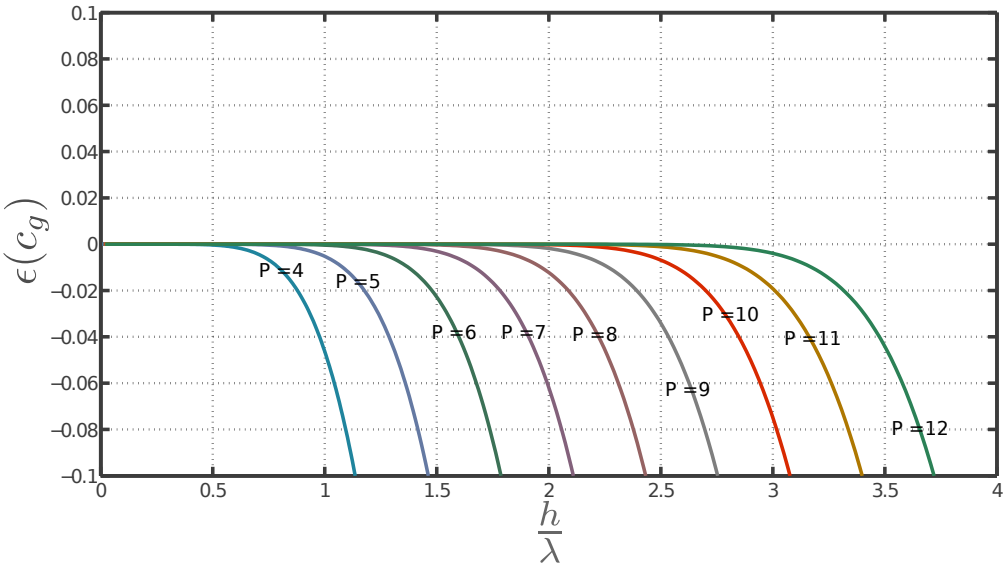

(b) Numerical group velocity dispersion error

Figure 3.11 The dispersion errors due to spatial discretization according to the Rayleigh Love theory, for different orders of polynomials used in Legendre one dimensional spectral element.

The measure of the grid resolution is taken to be the percentage of the wavelength covered by a single element, h/λ.

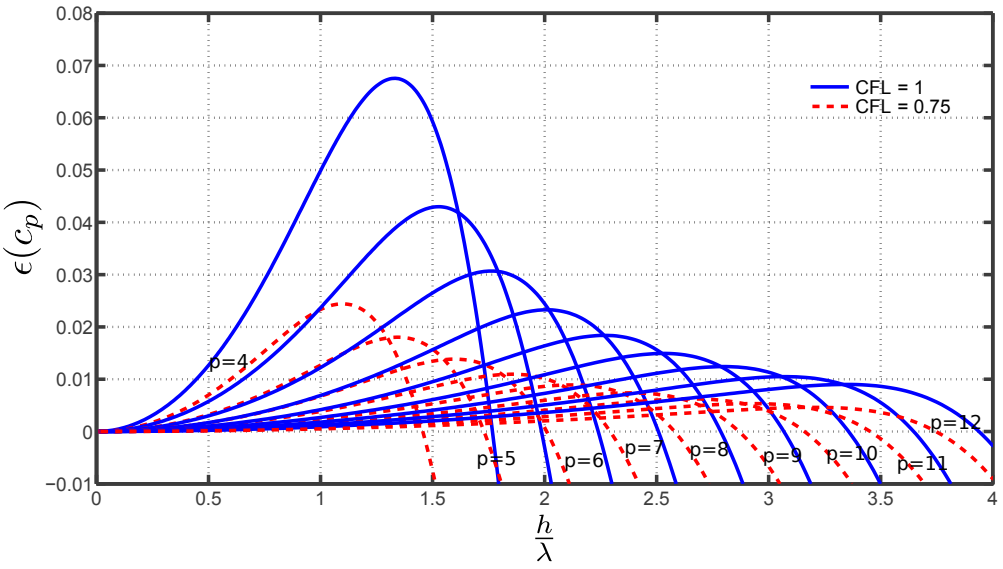

(a) CFL = 1, CFL = 0.75

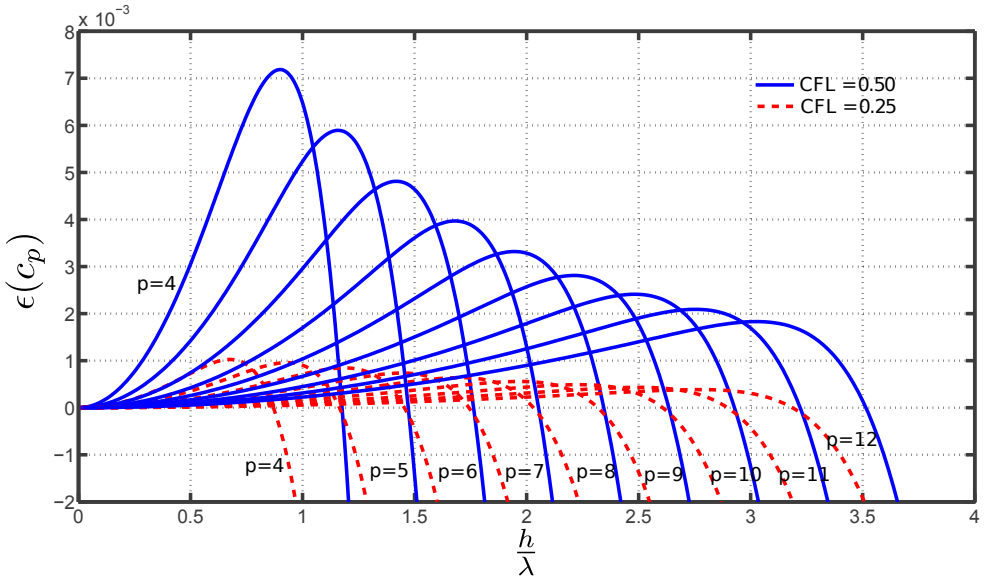

(b) CFL = 0.5, CFL = 0.25

Figure 3.12 Phase velocity dispersion errors for the Rayleigh Love theory due to both spatial and temporal discretization for polynomial orders from 4 to 12. For different CFL numbers.

The amount of dispersion is measured as the relative difference between the numerically propagated wave c_p^n to the phase velocity c_p. Where both the numerical and analytical phase velocities

are non-linearly dependent on the frequency.The error in phase and group velocity is defined as:

$$\epsilon(c_p) = \frac{c_p^n}{c_p} - 1; \quad \epsilon(c_g) = \frac{c_g^n}{c_g} - 1 \tag{3.58}$$

where c_p is the phase velocity as predicted by Eq. (3.22).

Figures 3.11(a) and 3.11(b) show the harmonic components of the phase, and group dispersion errors, respectively. A trend similar to the case of classical wave dispersion (Sec. 3.6.1), for the different polynomials, the numerical speed is underestimated by the spatial discretization.

The error in group velocity is more pronounced, and larger by an order of magnitude than the error in phase velocity. This may be explained by the fact that both the wavenumber and the slope of the change in the phase velocity are decreasing with the increase in the frequency. This leads to the sharper decrease in the group velocity as compared with the classical wave numerical dispersion.

Figures 3.12(a) and 3.12(b) illustrate a similar effect of the low order interaction with a high order approximation. The centered difference approximation tend to overestimate the phase velocity, this deviation tends ot decrease as the CFL number gets smaller. As with the CW theory, the lowering tendency of the high order spatial discretization tends to dominate the total dispersion error at larger element to wavelength ratios.

Figures 3.13(a) and 3.13(b) show the numerical dispersion errors on group velocity, with different CFL numbers. The major assertion that could be drawn from the results is that the group errors are more representative of the actual accuracy since it is the speed with which the wave packets will propagate. Thus, the meshing parameters *i.e.* the element size and the time step should be chosen based on the group dispersion analysis not the phase dispersion unless the analysis is in the frequency domain with harmonic excitation, in such case phase dispersion analysis provide an accurate measure of the expected accuracy of the simulation.

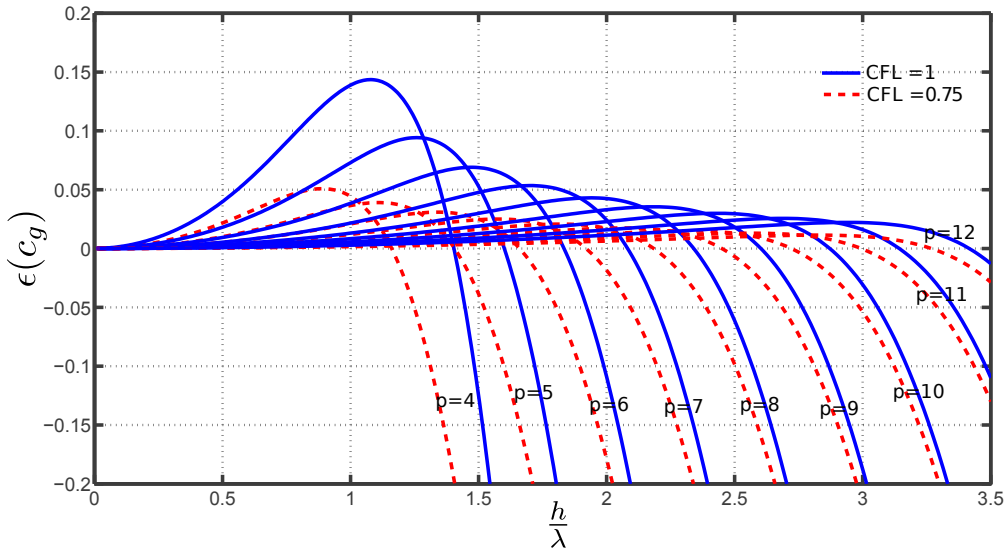

(a) CFL = 1, CFL = 0.75

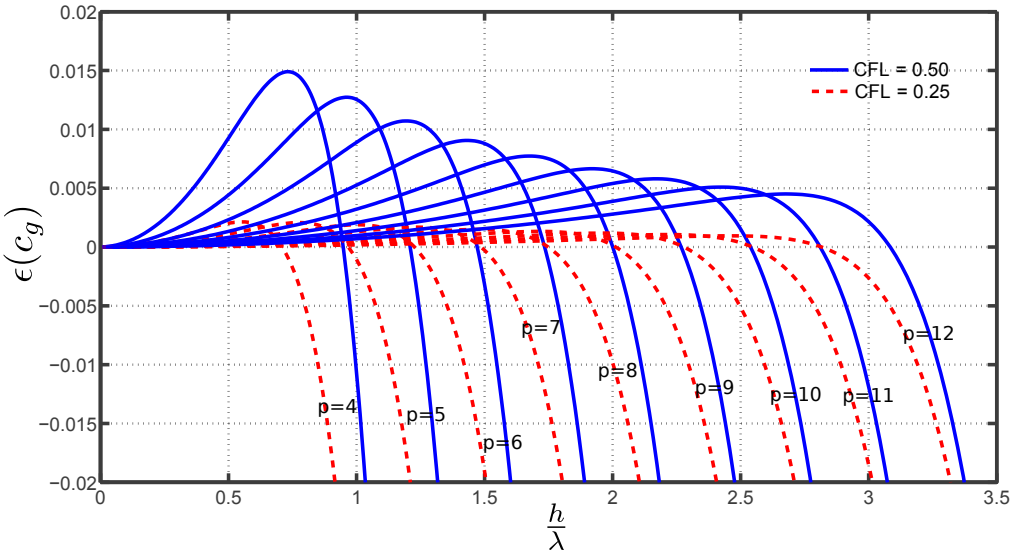

(b) CFL =0.50, CFL = 0.25

Figure 3.13 Group velocity dispersion errors for the Rayleigh Love theory due to both spatial and temporal discretization for polynomial orders from 4 to 12.

3.6.3 Rayleigh Bishop theory

Using the numerical values of material parameters of the aluminum rod as the previous two cases to generate the stiffness and mass matrices, the amount of dispersion is defined, as before, as the relative difference between the numerically propagated wave c_p^n to the phase velocity c_p. Where both the numerical and analytical phase velocities are non-linearly dependent on the frequency.

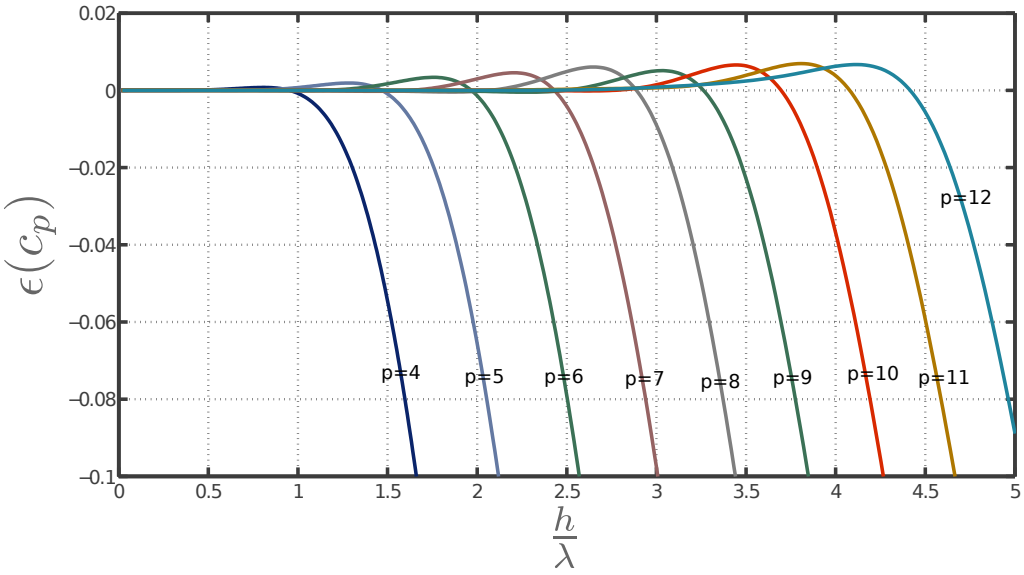

(a) Phase velocity dispersion errors

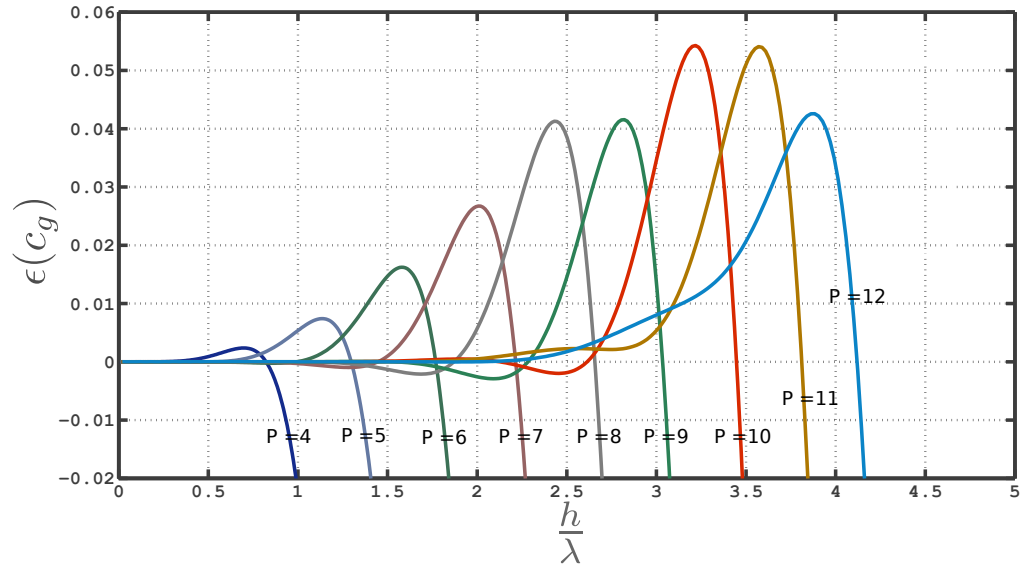

(b) Group velocity dispersion errors

Figure 3.14 The dispersion errors due to spatial discretization according to the Rayleigh Bishop theory, for different orders of polynomials used in Legendre one dimensional spectral element.

The error in phase and group velocity is defined as:

$$\epsilon(c_p) = \frac{c_p^n}{c_p} - 1; \quad \epsilon(c_g) = \frac{c_g^n}{c_g} - 1 \tag{3.59}$$

where c_p is the phase velocity as predicted by Eq. (3.23).

Figure 3.14(a) shows the phase dispersion induced by the spatial discretization alone, i.e. harmonic components of numerical dispersion. The error is quite small for a large portion of the $\frac{h}{\lambda}$. The noticeable difference from the previous two theories, is that the error tend to overestimate the phase velocity before decreasing sharply again. Figures 3.15(a) and 3.15(b) show the induced numerical dispersion due the both the temporal and spatial discretization. The effect of the positive error is magnified by the 2nd order accurate central difference time integration scheme.

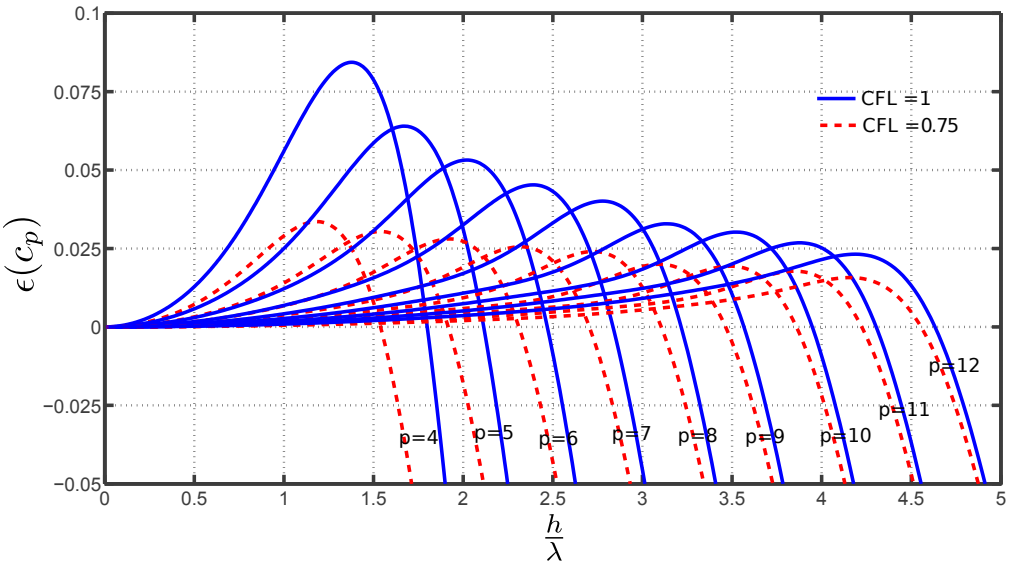

(a) CFL =1, CFL = 0.75

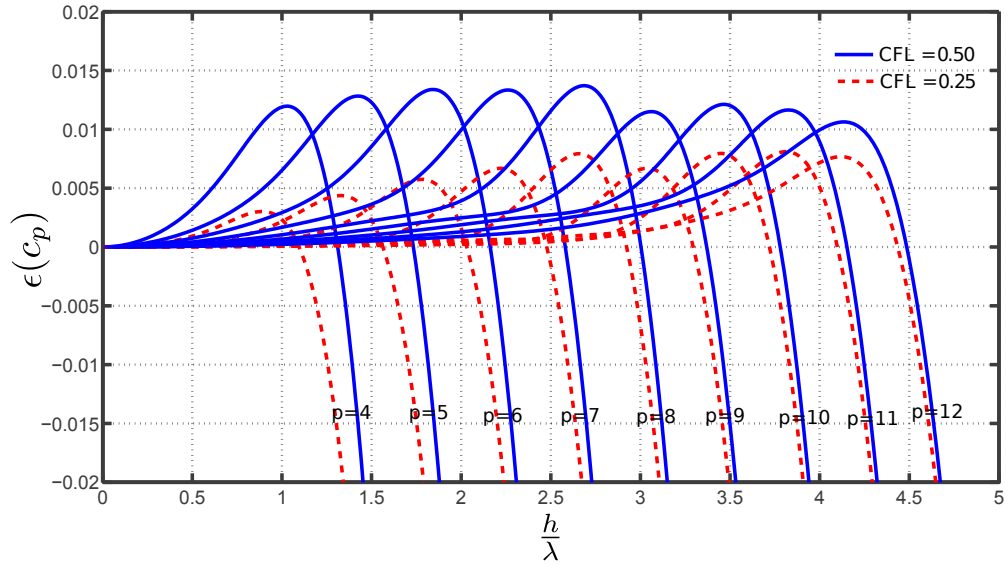

(b) CFL = 0.5, CFL =0.25

Figure 3.15 Phase dispersion errors for Rayleigh Bishop theory for different CFL numbers

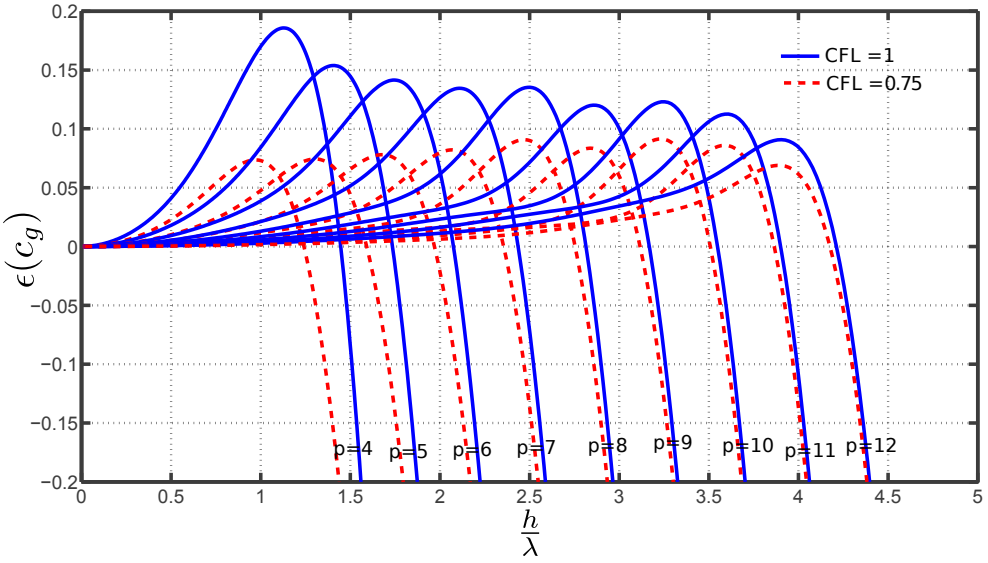

(a) CFL = 1, CFL = 0.75

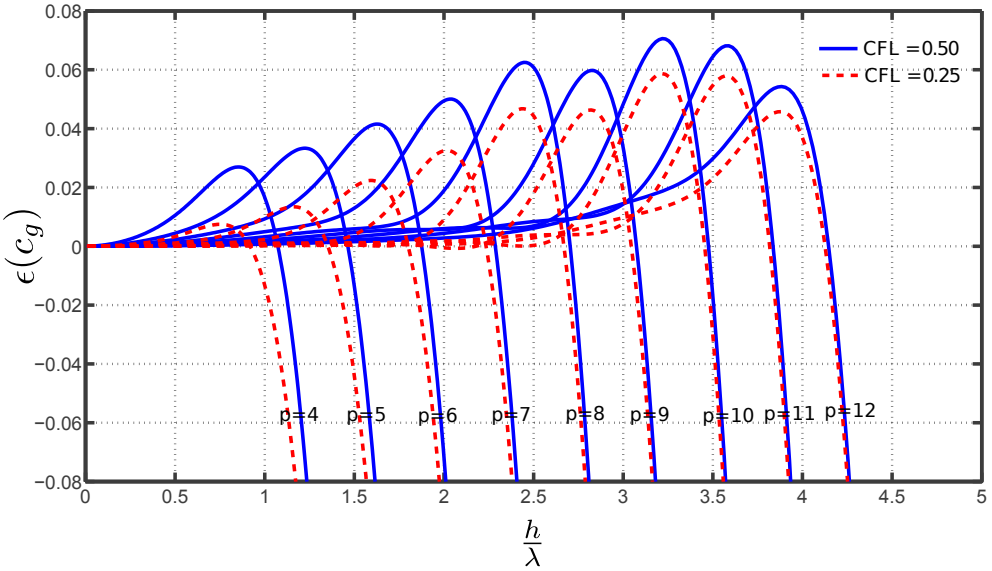

(b) CFL = 0.50, CFL =0.25

Figure 3.16 Group velocity dispersion errors for the Rayleigh Bishop theory due to both spatial and temporal discretization for polynomial orders from 4 to 12 with different CFL numbers

Figures 3.16(a) and 3.16(b) show the effect of different values of the CFL condition on the total numerical dispersion, the larger the CFL number the larger the departure from the accurate c_g velocity.

3.6.4 Mindlin Herrmann theory

For the case of the multiple modes, a special treatment of the matrix equation (3.33) is needed. Referring back to Sec. 3.6, we can write similar expansion for both DOFs u_0 and w_1:

$$\mathbf{u_0} = A_1 e^{ik\mathbf{x}} e^{-i\omega t}, \qquad \mathbf{w_1} = A_2 e^{ik\mathbf{x}} e^{-i\omega t} \tag{3.60}$$

Then substitute Eq. (3.60) into the discrete Eq. (3.33) to compute the approximate parameters $\mathbf{A} = (A_1, A_2)$ and Ω_n. Such a substitution yields

$$-{\Omega_n}^2 A_1 \, {}_{\mathbf{u}}\mathbf{M}\, \mathbf{w}(k) + A_1 \, {}_1\mathbf{K} + A_2 \, {}_2\mathbf{K}\, \mathbf{w}(k) = \mathbf{0} \tag{3.61}$$

$$-{\Omega_n}^2 A_2 \, {}_{\mathbf{w}}\mathbf{M}\, \mathbf{w}(k) + A_1 \, {}_2\mathbf{K}^{\mathrm{T}} \mathbf{w}(k) + A_2 \, {}_3\mathbf{K}\, \mathbf{w}(k) = \mathbf{0} \tag{3.62}$$

Where $\mathbf{w}(k) = e^{ik\mathbf{x}}$, We write the linear system into a block eigenvalue problem $\mathbf{Ky} = {\Omega_n}^2 \mathbf{My}$ where:

$$\mathbf{K} = \begin{pmatrix} {}_1\mathbf{K}^e & {}_2\mathbf{K}^e \\ {}_2\mathbf{K}^{e\mathrm{T}} & {}_3\mathbf{K}^e \end{pmatrix}; \quad \mathbf{M} = \begin{pmatrix} {}_u\mathbf{M}^e & \mathbf{0} \\ \mathbf{0} & {}_w\mathbf{M}^e \end{pmatrix}; \quad \mathbf{y} = \begin{pmatrix} A_1\mathbf{w} \\ A_2\mathbf{w} \end{pmatrix} \tag{3.63}$$

The best approximation Ω_n^2 exists and is given by the Rayleigh quotient

$$\Omega_n^2 = \frac{\overline{\mathbf{y}}^{\mathrm{T}} \mathbf{K} \mathbf{y}}{\overline{\mathbf{y}}^{\mathrm{T}} \mathbf{M} \mathbf{y}} \tag{3.64}$$

which is equivalent to the 2 by 2 eigenvalue problem

$$\begin{pmatrix} d_1 & d_2 \\ d_3 & d_4 \end{pmatrix} \begin{pmatrix} A_1 \\ A_2 \end{pmatrix} = \Omega_n^2 \begin{pmatrix} A_1 \\ A_2 \end{pmatrix} \tag{3.65}$$

where

$$d_1 = \frac{\overline{\mathbf{w}}^{\mathrm{T}} {}_1\mathbf{K}\, \mathbf{w}}{\overline{\mathbf{w}}^{\mathrm{T}} {}_{\mathbf{u}}\mathbf{M}\, \mathbf{w}}; \quad d_2 = \frac{\overline{\mathbf{w}}^{\mathrm{T}} {}_2\mathbf{K}\, \mathbf{w}}{\overline{\mathbf{w}}^{\mathrm{T}} {}_{\mathbf{u}}\mathbf{M}\, \mathbf{w}} \tag{3.66}$$

$$d_3 = \frac{\overline{\mathbf{w}}^{\mathrm{T}} {}_2\mathbf{K}^{\mathrm{T}}\, \mathbf{w}}{\overline{\mathbf{w}}^{\mathrm{T}} {}_{\mathbf{w}}\mathbf{M}\, \mathbf{w}}; \quad d_4 = \frac{\overline{\mathbf{w}}^{\mathrm{T}} {}_3\mathbf{K}\, \mathbf{w}}{\overline{\mathbf{w}}^{\mathrm{T}} {}_{\mathbf{w}}\mathbf{M}\, \mathbf{w}} \tag{3.67}$$

The following explicit solution to Eq. (3.65) is:

$$\Omega_n^2 = \frac{d_1 + d_4}{2} \pm \sqrt{\left(\frac{d_1 - d_4}{2}\right)^2 + d_2 d_3} \tag{3.68}$$

The error in phase velocity and group velocity is defined as:

$$\epsilon(c_p) = \frac{c_p^n}{c_p} - 1; \quad \epsilon(c_g) = \frac{c_g^n}{c_g} - 1 \tag{3.69}$$

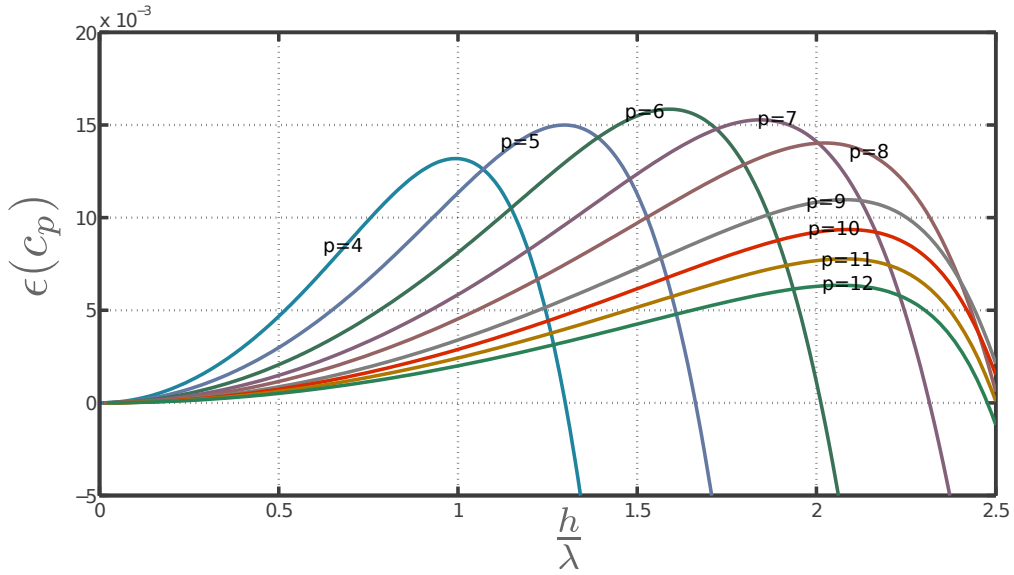

(a) Phase velocity dispersion errors

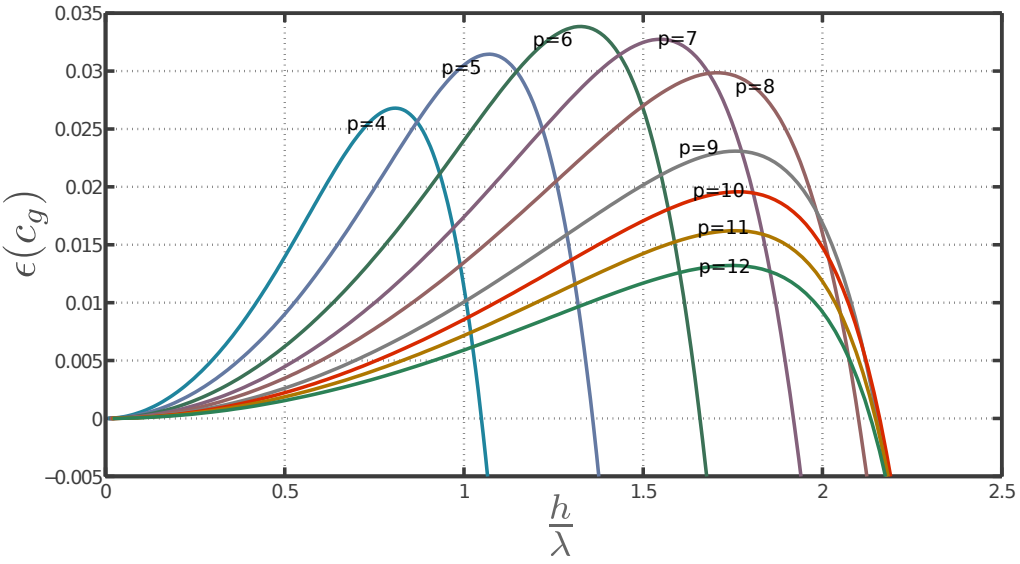

(b) Group velocity dispersion errors

Figure 3.17 The dispersion errors due to spatial discretization according to the Mindlin Herrmann theory, for different orders of polynomials (4-12) used in Legendre one dimensional spectral element.

Figures 3.17(a) and 3.17(b) show the numerical dispersion induced error in the phase and group velocity, respectively, for the first Mindlin Herrmann mode for different polynomial orders ($p = 4$ to 12). The errors tend to behave in a clustered fashion, as well as all the spatially induced dispersion tend to overestimate the velocity.

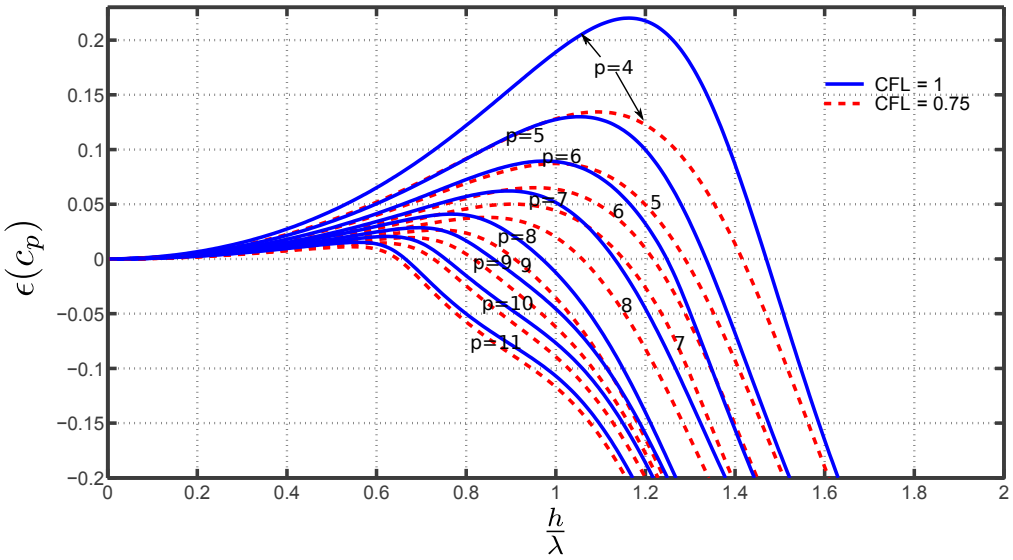

(a) CFL = 1, CFL = 0.75

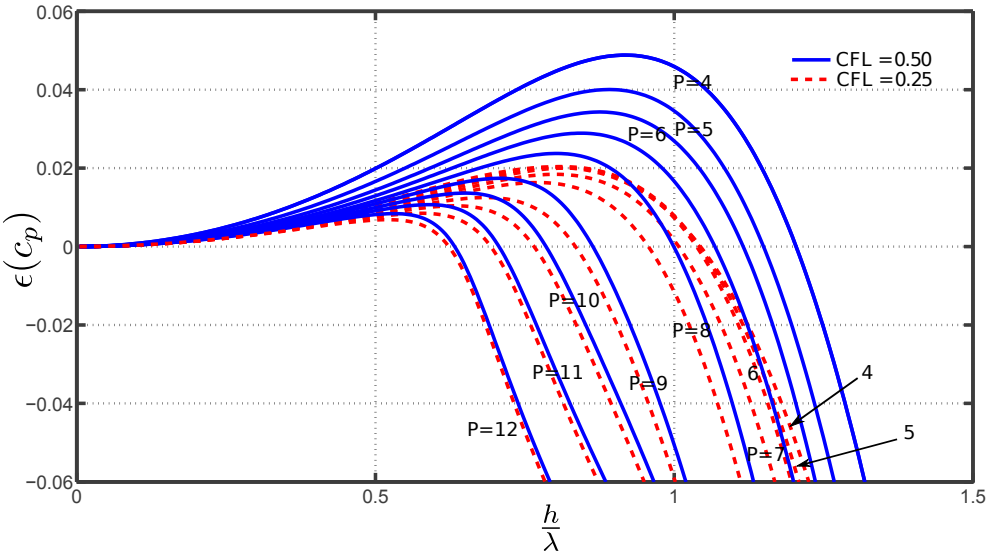

(b) CFL = 0.50 , CFL = 0.25

Figure 3.18 Phase dispersion errors for Mindlin Herrmann theory for different CFL numbers, for polynomial orders from 4 to 12.

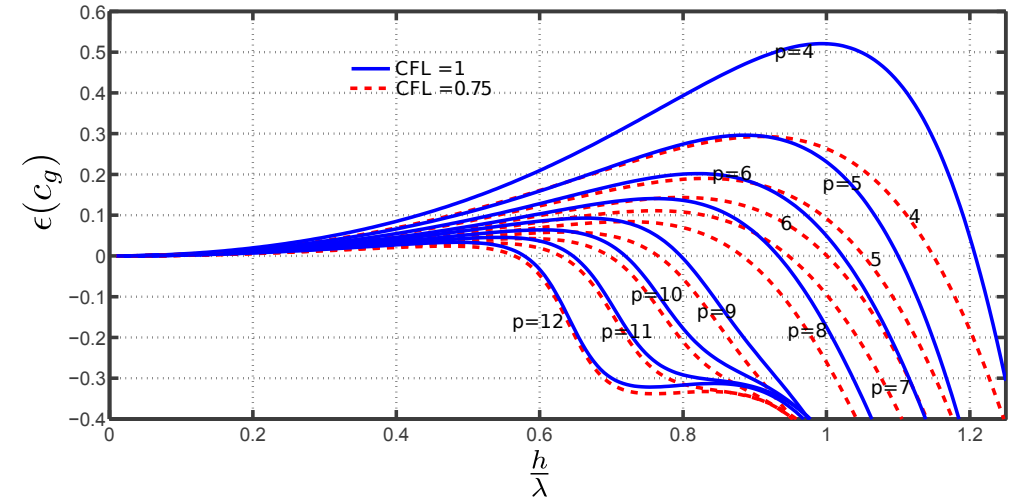

(a) CFL = 1, CFL = 0.75

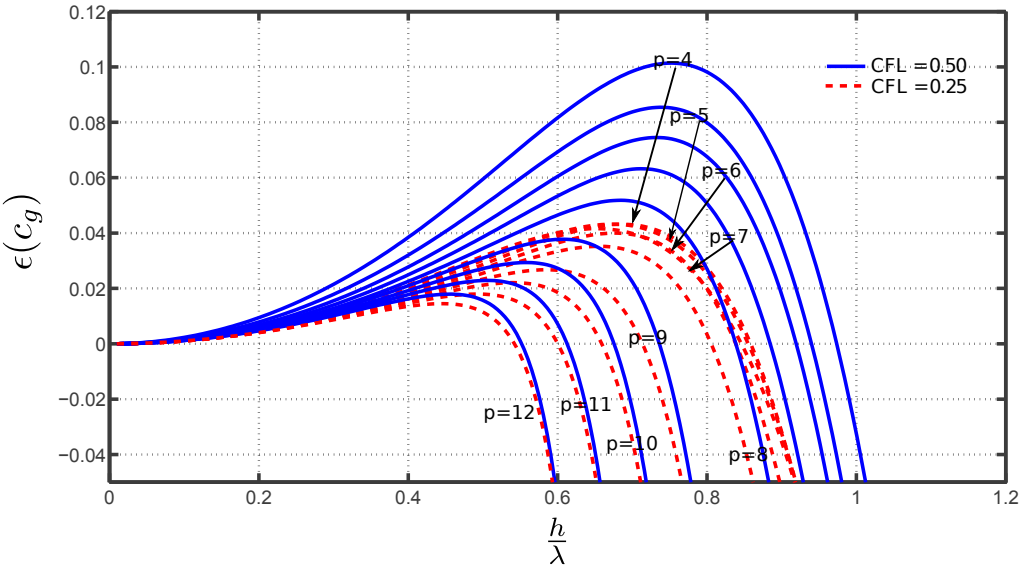

(b) CFL = 0.50, CFL = 0.25

Figure 3.19 Group velocity dispersion errors for the Mindlin Herrmann theory due to both spatial and temporal discretization for polynomial orders from 4 to 12.

Figures 3.18(a) and 3.18(b) show the dispersion errors induced by the temporal discretization, with CFL numbers 1, and 0.75. As the CFL number are decreased the dispersion errors are decreased, with a similar tendency to of the errors to cluster. Figures 3.19(a) and 3.19(b) show the effect of temporal discretization on the numerical group velocity. It confirms the suggestion that the group velocity should be considered a more accurate measure of the accuracy, since it

also predicts a deviation order of magnitude higher than that predicted by the phase velocity dispersion.

3.7 Conclusions

Distribution of nodes within spectral finite elements influence directly the elemental shape functions. In the case of the equidistant distribution of nodes the shape function exhibits undesired high oscillations near the element ends for high orders of approximation polynomials which is associated with the Runge phenomenon as recalled from Sec. 2.4.3. This behavior, however, is not present for the Legendre and Chebyshev node distributions. The accuracy of the spectral element approximation is demonstrated for the rod elements, for three different approximate theories of increasing complexity. This fact is manifested in the decrease of the numerical dispersion error at the same $\frac{h}{\lambda}$ with increasing polynomial order, which is a general observation for all the cases studied. In other words, it is not just the number of mesh nodes sampling the wavelength that controls the accuracy, but also the distribution of those nodes in the sampled wavelength.

For the case of higher order derivatives, normally encountered in the more complex engineering theories, the FEM, needs a special treatment for the continuity requirements, *e.g.* Hermite polynomials for beam elements. In the case of the spectral element, it is a straightforward extension of the concept of the differentiation matrices.

The conflict between orders of both temporal and spatial discretization, could become more beneficial than normally believed, since the error goes back to zero at fewer grid points than typically recommended in literature. This may be only valid for the simple geometries, but still a point that is worth exploration.

At the end, the effect of numerical dispersion on the group velocity is larger by a magnitude of order than its effect on the phase velocity, thus it makes a more accurate measure to set the mesh parameters based on the errors induced in group velocity.

A well known result from the mathematical analysis of FEM [Strang and Fix, 1988] is the underestimation of the eigenvalue by the discrete value, in the harmonic case $\omega^n \leq \omega$. Since in the previous results a similar trend was witnessed, it could be hypothesized that for any of the Jacobi family of polynomials, we could generalize this underestimation trend. For the temporal discretization, the conflict of order, would as well be seen, but may differ in the amount from one high order polynomial type to the other.

In the next chapter, the guided wave propagation in plates is studied, starting by laying the foundations of Lamb waves as a plane strain wave confined to the section of an infinite plate.

The dispersion relations of the classical plate theory and first order shear deformation theory as approximate models of guided waves in plates are deduced as well as compared with the exact solution. Next the spectral elements for those approximate mathematical models as well as the plane strain elastic wave propagation in both unbounded and doubly bounded media are formulated in detail. The numerical dispersion are analyzed for each model using and extending the same approach of Rayleigh quotient.

CHAPTER 4

Formulation and numerical dispersion analysis of spectral element for guided waves propagation in plates

> Whether in the world of truth [science] or in the world of beauty [art], the human mind, on its way towards the ultimate cognition, endeavors to understand the intrinsic nature of things; not to understand things as they are but as they must be–this is the intrinsic necessity
>
> CORNELIUS LANCZOS (1893-1974)

LAMB waves (LW) are guided waves that propagate in *infinite* doubly bounded medium, in the sagittal plane, due to the presence of two traction free boundaries (*i.e.* in contact with vacuum), for which displacements occur both in the direction of wave propagation and normal to the plane of the plate. Lamb waves were first predicted mathematically and described by H. Lamb [Lamb, 1917].

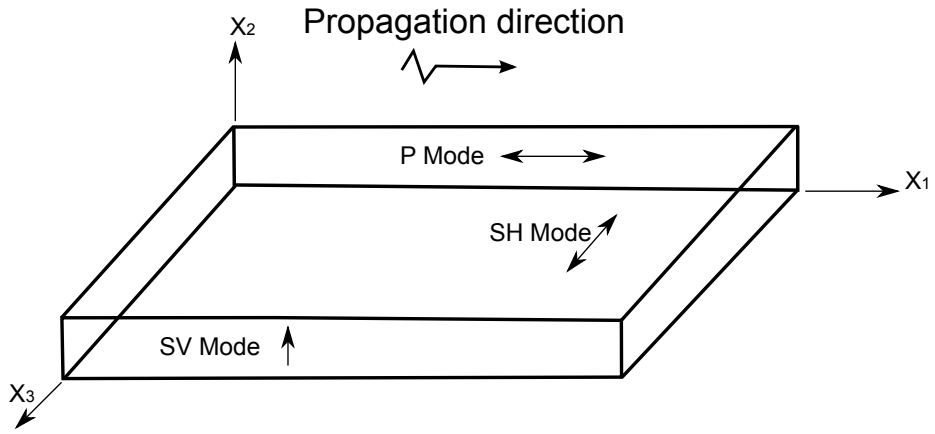

Figure 4.1 Coordinate system, and the polarization directions of the three principal wave propagation modes.

Being two dimensional, Lamb waves can propagate over considerable distances without much attenuation, and since they produce stresses throughout the plate (shell) thickness, the entire thickness of the plate (shell) could be scanned, offering an opportunity for damage detection in plate-like structures [Staszewski *et al.*, 2004; Viktorov, 1967]. Unfortunately, Lamb waves are dispersive and have at least two coexisting propagating modes at a specific frequency-thickness product (fd) [Royer and Dieulesaint, 2000].

Figure 4.1 depicts the coordinate system used to define the different modes that can propagate in the plate. The sagittal plane (x_1, x_2), is the plane of polarization of LW, based on the plane strain assumption, there is no coupling between the shear horizontal (SH) modes, polarized in the x_3 direction, and the two P-SV modes. The primary (P) mode is polarized in the x_1 direction - the direction of wave propagation, i.e. primary mode is longitudinal - and shear vertical (SV) mode is polarized in the x_2 direction.

In the rest of the chapter; a review of the derivation of Rayleigh-Lamb frequency equations are summarized mainly in order to unify the terminology and to lay the necessary background for understanding the presented results. In the sections that follow two major engineering approximate theories are covered

4.1 Exact solution: Rayleigh-Lamb frequency equations

The target of this deduction is twofold the first is to explain how the coupling between the P and SV propagation modes emerge due to the presence of the traction free boundaries, thus leading to specific Lamb modes. The second aim is to illustrate the plane wave nature of the Lamb modes, which will play a major rule in the numerical dispersion analysis.

Based on Stokes-Helmholtz decomposition of the displacement field, the displacement field $\mathbf{u}$ can be represented as:

$$\mathbf{u} = \nabla\phi + \nabla \times \Psi \tag{4.1}$$

Where ∇ is the divergence operator, in Cartesian coordinates $\nabla = \frac{\partial}{\partial x_1}\mathbf{e}_1 + \frac{\partial}{\partial x_2}\mathbf{e}_2 + \frac{\partial}{\partial x_3}\mathbf{e}_3$, ϕ is a scalar potential, and Ψ is a vector potential. This is complemented with a gage condition to insure uniqueness between the displacement field components u_1, u_2, u_3 and both the scalar potential field ϕ, and vector potential field components Ψ_1, Ψ_2, Ψ_3.

$$\nabla \cdot \Psi = 0 \tag{4.2}$$

On substitution in Navier's equations for isotropic linearly elastic medium, with the absence of body forces:

$$(\lambda + 2\mu)\nabla(\nabla \cdot \mathbf{u}) - \mu\nabla \times \nabla \times \mathbf{u} = \rho\ddot{\mathbf{u}} \tag{4.3}$$

one obtains two uncoupled wave equations:

$$\nabla^2\phi - \tfrac{1}{c_l^2}\ddot{\phi} = 0, \quad c_l^2 = \frac{(\lambda + 2\mu)}{\rho} \tag{4.4}$$

$$\nabla^2\Psi - \tfrac{1}{c_t^2}\ddot{\Psi} = 0, \quad c_t^2 = \frac{\mu}{\rho} \tag{4.5}$$

where λ and μ are Lamé's constants, c_l, c_t are longitudinal wave velocity, and transverse wave velocity, respectively. Equations (4.4)) and (4.5) have a solution of the form

$$\phi(\mathbf{x}, t) = \phi(\mathbf{n} \cdot \mathbf{x} - c_l t) \tag{4.6}$$

$$\Psi(\mathbf{x}, t) = \Psi(\mathbf{n} \cdot \mathbf{x} - c_t t) \tag{4.7}$$

Using the coordinate system depicted in Fig. 4.1, both potentials are independent of x_3 coordinate, due to the plane strain assumption. Thus if $\Psi_1 = \Psi_2 = 0$, leaving only Ψ_3, the two potential functions $\phi(x_1, x_2, t)$ and $\Psi_3(x_1, x_2, t)$ give the following displacement components [Achenbach, 1973; Graff, 1991]:

$$u_1 = \frac{\partial\phi}{\partial x_1} + \frac{\partial\Psi_3}{\partial x_2} \tag{4.8}$$

$$u_2 = \frac{\partial\phi}{\partial x_2} - \frac{\partial\Psi_3}{\partial x_1} \tag{4.9}$$

so that Eqs. (4.4) and (4.5) can be written explicitly:

$$\frac{\partial^2\phi}{\partial x_1^2} + \frac{\partial^2\phi}{\partial x_2^2} = \frac{1}{c_l^2}\frac{\partial^2\phi}{\partial t^2} \tag{4.10}$$

$$\frac{\partial^2\Psi_3}{\partial x_1^2} + \frac{\partial^2\Psi_3}{\partial x_2^2} = \frac{1}{c_t^2}\frac{\partial^2\Psi_3}{\partial t^2} \tag{4.11}$$

These equations have a solution of the form [1]:

$$\begin{aligned} \phi &= \Phi(x_2)e^{i(k_1 x_1 - \omega t)} = \Phi(x_2)e^{i\xi} \\ \Psi_3 &= i\psi(x_2)e^{i(k_1 x_1 - \omega t)} = i\psi(x_2)e^{i\xi} \end{aligned} \tag{4.12}$$

and, after substitution into the wave equations, this reduces to a couple of linear homogeneous second order ordinary differential equations in both φ, and ψ, admitting the following form of

1. The derivation is following that given by Graff [Graff, 1991].

solution:

$$\phi = A\sin\alpha x_2 + B\cos\alpha x_2, \qquad \alpha^2 = \frac{\omega^2}{c_l^2} - k_1^2 = k_1^2\left(\frac{c_p^2}{c_l^2} - 1\right) \tag{4.13}$$

$$\psi = C\sin\beta x_2 + D\cos\beta x_2, \qquad \beta^2 = \frac{\omega^2}{c_t^2} - k_1^2 = k_1^2\left(\frac{c_p^2}{c_t^2} - 1\right) \tag{4.14}$$

From Eqs. (4.8) and (4.9) we have:

$$u_1 = i(Bk_1\cos\alpha x_2 + C\beta\cos\beta x_2) + i(Ak_1\sin\alpha x_2 - D\beta\sin\beta x_2) \tag{4.15a}$$

$$u_2 = (-B\alpha\sin\alpha x_2 + Ck_1\sin\beta x_2) + (A\alpha\cos\alpha x_2 + Dk_1\cos\beta x_2) \tag{4.15b}$$

where $e^{i\xi}$ is implied, and from this form the main advantage of the method of potential is seen: the possibility of separating the symmetric and asymmetric modes. The first bracket in each equation refers to the symmetric displacement with respect to the plane of symmetry ($x_2 = 0$) (see Fig. 4.2), while the second bracket is for the asymmetric mode.

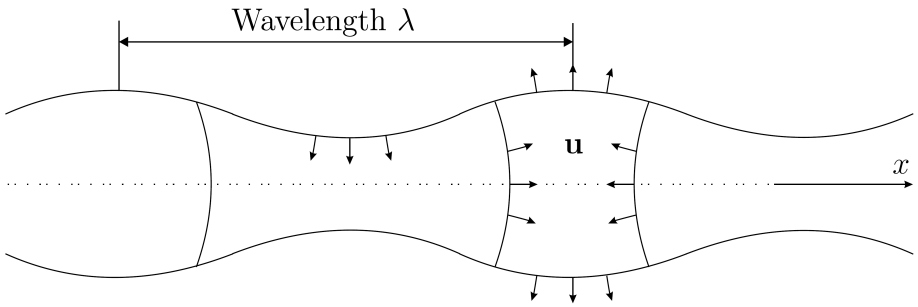

(a) Symmetric

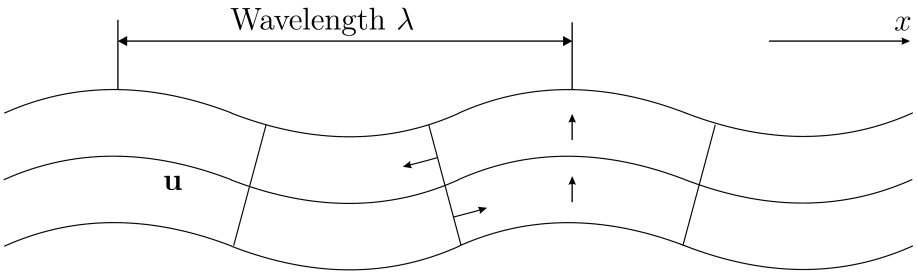

(b) Antisymmetric

Figure 4.2 Mode shapes of symmetric (a) and antisymmetric (b) fundamental Lamb wave modes. Longitudinal displacements of symmetric (antisymmetric) wave modes are equal (opposite) on either side of the median plane, transverse (vertical) displacements are opposite (equal) [Royer and Dieulesaint, 2000].

After imposing the natural boundary conditions,

$$\sigma_{22} = \sigma_{12} = \sigma_{23} = 0, \qquad y = \pm d/2, \tag{4.16}$$

we arrive after some manipulation to the Rayleigh-Lamb dispersion equations.

$$\frac{\tan \beta d/2}{\tan \alpha d/2} + \left(\frac{4\alpha\beta k_1^2}{\left(k_1^2 - \beta^2\right)^2} \right)^{\pm 1} = 0, \quad \begin{cases} +1 & \text{symmetric} \\ -1 & \text{asymmetric} \end{cases} \tag{4.17}$$

The transcendental Rayleigh-Lamb dispersion equations do not have a closed form solution. Moreover, more complicated dispersion equations for the anisotropic plate, multilayered isotropic and multilayered anisotropic plates. Numerical solution of the characteristic equations is the only method available for solution. One way for finding the roots is to fix one of the variables and then vary the other, looking for a change of sign of the function [Kelly, 1995]. However, this approach suffers from a serious shortcoming, when two roots are in close proximity, for example near the crossing points of two modes, the function changes sign twice and such schemes can be unstable. It is therefore safer to use a slower iteration technique such as bisection and to look for a minimum of the absolute value of the function rather than a sign change [Lowe, 1992, 1995; Pavlakovic and Lowe, 2003].

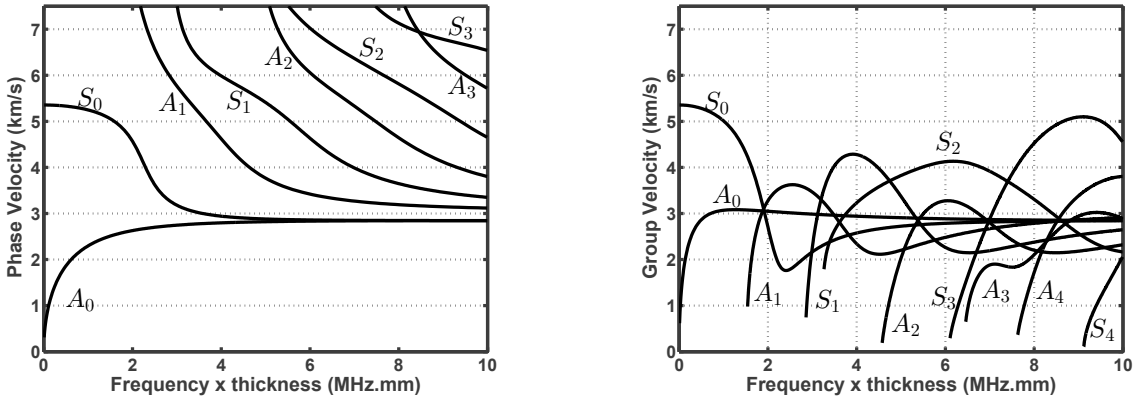

(a) Phase velocity

(b) Group velocity

Figure 4.3 Phase (a) and group (b) velocities of Lamb symmetric S_n and anti-symmetric A_n modes in an Al plate (c_l= 6.420 $mm/\mu s$, c_t= 3.040 $mm/\mu s$) as a function of the frequency thickness product fd [Vallen, 2009].

A better technique for the calculation of a dispersion curve is to employ some curve tracing algorithm which starts from a known solution. Initially, roots are found by varying the phase velocity at fixed frequency, or the frequency at fixed velocity. Each of these roots is the starting

point for the calculation of a dispersion curve. To calculate a dispersion curve, the wavenumber is incremented steadily and a new solution is found at each fixed increment by iteration on the frequency. The loci of roots of the characteristic function are the dispersion curves. They are usually displayed as phase velocity against frequency thickness product [Rose, 2003]. Figure 4.3 shows the dispersion curves for aluminum plate, where S_n and A_n stand for the n^{th} symmetric and anti-symmetric propagating modes, respectively. The two fundamental modes S0 and A0 are the only coexisting modes at low frequency-thickness fd. As the fd product approaches zero, the S0 and A0 modes degenerate into the basic axial and flexural plate modes. At the other extreme, as $fd \to \infty$, Lamb wave modes degenerate into Rayleigh wave confined to the plate surface with a constant unique velocity c_R.

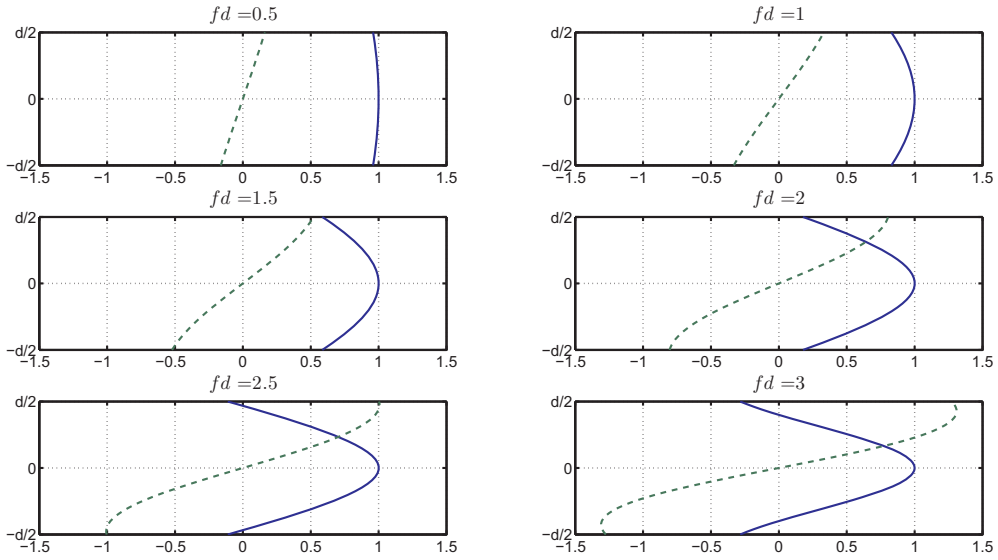

Figure 4.4 Mode shape of S0 at different fd values for Aluminum plate. The normalized longitudinal displacement u_1 (solid line) and transverse displacement u_2 (dashed line).

Mode shapes of different modes play an important role in controlling the mode sensitivity to defects, the fundamental S0 mode shapes at different fd are shown in Fig. 4.4 where both u_1 and u_2 were normalized by the maximum value of the longitudinal displacement u_1. The fundamental A0 mode shapes at different fd are shown in Fig. 4.5 where both u_1 and u_2 were normalized by the maximum value of the transverse displacement u_2. It is apparent that the oscillation in the mode shapes increase as the frequency thickness product increases. The fundamental modes (S0, A0) are normally used in practice, typically confined to the almost non-dispersive region of the frequency thickness product, targeting nearly constant group velocity c_g by using a narrow bandwidth excitation signal. S0 is more sensitive to through-thickness defects, while A0 is more

sensitive to surface defects. Utilization of A0 is increasing due to its short wavelength, since the wavelength of the selected mode must be lower than or equal to the size of the damage to be detected [Su *et al.*, 2006].

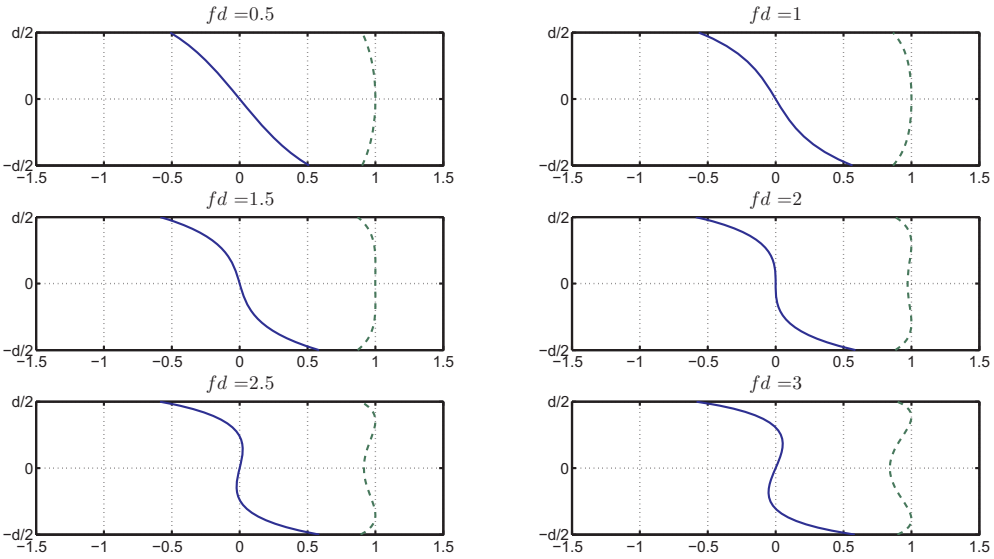

Figure 4.5 Mode shape of A0 at different fd values for Aluminum plate. The normalized longitudinal displacement u_1 (solid line) and transverse displacement u_2 (dashed line).

4.2 Approximate plate waves theories

The 2D models exploited here are based on the so called *axiomatic approach* [Carrera *et al.*, 2011]. In this approach, the displacement field and/or stress field are postulated in the thickness direction z:

$$f(x,y,z) = f_1(x,y)F_1(z) + f_2(x,y)F_2(z) + \cdots + f_n(x,y)F_n(z) \tag{4.18}$$

where the generic function f can be the vector of displacements $\mathbf{u} = (u,v,w)$ in the case of a displacement formulation, the vector of strain components $\boldsymbol{\epsilon}$ in the case of a strain formulation, and the vector of stress components $\boldsymbol{\sigma}$ in the case of a stress formulation. The f_i functions are the introduced unknowns that are defined on the domain, and F_i are the polynomials which have been introduced as the base functions of the expansion in z. n is the order of expansion in the z direction.

4.2.1 Classical plate theory

Classical plate theories were originally developed for one-layered isotropic structures. These theories can be divided into two main groups: Love first-approximation theories(LFAT) and Love second-approximation theories (LSAT). LFAT are based on the well-known Cauchy-Poisson-Kirchhoff-Love thin shell assumptions. The main postulates of the LFAT theories is that normals to the reference surface remain normal in the deformed states and do not change in length. This means that transverse shear and transverse normal strains are negligible with respect to the other strains. When one or more of these LFAT postulates are relaxed, we obtain the so-called LSAT, which means the effects of transverse shear and/or transverse normal stresses can be taken into account.

Classical plate theory (CPT) is based on Kirchhoff assumptions

- straight lines that are perpendicular to the midsurface (i.e., transverse normals) before deformation remain straight after the deformation;
- the transverse normals do not experience elongation (i.e., they are inextensible);
- the transverse normals rotate so that they remain perpendicular to the midsurface after the deformation.

The first two assumptions imply that transverse displacement is independent of the transverse (or thickness) coordinate and the transverse normal strain is zero. The third assumption results in zero transverse shear strains: $\gamma_{xz} = \gamma_{yz} = 0$. The displacement field for a CPT thus is described by:

$$u(x, y, z) = u_o(x, y) - z\partial_x w_o \tag{4.19a}$$

$$v(x, y, z) = v_o(x, y) - z\partial_y w_o \tag{4.19b}$$

$$w(x, y, z) = w_o(x, y) \tag{4.19c}$$

Only three degrees of freedom are used for this 2D theory: the displacements in the three directions that refer to the midsurface. In CPT, in order to avoid the Poisson locking phenomenon, the $\sigma_{zz} = 0$ condition must be enforced in the constitutive equations.

By setting $u_o(x, y)$, and $v_o(x, y)$ equal to zero, we ignore the thickness deformations, and allow only for the flexural modes of deformation. The equation of motion of the CPT then becomes [Graff, 1991].

$$D\left(\partial_x^4 w_o + 2\partial_x^2\partial_y^2 w_o + \partial_y^4 w_o\right) = -\rho d\ddot{w}_o \tag{4.20}$$

where $D = \frac{Ed^3}{12(1-\nu^2)}$ is the plate flexural stiffness.

4.2.2 First order shear deformation theory (FSDT)

One of the typical LSAT is the first-order shear deformation theory (FSDT). The third of the Kirchhoff hypotheses is relaxed, therefore the transverse normals do not remain perpendicular to the midsurface after deformation. This way, transverse shear strains γ_{xz} and γ_{yz} are included in the theory. However, the inextensibility of the transverse normal remains, therefore displacement w is constant in the thickness direction z. The displacement field for a FSDT thus is described by:

$$u(x,y,z) = u_o(x,y) - z\phi_x(x,y) \tag{4.21a}$$

$$v(x,y,z) = v_o(x,y) - z\phi_y(x,y) \tag{4.21b}$$

$$w(x,y,z) = w_o(x,y) \tag{4.21c}$$

The displacement field of FSDT has five unknowns (there were three for CPT): the midsurface displacements (u_o, v_o, w_o) and the rotations of a transverse normal around the x and y axes (ϕ_x, ϕ_y). In the case of CPT, the rotations coincide with the derivatives $\phi_x = \partial_x w_o$ and $\phi_y = \partial_y w_o$. Only ϵ_{zz} is zero, therefore σ_{xz} and σ_{yz} are different from zero. Poisson locking phenomena still exist because the transverse normal strain ϵ_{zz} remains zero, but it can be avoided by enforcing the $\sigma_{zz} = 0$ condition in constitutive equations.

By nulling $u_o(x,y)$, and $v_o(x,y)$, we ignore the thickness deformations, and allow only for the flexural modes of deformation [Graff, 1991], leading to the following equations of motion:

$$\kappa G d\left(\nabla^2 w_o + \partial_x\phi_x + \partial_y\phi_y\right) = \rho d\ddot{w}_o \tag{4.22}$$

$$-\kappa G d\left(\partial_x w_o + \phi_x\right) + \tfrac{D}{2}\left((1+\nu)\partial_x(\partial_x\phi_x + \partial_y\phi_y) + (1-\nu)\nabla^2\phi_x\right) = \tfrac{\rho d^3}{12}\ddot{\phi}_x \tag{4.23}$$

$$-\kappa G d\left(\partial_y w_o + \phi_y\right) + \tfrac{D}{2}\left((1+\nu)\partial_y(\partial_x\phi_x + \partial_y\phi_y) + (1-\nu)\nabla^2\phi_y\right) = \tfrac{\rho d^3}{12}\ddot{\phi}_y \tag{4.24}$$

where κ is the shear correction factor, and G is the shear modulus. For further simplification we shall use the following abbreviations:

$$G_1 = \kappa G d, \quad D_1 = \frac{D(1-\nu)}{2}, \quad D_2 = \frac{D(1+\nu)}{2}, \quad I_0 = \rho d, \quad \text{and} \quad I_2 = \frac{\rho d^3}{12}$$

The shear strain is assumed to be constant across the thickness of the plate. This is inconsistent with the assumption that the shear stress is distributed as a parabolic function. To account for the inaccuracy in the shear strain, a shear correction factor (κ) is applied so that the correct amount of internal energy is predicted by the theory. The value chosen for the shear correction factor κ determine how asymptotically the approximate theory approaches the exact one.

4.3 Dispersion analysis of approximate theories

In this section, we analyze the dispersion behavior of the approximate theories covered so far, since they were developed originally for flexural modes, the analysis is confined to those modes.

4.3.1 Classical plate theory

In order to study the dispersion relations of the CPT for flexural modes, we assume that the displacement is a plane wave of the form $w_o = A \exp i(\omega t - \mathbf{k}.\mathbf{r})$. Where $\mathbf{r}$ is the position vector of a point in the plate mid-plane $\mathbf{x_1} - \mathbf{x_3}$. So, substituting this assumed field into Eq. (4.20), we obtain the dispersion relation:

$$D(k_x^2 + k_y^2)^2 = D(k^2(\cos^2\theta + \sin^2\theta))^2 = \rho d\omega^2$$

$$\omega^2 = k^4 \frac{D}{\rho d} \tag{4.25}$$

It is apparent that CPT gives the unrealistic prediction that $c_p \to \infty$ as $\omega \to \infty$, which limits the applicability of the theory in the wave propagation studies, limiting its use only to very low frequency regime as could be seen from Fig. 4.6(a). This inconsistency is what motivated the first attempt to include the rotary inertia and then shear deformation to have a more realistic limiting behavior for the asymptotic high frequency. i.e. $c_p \to c_R$ or at least a speed close to Rayleigh surface wave speed as the frequency goes to ∞.

4.3.2 First order shear deformation theory

For the FSDT we substitute a plane wave approximation for each component of the displacement vector $[w_o, \quad \phi_x, \quad \phi_y]^{\mathrm{T}}$ to get the following system of equations:

$$\begin{pmatrix} G_1k^2 + I_0\omega^2 & -iG_1k_x & -k_y iG_1 \\ iG_1k_x & D_1D_2k^2k_x^2 + I_2\omega^2 + G_1 & D_2k_xk_y \\ iG_1k_x & D_2k_xk_y & D_1k^2 + D_2k_y^2 + I_2\omega^2 + G_1 \end{pmatrix} \begin{pmatrix} A \\ B \\ C \end{pmatrix} = \begin{pmatrix} 0 \\ 0 \\ 0 \end{pmatrix} \tag{4.26}$$

Setting the determinant of the coefficients' matrix equal to zero, we obtain a 6th order polynomial equation which when factored yields:

$$\omega^2 = \frac{\frac{k^2d^2}{12}G_1 + Dk^2 + G_1 \pm \sqrt{\left(-\frac{k^2d^2}{12}G_1 - Dk^2 - G_1\right)^2 - 4\frac{D}{\rho d}G_1 I_2 k^4}}{2I_2} \tag{4.27}$$

$$\omega^2 = \frac{G_1 + k^2 D_1}{I_2} \tag{4.28}$$

Application of Eq. (4.27), leads to dispersion relation for two modes w_1 and w_2; the second as stated by [Stephen, 1997], is irrelevant. Equation (4.28), gives the dispersion relation of the SH mode. For the determination of the shear coefficient, Mindlin [Graff, 1991], based on asymptotic analysis for the high frequency behavior, adopts a value of $\kappa = \frac{c_R}{c_t}$. However, after a careful analysis, based on second order approximation of the exact theory, [Stephen, 1997], suggests a value of $\frac{5}{6-\nu}$.

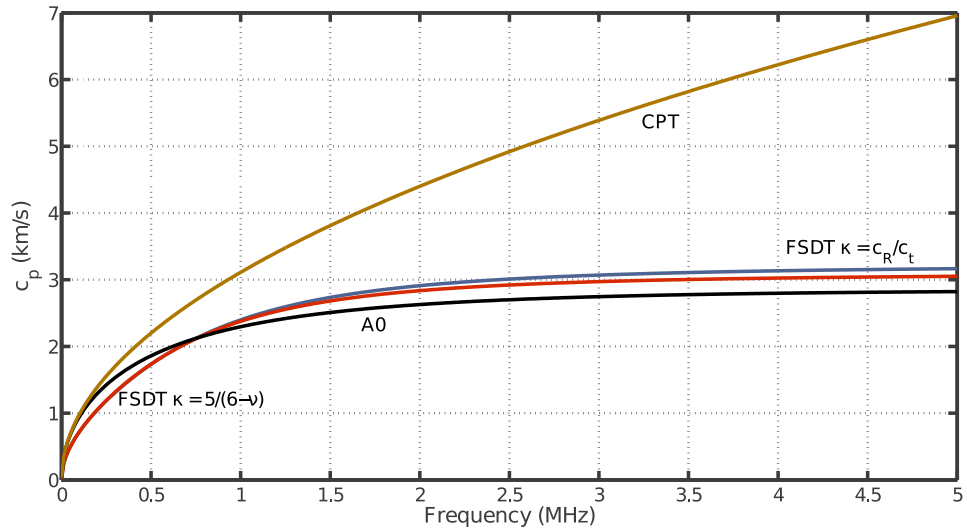

(a) The Phase velocity of CPT, FSDT, and Lamb A0 mode

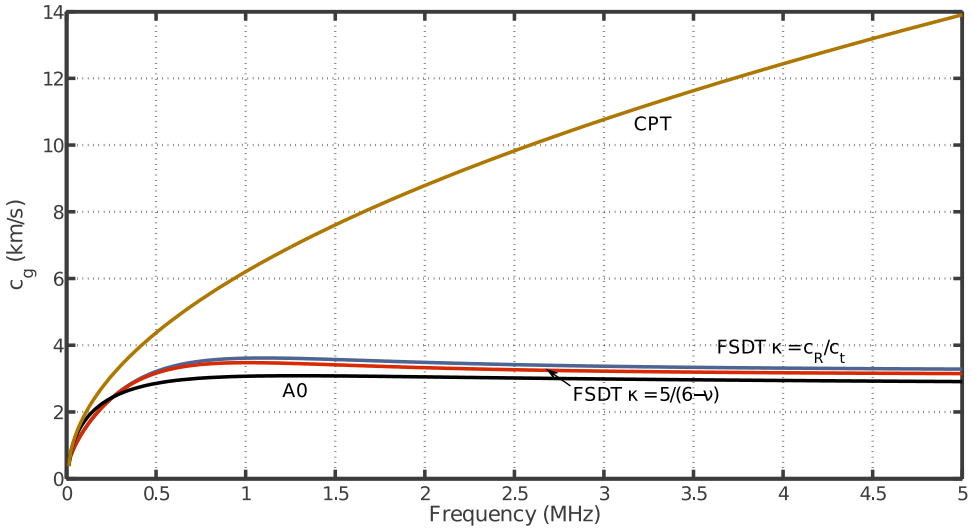

(b) The group velocity of CPT, FSDT, and Lamb A0 mode

Figure 4.6 The phase and group velocities of CPT, FSDT, and Lamb A0 modes, for aluminum plate 1 mm thick., $c_L = 6.334$ km/s, $c_T = 3.042$ km/s, $c_p = 5.33$ km/s, and $\nu = 0.35$.

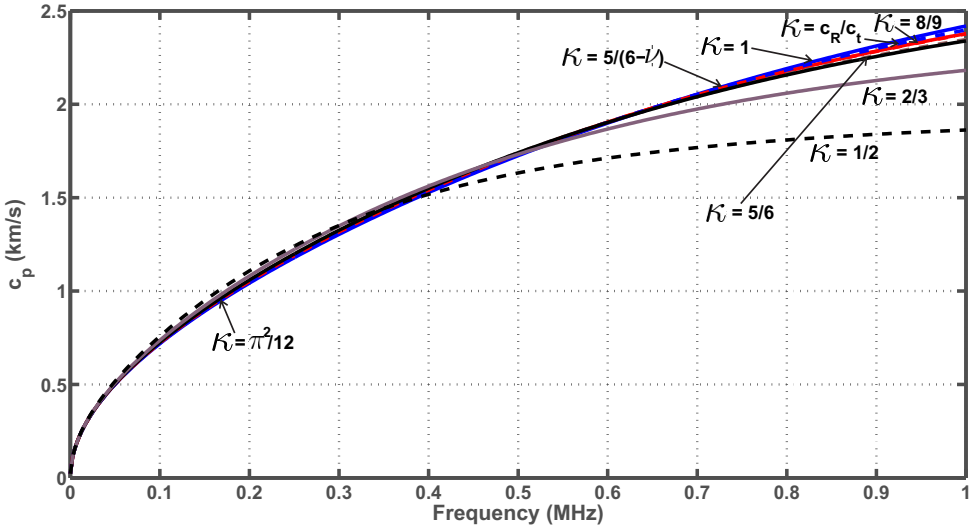

(a) Dispersion curves for different values of shear correction factor

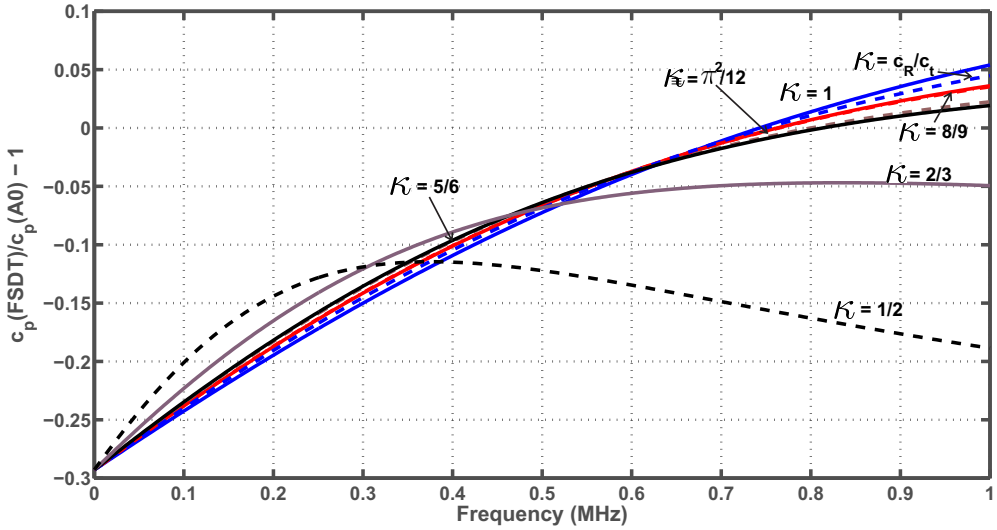

(b) Error with respect to A0 mode velocity, for different values of shear factor

Figure 4.7 Phase dispersion curves of FSDT and its errors with respect to the exact A0 mode, for frequency range 100 Hz to 1 MHz.

Figure 4.6(a), and Fig. 4.6(b) shows the dispersion curves: phase and group velocities respectively. The two values of the shear correction factor employed are those normally adopted in literature for higher spectra agreement. Figure 4.7(a), shows the effect of different choices of correction factor on the phase velocity, for a frequency range 100 Hz to 1 MHz. The errors with respect to the fundamental Lamb antisymmetric mode A0 is plotted for the same frequency range in Fig. 4.30(b). The major observation is that the agreement is better at high frequency range, which

is the main design goal of the approximate theory; i.e. to remove the unrealistic tendency of the flexural waves according to CPT to propagate at infinite speeds as the frequency increases. The low frequency range is not in agreement with the A0 mode, this may be attributed to the plane stress assumption that is inherent in almost all approximate plate theories.

4.4 Two dimensional spectral element

The two dimensional spectral element formulation starts with discretization of the physical domain Ω into small geometrically conforming n_{el} quadrilateral subdomains Ω_e, $e = 1, \cdots, n_{el}$ in a similar way to the FEM.

4.4.1 Shape functions

As in the one dimensional element, we initially partition the 1D domain L into n_e elements of equal size $h = L/n_e$ subdivided into N interior subintervals, so that the total number of nodes is $\mathcal{N} = Nn_e + 1$. The numbering of the elements $1 \leq e \leq n_e + 1$, while the local index $1 \leq j \leq N + 1$ locates a node within an element. These two indices provide a global ordering of all grid nodes, which is given by $l = j + (e-1)N$. The grid coordinates are defined by $x_l = (e - 1 + \xi_j)h$, where ξ_j is the jth collocation point in the reference interval [-1, 1]. The two dimensional mesh is defined as a tensor product [2] of the 1D mesh; that is, we have n_e^2 elements with N^2 interior nodes. The coordinates of the mesh nodes are (x_l, y_m) defined by:

$$(x|y)_{l|m} = (e_{x|y} - 1 + \xi_j)h, \quad l|m = j_{x|y} + (e_{x|y} - 1)N \tag{4.29}$$

Discretized computations often require a scalar index rather than an ordered pair of indices. For this purpose, we define

$$e = e_x + (e_y - 1)n_e; \quad i = j_x + (j_y - 1)(N + 1) \tag{4.30}$$

So, we can define the 2D shape function as shown in Fig. 4.8, as the tensor product of one dimensional shape function introduced earlier in Chapter 3:

$$\phi_i(x, y) = \phi_{j_x}(x) \otimes \phi_{j_y}(y) \tag{4.31}$$

where both have the same order.

2. the Kronecker (or tensor) product operator: the Kronecker product $C = A \otimes B$ of $N_2 \times M_2$ matrix A and $N_1 \times M_1$ matrix B is an $N_1N_2 \times M_1M_2$ matrix defined as $C(p_1 + p_2M_1, q_1 + q_2M_2) = A(p_2, q_2)B(p_1, q_1)$.

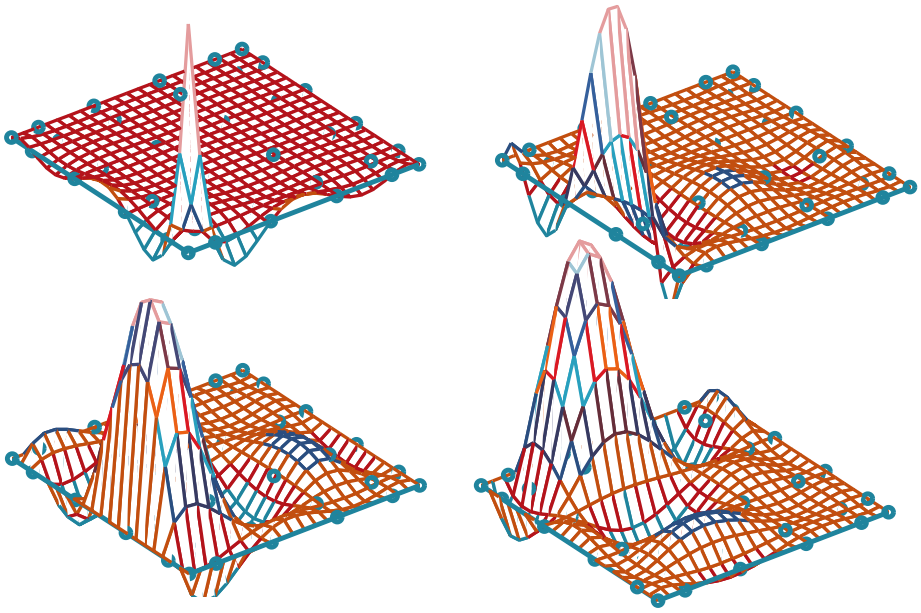

Figure 4.8 Two dimensional (6×6) Legendre shape functions, used as interpolating function for the nodal unknown solution

4.4.2 Spectral element matrices for two dimensional elastic wave equation

We can now use the weak formulation of the elastic wave equation derived in Sec. B.4.1 to obtain a system of ODEs by substituting the shape functions. The shape functions need to be substituted in each of the two components of $\mathbf{u}$ and $\mathbf{v}$. Substituting for $\mathbf{u}$ the following approximation:

$$\mathbf{u}(x, y, t) = [u_{1_i}\phi_i(x, y) \quad u_{2_i}\phi_i(x, y)]^{\mathbf{T}} \tag{4.32}$$

where u_{1_i} and u_{2_i} are the nodal unknowns of the approximations to the horizontal and vertical displacement respectively, and substituting $\mathbf{v} = [\phi_i \quad 0]$ for $\mathbf{u_1}$, and $\mathbf{v} = [0 \quad \phi_i]$ for $\mathbf{u_2}$ we obtain the following system of equations:

$$\mathbf{M}\ddot{\mathbf{u}}_1(t) + \mathbf{K_1}\mathbf{u}_1(t) + \mathbf{K_2}\mathbf{u}_2(t) = 0 \tag{4.33a}$$

$$\mathbf{M}\ddot{\mathbf{u}}_2(t) + \mathbf{K_2}^{\mathrm{T}}\mathbf{u}_1(t) + \mathbf{K_3}\mathbf{u}_2(t) = 0 \tag{4.33b}$$

where

$$
\begin{aligned}
M^e_{ij} &= \left(\frac{r}{c_l}\right)^2 \int_\Omega \phi_i(x,y)\phi_j(x,y)\,dxdy \\
K_{1\,ij} &= r^2 \int_\Omega \partial_x\phi_i(x,y)\partial_x\phi_j(x,y)\,dxdy + \int_\Omega \partial_y\phi_i(x,y)\partial_y\phi_j(x,y)\,dxdy \\
K_{2\,ij} &= (r^2-1)\int_\Omega \partial_x\phi_i(x,y)\partial_y\phi_j(x,y)\,dxdy \\
K_{3\,ij} &= \int_\Omega \partial_x\phi_i(x,y)\partial_x\phi_j(x,y)\,dxdy + r^2\int_\Omega \partial_y\phi_i(x,y)\partial_y\phi_j(x,y)\,dxdy
\end{aligned} \tag{4.34}
$$

Where $r = \frac{c_l}{c_t}$ is the P- to S-wave velocity ratio. The unknowns of the linear system Eq. (4.33) are the vectors $\mathbf{u}_1(t)$ and $\mathbf{u}_2(t)$ which are the nodal approximations of the exact solution while the matrices $\mathbf{M}$ and $\mathbf{K_i}$ are assembled from the elemental local matrices.

4.4.3 Spectral element matrices for first order shear deformation theory

The propagation of FSDT flexural waves is approximated by three degrees of freedom per node. So, we define a vector of nodal variables $\mathbf{d}^e = [\mathbf{w}, \mathbf{S^x}, \mathbf{S^y}]^{\mathrm{T}}$, that approximate the degrees of freedom at each node. To avoid confusion we will explicitly formulate the problem in detail, starting by assuming different interpolation functions:

$$w_o(x,y,t) \approx \phi(x,y)\mathbf{w}(t) \tag{4.35}$$

$$\phi_x(x,y,t) \approx \psi(x,y)\mathbf{S^x}(t) \tag{4.36}$$

$$\phi_y(x,y,t) \approx \psi(x,y)\mathbf{S^y}(t) \tag{4.37}$$

where each of the interpolating functions $\phi(x,y)$, $\psi(x,y)$ is expressed as a $(p+1)\times(p+1)$ matrix, containing the Lagrange interpolation functions based on the Legendre nodes, and each of the degrees of freedom are expressed as a square matrix, that then unfold into a column vector of length $(p+1)^2$. This means that for the case of evaluating the derivatives, the tensor product of an identity matrix $\mathbf{I}$ of the same size as the interpolating matrix is used, and the partial derivatives can be evaluated as [Trefethen, 2001]:

$$\partial_x w = (\mathbf{I}\otimes\phi')\mathbf{w} = \mathrm{H_x}\mathbf{w}, \quad \partial_y w = (\phi'\otimes\mathbf{I})\mathbf{w} = \mathrm{H_y}\mathbf{w} \tag{4.38}$$

where ϕ' is the familiar differentiation matrix (see App. C), and the differentiation matrix with respect to x is abbreviated as $\mathrm{H_x}$, and with respect to y as $\mathrm{H_y}$. Each differentiation matrix is

$(p+1)^2 \times (p+1)^2$. Then we have the semi-discrete system of equations per element as [Reddy, 2002; Wang *et al.*, 2000]:

$$\begin{pmatrix} \mathbf{K}^e_{11} & \mathbf{K}^e_{12} & \mathbf{K}^e_{13} \\ \mathbf{K}^{e\ \mathrm{T}}_{12} & \mathbf{K}^e_{22} & \mathbf{K}^e_{23} \\ \mathbf{K}^{e\ \mathrm{T}}_{13} & \mathbf{K}^{e\ \mathrm{T}}_{23} & \mathbf{K}^e_{33} \end{pmatrix} \begin{pmatrix} \mathbf{w} \\ \mathbf{S^x} \\ \mathbf{S^y} \end{pmatrix} + \begin{pmatrix} \mathbf{M}^e_{11} & 0 & 0 \\ 0 & \mathbf{M}^e_{22} & 0 \\ 0 & 0 & \mathbf{M}^e_{33} \end{pmatrix} \begin{pmatrix} \ddot{\mathbf{w}} \\ \ddot{\mathbf{S}}_\mathbf{x} \\ \ddot{\mathbf{S}}_\mathbf{y} \end{pmatrix} = \mathbf{f} \tag{4.39}$$

where

$$K_{11\,ij} = \kappa G d \int_\Omega \left(\partial_x \phi_i \partial_x \phi_j + \partial_y \phi_i \partial_y \phi_j \right) dxdy \tag{4.40}$$

$$K_{12\,ij} = \kappa G d \int_\Omega \partial_x \phi_i \psi_j \, dxdy \tag{4.41}$$

$$K_{13\,ij} = \kappa G d \int_\Omega \partial_y \phi_i \psi_j \, dxdy \tag{4.42}$$

$$K_{22\,ij} = \int_\Omega \left(D \partial_x \psi_i \partial_x \psi_j + \frac{G d^3}{12} \partial_y \psi_i \partial_y \psi_j + \kappa G d \psi_i \psi_j \right) dxdy \tag{4.43}$$

$$K_{23\,ij} = \int_\Omega \nu D \partial_x \psi_i \partial_y \phi_j + \frac{G d^3}{12} \partial_y \psi_i \partial_x \psi_j \, dxdy \tag{4.44}$$

$$K_{33\,ij} = \int_\Omega \frac{G d^3}{12} \partial_x \psi_i \partial_x \psi_j + D \partial_y \psi_i \partial_y \psi_j + \kappa G d \psi_i \psi_j \, dxdy \tag{4.45}$$

$$M_{11\,ij} = \int_\Omega I_0 \phi_i \phi_j \, dxdy, \quad M_{22\,ij} = M_{33\,ij} = \int_\Omega I_2 \psi_i \psi_j \, dxdy \tag{4.46}$$

So, in order to express these matrices in spectral element setting, we have the following substitutions, assuming that we will use the same interpolation function for all degrees of freedom:

$$\partial_x \phi_i \partial_x \phi_j \rightarrow \mathrm{H_x}^{\mathrm{T}} \mathrm{H_x}, \quad \partial_y \phi_i \partial_y \phi_j \rightarrow \mathrm{H_y}^{\mathrm{T}} \mathrm{H_y}, \quad \partial_y \psi_i \partial_x \psi_j \rightarrow \mathrm{H_x}^{\mathrm{T}} \mathrm{H_y}, \text{ and so on} \tag{4.47}$$

4.4.4 Quadrature rules

Derivatives are easily converted from one coordinate system to the other by means of the chain rule of partial differentiation, best expressed in matrix form for two dimensions by:

$$\begin{pmatrix} \partial_\xi \\ \partial_\eta \end{pmatrix} = \begin{pmatrix} \partial_\xi x & \partial_\xi y \\ \partial_\eta x & \partial_\eta y \end{pmatrix} \begin{pmatrix} \partial_x \\ \partial_y \end{pmatrix} = (\mathbf{J}) \begin{pmatrix} \partial_x \\ \partial_y \end{pmatrix} \tag{4.48}$$

or alternatively

$$\begin{pmatrix} \partial_x \\ \partial_y \end{pmatrix} = (\mathbf{J})^{-1} \begin{pmatrix} \partial_\xi \\ \partial_\eta \end{pmatrix} \tag{4.49}$$

where **J** is the Jacobian matrix. The determinant of this matrix, det(**J**) must also be evaluated because it is used in the transformed quadratures as follows:

$$\int_{\Omega} dxdy = \int_{\Pi} \det(\mathbf{J}) d\xi d\eta \tag{4.50}$$

For each of the spectral elements mapped subparametrically into the reference domain, that is defined in a local system of coordinates (ξ, η) on the square $\Pi = [-1, 1]^2$, the integration of a function $f(x, y)$ is computed numerically as:

$$\int_{\Omega} f(x, y)\, dxdy = \int_{\Pi} f(x(\xi, \eta), y(\xi, \eta)) \det(\mathbf{J}) d\xi d\eta \approx \sum_{i=1}^{nx} \sum_{j=1}^{ny} w_i w_j f(\xi_i, \eta_j) \tag{4.51}$$

where nx are the number of nodes of the spectral element in the ξ direction, as well as ny is the number of nodes in the η direction.

4.4.5 Four corner nodes element

The element Ω_e with four corner nodes (x_i, y_i) , $i = 1 \cdots 4$, is mapped into the reference domain $\Pi\,(\xi, \eta)$ via 1st order Lagrange polynomials $l_0^1(\xi) = \frac{1}{2}(1 - \xi)$ and $l_1^1(\xi) = \frac{1}{2}(1 + \xi)$. The coordinates of the corner nodes is defined in a 4 by 2 matrix as:

$$\mathbf{coord}^{\mathrm{T}}(x, y) = \begin{pmatrix} x_1 & x_2 & x_3 & x_4 \\ y_1 & y_2 & y_3 & y_4 \end{pmatrix} \tag{4.52}$$

with the four shape functions **N** written in matrix form:

$$\begin{aligned} \mathbf{N} &= \begin{pmatrix} l_0^1(\xi) l_0^1(\eta) & l_1^1(\xi) l_0^1(\eta) & l_0^1(\xi) l_1^1(\eta) & l_1^1(\xi) l_1^1(\eta) \end{pmatrix} \\ &= \begin{pmatrix} \frac{1}{4}(1 - \xi)(1 - \eta) & \frac{1}{4}(1 + \xi)(1 - \eta) & \frac{1}{4}(1 + \xi)(1 + \eta) & \frac{1}{4}(1 - \xi)(1 + \eta) \end{pmatrix} \end{aligned} \tag{4.53}$$

Such that any point **x** with a given coordinate in the reference domain can be mapped back into the physical domain via

$$\mathbf{x}(\xi, \eta) = \mathbf{N}(\xi, \eta)\mathbf{coord}(x, y) \tag{4.54}$$

and the Jacobian matrix is evaluated at each node based on this mapping, as well as the inverse is evaluated numerically at each node.

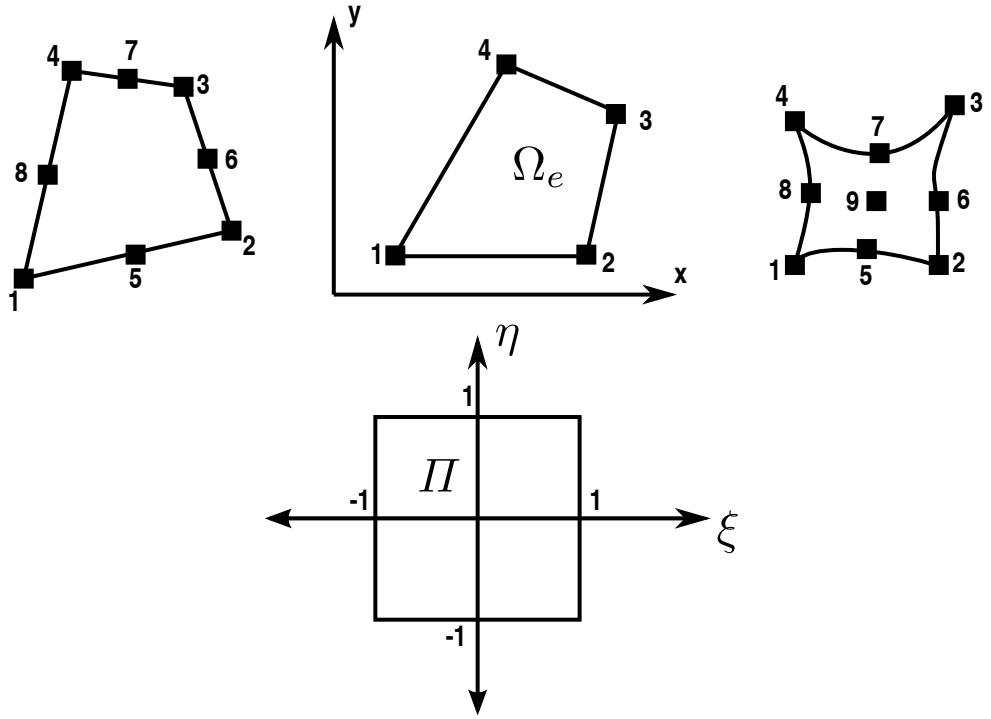

Figure 4.9 Mapping the two dimensional element Ω_e into the standard square element Π, with node numbering corresponding to shape functions $\mathbf{N}$ for 4, 8, and 9 corner nodes.

4.4.6 Eight corner nodes element

Higher order subparametric mapping may be sometimes needed for the case of curved element boundaries as in Fig. 4.9. The element Ω_e with eight corner nodes (x_i, y_i) , $i = 1 \cdots 8$, is mapped into the reference domain $\Pi\,(\xi, \eta)$ via 2nd order Lagrange polynomials $l_0^2(\xi) = \frac{1}{2}\xi(\xi - 1)$, $l_1^2(\xi) = (1 - \xi^2)$ and $l_2^2(\xi) = \frac{1}{2}\xi(1 + \xi)$, with:

$$\mathbf{coord}^{\mathrm{T}}(x, y) = \begin{pmatrix} x_1 & x_2 & x_3 & x_4 & x_5 & \cdots & x_8 \\ y_1 & y_2 & y_3 & y_4 & y_5 & \cdots & y_8 \end{pmatrix} \tag{4.55}$$

with the eight shape functions

$$\mathbf{N}^{\mathrm{T}} = \begin{pmatrix} l_0^2(\xi)l_0^2(\eta) \\ l_2^2(\xi)l_0^2(\eta) \\ l_2^2(\xi)l_2^2(\eta) \\ l_0^2(\xi)l_2^2(\eta) \\ l_1^2(\xi)l_0^2(\eta) \\ l_2^2(\xi)l_1^2(\eta) \\ l_1^2(\xi)l_2^2(\eta) \\ l_0^2(\xi)l_1^2(\eta) \end{pmatrix} = \begin{pmatrix} \frac{1}{4}\xi\eta(\xi-1)(\eta-1) \\ \frac{1}{4}\xi\eta(\xi+1)(\eta-1) \\ \frac{1}{4}\xi\eta(\xi+1)(\eta+1) \\ \frac{1}{4}\xi\eta(\xi-1)(\eta+1) \\ \frac{1}{2}(1-\xi^2)\eta(\eta-1) \\ \frac{1}{2}(1+\xi)(1-\eta^2) \\ \frac{1}{2}(1-\xi^2)\eta(\eta+1) \\ \frac{1}{2}(\xi-1)(1-\eta^2) \end{pmatrix} \tag{4.56}$$

Using the same multiplication in Eq. (4.54), we can map back the point $\mathbf{x}$ into the physical domain. Appendix C.2 presents an illustrative example of the mapping and the computation of the Jacobian, and its inverse.

4.5 Dispersion analysis of numerical implementations

In this section, the numerical dispersion relations will be calculated for: 1) the previously developed semidiscrete equations which is typically referred to as the spatial discretization, and 2) for the fully discrete equations i.e. temporal discretization case; through the same Rayleigh quotient approach as best approximation of the maximum eigenvalues. The approach is based on a generalized eigenvalue problem similar to the one utilized in Chapter 3 and the eigenvalue problem is generally large. A use of a generalization of the eigenvalue decomposition introduced by [Cohen, 2002] for the acoustic wave, and developed further for the case of plane strain elastodynamic equation by [Basabe and Sen, 2007; Seriani and Oliveira, 2008], is utilized to numerically separate the longitudinal velocity from the shear velocity for the case of two dimensional wave equation and for numerically extracting the three modes of the FSDT, an approach quite similar to the one used in the numerical dispersion analysis of the spectral element formulation of Mindlin Herrmann rod theory in Sec. 3.6.4. In this section, although the case of 2D plane strain has been analyzed by Seriani and Oleveira [Seriani and Oliveira, 2008], they only analyzed odd polynomial orders, due to the algebraic reduction they used to compute the eigenvalues for a single element. Here it is numerically computed for the whole assembled domain, thus we present both odd and even polynomial orders. It is also the first time, to the knowledge of the author, that a numerical dispersion analysis of the spectral element implementation of the FSDT is presented.

4.5.1 Two dimensional elastic wave equation

This analysis is based on the von Neumann method [Hughes, 1987], which assumes a plane-wave propagating through the discretized domain. Furthermore, we will assume that all the elements in the domain are square with equal sides h. Note that with this assumption, the nodes are periodic following the tensor product ordering, in both directions. We start by assuming that the solution is a plane wave, then u_{x_j}, and u_{y_j} have the form

$$u_{x_j}(t) = A_j e^{i(\mathbf{k}\cdot\mathbf{x}_j - \omega t)} \tag{4.57}$$

$$u_{y_j}(t) = B_j e^{i(\mathbf{k}\cdot\mathbf{x}_j - \omega t)} \tag{4.58}$$

where $\mathbf{k} = k[\cos(\theta) \quad \sin(\theta)]$ is the wavenumber vector, $\mathbf{x}_j$ is a vector containing the jth node coordinates, and A_j, B_j is an arbitrary amplitudes. Equations (4.57) and (4.58) represents a plane wave evaluated at the jth node. Substituting Eq. (4.58) in Eq. (4.33) we get:

$$\Lambda M_{ij}\, u_{x_j} = K_{1\,ij} u_{x_j} + K_{2\,ij} u_{y_j} \tag{4.59}$$

$$\Lambda M_{ij}\, u_{y_j} = K_{2\,ji} u_{x_j} + K_{4\,ij} u_{y_j} \tag{4.60}$$

The eigenvalue is given by $\Lambda = \omega_n^2$, for the spatially discretized equations, and for the temporally discretized equations is given by

$$\Lambda = \frac{4}{\Delta t^2} \sin^2 \frac{\omega_n \Delta t}{2} \tag{4.61}$$

The above equations represent a generalized eigenvalue problem; this is clearly seen if we write it in the form:

$$\Lambda \begin{pmatrix} \mathbf{M} & \mathbf{0} \\ \mathbf{0} & \mathbf{M} \end{pmatrix} \begin{pmatrix} \mathbf{u_1} \\ \mathbf{u_2} \end{pmatrix} = \begin{pmatrix} \mathbf{K_1} & \mathbf{K_2} \\ \mathbf{K_2}^{\mathrm{T}} & \mathbf{K_4} \end{pmatrix} \begin{pmatrix} \mathbf{u_1} \\ \mathbf{u_2} \end{pmatrix} \tag{4.62}$$

The best approximation ω_n^2 exists and is given by the Rayleigh quotient

$$\omega_n^2 = \frac{\overline{\mathbf{y}}^{\mathrm{T}} \mathbf{K} \mathbf{y}}{\overline{\mathbf{y}}^{\mathrm{T}} \mathbf{M} \mathbf{y}} \tag{4.63}$$

where $\mathbf{y} = e^{i\mathbf{k}\cdot\mathbf{x}}$, This generalized eigenvalue problem can be decomposed as done in Sec. 3.6.4 reducing the problem to the equivalent 2 by 2 eigenvalue problem:

$$\begin{pmatrix} d_1 & d_2 \\ \overline{d_2} & d_3 \end{pmatrix} \begin{pmatrix} A_1 \\ A_2 \end{pmatrix} = \omega_n^2 \begin{pmatrix} A_1 \\ A_2 \end{pmatrix} \tag{4.64}$$

where

$$d_1 = \frac{\overline{\mathbf{y}}^{\mathrm{T}}\mathbf{K_1}\,\mathbf{y}}{\overline{\mathbf{y}}^{\mathrm{T}}\,\mathbf{M}\,\mathbf{y}}; \quad d_2 = \frac{\overline{\mathbf{y}}^{\mathrm{T}}\mathbf{K_2}\,\mathbf{y}}{\overline{\mathbf{y}}^{\mathrm{T}}\,\mathbf{M}\,\mathbf{y}} \tag{4.65}$$

$$\overline{d_2} = \frac{\overline{\mathbf{y}}^{\mathrm{T}}\mathbf{K_2}^{\mathrm{T}}\,\mathbf{y}}{\overline{\mathbf{y}}^{\mathrm{T}}\,\mathbf{M}\,\mathbf{y}}; \quad d_4 = \frac{\overline{\mathbf{y}}^{\mathrm{T}}\mathbf{K_3}\,\mathbf{y}}{\overline{\mathbf{y}}^{\mathrm{T}}\,\mathbf{M}\,\mathbf{y}} \tag{4.66}$$

Which has an explicit solution in the form:

$$\omega_n^2 = \frac{d_1 + d_3}{2} \pm \sqrt{\left(\frac{d_1 - d_3}{2}\right)^2 + d_2^2} \tag{4.67}$$

where the larger value of ω_n is associated with the longitudinal wave ω_l^n, and the smaller one with the shear wave ω_t^n.

Figure 4.10(a), shows the spatial discretization induced error in the longitudinal velocity, for polynomial orders 8, 6, and 4 respectively at three different values of the incidence angle of the plane wave. The numerical values used to compute the curves are those of aluminum, $c_l = 6.334$ km/s, $c_t = 3.042$ km/s, and $\nu = 0.35$. The measure of the grid resolution is taken to be the percentage of the wavelength covered by a single element, h/λ where here h is the length of the edge of a square element, and the wavelength is that of the longitudinal wave velocity for all the figures. The amount of dispersion is measured as the ratio between the numerically propagated wave c_l^n or c_t^n to the longitudinal or shear velocity. The error is defined as:

$$\epsilon(c_l) = \frac{c_l^n}{c_l} - 1, \quad \epsilon(c_t) = \frac{c_t^n}{c_t} - 1 \tag{4.68}$$

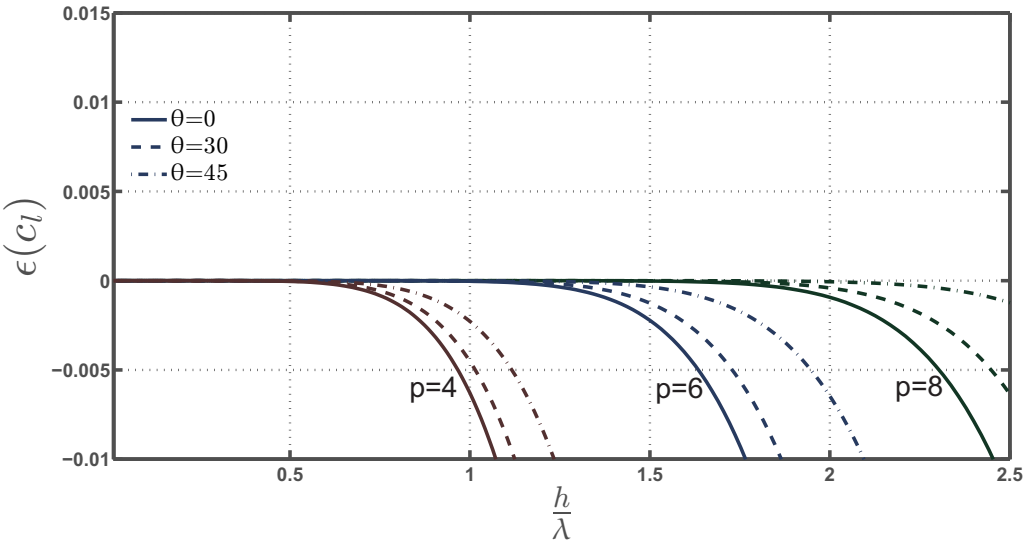

(a) Phase velocity dispersion errors in longitudinal wave c_l

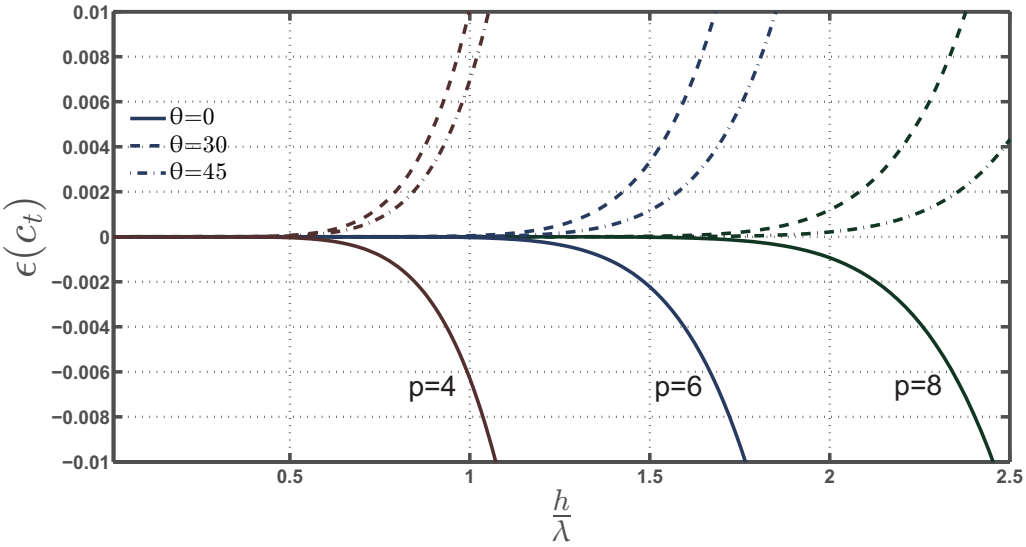

(b) Phase velocity dispersion errors in shear wave c_t

Figure 4.10 The error induced by spatial discretization in longitudinal and shear wave velocities induced by the spatial discretization, for polynomial orders 8, 6, and 4 with different values of θ. Total number of one dimensional nodes are 24.

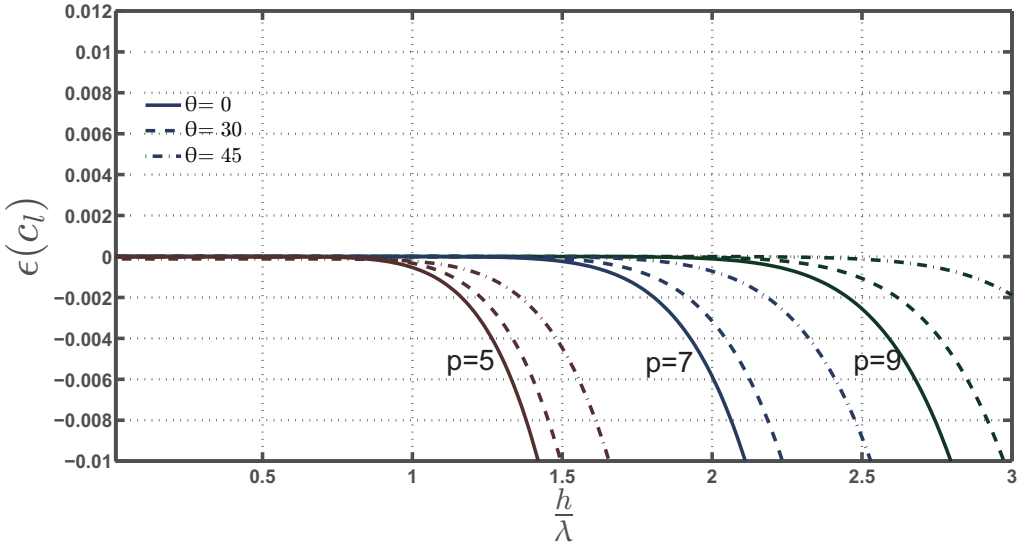

(a) Phase velocity dispersion errors in longitudinal wave c_l

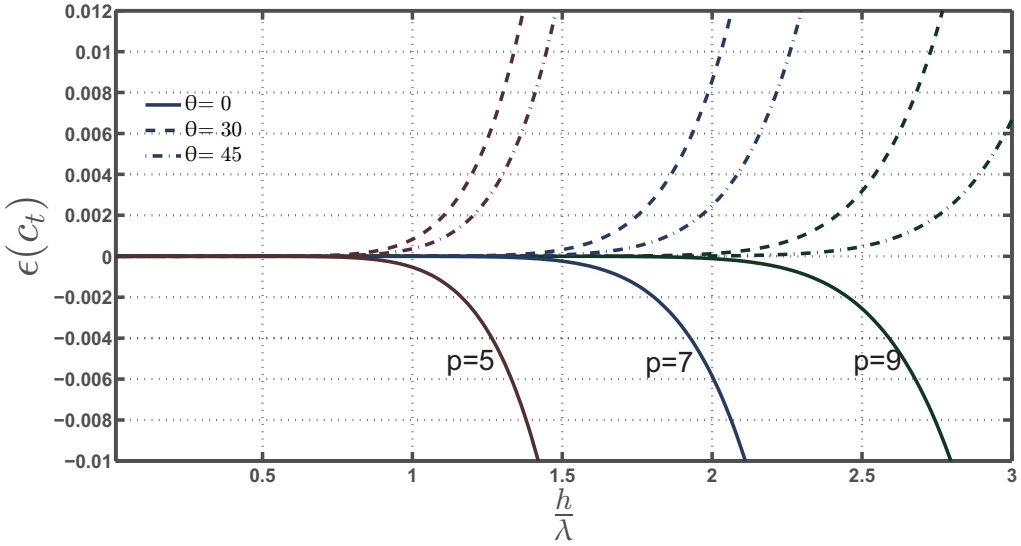

(b) Phase velocity dispersion errors in shear wave c_t

Figure 4.11 The error induced by spatial discretization in longitudinal and shear wave velocities, for polynomial orders 9, 7, and 5 with different values of θ. Total number of one dimensional nodes are 35.

While in Fig. 4.10(b), the computed error in the shear wave velocity, in the harmonic case are shown, where as expected the errors of zero angle of incidence coincide.

The main rule of thumb, that emanates from the dispersion analysis of the acoustic wave discretization by the spectral element [Cohen, 2002; Komatitsch *et al.*, 1999; Kudela *et al.*, 2007b], that a 4 or 5 grid point per wavelength is enough to preserve the dispersion error below 1 %, is

demonstrated. The major difference is that in the present approach we assembled the matrices over a large domain, on the contrary to the approach of [Basabe and Sen, 2007; Seriani and Oliveira, 2008], where both reduced the problem after some simplifying assumptions to an algebraic problem for a single element, their assumptions make the algebraic reduction valid only for even polynomial orders.The reason that here we reverted to the fully computational approach, was to allow also for an analysis of odd polynomial orders, as well as to check whether the assembly procedure have an effect on the computed eigenvalues as to whether it is robust against round-off errors.

Figure 4.11(a), shows error induced by the spatial discretization in the longitudinal velocity, for polynomial orders 9, 7, and 5 respectively at three different values of the incidence angle of the plane wave. While in Fig. 4.11(b), the computed errors in the shear wave velocity, in the harmonic case are shown, where as expected the errors of zero angle of incidence coincide.

The dispersion error in group velocity is computed by a numerical approximation of the directional derivative:

$$c_g = \nabla_{\vec{k}}\omega^n = (\partial_{k_x}\omega^n\vec{i} + \partial_{k_y}\omega^n\vec{j}) \cdot \frac{\vec{\mathbf{k}}}{|\mathbf{k}|} \tag{4.69}$$

$$\epsilon_g(c_l) = c_g(\omega_l^n) = \frac{c_g(c_l)}{c_l} - 1, \quad \epsilon_g(c_t) = c_g(\omega_t^n) = \frac{c_g(c_t)}{c_t} - 1 \tag{4.70}$$

Figure 4.12(a), shows the error in the group velocity propagation $\epsilon_g(c_l)$ in the longitudinal wave, as well as the shear group velocity errors is depicted in Fig. 4.12(b). The main observation is that the group velocity departs from the accurate representation of the real velocity faster, the error in group velocity is larger at the same $\frac{h}{\lambda}$ ratio when compared to the phase velocity errors. Again confirming the same conclusion that was drawn from the previous one dimensional results (see Sec. 3.7), that the dispersion error in group velocity is more representative estimate of the accuracy of the numerical method. Figures 4.13(a) and 4.13(b) shows the error in group velocity in both longitudinal and shear waves, respectively, for polynomial orders 9, 7, and 5. The reason for analyzing the group velocity in the case of plane strain two-dimensional elastic wave, despite the fact that they do not have a physical counterpart, is the observation that even if the mesh was optimized based on the phase dispersion without the knowledge of the group numerical velocity, this may lead to erroneous estimation of the propagation speed of the energy or wave packets, which is pertinent to any time-of-flight post processing procedure.

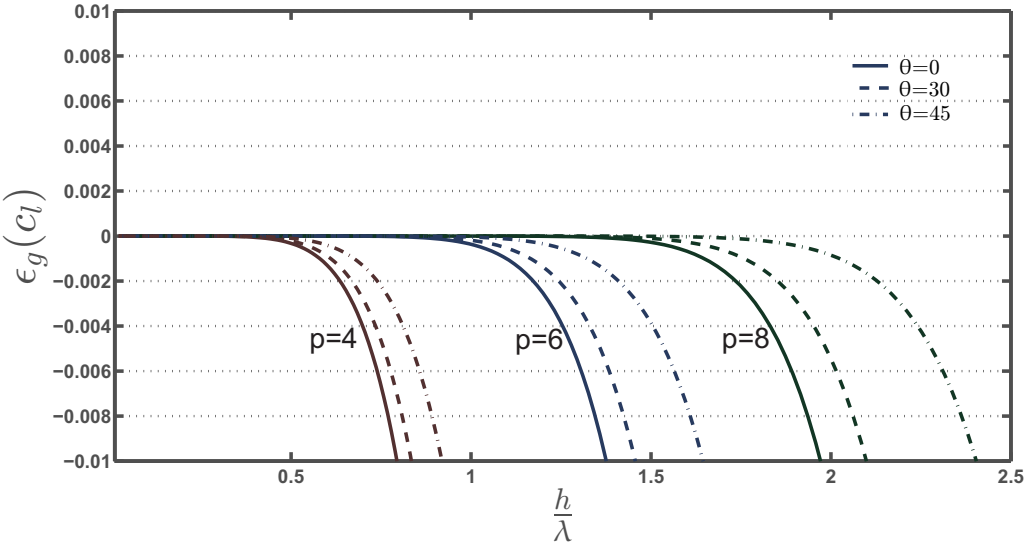

(a) Group velocity dispersion errors in longitudinal wave c_l

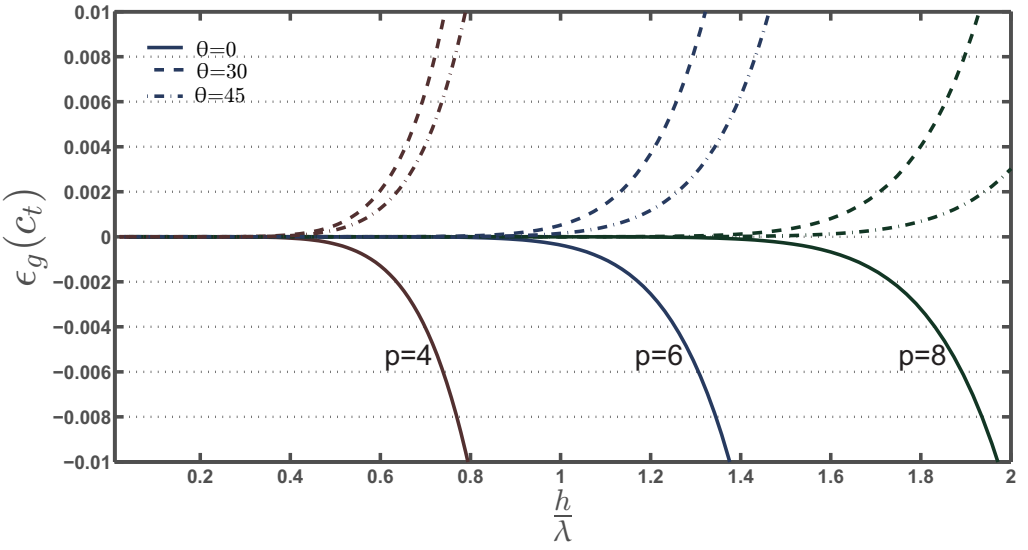

(b) Group velocity dispersion errors in shear wave c_t

Figure 4.12 The numerical group dispersion error induced by spatial discretization in longitudinal and shear wave velocities, for polynomial orders 8, 6, and 4 with different values of θ. Total number of one dimensional nodes are 24.

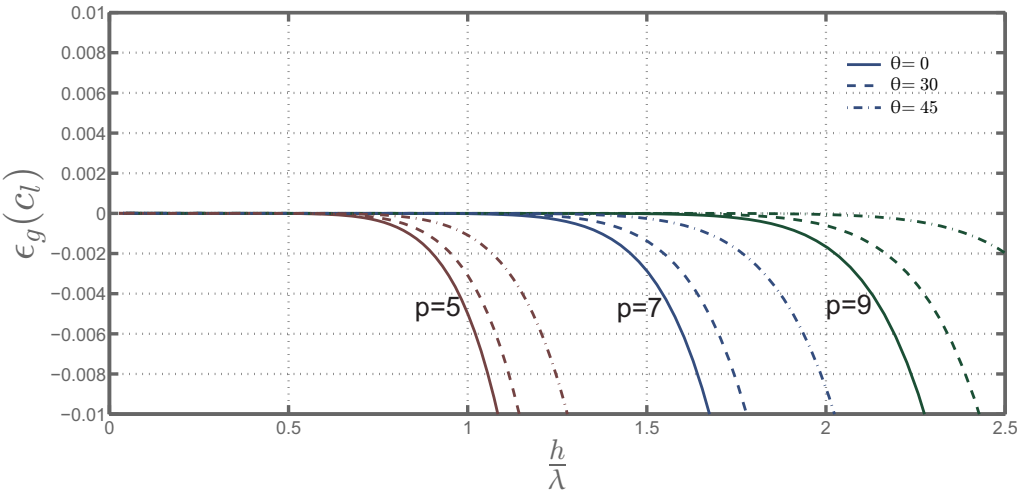

(a) Group velocity dispersion errors in longitudinal wave c_l

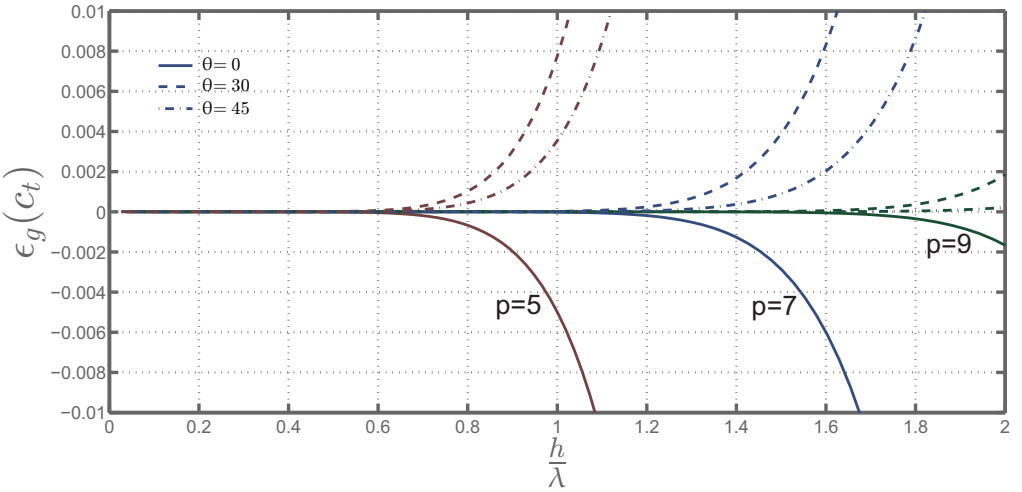

(b) Group velocity dispersion errors in shear wave c_t

Figure 4.13 The numerical group dispersion error induced by spatial discretization in longitudinal and shear wave velocities, for polynomial orders 9, 7, and 5 with different values of θ. Total number of one dimensional nodes are 35.

For the temporal discretization, the time step is computed based on the fastest wave c_l:

$$\Delta t = \frac{\text{CFL}}{c_l}\left(\frac{1}{\sqrt{1/\Delta x_{min}^2 + 1/\Delta y_{min}^2}}\right) = \frac{\text{CFL}}{c_l}\left(\frac{1}{\sqrt{2/\Delta x_{min}^2}}\right) \tag{4.71}$$

Where for the square element $\Delta x_{min} = \Delta y_{min}$.

Figure 4.14 Shows the temporal discretization induced errors, for even number polynomial orders. The effect of decreasing the CFL number reduces the error markedly, as well as the conflict of order is evident.

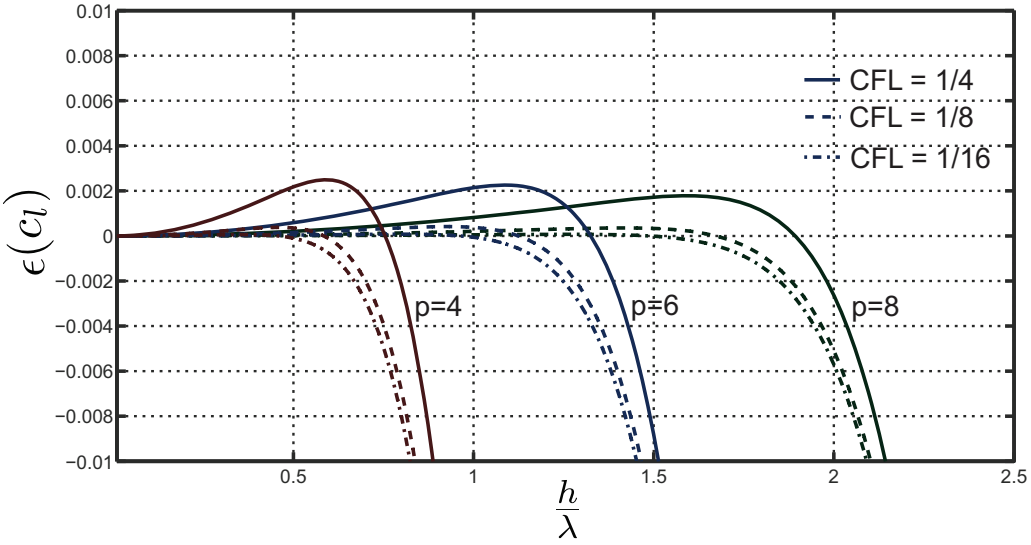

(a) Phase velocity dispersion errors in longitudinal wave c_l

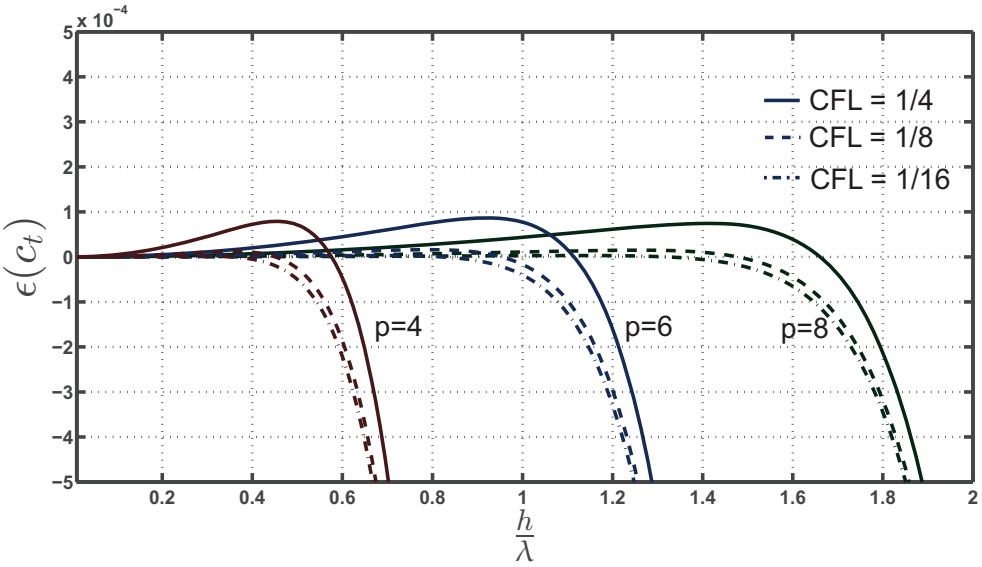

(b) Phase velocity dispersion errors in shear wave c_t

Figure 4.14 The numerical dispersion error due to temporal discretization in longitudinal and shear phase wave velocities, for polynomial orders 8, 6, and 4 with different values of CFL, and θ =0. Total number of one dimensional nodes are 24.

since the low order temporal integration tends to overestimate the phase velocity, while the high order spatial discretization tend to underestimate the phase velocity, this is what is referred to

as the conflict of order. Decreasing the CFL number, tends to reduce the effect of the temporal discretization. This makes the harmonic errors (spatial discretization alone) as the limiting value of the induced errors.

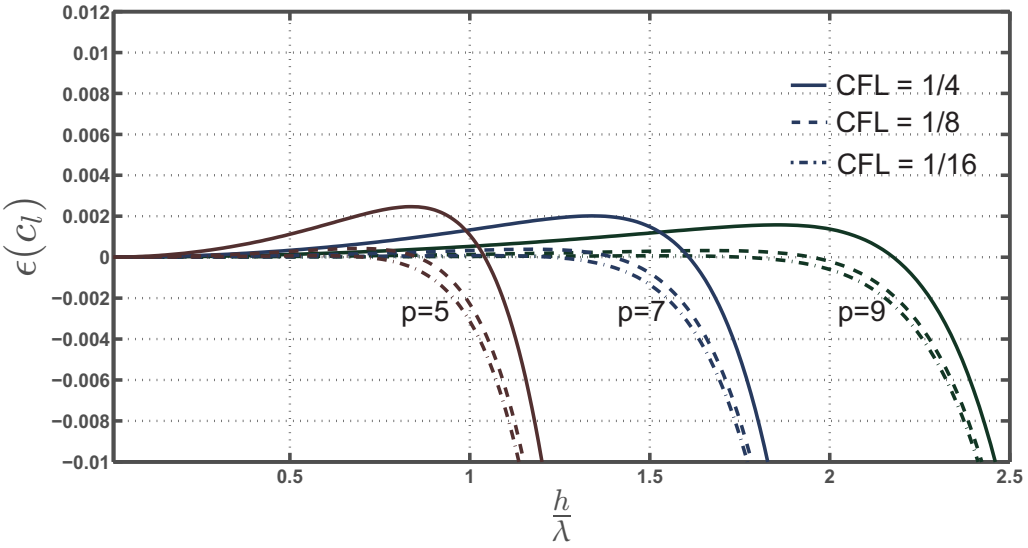

(a) Phase velocity dispersion errors in longitudinal wave c_l

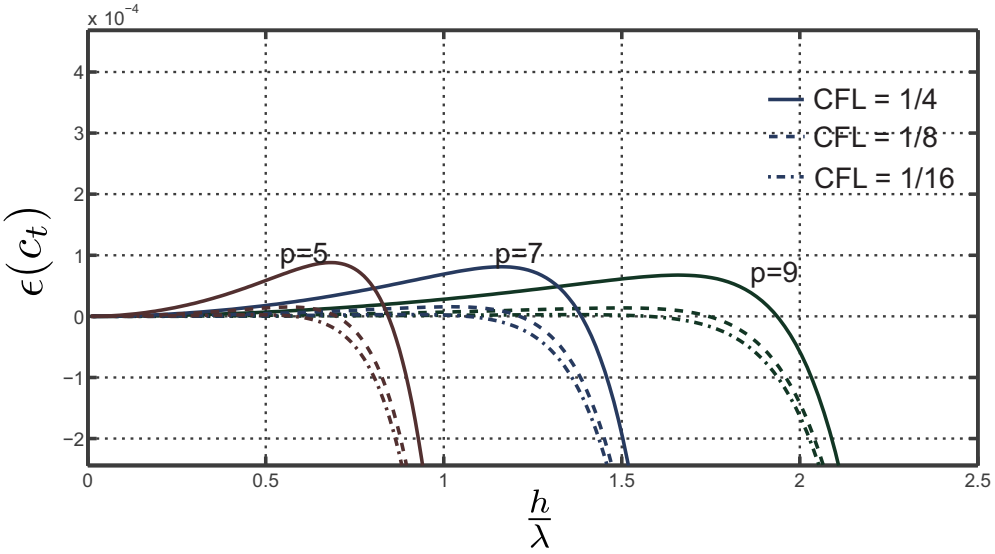

(b) Phase velocity dispersion errors in shear wave c_t

Figure 4.15 The numerical dispersion error due to temporal discretization in longitudinal and shear phase wave velocities, for polynomial orders 9, 7, and 5 with different values of CFL, and θ =0. Total number of one dimensional nodes are 35.

Figure 4.15 Shows the temporal discretization induced errors for both the longitudinal phase and group velocities, for odd number polynomial orders. It shows a similar behavior to the even polynomial orders.

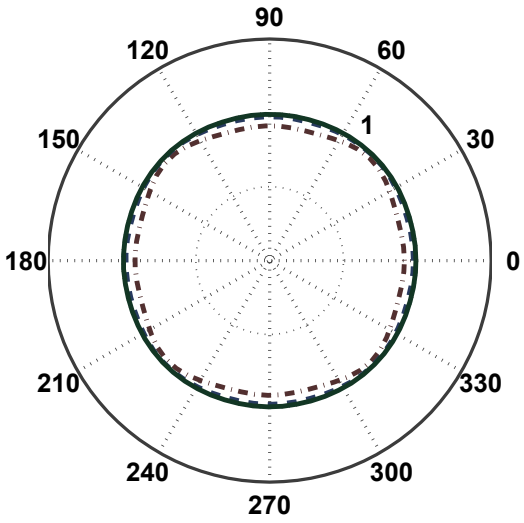

(a) Phase velocity dispersion errors in longitudinal wave c_l

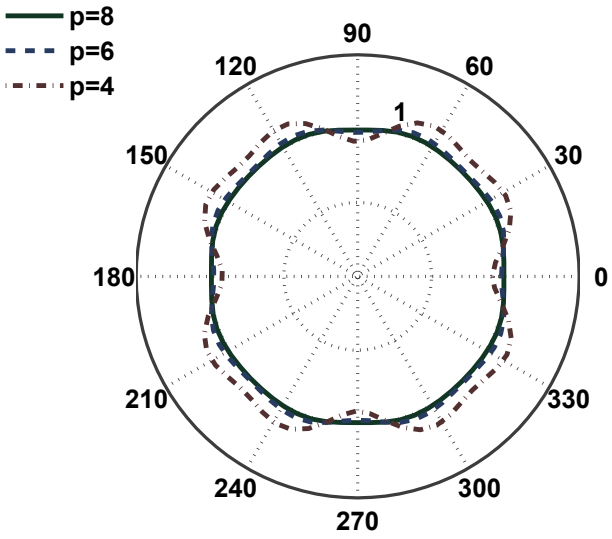

(b) Phase velocity dispersion errors in shear wave c_t

Figure 4.16 Phase error as a function of the incidence angle θ of spatial discretization with polynomial order of 8, 6, and 4, at approximately five points per wavelength $\frac{h}{\lambda} = 1.9$, $\frac{h}{\lambda} = 1.4$, $\frac{h}{\lambda} = 0.95$, respectively. The error is scaled as $1 + 20\epsilon(c_l)$ for the longitudinal velocity (a) and $1 + 20\epsilon(c_t)$ for shear velocity (b).

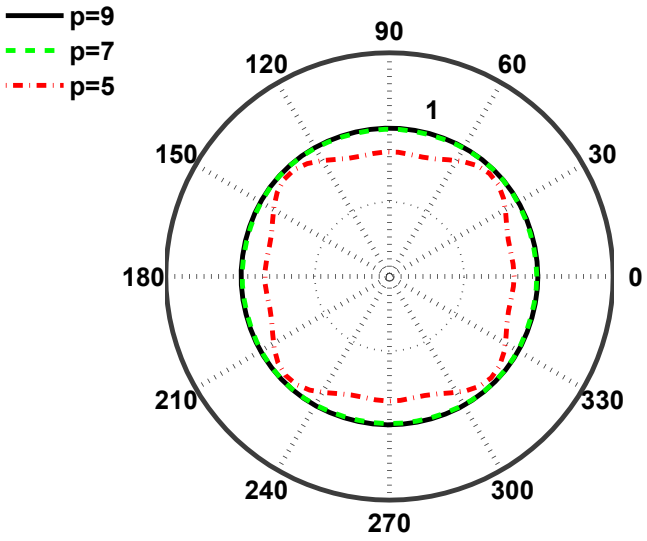

(a) Phase velocity dispersion errors in longitudinal wave c_l

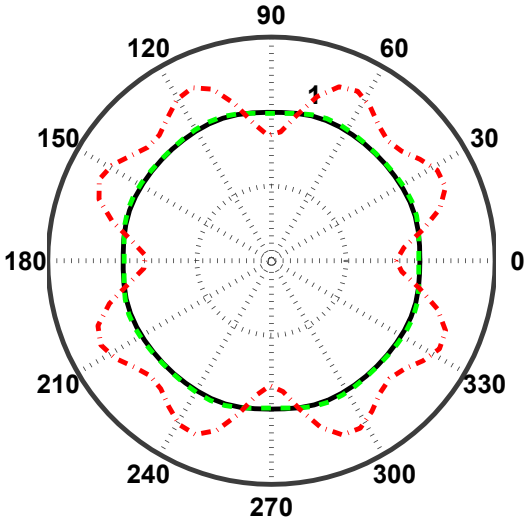

(b) Phase velocity dispersion errors in shear wave c_l

Figure 4.17 Phase error as a function of the incidence angle θ of spatial discretization with polynomial order of 9, 7, and 5, at approximately five points per wavelength $\frac{h}{\lambda} = 1.9$, $\frac{h}{\lambda} = 1.4$, $\frac{h}{\lambda} = 1.13$, respectively. The error is scaled as $1 + 100\epsilon(c_l)$ for the longitudinal velocity (a) and $1 + 100\epsilon(c_t)$ for shear velocity (b).

Figures 4.17 and 4.16 shows the dependence of the error in phase velocities on the incidence angle for the harmonic case. The numerical anisotropy are very small and could be neglected.

4.5.2 Lamb waves

As explained in Sec. 4.1, Lamb waves are a special case of the plane strain two dimensional elastic wave. The previous numerical dispersion analysis was for unbounded media, and no account for the boundary conditions was made. In order to understand the effect of the numerical dispersion of the plane strain wave propagation on Lamb waves simulation, we need to modify the analysis procedure to include the effect of the traction free boundaries at the upper and lower surfaces of the plate.

The mesh is discretized in the x direction with rectangular elements of length h, the height of the element is fixed and was taken equal to the thickness of the plate. Then the free traction boundary condition is satisfied via the assumed displacement field. So, as for the case of the bulk waves, the effect of the sampling at a specific grid points on the eigenvalues of the assembled matrices is evaluated. We can extend this analysis to the assumed displacement fields which are satisfying the plane strain discrete equations approximately, and see the effect of specific grid sampling on the eigenvalues of the problem.

Symmetric modes

The displacement fields in the plate associated with the symmetric mode (Eqs. (4.15)) could be rewritten in the plane wave form as:

$$u_x = \frac{iC}{2}\left(\beta\left(e^{i(kx-\beta y-\omega t)} + e^{i(kx+\beta y-\omega t)}\right) + \frac{Bk}{C}\left(e^{i(kx-\alpha y-\omega t)} + e^{i(kx+\alpha y-\omega t)}\right)\right) \tag{4.72}$$

$$u_y = \frac{iC}{2}\left(k\left(e^{i(kx-\beta y-\omega t)} - e^{i(kx+\beta y-\omega t)}\right) + \frac{B\alpha}{C}\left(e^{i(kx-\alpha y-\omega t)} + e^{i(kx+\alpha y-\omega t)}\right)\right) \tag{4.73}$$

where the amplitude ratio at any specific frequency is constant and given by [Graff, 1991]:

$$\frac{B}{C} = \frac{(k^2-\beta^2)\sin\beta d/2}{2k\alpha\sin\alpha d/2} \tag{4.74}$$

where d is the thickness of the plate, which explicitly shows the plane nature of the wave propagation. These displacements satisfy the free traction boundary condition as long as α and β satisfy the dispersion relations for the symmetric modes. This means that the displacement of the nodes are coupled together, the dispersion analysis could be interpreted as a test of how efficient a specific number and distribution of nodes will sample this coupled motion.

For the purpose of dispersion analysis, we substitute the assumed displacement fields for the symmetric mode. Where first the solution of the dispersion equation for the S0 mode is computed, and then values of α^2 , and β^2 is determined. From this information, the assumed displacement

fields is constructed, knowing that they satisfy the traction free boundary conditions. The last step is a substitution into the assembled discrete equations the u_x and u_y. Since the $\frac{B}{C}$ are known and constant for a specific frequency, this means that only one approximate eigenvalue is required to be evaluated, *i.e.* the one associated with the arbitrary amplitude C.

Recalling the plane strain discrete equation (4.62):

$$\Lambda \begin{pmatrix} \mathbf{M} & \mathbf{0} \\ \mathbf{0} & \mathbf{M} \end{pmatrix} \begin{pmatrix} \mathbf{u_1} \\ \mathbf{u_2} \end{pmatrix} = \begin{pmatrix} \mathbf{K_1} & \mathbf{K_2} \\ \mathbf{K_2}^{\mathrm{T}} & \mathbf{K_4} \end{pmatrix} \begin{pmatrix} \mathbf{u_1} \\ \mathbf{u_2} \end{pmatrix} \tag{4.75}$$

where

$$\mathbf{u_1} = u_x(k, x_i, y_i), \qquad \mathbf{u_2} = u_y(k, x_i, y_i) \tag{4.76}$$

where (x_i, y_i) are the spectral node coordinates. For the computation of Rayleigh quotient, the approximate eigenvector $\mathbf{y}$ becomes $[\mathbf{u_1}\ \ \mathbf{u_2}]$ and the matrices are assembled per location according to the elemental connectivity map.

Figures 4.18(a), and 4.18(b), show the dispersion curves computed for aluminum plate, 1 mm thick, with exactly the same properties used in the previous section. The length of the plate in the x direction was 40 mm. The polynomial order 5, and as illustrated, increasing the elements number (which increases only in the length direction), increases markedly the accuracy of the spatial discretization as manifested in a decrease in the deviation of the numerical phase velocity from the exact one.

The main noticeable remark is that though the error in Fig. 4.18(a) is highly sensitive to the number of nodes in length direction, which is a valid assumption regardless of the number of nodes in the thickness direction till the Lamb fundamental symmetric mode approaches the asymptotic Rayleigh surface wave (around 4 MHz). After that increasing the number of nodes in the length direction do reduce the error as shown in Fig. 4.19(a) but in a slower rate than in Fig. 4.18(a). The resolution after 4 MHz is mainly controlled by the number of nodes in the thickness direction, *i.e.* as the Lamb wave approaches the surface wave, the numerical error is less controlled by the number of elements in the length direction, and more dominated by the number of nodes in the thickness direction as could be seen from Fig. 4.19(a). This may be intuitively explained by the fact that as the particle motion tends to be more confined to the surface, the number of nodes used to sample the motion in that direction plays a more pronounced rule, which means that the controlling factor in the dispersion error is the number of nodes in the thickness direction in the high frequency regime.

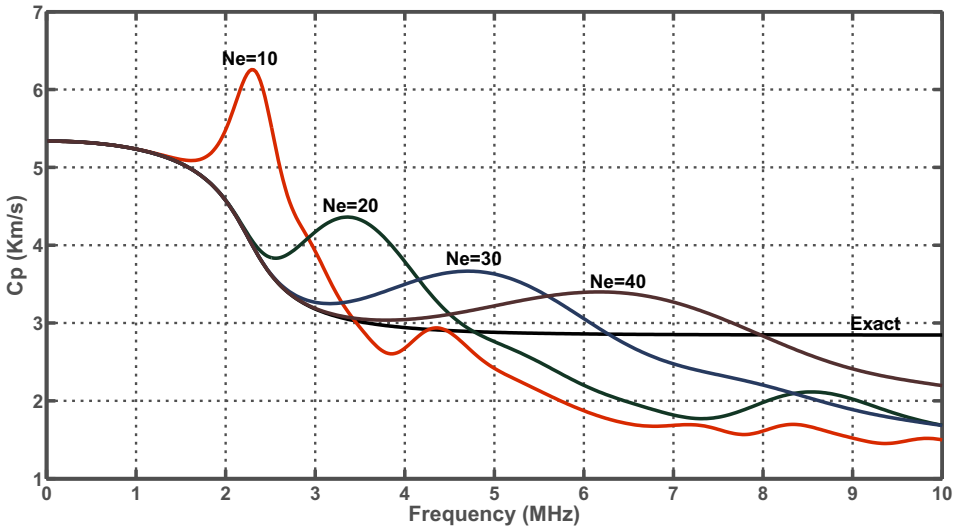

(a) Phase velocity dispersion curves

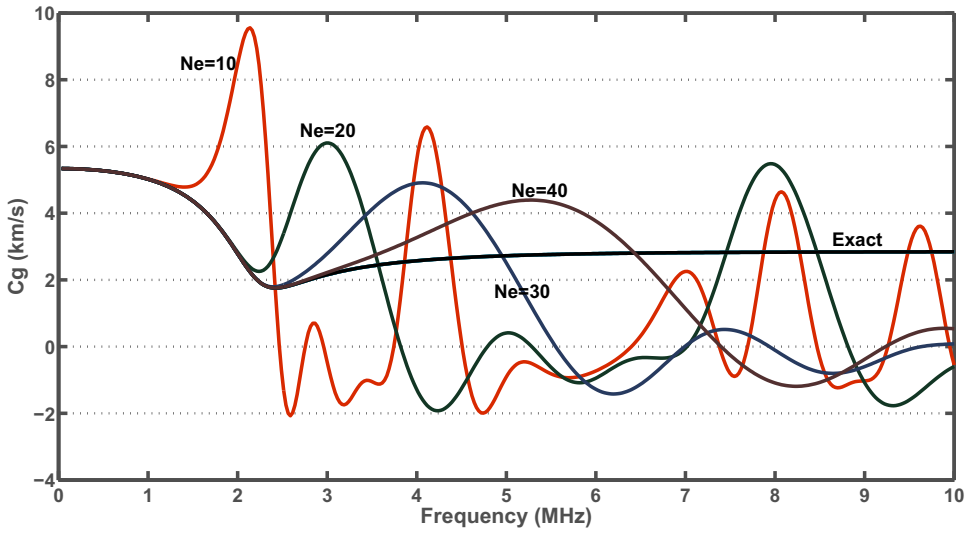

(b) Group velocity dispersion curves

Figure 4.18 Numerical spatial dispersion of S0 mode, for spectral element of polynomial order 5, for 10, 20, 30 and 40 elements. The computations were for aluminum plate 1 mm thick, and 40 mm long

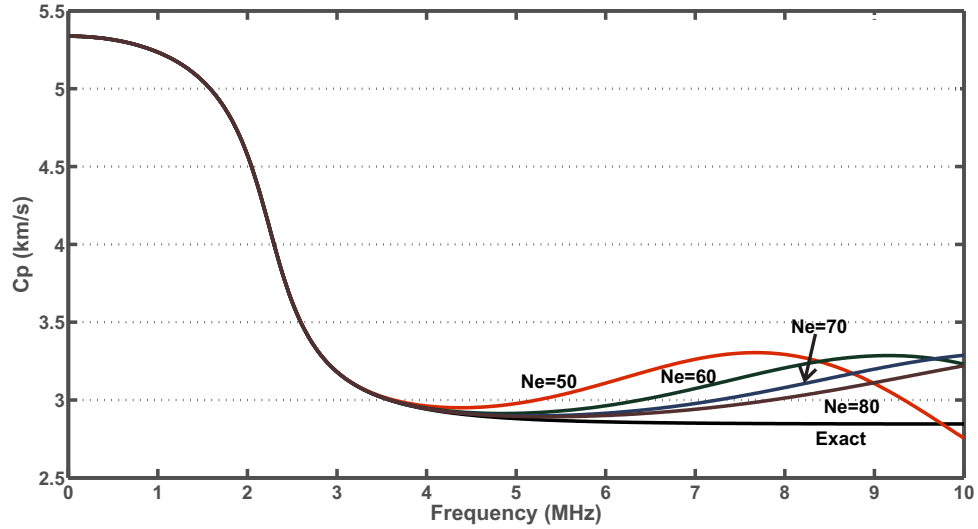

(a) Phase velocity dispersion curves

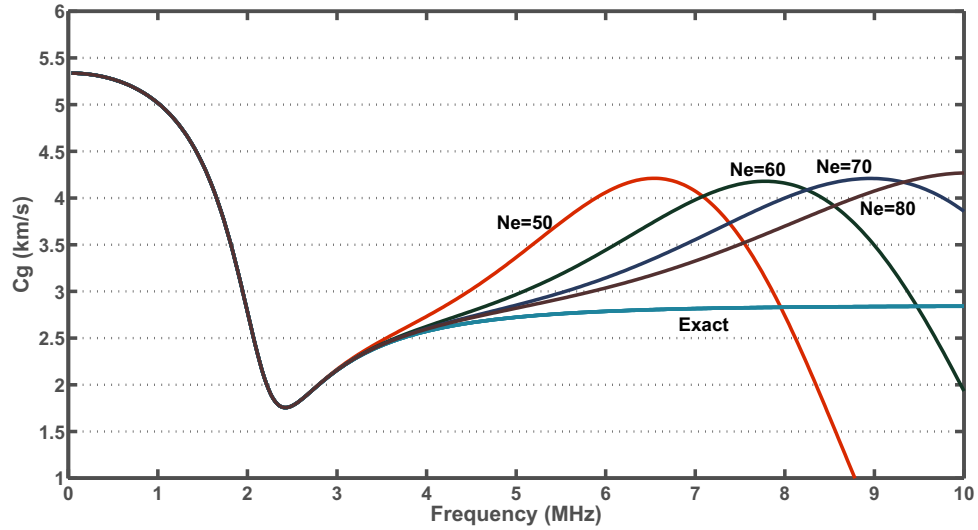

(b) Group velocity dispersion curves

Figure 4.19 Numerical spatial dispersion of S0 mode, for spectral element of polynomial order 5, and for 50, 60, 70 and 80 elements. The computations were for aluminum plate 1 mm thick, and 40 mm long.

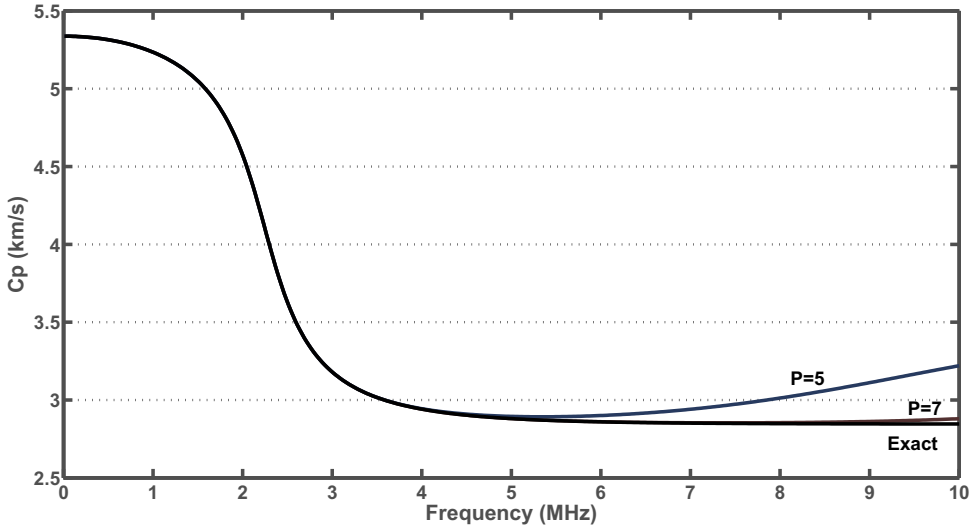

(a) Phase velocity dispersion curves

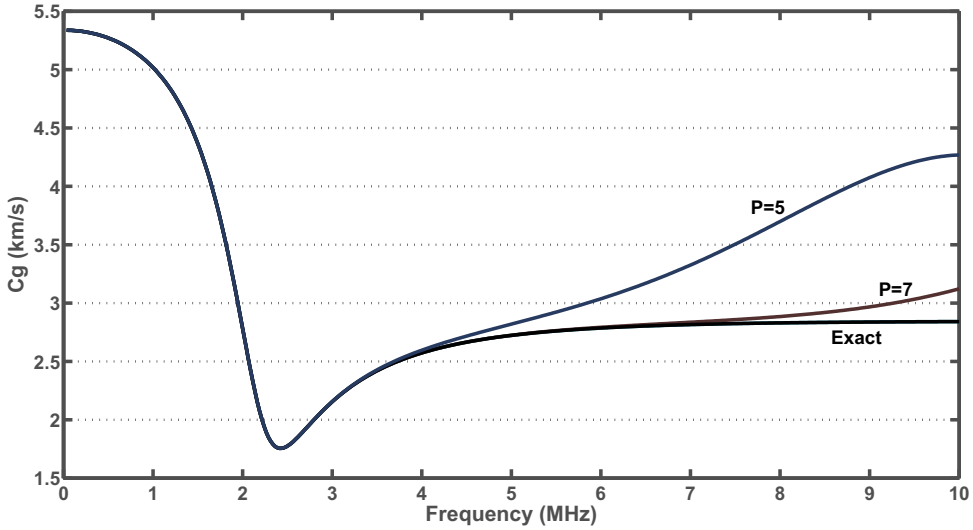

(b) Group velocity dispersion curves

Figure 4.20 Numerical spatial dispersion of S0 mode, for spectral element of polynomial order 5 and 7 for 80 elements in length direction. The computations were for aluminum plate 1 mm thick, and 40 mm long.

In order to verify this hypothesis, we plot two different polynomial orders, 5 and 7, which corresponds to the 6 and 8 nodes per thickness respectively, while fixing the number of elements in the length direction to 80 elements in Fig. 4.20(a). The results confirm the previous interpretation of the shift of the error sensitivity from being dominated by the sampling in the length direction

to being dominated by the sampling in the thickness direction, this is as the Lamb fundamental symmetric mode starts degenerating form a plane strain wave to surface wave (roughly at 4 MHz).

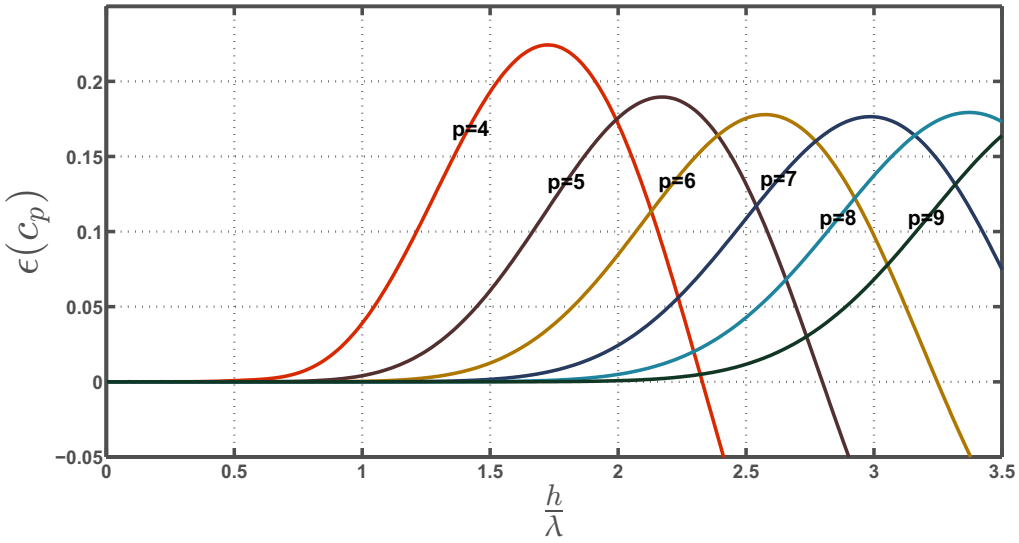

(a) Phase velocity dispersion curves

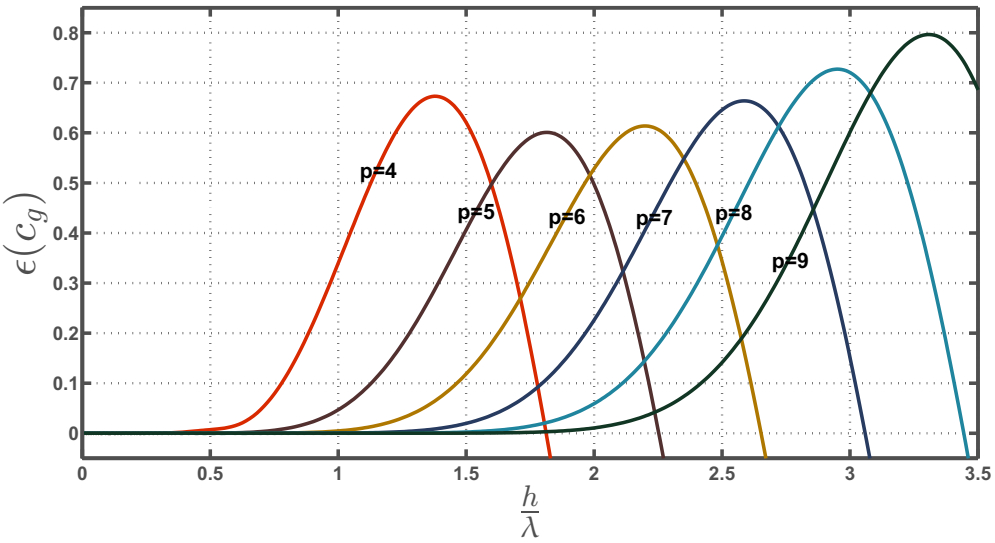

(b) Group velocity dispersion curves

Figure 4.21 Numerical Dispersion of S0 mode, for different polynomial orders. The computations were for aluminum plate 1 mm thick, and 40 mm long.

Figures 4.21(a) and 4.21(b) show the amount of error induced by spatial discretization alone, with different polynomial orders, on the phase and group velocities of the fundamental symmetric Lamb mode, respectively. The resolution parameters, is taken as the amount of the wavelength

covered by a single element. The interesting observation, that for a fixed $\frac{h}{\lambda}$ the increase in accuracy due to the change of the polynomial order 4 to 5 is more pronounced than the form 5 to 6. After polynomial order 5, the error curves seem to follow a parallel pattern. This reflects the efficiency of the representing the coupled motion of the nodes as dictated by the assumed displacement. So, not all polynomial orders provide a good sampling for the mode shape.

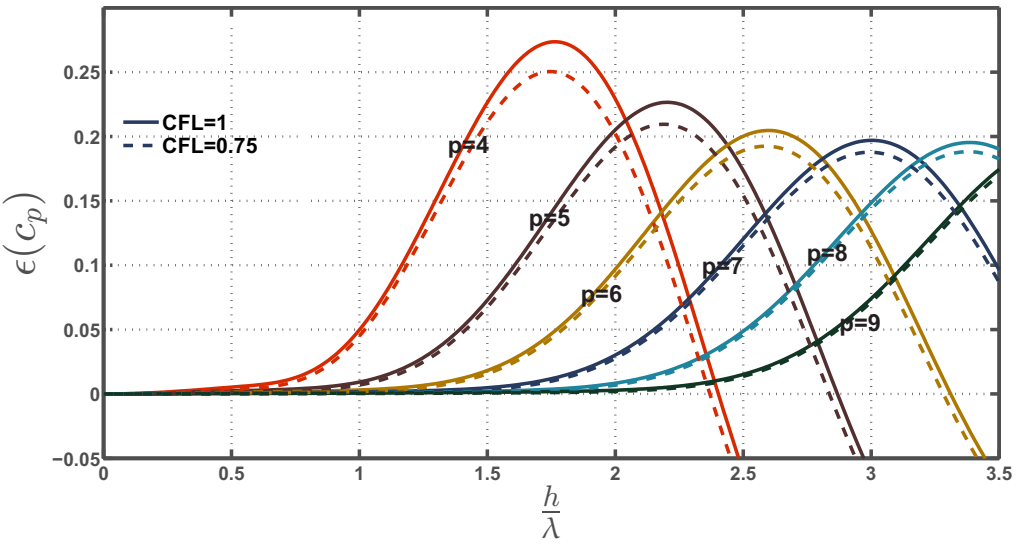

(a) CFL = 1, 0.75

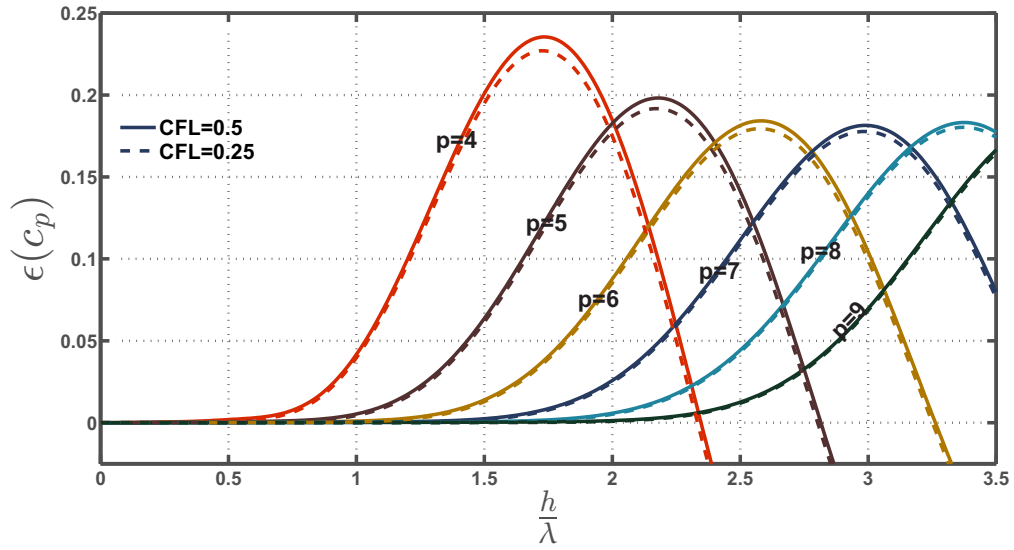

(b) CFL = 0.5, 0.25

Figure 4.22 Temporal numerical Dispersion of S0 mode, for different polynomial orders, with CFL number, 1, 0.75, 0.5 and 0.25. The computations were for aluminum plate 1 mm thick, and 40 mm long.

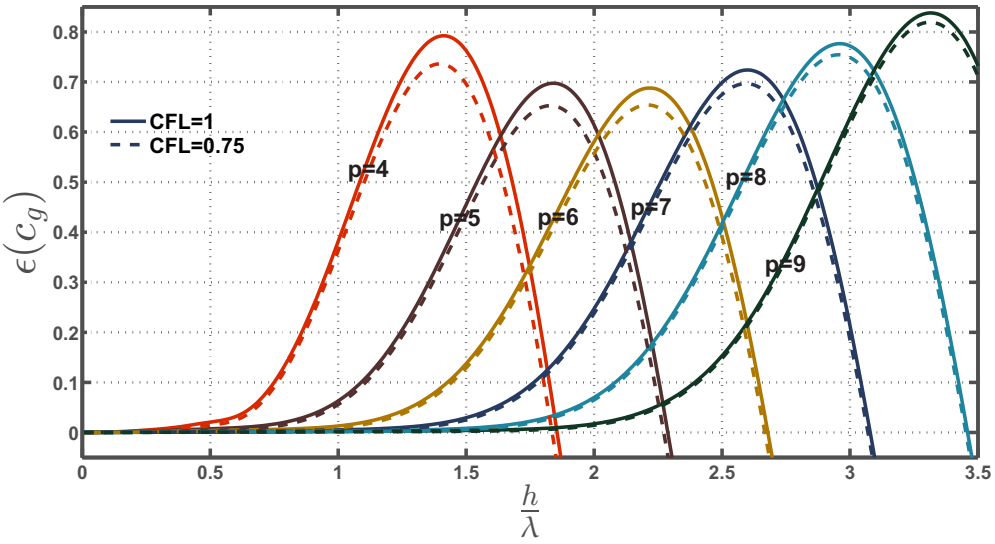

(a) CFL = 1, 0.75

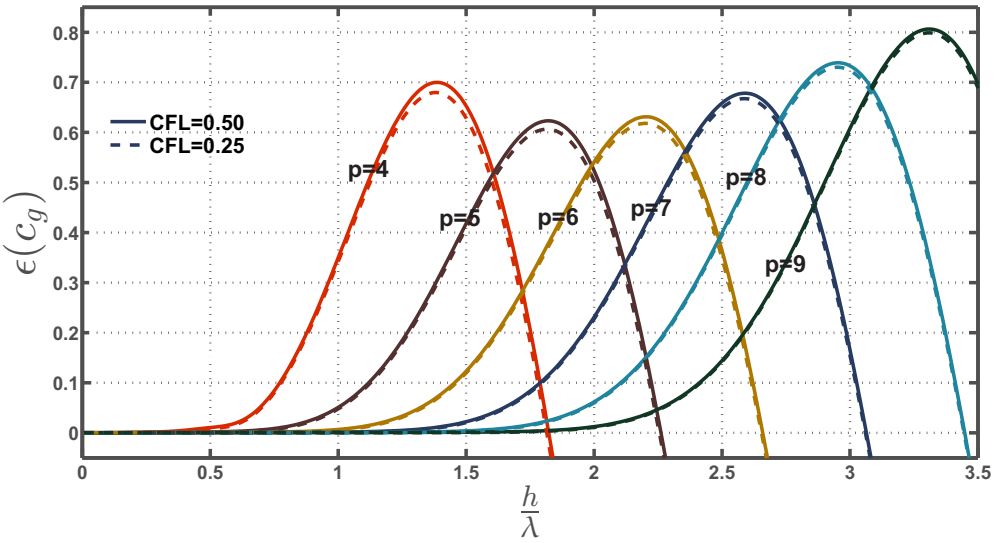

(b) CFL = 0.5, 0.25

Figure 4.23 Temporal numerical group dispersion of S0 mode, for different polynomial orders, with CFL number, 1, 0.75, 0.5 and 0.25. The computations were for aluminum plate 1 mm thick, and 40 mm long.

Figures 4.22(a) and 4.22(b) show the numerical error in phase velocity of the fundamental symmetric mode S0 due to the temporal discretization with different values of CFL number. Similarly, Figures 4.23(a) and 4.23(a) show the error induced by the temporal discretization on the group velocity of the S0 mode. The same procedure of computing the temporal discretization error as the one used for the plane strain two dimensional wave equation was used to compute

the error in those figures. The effect of decreasing the CFL condition plays a slight role in reducing the errors induced by the temporal discretization. So, for efficient Lamb waves time domain simulation using the spectral element, it would be recommended to focus on choosing the appropriate polynomial order, and element size with less emphasis on undue over reduction in the time step.

As could be seen from the figures, the overall behavior is that the group velocity dispersion error is several orders of magnitude higher at the same $\frac{h}{\lambda}$ ratio compared to the phase errors. This confirms the conclusion that was drawn earlier from the dispersion analysis of the one dimensional element and the two dimensional elastic wave equation. Namely, it is more accurate to set the discretization parameters on the group velocity, since the group velocity is more sensitive to the numerical dispersion errors.

Antisymmetric modes

The displacement fields in Eq. (4.15) in the plate associated with the antisymmetric mode are:

$$u_x = iD(\tfrac{A}{D}k_1 \sin\alpha x_2 - \beta \sin\beta x_2) \tag{4.77}$$

$$u_y = D(\tfrac{A}{D}\alpha \cos\alpha x_2 + k_1 \cos\beta x_2) \tag{4.78}$$

where the amplitude ratio at any specific frequency is constant and given by [Graff, 1991]:

$$\frac{A}{D} = -\frac{(k^2-\beta^2)\cos\beta d/2}{2k\alpha\cos\alpha d/2} \tag{4.79}$$

These displacements satisfy the free traction boundary condition as long as α and β satisfy the dispersion relations for the antisymmetric modes.

For the purpose of dispersion analysis, we substitute the assumed displacement fields for the antisymmetric mode, where we first compute the solution of the dispersion equation for the A0 mode, and then compute the α^2 , and β^2. From this information we can construct the assumed displacement fields that satisfy the traction free boundary conditions. Then, we substitute into the assembled discrete equations the u_x and u_y. Since the $\frac{A}{D}$ are known and constant for a specific frequency, this means that we need only one approximate eigenvalue, associated with the arbitrary amplitude D.

$$\Lambda\begin{pmatrix}\mathbf{M} & \mathbf{0}\\ \mathbf{0} & \mathbf{M}\end{pmatrix}\begin{pmatrix}\mathbf{u_1}\\ \mathbf{u_2}\end{pmatrix} = \begin{pmatrix}\mathbf{K_1} & \mathbf{K_2}\\ \mathbf{K_2}^{\mathrm{T}} & \mathbf{K_4}\end{pmatrix}\begin{pmatrix}\mathbf{u_1}\\ \mathbf{u_2}\end{pmatrix} \tag{4.80}$$

where

$$\mathbf{u_1} = u_x(k, x_i, y_i), \qquad \mathbf{u_2} = u_y(k, x_i, y_i) \tag{4.81}$$

where (x_i, y_i) are the spectral node coordinates. For the computation of Rayleigh quotient, the approximate eigenvector $\mathbf{y}$ becomes $[\mathbf{u_1}\ \ \mathbf{u_2}]$. And the matrices are assembled per location according to the elemental connectivity map. A similar behavior to the S0 mode is observed, as the number of elements per length increase with a fixed polynomial order, the reduction in the dispersion error tends be less. This is due to the same effect, i.e the sensitivity of the dispersion error shifts toward the sampling density in the thickness direction as the wave moves toward a surface wave.

Figure 4.24(a) shows the numerical dispersion curves and the exact dispersion curves for an aluminum plate, the values are differing in the orders of 10^{-8} km/s in the region of low frequency, which is negligible, as the frequency increases the discrepancy from the exact value increases and fluctuates, though the fluctuation is bounded (stability measure). With an increase in the number of elements in the length direction as shown in Fig. 4.25(a), the agreement between the exact and numerical velocity is increased, till a similar effect to the one observed earlier in the S0 is witnessed. Increasing of elements number in the length direction, as the exact velocity degenerate into Rayleigh wave, is less effective in reducing the error. This could be explained by the fact that as the frequency increases the particle motion becomes more and more confined into the surface region of the plate and as such the numerical eigenvalue becomes more sensitive to the number of nodes used in the thickness direction rather than the number of nodes used in the propagation direction.

Figures 4.24(b) and 4.25(b) show the group velocity computed for different element numbers per plate length for the same polynomial order 5. The group velocity witness a higher discrepancy from the exact value, which again enforces the previous recommendation of basing the accuracy of the numerical simulation on the group velocity. The deviation is following the same pattern as for the phase velocity, but larger magnitude, *e.g.* at 1 MHz the phase velocity is around 3.2 km/s while the group velocity is 5 km/s. This again confirms the conclusion that was drawn earlier, that group velocity errors should be the major concern in the spectral element simulation of elastic wave propagation, and the mesh parameters should be chosen based on the group velocity errors as a more conservative estimate.

Both the phase and group errors, with respect to the exact A0 group and phase velocity are shown in Figs. 4.26(a) and 4.26(b). On the contrary to the case of the symmetric mode, where polynomial orders higher than 4 behaved in the same matter except the polynomial order 4 which

witnessed a larger discrepancy at the same wavelength to element size ratio, the polynomial orders behave in the same pattern from 4 to 9, with an increasing errors at higher frequencies.

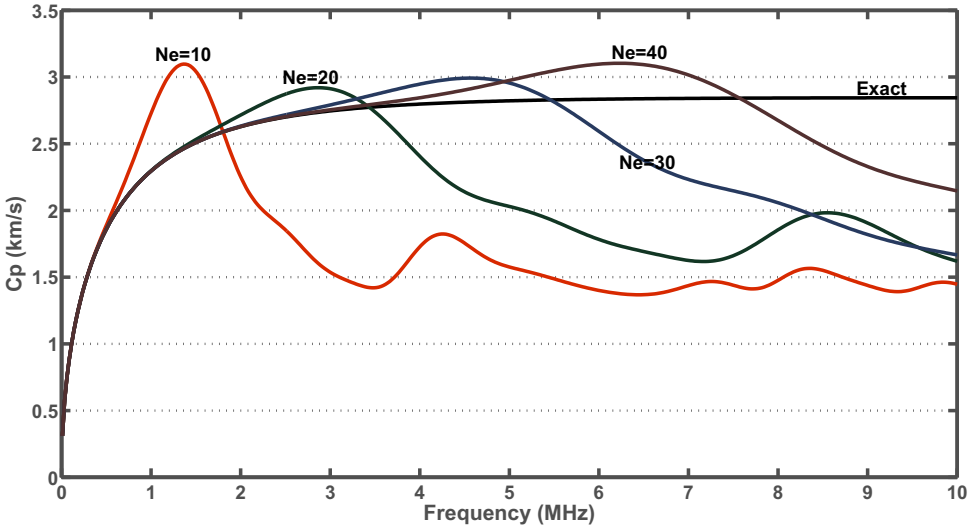

(a) Phase velocity dispersion curves

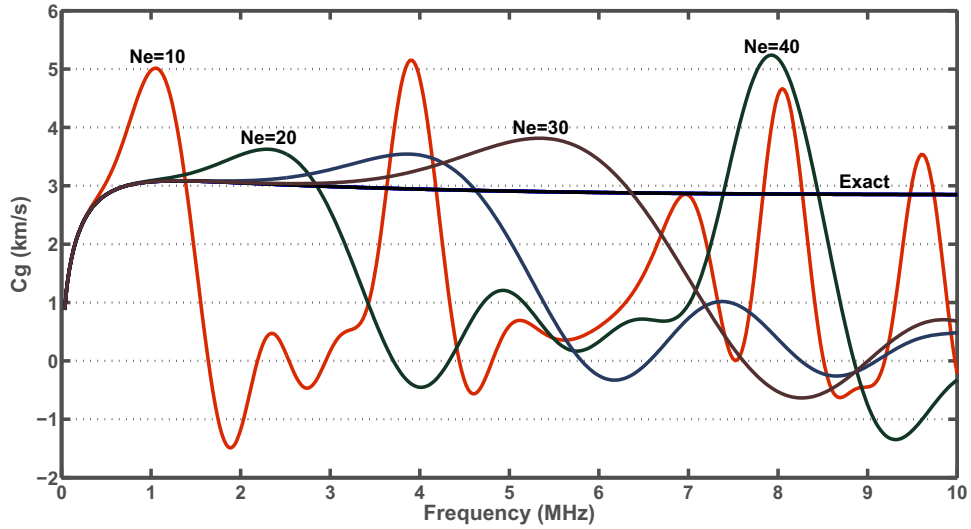

(b) Group velocity dispersion curves

Figure 4.24 Numerical Dispersion of A0 mode, for spectral element of polynomial order 5, for 10, 20, 30 and 40 elements. The computations were for aluminum plate 1 mm thick, and 40 mm long

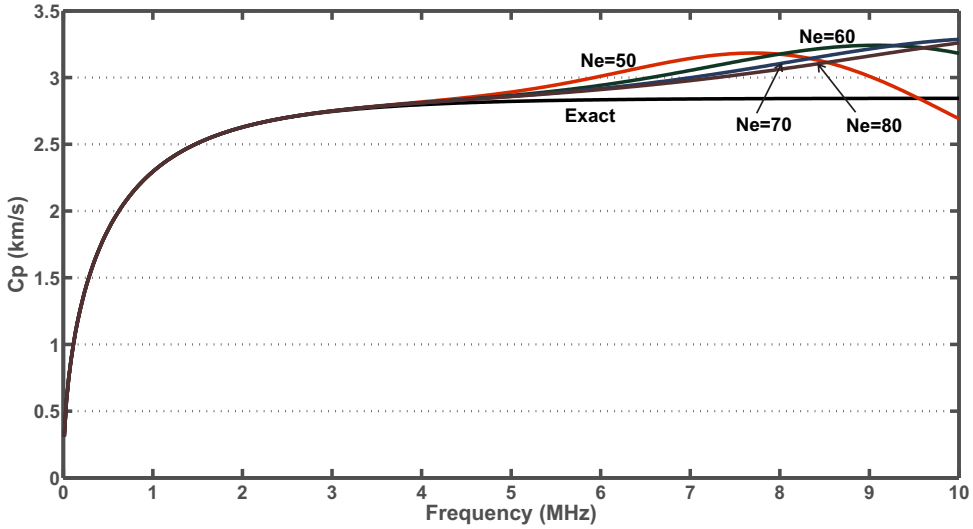

(a) Phase velocity dispersion curves

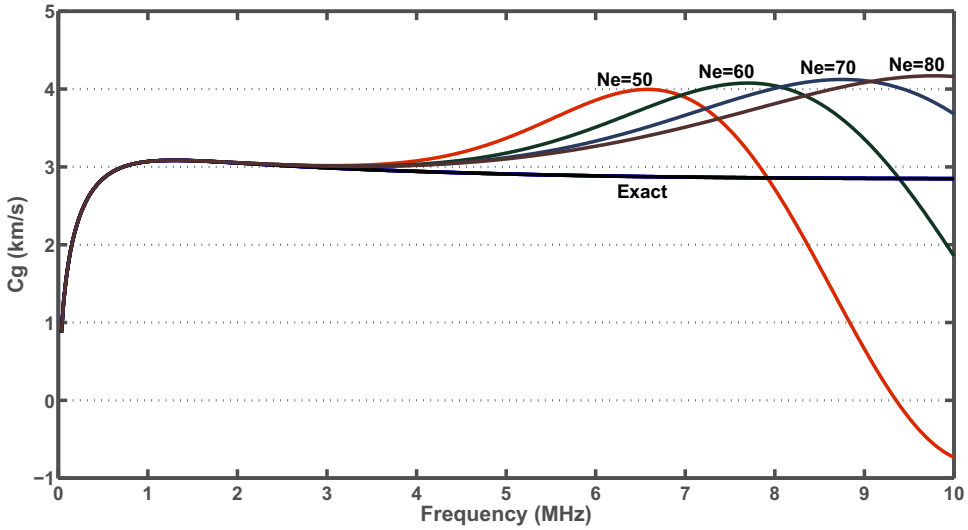

(b) Group velocity dispersion curves

Figure 4.25 Numerical Dispersion of A0 mode, for spectral element of polynomial order 5, and for 50, 60, 70 and 80 elements. The computations were for aluminum plate 1 mm thick, and 40 mm long.

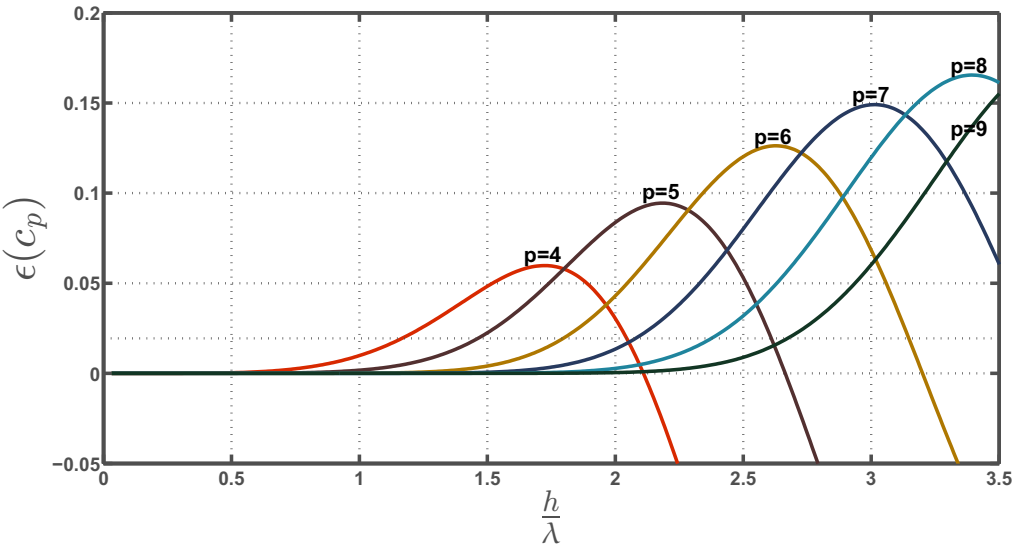

(a) Phase velocity dispersion curves

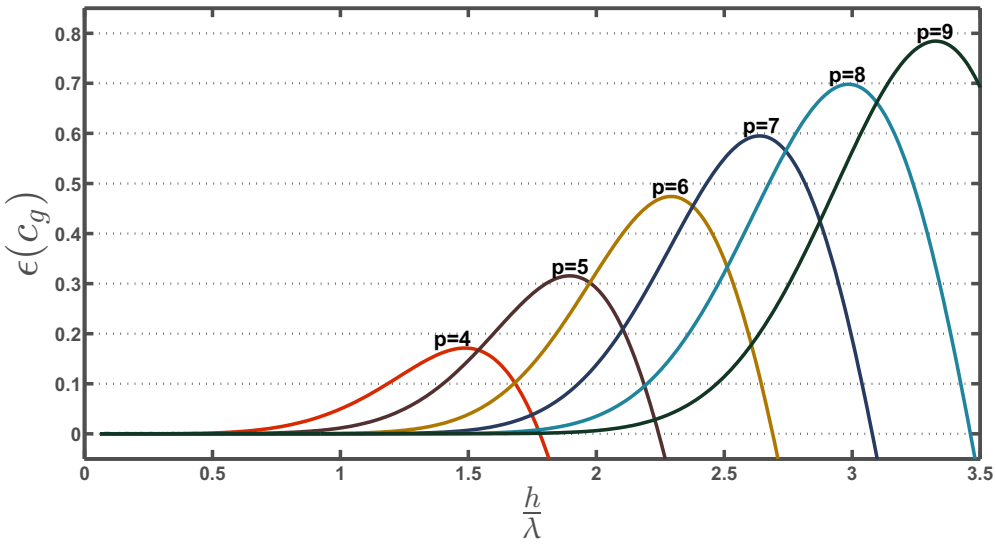

(b) Group velocity dispersion curves

Figure 4.26 Numerical Dispersion of A0 mode, for different polynomial orders. The computations were for aluminum plate 1 mm thick, and 40 mm long.

Figures 4.27(a) and 4.27(b) show the effect of different values of CFL number on the dispersion behavior, in terms of the errors induced by the spatial and temporal discretizations. The time step and the numerical eigenvalues are computed in exactly similar manner to the elastic wave, since Lamb waves are a special case of plane strain waves. The error is magnified by the temporal discretization, but the overall pattern of the error is the same, *i.e.* the temporal discretization is acting as an amplifier of the errors induced by the spatial discretization on the contrary to the

cases studied in the one dimensional case and the plane strain two dimensional case where the time discretization changed the trend of the error.

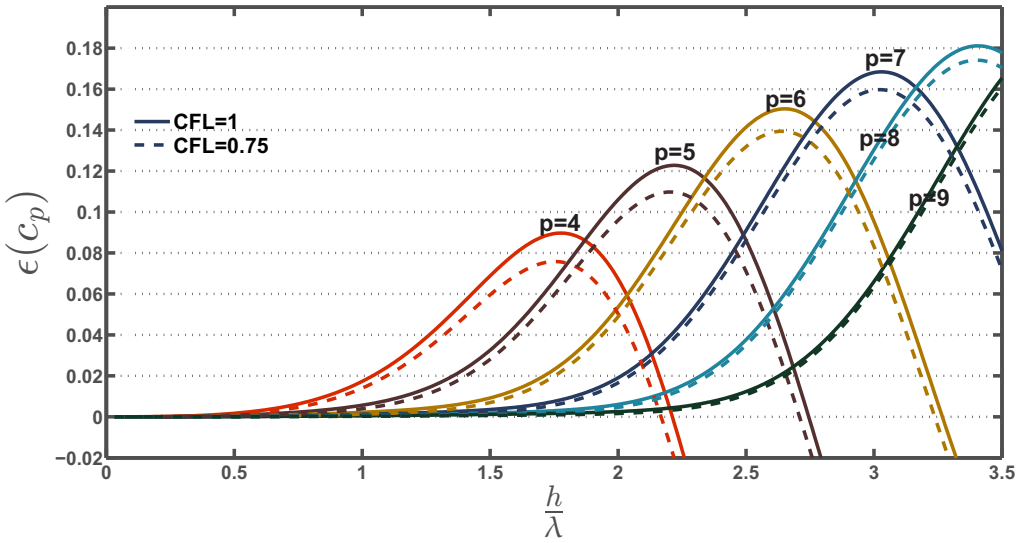

(a) CFL = 1, 0.75

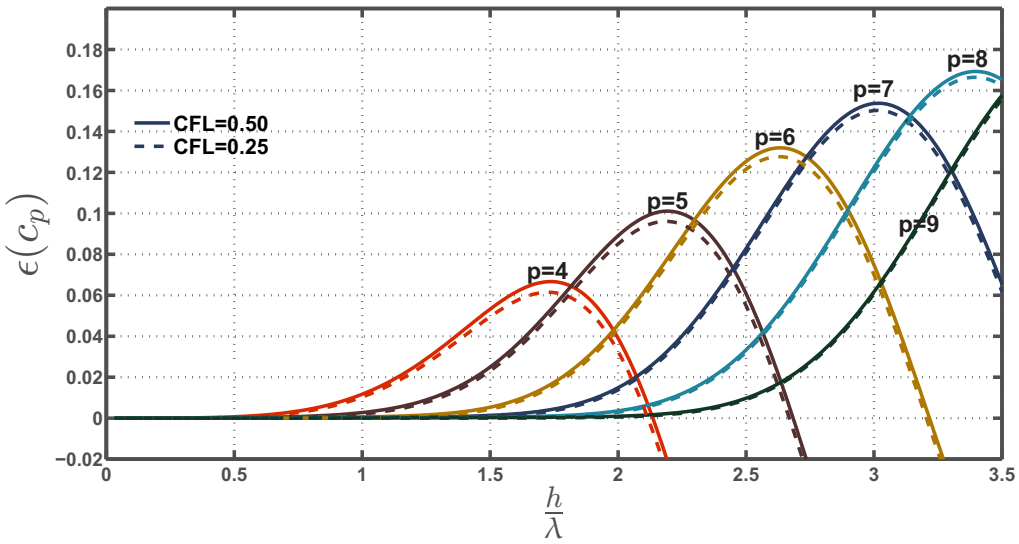

(b) CFL = 0.5, 0.25

Figure 4.27 Temporal numerical dispersion of A0 mode, for different polynomial orders, with CFL number, 1, 0.75, 0.5 and 0.25. The computations were for aluminum plate 1 mm thick, and 40 mm long.

Interestingly, the decrease of CFL number and correspondingly the time step does not reduce much the errors unlike in the case of the two dimensional unbounded plane strain wave, where the reduction in the CFL number reduced the errors with a tendency to return to the harmonic

results. This remark is valid for both the errors induced in phase velocity and group velocity depicted in Figs. 4.28(a) and 4.28(b). This could be understood in light of the fact of the absence of conflict of order phenomenon, since the temporal errors interact linearly with the spatial errors, acting as an amplification of the spatial discretization errors, reducing the time step, only reduced the amplification.

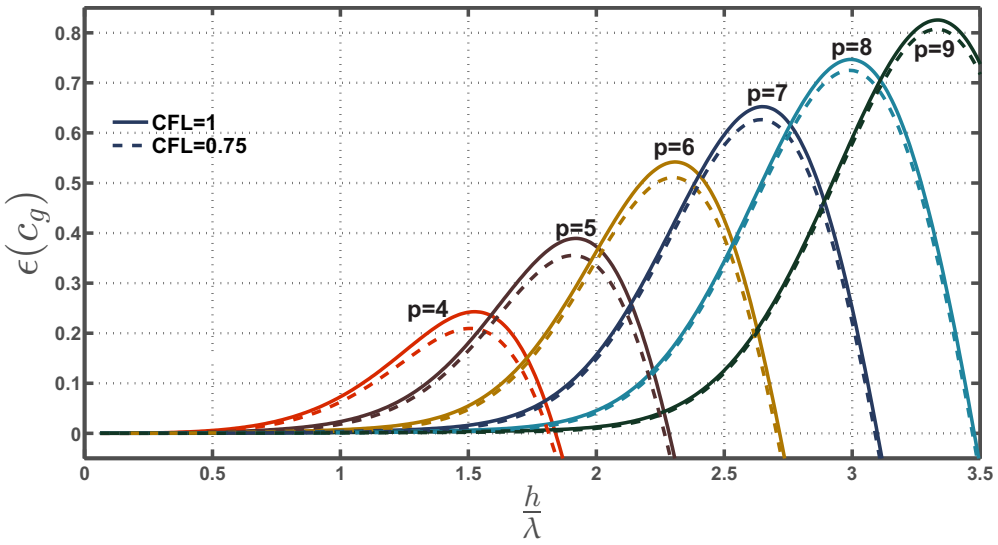

(a) CFL = 1, 0.75

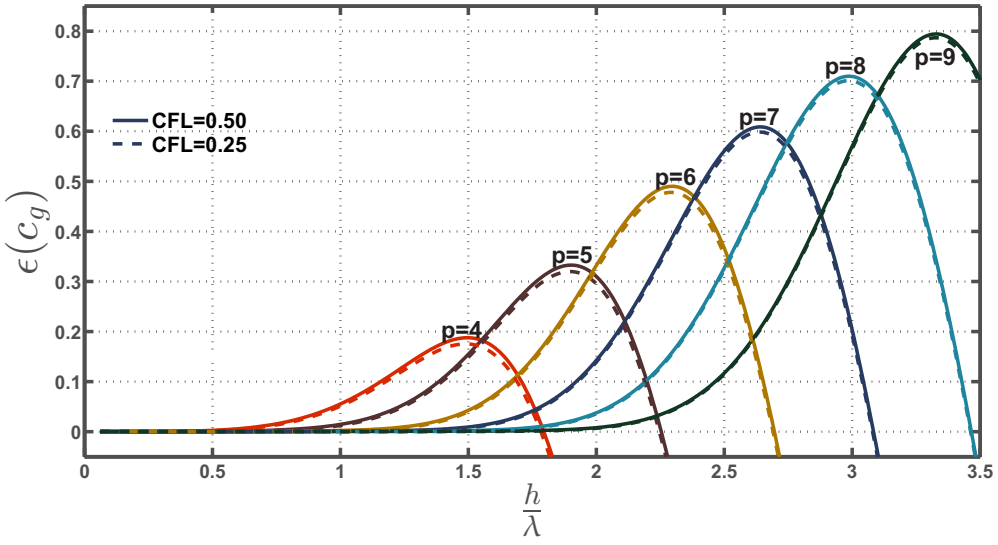

(b) CFL = 0.5, 0.25

Figure 4.28 Temporal numerical group dispersion of A0 mode, for different polynomial orders, with CFL number, 1, 0.75, 0.5 and 0.25. The computations were for aluminum plate 1 mm thick, and 40 mm long.

To summarize, the errors induced by the temporal discretization is typically a nonlinear function of the spatially induced errors of discretization. This is because the time integration scheme is low order, while the spatial discretization is a high order interpolation. This phenomena are referred to as "*conflict of order*". The conflict of order is manifested in a change of the trend of the dispersion errors, from underestimating the phase and group velocities in the harmonic case (spatial discretization alone) to an overestimating both the velocities when temporal discretization interacts with the spatial errors. This have been observed in the case of plane strain two dimensional elastic waves. But in the special case of Lamb waves, it was absent. In the case of Lamb waves the temporal discretization error are acting as a linear multiplier, and there is no conflict of order. This is reflected in the smaller effect when reducing the CFL number on the accumulative dispersion errors in the temporal discretization case.

4.5.3 First order shear deformation theory

For the FSDT, there are three degrees of freedom per material particle, and consequently three modes, one associated with each degree of freedom. We start by postulating a plane wave as a solution for each degree of freedom:

$$w_i = Ae^{i(\mathbf{k}\cdot\mathbf{x_i}-\omega t)} \tag{4.82}$$

$$S_i^x = Be^{i(\mathbf{k}\cdot\mathbf{x_i}-\omega t)} \tag{4.83}$$

$$S_i^y = Ce^{i(\mathbf{k}\cdot\mathbf{x_i}-\omega t)} \tag{4.84}$$

where $\mathbf{k} = [k\cos\theta, \quad k\sin\theta]$, and $\mathbf{x_i} = [x_i, \quad y_i]$ is a vector containing the coordinates of the ith node. After substituting these assumed fields into the semidiscrete equations Eqs. (4.46), we arrive at a generalized eigenvalue problem $\mathbf{Kd} = \chi\mathbf{Md}$, where $\chi = (\omega^n)^2$, and:

$$\mathbf{K} = \begin{pmatrix} \mathbf{K}_{11} & \mathbf{K}_{12} & \mathbf{K}_{13} \\ \mathbf{K}_{12}{}^{\mathrm{T}} & \mathbf{K}_{22} & \mathbf{K}_{23} \\ \mathbf{K}_{13}{}^{\mathrm{T}} & \mathbf{K}_{23}{}^{\mathrm{T}} & \mathbf{K}_{33} \end{pmatrix}, \quad \mathbf{d} = \begin{pmatrix} \mathbf{w} \\ \mathbf{S^x} \\ \mathbf{S^y} \end{pmatrix}, \quad \mathbf{M} = \begin{pmatrix} \mathbf{M}_{11} & 0 & 0 \\ 0 & \mathbf{M}_{22} & 0 \\ 0 & 0 & \mathbf{M}_{33} \end{pmatrix} \tag{4.85}$$

Then we approximate χ by the Rayleigh quotient of the system, which also is equivalent to the decomposed eigenvalue problem:

$$\begin{pmatrix} d_1 & d_2 & d_3 \\ d_3 & d_4 & d_6 \\ d_7 & d_8 & d_9 \end{pmatrix} \begin{pmatrix} A \\ B \\ C \end{pmatrix} = \chi \begin{pmatrix} A \\ B \\ C \end{pmatrix} \tag{4.86}$$

and the coefficients are:

$$d_1 = \frac{\overline{\mathbf{W}}^{\mathrm{T}}\mathbf{K_{11}}\mathbf{W}}{\overline{\mathbf{W}}^{\mathrm{T}}\mathbf{M_{11}}\mathbf{W}}, \quad d_2 = \frac{\overline{\mathbf{W}}^{\mathrm{T}}\mathbf{K_{12}}\mathbf{W}}{\overline{\mathbf{W}}^{\mathrm{T}}\mathbf{M_{11}}\mathbf{W}}, \quad d_3 = \frac{\overline{\mathbf{W}}^{\mathrm{T}}\mathbf{K_{13}}\mathbf{W}}{\overline{\mathbf{W}}^{\mathrm{T}}\mathbf{M_{11}}\mathbf{W}} \tag{4.87a}$$

$$d_4 = \frac{\overline{\mathbf{W}}^{\mathrm{T}}\mathbf{K_{12}}^{\mathrm{T}}\mathbf{W}}{\overline{\mathbf{W}}^{\mathrm{T}}\mathbf{M_{22}}\mathbf{W}}, \quad d_5 = \frac{\overline{\mathbf{W}}^{\mathrm{T}}\mathbf{K_{22}}\mathbf{W}}{\overline{\mathbf{W}}^{\mathrm{T}}\mathbf{M_{22}}\mathbf{W}}, \quad d_6 = \frac{\overline{\mathbf{W}}^{\mathrm{T}}\mathbf{K_{23}}\mathbf{W}}{\overline{\mathbf{W}}^{\mathrm{T}}\mathbf{M_{22}}\mathbf{W}} \tag{4.87b}$$

$$d_7 = \frac{\overline{\mathbf{W}}^{\mathrm{T}}\mathbf{K_{13}}^{\mathrm{T}}\mathbf{W}}{\overline{\mathbf{W}}^{\mathrm{T}}\mathbf{M_{33}}\mathbf{W}}, \quad d_8 = \frac{\overline{\mathbf{W}}^{\mathrm{T}}\mathbf{K_{23}}^{\mathrm{T}}\mathbf{W}}{\overline{\mathbf{W}}^{\mathrm{T}}\mathbf{M_{33}}\mathbf{W}}, \quad d_9 = \frac{\overline{\mathbf{W}}^{\mathrm{T}}\mathbf{K_{33}}\mathbf{W}}{\overline{\mathbf{W}}^{\mathrm{T}}\mathbf{M_{33}}\mathbf{W}} \tag{4.87c}$$

The computed eigenvalues of the equivalent system are, after sorting, associated, from smaller to larger values, with the $(\omega^n)^2$ of the w, S_x and S_y speeds. The first of which is the equivalent for the flexural mode.

Figures 4.29(a) and 4.29(b) show the phase and group velocities of the three modes associated with the discrete mesh of a very high density mesh of 2 element by 2 elements of a 4 mm by 4 mm by 1 mm thick aluminum plate, with a spectral element of polynomial order 6. w, S_x, and S_y, as well as the theoretical FSDT dispersion curve, and the exact A0 Lamb mode. The w mode of the spectral element is in large discrepancy from both the exact A0 mode and the theoretical FSDT phase velocity. This may be understood, in light of the idea, that the plane wave does not solve the semidiscrete system of equations based on the FSDT assumptions accurately. Although the asymptotic behavior is tending to the surface wave velocity, the agreement at the low frequency regime cannot be taken as accurate approximation of the A0 mode.

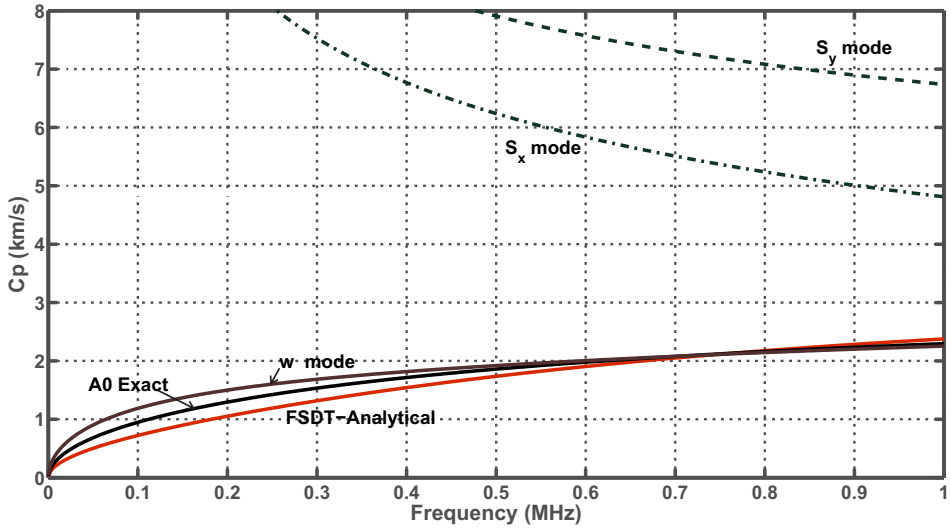

(a) Numerical phase velocity dispersion curve for the default value of the correction factor

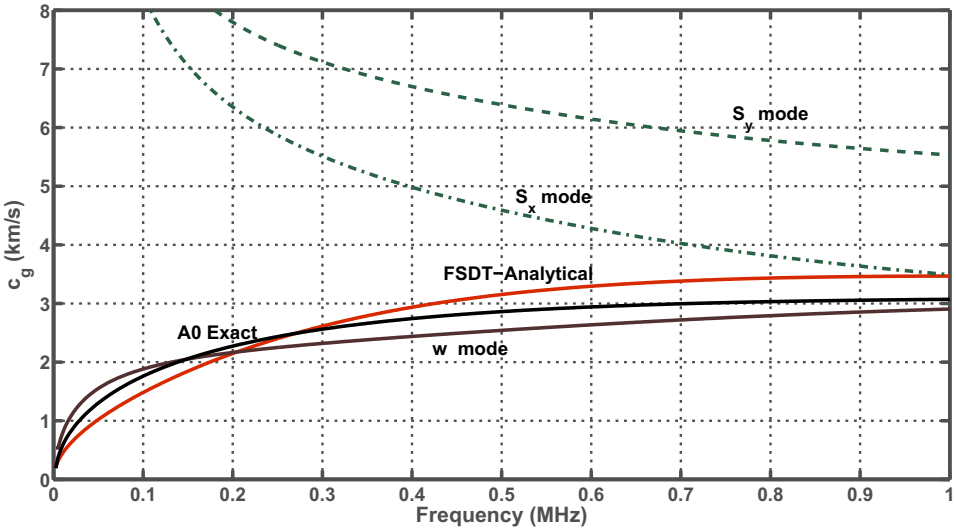

(b) Numerical group velocity dispersion curve for the default value of the correction factor

Figure 4.29 Spatial discretization numerical dispersion of FSDT three modes, and analytical FSDT dispersion curve for w mode and the exact A0 mode, for highly dense mesh, 4 by 4 mm aluminum plate, and 1 mm thick, the element used was p = 6, and 2 elements per square plate length.

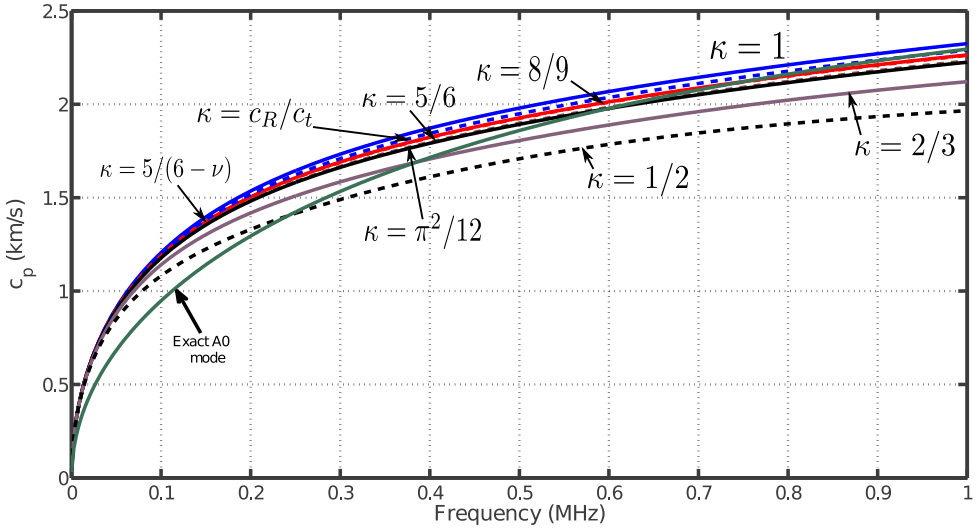

(a) Numerical phase dispersion curves for different values of shear correction factor

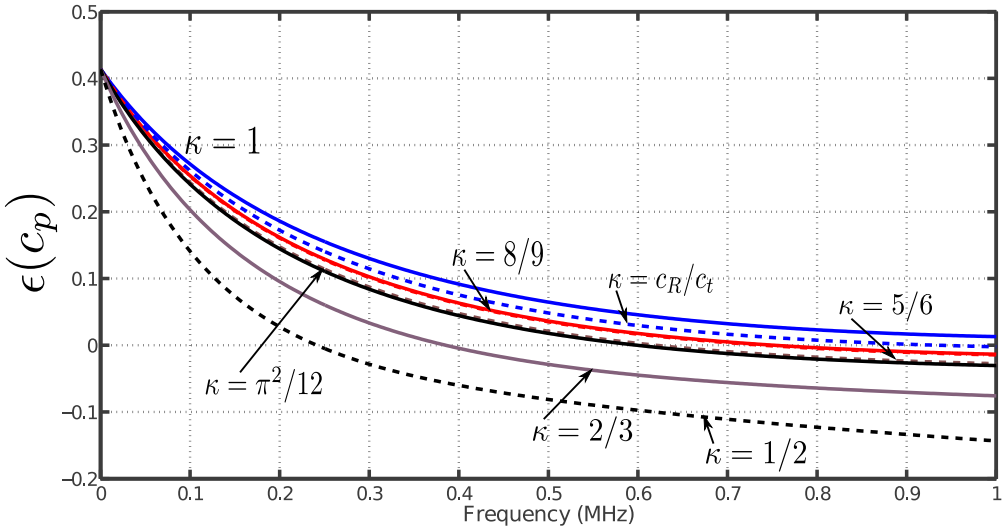

(b) Error with respect to A0 mode velocity, for different values of shear factor

Figure 4.30 Spatial discretization numerical phase dispersion of FSDT and its errors with respect to the exact A0 mode, for highly dense mesh, 4 by 4 mm aluminum plate, and 1 mm thick, the element used was p = 6, and 2 elements per square plate length.

Figure 4.30(a) shows the effect of different choices of shear correction factor κ on the numerical phase speed of the semdiscrete equations based on the FSDT. The error with respect to the fundamental antisymmetric Lamb mode A0 is shown for the same values of the shear correction

factor in Fig. 4.30(b), the errors were computed as:

$$\epsilon(c_p) = c_p^n / c_p(A0) - 1 \tag{4.88}$$

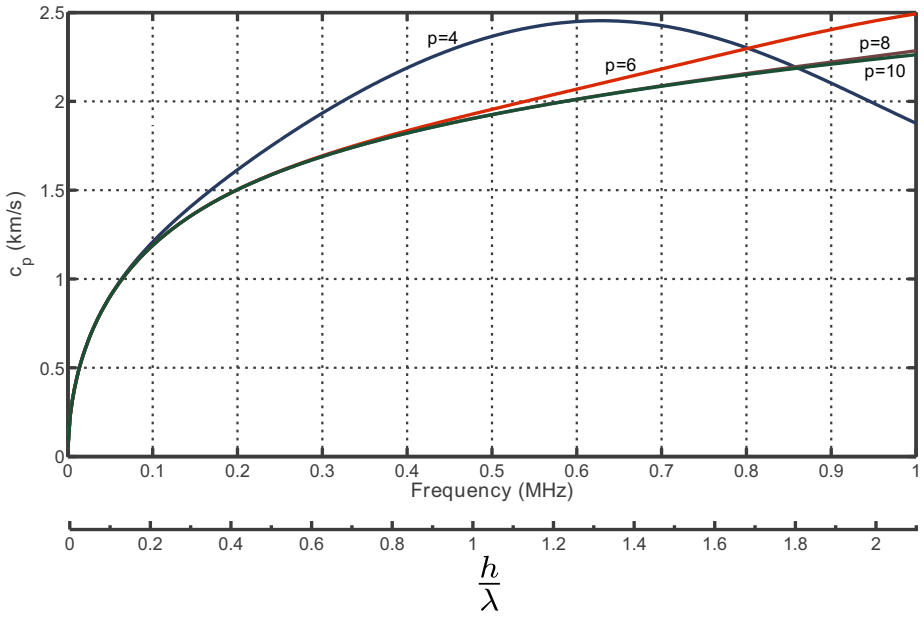

(a) even polynomial orders

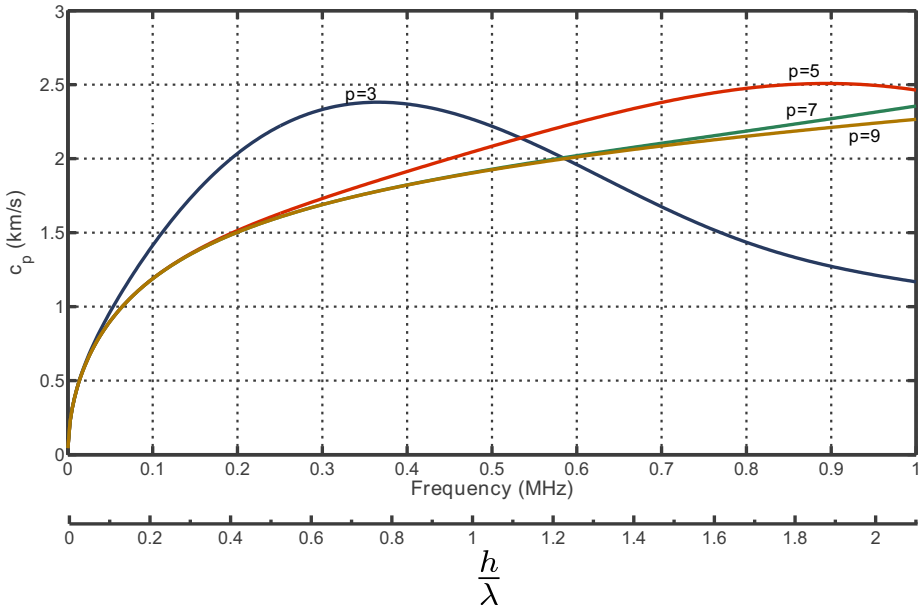

(b) odd polynomial orders

Figure 4.31 Spatial discretization numerical dispersion of FSDT flexural mode for different polynomial orders.

Figures 4.31(a) and 4.31(b) show the numerically extracted phase dispersion curves for the harmonic case, *i.e* the errors induced by the spatial discretization alone, for polynomial orders from 3 to 10.

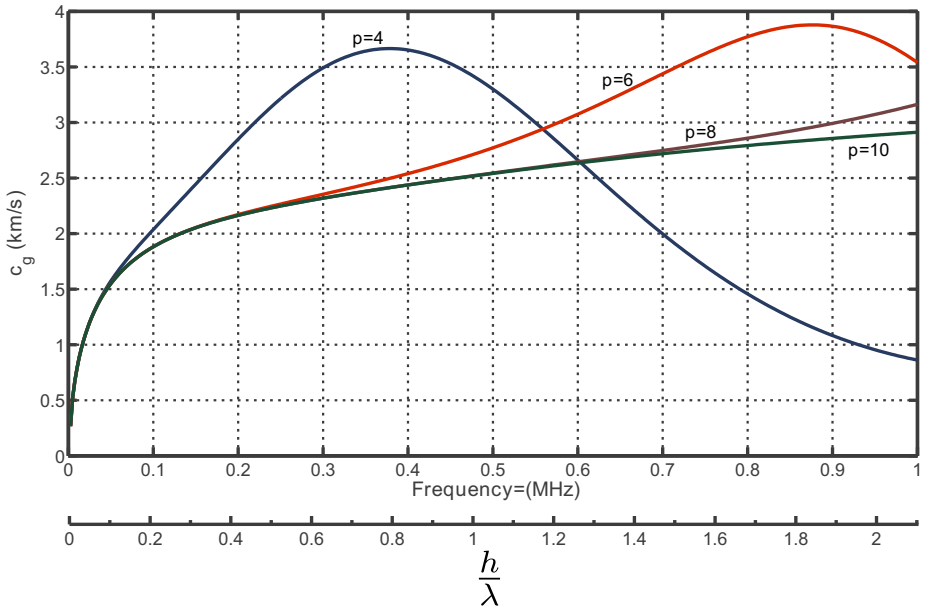

(a) even polynomial orders

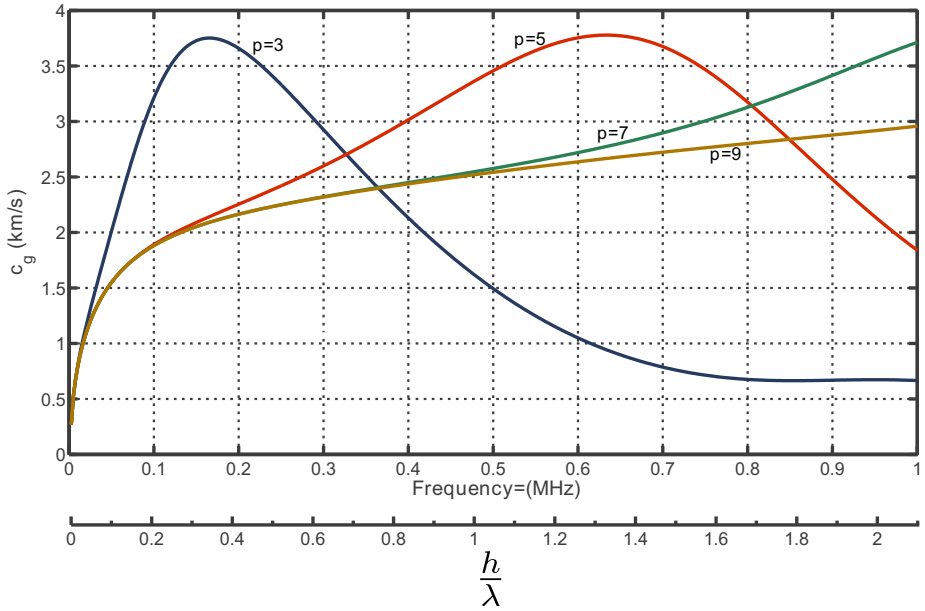

(b) odd polynomial orders

Figure 4.32 Spatial discretization numerical dispersion of FSDT flexural mode for different polynomial orders.

The curves illustrate the well known shear locking behavior due to over constraining for low order polynomial (*i.e.* p=3, and high order quadrature, which is normally remedied in the FEM by reduced Gauss integration), the remaining higher order polynomials are following more or less the same trend. The estimation of accuracy is rather difficult in the case of FSDT, since the nodal approximations are not accurate approximations of the eigenvectors of the discrete system, there is less information in comparing the extracted numerical speeds with a standard reference. For this reason we have reverted to representing the dispersion curves in the same sense that normal convergence tests are done in the conventional FEM literature. All of the presented results were for an incidence angle of 0. The idea of the convergence is to refine the mesh incrementally until the results are not affected, in this case we study the frequency convergence behavior, in the sense that increasing the h/λ ratio, would not affect the global behavior of the numerical dispersion. Figures 4.32(a) and 4.32(b) show the numerical group dispersion curves for the harmonic case, the results were repeated with finer and finer mesh until no noticeable effect witnessed by the numerical group velocity. The equivalent element to wavelength ratio to the frequency range is also shown on the same curves, in order to be able to compare the resolution parameters between different curves. Figures 4.33(a) and 4.33(b) show the temporally effected numerical phase velocity for different polynomial orders (3 to 10), and the effect of the CFL number used in the explicit time integration. As could be seen the low polynomial orders similarly manifest the shear locking behavior which the higher order elements are free from. A similar convergence study was done, and the plotted values are the ones that show no further change after refining the mesh. The CFL number was computed with respect to the analytical value of the phase velocity:

$$\Delta t = \frac{\mathrm{CFL}}{c_p}\left(\frac{1}{\sqrt{1/\Delta x_{min}^2 + 1/\Delta y_{min}^2}}\right) = \frac{\mathrm{CFL}}{c_p}\left(\frac{1}{\sqrt{2/\Delta x_{min}^2}}\right) \tag{4.89}$$

while temporal numerical speed is computed from the extracted eigenvalue χ:

$$\omega_n = \frac{2\sin^{-1} 0.5\sqrt{\chi}\Delta t}{\Delta t} \tag{4.90}$$

Figures 4.34(a) and 4.34(b) show the effect of further decreasing the CFL number, the effect is hardly noticeable for higher order polynomials.

Figures 4.36(a) and 4.36(b) show the group velocity dispersion curves for even and odd polynomial orders. Figures 4.37(a) and 4.37(b) show the angular dependence of the numerical phase velocity. The circular symmetry is evident, i.e. the FSDT spectral element is free from the numerical anisotropy, which justify generalizing the previous dispersion curves, that was computed for $\theta = 0$ to all the incidence angles. Which is not the case for the plane two dimensional wave

where is suffers from numerical anisotropy (see Figs. 4.17(a) and 4.16(a) for example), albeit in a very small percentage.

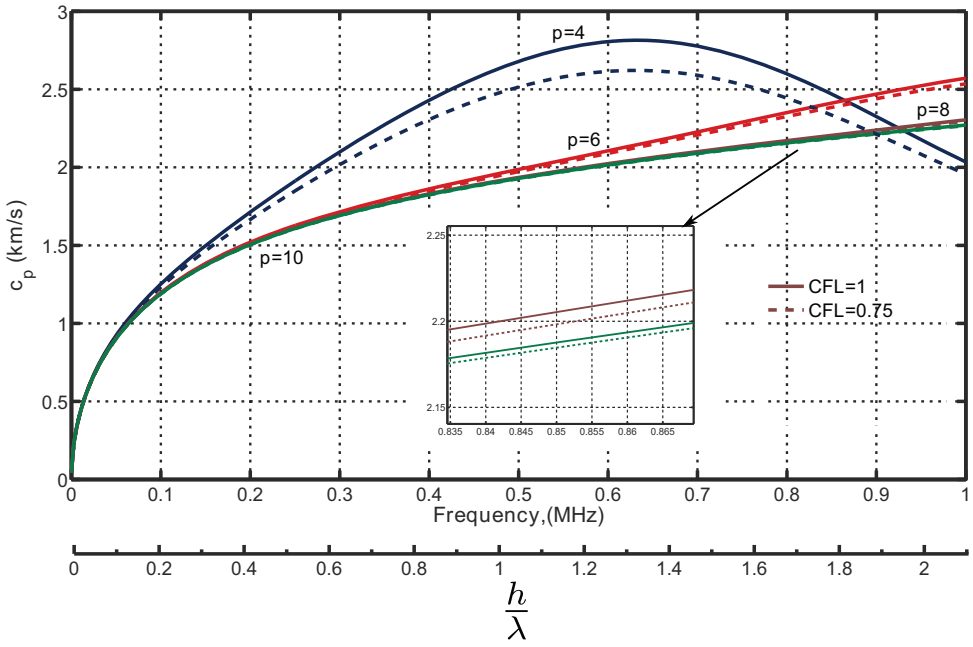

(a) even polynomial orders

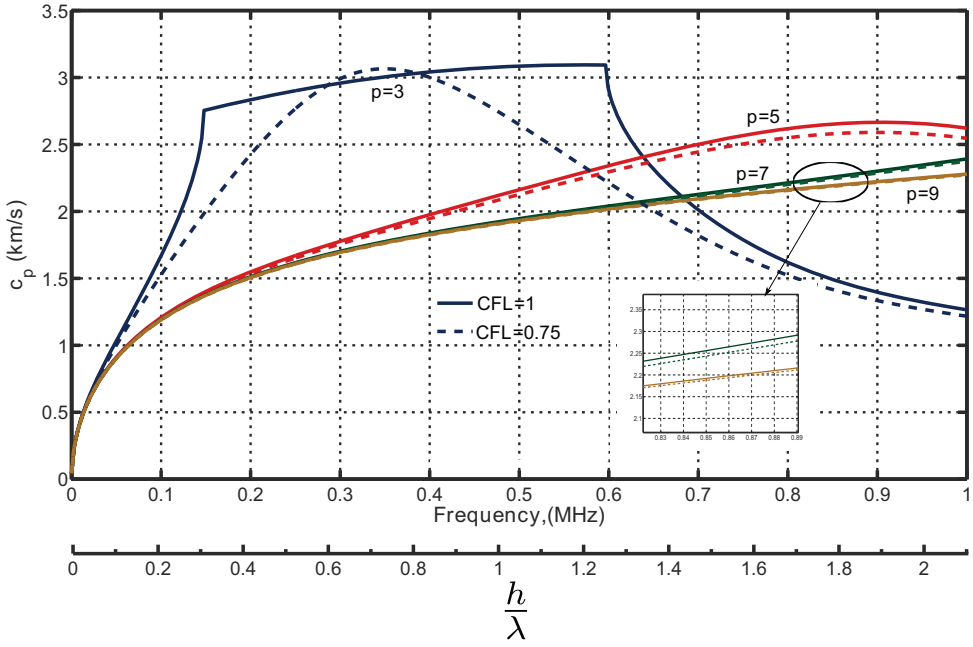

(b) odd polynomial orders

Figure 4.33 Temporal discretization numerical dispersion of FSDT flexural mode for different polynomial orders, and CFL number of 1 and 0.75.

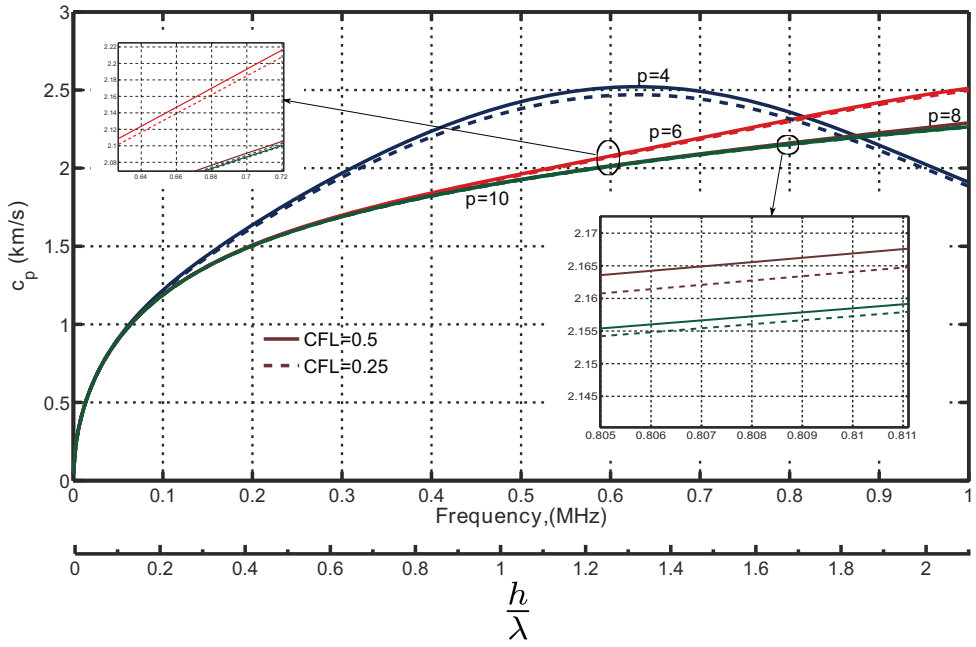

(a) even polynomial orders

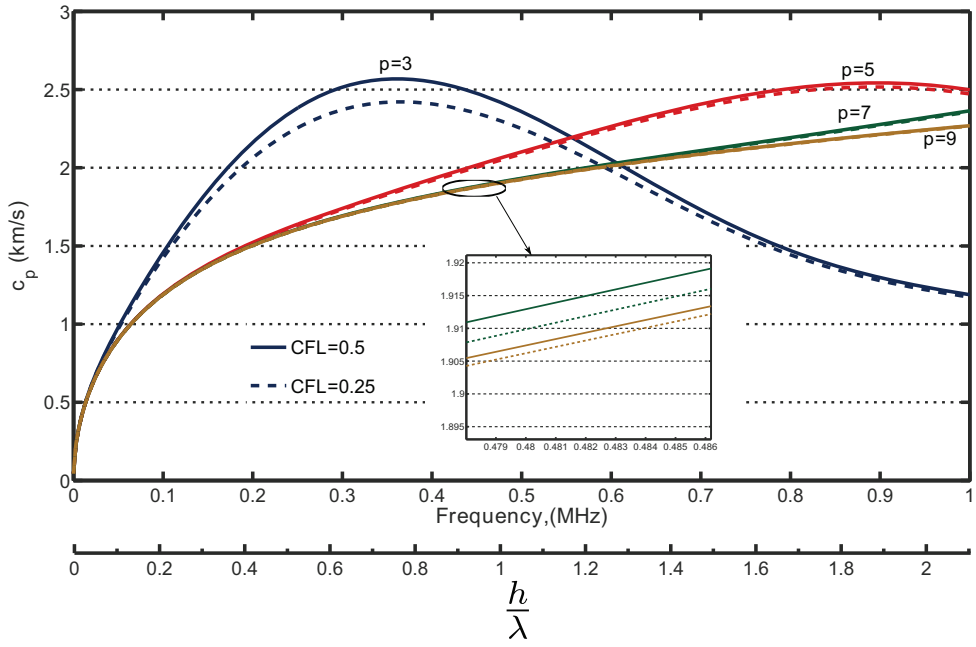

(b) odd polynomial orders

Figure 4.34 Temporal discretization numerical dispersion of FSDT flexural mode for different polynomial orders, and CFL number of 0.50 and 0.25.

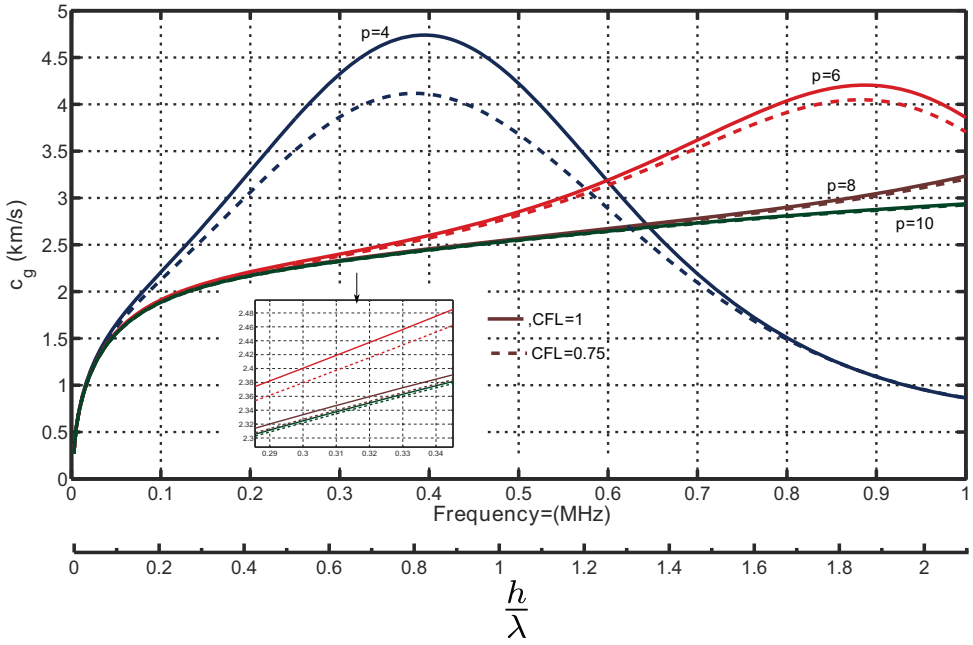

(a) even polynomial orders

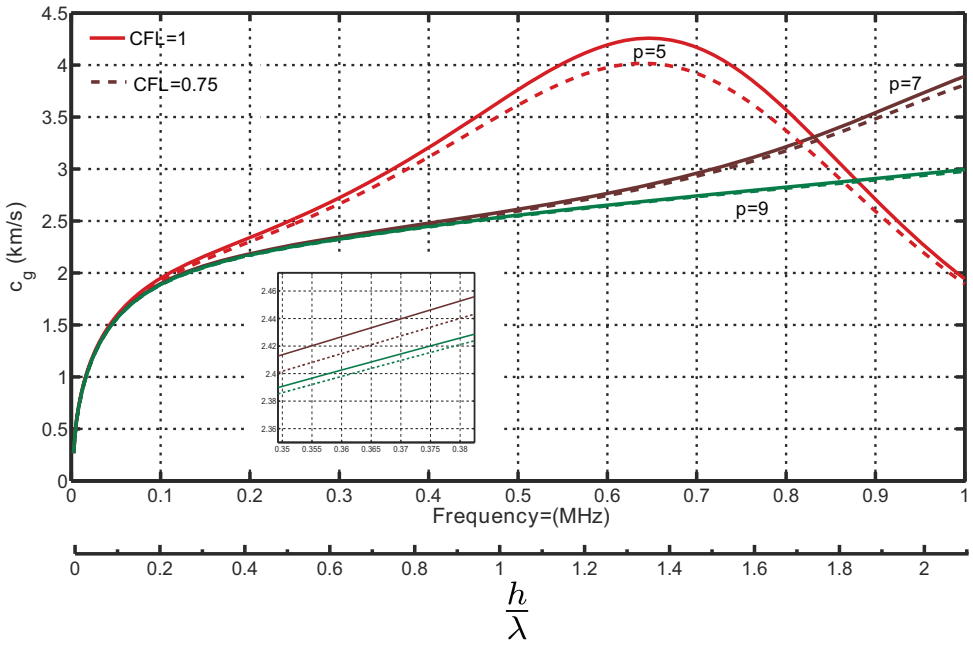

(b) odd polynomial orders

Figure 4.35 Temporal discretization numerical group dispersion of FSDT flexural mode for different polynomial orders, and CFL number of 1 and 0.75.

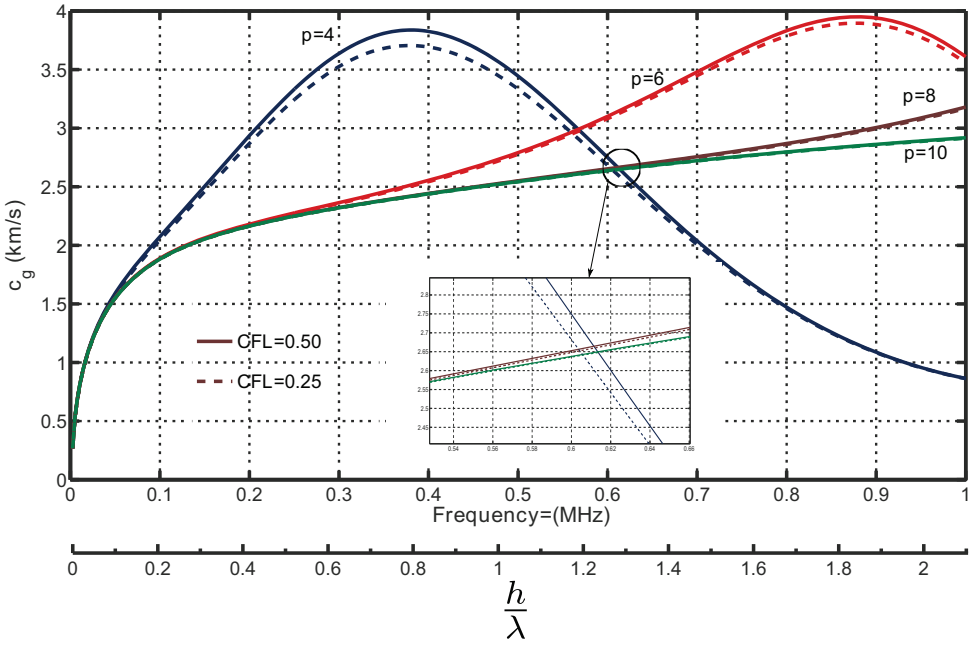

(a) even polynomial orders

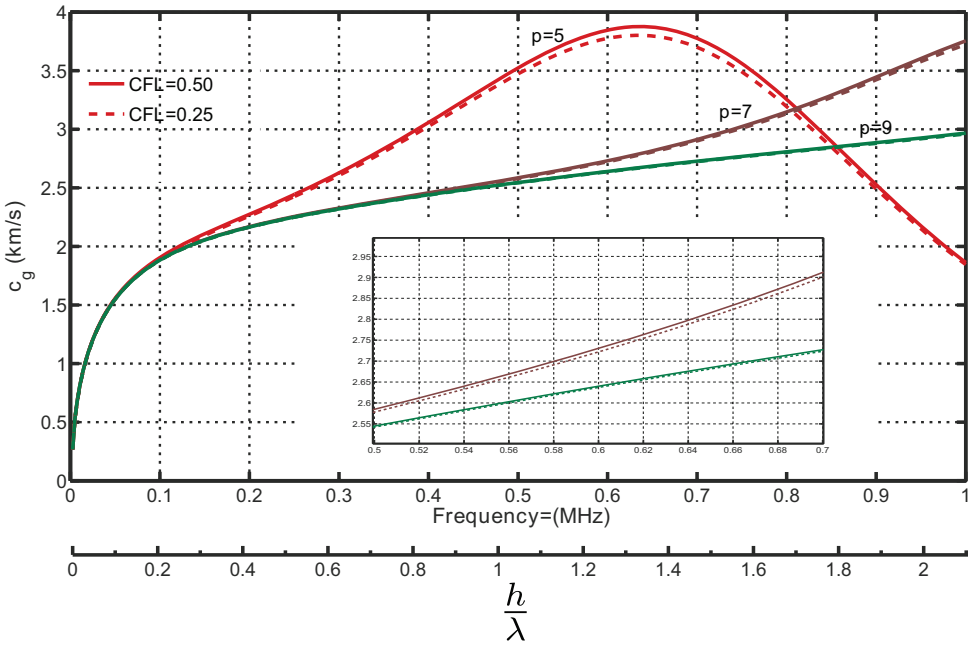

(b) odd polynomial orders

Figure 4.36 Temporal discretization numerical group dispersion of FSDT flexural mode for different polynomial orders, and CFL number of 0.5 and 0.25.

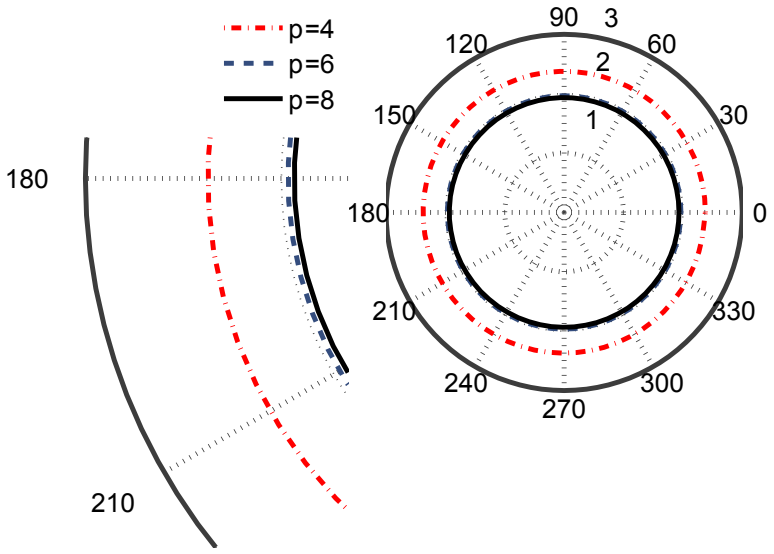

(a) even polynomial orders

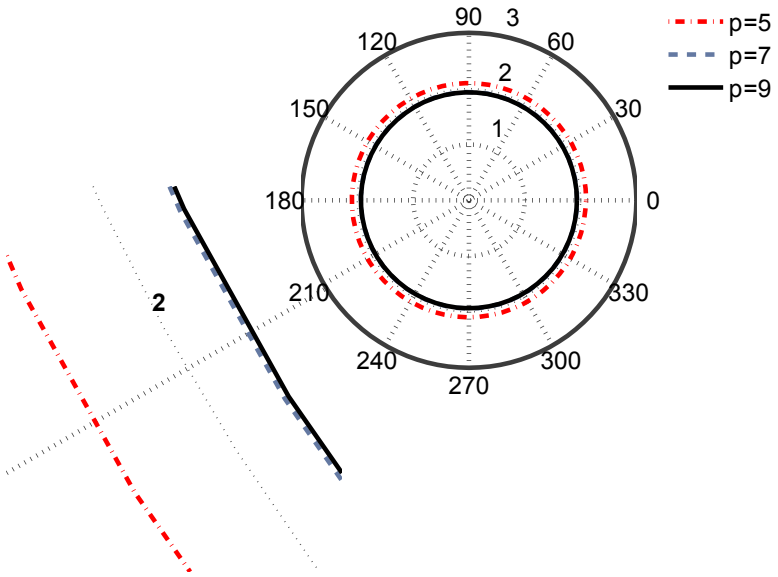

(b) odd polynomial orders

Figure 4.37 Spatial discretization phase dispersion of FSDT as a function of incidence angle, at frequency 500 kHz.

4.6 Conclusion

In this chapter, spectral element was developed for the two dimensional elastic wave equation under a plane strain assumption, the numerical dispersion characteristics of the spectral element implementation was studied using Rayleigh quotient approach for estimating the eigenvalues.

The conflict between orders of both temporal and spatial discretization, a previously observed phenomena in rod elements, is also observed for the case of the spectral element developed for the unbounded two dimensional elastic wave propagation, *i.e.* the change of the trend of the error from underestimating the phase and group velocity in the harmonic case, to overestimation induced by the low order temporal discretization. This phenomenon could also become more beneficial than normally believed, since the error goes back to zero at fewer grid points, but the fact that there at two propagating wave simultaneously might limit the applicability of this kind of targeting zero error at few grid points.

The generality of using Rayleigh quotient in the numerical dispersion analysis suggests a new interpretation: it could be viewed as a test for the efficiency of the sampling of an assumed displacement continuous field at a certain number and locations of discrete points. This interpretation opens a vista of applications for this numerical dispersion analysis technique, and one of those possibilities are extending the analysis to Lamb waves. In the present chapter, we utilized this point of view to study, for the first time, the numerical dispersion of elastic wave propagation in bounded media. The spectral element formulated earlier for the plane strain elastic wave propagation was used for the special case of Lamb waves, which is essentially a plane strain wave propagation in a doubly bounded media. The traction free boundaries are included in the analysis in terms of the assumed displacement fields satisfying the traction free boundary conditions.

On the contrary to the previously observed phenomena of the conflict of order between the high order spatial discretization and low order temporal discretization, leading to a change in the behavior of the dispersion error in the case of the unbounded two dimensional elastic wave, this behavior is absent in the Lamb wave spectral element simulation. The Lamb waves numerical dispersion errors induced by the spatial discretization does not change the pattern when interacting with the errors coming from the temporal discretization, rather the temporally induced errors act as an amplification of the spatial errors. This and the fact the decreasing the CFL numbers does not affect much the accuracy, suggests that spectral element is very well suited to the simulating the Lamb waves in both the frequency and the time domain efficiently.

The first order shear theory dispersion was studied for both the mathematical model and its spectral element numerical implementation, *i.e.* in terms of the verification and validation phases. The accuracy of the first order shear deformation as an approximate theory for the Lamb

fundamental antisymmetric mode is poor. But this inaccuracy emanates from the nature of the mathematical assumptions, not from the implementation, thus the limitation to low frequency behavior of several results reported in literature.

Besides shinning the light on the limitations of the applicability of the FSDT to low frequency regime as far as Lamb waves simulation is concerned, the presented analysis offered a beneficial demonstration of the absence of the shear locking behavior for the spectral element (when using polynomial orders $p > 3$), and the complete absence of the numerical anisotropy.

In the next chapter, having established the meshing parameters for an accurate simulation of Lamb waves, a utilization of this knowledge in performing a parametric study of the different effects of strongly coupled PZT generation of Lamb waves is studied.

CHAPTER 5

Application of SEM in SHM: formulation and case studies

> Mathematics is the part of physics where experiments are cheap.
>
> VLADIMIR I. ARNOLD (1937-2010)

ACTIVE SHM schemes based on the guided waves propagation requires a guided waves generation agent, and according to its advantages the piezoelectric patches or elements provide the best candidate for establishing a viable non-intrusive active guided waves SHM scheme.

In this chapter, the problem of piezoelectric element strongly coupled with an elastic substructure is formulated, and the spectral element implementation is covered in details. Then the developed implementation is utilized in performing a set of parametric studies of the effects of the actuator thickness, the adhesive layer thickness and material on the modal amplitude variation with frequency *i.e. mode tuning curves*. At the last part of the chapter the results of experimental verifications for two case studies are reproduced from previously published papers by the author [Mohamed and Masson, 2010b, 2011].

5.1 Formulation: piezoelectric generation of guided waves

The most common of piezoelectric ceramics are the piezoceramic barium titanate ($BaTiO_3$) and lead zirconate titanate (PZT). The crystal lattice of piezoelectric materials is of the face-centered cubic (FCC) kind. Metallic atoms are located at the corners of the cubic unit cell as shown in Fig. 5.1, while oxygen atoms remain at the center of the unit cell. A heavier atom is located at the center and it can shift to positions with lower energy, with a consequent distortion of the crystal lattice (metastable structure). If an electric field is applied to the structure, the central atom can exceed the potential well threshold and move to a lower energy state. This is followed by a rupture of symmetry yielding an electric dipole (Fig. 5.1). The previous phenomenon is possible only below the so-called Curie temperature [Carrera *et al.*, 2011].

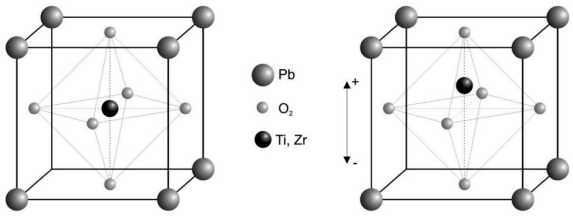

Figure 5.1 Piezoceramic cell before (left) and after (right) polarization.

Above Curie temperature, the piezoelectric effect disappears due to high thermal agitation. Polarized piezoceramics are obtained by heating them above their Curie temperature and subjecting the material to an intense electric field during cooling. In doing so, all the dipoles become aligned in the same direction and the material ends with a stable polarization. Moreover, apart from a residual polarization, the crystal lattice of the polarized piezoceramic will also undergo a residual deformation. After the polarization process, a very small electric potential will be sufficient to obtain a temporary deformation and vice versa. Even if the electromechanical coupling is a nonlinear phenomenon, piezoelectric problems are usually studied using linear analysis.

5.1.1 Piezoelectric domain

For the purpose of completeness, we review here the fundamentals of the weak form derivation of the piezoelectric domain [Carrera *et al.*, 2011]. Consider the piezoelectric domain Ω depicted in Fig. 5.2(a), within which the displacement field, $\mathbf{u}$, and electric potential field, ϕ, are to be determined. The $\mathbf{u}$ and ϕ fields satisfy a set of differential equations that represent the physics of the continuum problem considered. Boundary conditions are usually imposed on the domain's boundary, Γ, to complete the definition of the problem.

The constitutive relations for piezoelectric media may be derived in terms of their associated thermodynamic potentials. For linear piezoelectric materials, the interaction between the electrical and mechanical variables can be described by linear relations (ANSI/IEEE Standard 176-1987 [ANSI/IEEE, 1987]). Under isothermal conditions, a constitutive relation is established between mechanical and electrical variables in Voigt notation as:

$$\mathbf{T} = \mathbf{c}^E\mathbf{S} - \mathbf{e}^{\mathrm{T}}\mathbf{E}, \tag{5.1}$$

$$\mathbf{D} = \mathbf{e}\,\mathbf{S} + \varepsilon^S\mathbf{E}, \tag{5.2}$$

On the domain, Ω, and its boundary, Γ, (where the normal is directed outward from the domain), the fundamental dynamics must satisfy the equilibrium conditions:

$$\rho \ddot{u}_i = \partial_{x_j} \mathrm{T}_{ij} \tag{5.3}$$

where $\mathbf{u}$ is the displacement vector, ρ the mass density of the material, t the time, $\mathbf{T}$ the stress tensor, and x_i where $i = 1, 2, 3$, unit vector in the Cartesian coordinate system. When no macroscopic charges are present in the medium, Gauss' theorem imposes for the electric displacement vector, $\mathbf{D}$:

$$\partial_{x_i} D_i = 0 \tag{5.4}$$

Assuming electrostatic conditions, the electrostatic potential, ϕ, is related to the electric field $\mathbf{E}$ by:

$$E_i = -\partial_{x_i} \phi \tag{5.5}$$

Thus the governing equations becomes:

$$\rho \ddot{u}_i = \partial_{x_j} c^E_{ijkl} S_{kl} - e_{kij} E_k \tag{5.6}$$

$$\partial_{x_j} (e_{ikl} S_{kl} + \varepsilon^S_{ij} E_j) = 0 \tag{5.7}$$

In order to complete the description of the problem in a way that ensures the uniqueness of the solution, we need to complement the governing equations with the boundary conditions. The mechanical conditions are as follows: The Dirichlet condition (essential) on the displacement field, $\mathbf{u}$, is given by:

$$u_i = u^o_i \tag{5.8}$$

where u^o_i is a known given vector. The Neumann condition on the stress field, $\mathbf{T}$, is given by:

$$T_{ij} \cdot n_j = f^o_i \tag{5.9}$$

where $\mathbf{n}$ is the vector normal to Γ_f, directed outward, and f^o_i is a known traction vector. The electrical conditions are as follows: The conditions for the excitation of the electric field between those surfaces of the piezoelectric material that are not covered with an electrode and are, therefore, free of surface charges is given by:

$$D_i \cdot n_i = 0 \tag{5.10}$$

where **n** is the vector normal to the surface. When considering the conditions for the potential and excitation of the electric field between those surfaces of the piezoelectric material that are covered with electrodes, we assume that there are p electrodes in the system. The potential on the whole surface of the p^{th} electrode is:

$$\phi = \phi_p \tag{5.11}$$

The charge on that electrode is:

$$-\iint_{dS_p} D_i n_i \, dS_p = Q_p \tag{5.12}$$

In some cases, the potential is used, and in others it is the charge. In the former case, ϕ_p is known and Eq. (5.12) is used to determine Q_p. In the latter case, Q_p is known and Eq. (5.11) is used to determine ϕ. Finally, in order to define the origin of the potentials, it is necessary to impose the condition that the potential at one of the electrodes be zero ($\phi_o = 0$) *i.e.* ensure that one of the electrodes are grounded [Kaltenbacher, 2007; Uchino, 2013].

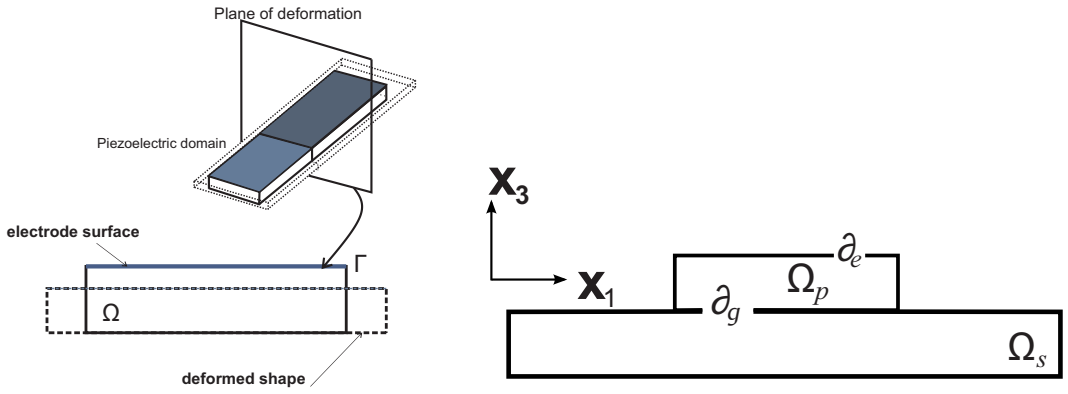

(a) A schematic of a piezoelectric domain Ω and boundary Γ

(b) A coupled piezoelectric domain with an elastic substructure

Figure 5.2 Schematic of single piezoelectric domain and a piezoelectric domain coupled to a substructure.

Since Lamb waves are plane strain waves, it is assumed that the actuator is acting dominantly in the plane strain (*i.e.* extending to infinity in the z direction) as shown in Fig. 5.6. This assumption limits the applicability of the presented results, since it excludes the possible electromechanical resonances that could be excited by axisymmetric and three dimensional models.

5.1.2 Coupled piezoelectric domain with substructure

Figure 5.2(b) illustrates the domain decomposition needed for the case of coupling a piezoelectric element into an elastic substructure, where Ω_p and Ω_s are the domains of the piezoelectric and the substructure, respectively. ∂_p, ∂_s, and ∂_g are the domain boundaries of the piezoceramic, the substructure, and the interface, respectively. We first introduce the two differential operators $\boldsymbol{\mathcal{B}}$, and $\boldsymbol{\nabla}$, and the unit normal $\mathbf{n}$:

$$\boldsymbol{\mathcal{B}} = \begin{pmatrix} \partial_{x_1} & 0 \\ 0 & \partial_{x_3} \\ \partial_{x_3} & \partial_{x_1} \end{pmatrix} \quad , \quad \boldsymbol{\nabla} = \begin{pmatrix} \partial_{x_1} \\ \\ \partial_{x_3} \end{pmatrix} \quad , \quad \mathbf{n} = \begin{pmatrix} n_1 & 0 \\ 0 & n_3 \\ n_3 & n_1 \end{pmatrix} \tag{5.13}$$

where for the 2D plane strain case considered in the present work, and since the PZT is transversely isotropic:

$$\mathbf{T} = \begin{pmatrix} T_1 \\ T_3 \\ T_5 \end{pmatrix}, \mathbf{S} = \begin{pmatrix} S_1 \\ S_3 \\ S_5 \end{pmatrix}, \mathbf{D} = \begin{pmatrix} D_1 \\ \\ D_3 \end{pmatrix}, \mathbf{E} = \begin{pmatrix} E_1 \\ \\ E_3 \end{pmatrix}, \boldsymbol{\varepsilon}^S = \begin{pmatrix} \varepsilon_{11} & 0 \\ \\ 0 & \varepsilon_{33} \end{pmatrix},$$
$$\mathbf{c}^E = \begin{pmatrix} c_{11} & c_{13} & 0 \\ c_{13} & c_{33} & 0 \\ 0 & 0 & c_{55} \end{pmatrix}, \mathbf{e} = \begin{pmatrix} 0 & 0 & e_{15} \\ \\ e_{31} & e_{33} & 0 \end{pmatrix} \tag{5.14}$$

In Eq. (5.14), $\mathbf{T}$ is a vector containing the corresponding Cauchy stress 2nd order tensor elements, $\mathbf{S}$ a vector containing the corresponding infinitesimal strain 2nd order tensor elements, $\mathbf{D}$ electrical displacement vector, $\boldsymbol{\varepsilon}^S$ the 2D elements of dielectric permittivity 2nd order tensor, $\mathbf{c}^E$ the 2D elements of the elastic 4th order tensor of piezoelectric material, $\mathbf{e}$ the 2D elements of 3rd order tensor of piezoelectric stress constants, and $\mathbf{E}$ electric field vector.

The superscripts E and S indicate that the corresponding material parameters have to be determined at constant electric field intensity E and at constant mechanical strain S, respectively. The direct piezoelectric effect (sensor) is reflected in Eq. (5.2), while Eq. (5.1) refers to the converse piezoelectric effect (actuator). The strong form of the governing equations in the absence of body forces are:

$$\boldsymbol{\mathcal{B}}^{\mathrm{T}}(\mathbf{c}^E \boldsymbol{\mathcal{B}} \mathbf{u}_p + \mathbf{e}^{\mathrm{T}} \boldsymbol{\nabla}\phi) = \rho_p \ddot{\mathbf{u}}_p \quad \forall \quad \mathbf{x} \in \Omega_p \tag{5.15a}$$
$$\boldsymbol{\nabla}^{\mathrm{T}}(\mathbf{e} \boldsymbol{\mathcal{B}} \mathbf{u}_p - \boldsymbol{\varepsilon}^S \boldsymbol{\nabla}\phi) = 0 \quad \forall \quad \mathbf{x} \in \Omega_p \tag{5.15b}$$
$$\boldsymbol{\mathcal{B}}^{\mathrm{T}} \mathbf{c}_s \boldsymbol{\mathcal{B}} \mathbf{u}_s = \rho_s \ddot{\mathbf{u}}_s \quad \forall \quad \mathbf{x} \in \Omega_s \tag{5.15c}$$

The displacement field of the PZT element is $\mathbf{u}_p$, while that of the substructure is $\mathbf{u}_s$, and ϕ is the electric potential field defined in the domain of the PZT element. Assuming an ideal bonding, the tractions and displacements at the interface between the two domains Ω_p and Ω_s should be continuous, with the following boundary conditions:

Electrical:		**Traction:**		**Coupling:**	
$\phi = 0$	on ∂_g	$\mathbf{n}_p^{\mathrm{T}}\mathbf{T}_p = 0$	on $\partial\Omega_p - \partial_g$	$\mathbf{n}_s^{\mathrm{T}}\mathbf{T}_s = -\mathbf{n}_p^{\mathrm{T}}\mathbf{T}_p$	on ∂_g
$\phi = \phi_l(t)$	on ∂_e	$\mathbf{n}_s^{\mathrm{T}}\mathbf{T}_s = 0$	on $\partial\Omega_s - \partial_g$	$\mathbf{u}_s = \mathbf{u}_p$	on ∂_g
$\mathbf{n}_p^{\mathrm{T}}(\mathbf{e}\mathcal{B}\mathbf{u}_p - \varepsilon^S\boldsymbol{\nabla}\phi) = 0$	on	$\partial\Omega_p - (\partial_e \cup \partial_g)$			

where ∂_e is the electroded boundary of the PZT element, and ∂_g is the dynamic interface electrically grounded boundary. To complete the formulation, the initial conditions are all assumed to be zero. The corresponding weak form (derived in Appendix B.5) is obtained by finding $\mathbf{u} \in H^1_{\mathcal{B}}$ and $\phi \in H^1_{\nabla}$ satisfying $\phi(\partial_e, t) = \phi_l(t)$ such that

$$\int_{\Omega_s} \mathbf{w}^{\mathrm{T}}\rho_s\ddot{\mathbf{u}}\,d\Omega + \int_{\Omega_p} \mathbf{w}^{\mathrm{T}}\rho_p\ddot{\mathbf{u}}\,d\Omega + \int_{\Omega_s} (\mathcal{B}\mathbf{w})^{\mathrm{T}}\mathbf{c}_s\mathcal{B}\mathbf{u}\,d\Omega + \int_{\Omega_p} (\mathcal{B}\mathbf{w})^{\mathrm{T}}\mathbf{c}^E\mathcal{B}\mathbf{u}\,d\Omega + \int_{\Omega_p} (\mathcal{B}\mathbf{w})^{\mathrm{T}}\mathbf{e}^{\mathrm{T}}\boldsymbol{\nabla}\phi\,d\Omega = 0, \tag{5.16a}$$

$$\int_{\Omega_p} (\boldsymbol{\nabla}v)^{\mathrm{T}}\mathbf{e}\mathcal{B}\mathbf{u}_p\,d\Omega - \int_{\Omega_p} (\boldsymbol{\nabla}v)^{\mathrm{T}}\varepsilon^S\boldsymbol{\nabla}\phi\,d\Omega = 0, \tag{5.16b}$$

$$\forall \quad \mathbf{w} \in H^1_{\mathcal{B}}(\Omega_s \cup \Omega_p) \quad \text{and} \quad v \in H^1_{\nabla}(\Omega_p)$$

5.1.3 Semidiscrete spectral element formulation

The spectral element discretization of the weak formulation (see App. B.5) starts with meshing the physical domain Ω into small geometrically conforming n_{el} quadrilateral subdomains Ω_e, $e = 1, \cdots, n_{el}$ as in classical FEM. Each of these elements are subsequently mapped into the reference domain, defined in local system of coordinates (ξ, η) as a bi-unit square $\Pi = [-1, 1]^2$, using an invertible local mapping f, based on low degree Lagrange polynomials.

On the reference domain a set of basis functions is defined as Lagrange polynomials of degree 4 to 10 for the interpolation of functions. The $N + 1$ Lagrange polynomials $l_j^N(\xi)$, $j = 0, \ldots, N$ of degree N are defined in terms of $N + 1$ nodes $-1 \le \xi_j \le 1$, by

$$l_j^N(\xi) = \frac{q_N(\xi)}{(\xi - \xi_j)q'_N(\xi_j)}, \qquad q_N(\xi) = \prod_{j=0}^{N} (\xi - \xi_j) \tag{5.17}$$

The approximating function for displacement $u^e_N|_{\Omega_e}$ and electric potential $\phi^e_N|_{\Omega_e}$ used in the 2D case is:

$$\begin{aligned} u^e_N(\xi,\eta) &= \sum_{m=0}^{N}\sum_{n=0}^{N} u^e_{mn}(l^N_m(\xi)\otimes l^N_n(\eta)) = \mathbf{L}\mathbf{u}^e \\ \phi^e_N(\xi,\eta) &= \sum_{m=0}^{N}\sum_{n=0}^{N} \phi^e_{mn}(l^N_m(\xi)\otimes l^N_n(\eta)) = \mathbf{L}\boldsymbol{\phi}^e \end{aligned} \tag{5.18}$$

where, $\mathbf{u}^e$ and $\boldsymbol{\phi}^e$ are the vector of nodal values of the element's displacement and potential respectively; and $\mathbf{L}$ is the tensor product of the one dimensional Lagrange polynomials of degree N based on LGL nodes, which by definition equals one at the corresponding node and zero elsewhere (*i.e.* $l_m(\xi_i) = \delta_{mi}$).

On substitution of approximating functions in the weak form, we have the elements mass and stiffness matrices defined as:

$$\begin{aligned} \mathbf{M}^e_{u_s} &= \int_{\Omega_e} \rho_s \mathbf{L}^{\mathrm{T}}\mathbf{L}\, d\Omega, & \mathbf{M}^e_{u_p} &= \int_{\Omega_e} \rho_p \mathbf{L}^{\mathrm{T}}\mathbf{L}\, d\Omega, \\ \mathbf{K}^e_{u_s u_s,\, u_s\partial_g} &= \int_{\Omega_e} (\mathbf{B}^e)^{\mathrm{T}}\mathbf{c}_s\mathbf{B}^e\, d\Omega\,, & \mathbf{K}^e_{u_p u_p,\, u_p\partial_g} &= \int_{\Omega_e} (\mathbf{B}^e)^{\mathrm{T}}\mathbf{c}^E\mathbf{B}^e\, d\Omega, \\ \mathbf{K}^e_{u\phi} &= \int_{\Omega_e} (\mathbf{B}^e)^{\mathrm{T}}\mathbf{e}^{\mathrm{T}}\mathbf{Q}^e\, d\Omega \qquad \text{and} & \mathbf{K}^e_{\phi\phi} &= -\int_{\Omega_e} (\mathbf{Q}^e)^{\mathrm{T}}\boldsymbol{\varepsilon}^S\mathbf{Q}^e\, d\Omega \end{aligned} \tag{5.19}$$

where $\mathbf{B}^e$, and $\mathbf{Q}^e$ are defined as:

$$\mathbf{B}^e = \boldsymbol{\mathcal{B}}\otimes\mathbf{L} = \begin{pmatrix} \partial_{x_1}\mathbf{L} & \mathbf{0} \\ \mathbf{0} & \partial_{x_3}\mathbf{L} \\ \partial_{x_3}\mathbf{L} & \partial_{x_1}\mathbf{L} \end{pmatrix}, \qquad \mathbf{Q}^e = \boldsymbol{\nabla}\otimes\mathbf{L} = \begin{pmatrix} \partial_{x_1}\mathbf{L} \\ \\ \partial_{x_3}\mathbf{L} \end{pmatrix} \tag{5.20}$$

The integrals in the element matrices are evaluated numerically over each element. In SEM, a Legendre-Gauss-Lobatto (LGL) integration rule is used, because it leads to a diagonal mass matrix when used in conjunction with LGL interpolation points, a highly desirable advantage which allows for a very significant reduction in the computational cost, both in terms of code complexity and computation time. Numerical integration of $f(\mathbf{x})$ over elements is carried out as:

$$\int_{\Omega_e} f(\mathbf{x})\, d\Omega = \int_{\Pi} f(\mathbf{x}(\xi,\eta))\mathrm{J}(\xi,\eta)\, d\Omega = \sum_{\alpha,\beta=0}^{N,N} \omega_\alpha\omega_\beta f_{\alpha\beta}\mathrm{J}_{\alpha\beta} \tag{5.21}$$

where $\omega_\alpha > 0$, for $\alpha = 0,\ldots,N$, denote the weights of the LGL quadrature $\omega_i = 2/(N(N+1)P^2_N(\xi_i))$, and $\mathrm{J}_{\alpha\beta} = \mathrm{J}(\xi_\alpha,\eta_\beta)$ is the Jacobian of the mapping f. A polynomial of degree $\leq 2N-1$

is exactly integrated with $N+1$ nodes, using GL quadrature. Such a consistent integration scheme, *i.e.* the quadrature nodes are the same as the basis nodes, is shown to be sufficient for complex geometries [Maday and Rønquist, 1990].

Then the element matrices are assembled into the global coordinate system in a standard assembly procedure, and we finally end up with the global semidiscrete system:

$$\begin{pmatrix} \mathbf{M}_{u_s} & \mathbf{0} & \mathbf{0} & \mathbf{0} \\ \mathbf{0} & \mathbf{M}_{u_{\partial_g}} & \mathbf{0} & \mathbf{0} \\ \mathbf{0} & \mathbf{0} & \mathbf{M}_{u_p} & \mathbf{0} \\ \mathbf{0} & \mathbf{0} & \mathbf{0} & \mathbf{0} \end{pmatrix} \begin{pmatrix} \ddot{\mathbf{u}}_s \\ \ddot{\mathbf{u}}_{\partial_g} \\ \ddot{\mathbf{u}}_p \\ \ddot{\phi} \end{pmatrix} + \begin{pmatrix} \mathbf{K}_{u_s u_s} & \mathbf{K}_{u_s u_{\partial_g}} & \mathbf{0} & \mathbf{0} \\ \mathbf{K}^{\mathrm{T}}_{u_s u_{\partial_g}} & \mathbf{K}_{u_{\partial_g} u_{\partial_g}} & \mathbf{K}_{u_{\partial_g} u_p} & \mathbf{K}_{u_{\partial_g}\phi} \\ \mathbf{0} & \mathbf{K}^{\mathrm{T}}_{u_{\partial_g} u_p} & \mathbf{K}_{u_p u_p} & \mathbf{K}_{u_p \phi} \\ \mathbf{0} & \mathbf{K}^{\mathrm{T}}_{u_{\partial_g}\phi} & \mathbf{K}^{\mathrm{T}}_{u_p \phi} & \mathbf{K}_{\phi\phi} \end{pmatrix} \begin{pmatrix} \mathbf{u}_s \\ \mathbf{u}_{\partial_g} \\ \mathbf{u}_p \\ \phi \end{pmatrix} = \begin{pmatrix} \mathbf{0} \\ \mathbf{0} \\ \mathbf{0} \\ \mathbf{f_e} \end{pmatrix} \tag{5.22}$$

where the solution vector is split into $\mathbf{u}_s = (\mathbf{u}_1\ \mathbf{u}_3)^{\mathrm{T}}_s$ defined on $\Omega_s - \partial_g$, $\mathbf{u}_p = (\mathbf{u}_1\ \mathbf{u}_3)^{\mathrm{T}}_p$ defined on $\Omega_p - \partial_g$, $\mathbf{u}_{\partial_g} = (\mathbf{u}_1\ \mathbf{u}_3)^{\mathrm{T}}_{\partial_g}$ defined on ∂_g and ϕ defined over Ω_p, with $\mathbf{M}_{u_{\partial_g}}$ and $\mathbf{K}_{u_{\partial_g} u_{\partial_g}}$ taking contribution from both the PZT and the substructure element matrices. $\mathbf{f_e}$ is the contribution of the inhomogeneous Dirichlet electrical boundary condition representing the uniform excitation voltage. Eq. (5.22) could be written in partitioned form as:

$$\begin{pmatrix} \mathbf{M} & \mathbf{0} \\ \mathbf{0} & \mathbf{0} \end{pmatrix} \begin{pmatrix} \ddot{\mathbf{u}} \\ \ddot{\phi} \end{pmatrix} + \begin{pmatrix} \mathbf{K}_{uu} & \mathbf{K}_{u\phi} \\ \mathbf{K}^{\mathrm{T}}_{u\phi} & \mathbf{K}_{\phi\phi} \end{pmatrix} \begin{pmatrix} \mathbf{u} \\ \phi \end{pmatrix} = \begin{pmatrix} \mathbf{0} \\ \mathbf{f_e} \end{pmatrix} \tag{5.23}$$

Characteristic matrices of elements are aggregated to the global form in a fashion typical of the finite element method. Vectors of unknown displacements and electric potentials could theoretically be computed directly from Eqs. (5.23). However, for piezoelectric materials typical values of the matrix $\mathbf{K}^e_{uu}$ are of the order of 10^8, while those of the matrix $\mathbf{K}^e_{\phi\phi}$ are of the order of 10^{-11}. This huge difference in absolute values can lead to bad conditioning of the global system of equations, when considered as a whole. In order to overcome these difficulties one can perform matrix static condensation. In such a case Eqs. (5.23) are expressed in terms of displacements:

$$\mathbf{M}\ddot{\mathbf{u}} + (\mathbf{K}_{uu} - \mathbf{K}_{u\phi}\mathbf{K}^{-1}_{\phi\phi}\mathbf{K}^{\mathrm{T}}_{u\phi})\mathbf{u} = -\mathbf{K}_{u\phi}\mathbf{K}^{-1}_{\phi\phi}\mathbf{f_e} \quad \rightarrow \quad \mathbf{M}\ddot{\mathbf{U}} + \mathbf{K}\mathbf{U} = \mathbf{F} \tag{5.24}$$

Which almost recovers the classical form of matrix SEM/FEM equations.

5.2 Formulation: boundary effects

One of the complicating factors in numerical simulation of guided waves propagation is the presence of reflecting boundaries of the computational domain. This complicates the understanding of wave propagation characteristics in general, this becomes particularly true for Lamb waves due

to the mode conversion at the reflecting boundaries. This limits the ability to draw conclusions about the mode tuning behavior of a specific actuator-structure assembly. For that reason, in order to be able to eliminate the reflections from the boundaries, an absorbing layer with increasing damping was developed and implemented in the present work. The details of the developments and implementation are described in this section.

There are different types of damping that could be used. The two major categories are the structural damping and the viscous damping. In the structural damping the damping force is assumed to be proportional to the displacement:

$$\mathbf{M}\ddot{\mathbf{U}} + (\mathbf{K}+i\mathbf{H})\mathbf{U} = \mathbf{F} \tag{5.25}$$

were $\mathbf{H}$ represents the damping force. Viscous type damping can be used whatever the form of the excitation. The most common form of such damping is the so-called Rayleigh-type or proportional damping. In which the damping force is proportional to the particle velocity.

$$\mathbf{M}\ddot{\mathbf{U}} + \mathbf{C}\dot{\mathbf{U}} + \mathbf{K}\mathbf{U} = \mathbf{F} \tag{5.26}$$

$$\mathbf{C} = \alpha\mathbf{M} + \beta\mathbf{K} \tag{5.27}$$

In order to extract the amplitudes correctly while being faithful to the energy division between the two fundamental propagating modes, an absorbing layer with gradually increasing damping is added at the free edge of the plate. The absorbing layer used in the present study is a combination of two concepts proposed earlier in the literature.

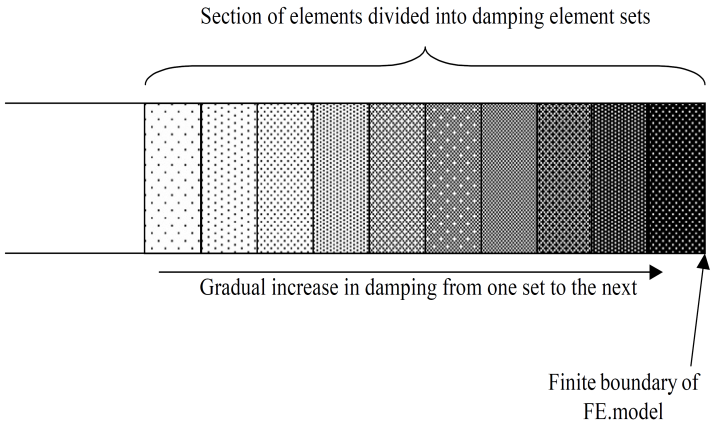

Figure 5.3 Artificial damping boundary section used by [Liu and Quek, 2003a].

The first one was that that proposed by [Liu and Quek, 2003a], where they introduced an exponentially increased damping coefficient. Where in order to create an artificial boundary to damp down the oscillations, They introduced a section of elements near the finite boundary that is being divided into n element sets as shown in Fig. 5.3. The damping coefficient and hence the damping force defined for each of these sets are gradually increased from the inner most set to the set next to the finite boundary.

While they used a gradual increase in damping force, Young's modulus was defined for the kth element set to be exponentially dependent on the set number:

$$E_k = E + i\alpha_o \xi^k E, \qquad k = 0, 1, 2, \cdots, n-1 \tag{5.28}$$

where α_o is the initial material loss factor for the artificial damping layer and ξ is a constant factor, and the damping model they used was a structural damping, (*i.e.* the damping was proportional to the displacement rather than to the particle velocity as in viscous damping). However, their procedure for insuring the absence of reflection is not sufficient for the case of guided waves because the way they used to verify the efficacy of the damping is iterative in nature (trial and error) where they increase the value of ξ, till the responses obtained for two (or more) cases of different boundary conditions at the ends show no significant differences. This is based on the concept that the damping has done its job such that the effects of the boundary are no longer significant.

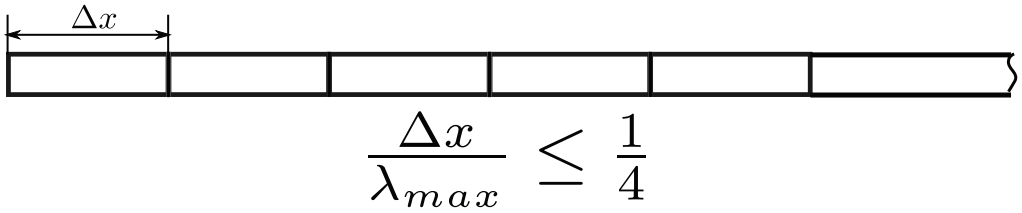

Figure 5.4 Sampling points for the frequency response, total of 512 equally spaced points for the reflection coefficient computation via a wavenumber transform.

The second concept was that of providing a less sharp change in the damping coefficient in order to avoid a high impedance mismatch. And it employs a viscous damping scheme, this concept was first introduced by [Drozdz *et al.*, 2007, 2006], and developed further by [Ke *et al.*, 2009].

The definition of the damping layer material properties are for purely elastic material defined as:

$$E^{AL} = E(1 - D(r)) + i(ED(r)) \tag{5.29}$$

$$\rho^{AL} = \frac{\rho}{(1 - D(r) + iD(r)} \tag{5.30}$$

$$D(r) = \left(\frac{r}{L_{ABS}}\right)^3 \tag{5.31}$$

where E and ρ are the material properties of the plate, and E^{AL}, ρ^{AL} is the variable Young's modulus and density of the absorbing layer, respectively. r represents the distance away from the interface separating the plate edge and damping layer of length L_{ABS}. Upon reformulating it into the proportional damping coefficients, we have for the k^{th} layer:

$$E_k^{AL} = E(1 - D) \tag{5.32}$$

$$\alpha_k = \frac{D}{1 - D} \tag{5.33}$$

$$\beta_k = \alpha_k \tag{5.34}$$

$$\rho_k^{AL} = \rho\frac{1 - d}{(1 - D)^2 + d^2} \tag{5.35}$$

This damping layer is assumed to be efficient when its length is equal to or greater than 1.5 of the maximum wavelength.

The problem with this layer formulation is that its damping is dependent on the frequency and that introducing a large mass proportional damping may introduce a large inertial effect into the system. They also used a similar technique to the one used by [Liu and Quek, 2003a] for checking for the absence of reflection.

The more accurate way to test for the absence of the reflection and is the one adopted in the present study is to record the displacement at equally spaced distances and perform a wavenumber transform on the frequency response [Alleyne and Cawley, 1990]. As depicted in Fig. 5.5(a) the reflected peaks will be located at the negative wavenumber side since it is propagating in the reverse direction while the incident peaks are located in the positive wavenumber region. But on implementation of the proposed damping layer by [Drozdz, 2008; Ke *et al.*, 2009] the frequency dependent viscous damping was not sufficient to damp all the reflections as plotted in Fig. 5.5(a).

The theoretical reflection coefficient for Eqs. (5.35) was computed for each mode separately:

$$A = \frac{Z_2 - Z_1}{(Z_2 + Z_1)^2} \tag{5.36}$$

$$Z = \rho^{AL} C^{AL}_{S0\|A0} \tag{5.37}$$

where the C_{S0}^{AL} or C_{A0}^{AL} is the phase speed of S0 and A0 modes, respectively, for each damping layer. Where the dispersion relation is solved numerically with the modified properties of the damping layer, and Z_2, Z_1 are acoustic impedance of two consecutive layers.

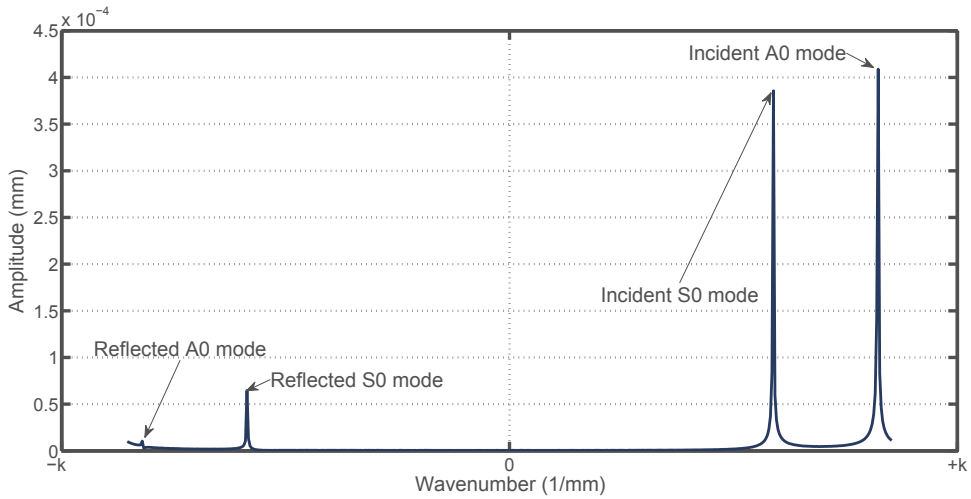

(a) Wavenumber tranform for 50 kHz with [Ke *et al.*, 2009] damping layer for the u_1 response

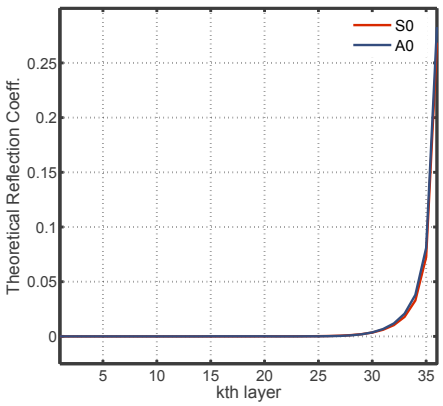

(b) Theoretical reflection coefficient for the cubic law damping variation

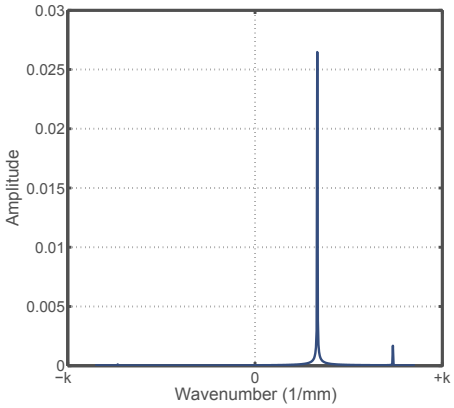

(c) An example of the reflection analysis for the modified cubic law damping variation adopted in the present study, at 175 kHz

Figure 5.5 The reflection analysis for checking the efficiency of the damping layer for multi-modal propagation. The different reflections for cubic law variation of damping in the ALID

Figure 5.5(b) shows the variation of the theoretical reflection coefficient with the number of damping layer at 50 kHz. This may explain the noticable reflection of the longer wavelength mode that was noticed in Fig. 5.5(a). The damping layer adopted in the present study are based on the combined definition of the structural damping that is proposed by [Liu and Quek, 2003a]

and the spatial variation according to the third order equation proposed by [Ke *et al.*, 2009]. The total number of damping layers used was 36 sets of elements, and the density was held constant. The length of the damping layer was 1.5 times the maximum wavelength.

As for the PML implemented in commercial finite element software, ANSYS [Ansys Inc., 2011] provide an implementation of PML in one and three dimensional frequency domain only. The same goes for COMSOL Multiphysics. ABAQUS in addition to the PML provide an implementation of infinite elements that provide a radiation boundary condition. The current proposed damping layer have an advantage that it could be implemented in both the time domain and frequency domain since it is only a gradual increase in the attenuation via location dependent material properties.

The k^{th} set of elements properties were taken as:

$$E_k^{AL} = E(1 - D) \tag{5.38}$$

$$\xi^k = D \tag{5.39}$$

were ξ^k is the percentage of the critical damping in the kth layer. The efficacy of this damping layer are tested for each frequency using the wavenumber transform. An exemplary result of such an analysis is depicted in Fig. 5.5(c). Throughout a frequency range of 50 kHz to 800 kHz, with steps of 25 kHz, the maximum reflection never exceeded 0.01.

5.3 Actuator thickness effect

In the following sections a parametric study of the effect of the thickness of PZT element fully coupled is compared with the pin force model. The first section includes the results of the harmonic analysis, both forced response and normal modes analysis for a bounded plate, *i.e.* includes the reflection from the edges of of the plate. The second section includes the forced response simulation results with the absorbing layer with increased damping (AIDL) in the form of the mode tuning curves extracted from the results of the forced frequency response.

Table 5.1 Material properties used in the parametric study of the PZT thickness effect

Component	Property	Value
Aluminum Plate	Length	1.0 m
	Thickness	$1 \times 10^{-}3$ m
	Young's modulus	67.5 GPa
	Density	2700 kg/m^3
	Poisson's ratio	0.35
PZT Element	Diameter	$10 \times 10^{-}3$ m
	Thickness	$0.25, 0.5,$ and $1 \times 10^{-}3$ m
	Density	7650 kg/m^3
	Piezoelectric type	PZT-5H
	d_{31}	-2.74 $\times 10^{-10}$ (m/V)
	d_{33}	5.93 $\times 10^{-10}$ (m/V)
	d_{15}	7.41 $\times 10^{-10}$ (m/V)
	ϵ_{11}	1704 $\times \epsilon_o$ (F/m)
	ϵ_{22}	1433 $\times \epsilon_o$ (F/m)
	ϵ_{33}	1704 $\times \epsilon_o$ (F/m)
	S_{11}	1.65 $\times 10^{-11}$ (m^2/N)
	S_{12}	-4.78 $\times 10^{-12}$ (m^2/N)
	S_{13}	-8.45 $\times 10^{-12}$ (m^2/N)
	S_{33}	2.07 $\times 10^{-11}$ (m^2/N)

5.3.1 Harmonic analysis

The steady state response can also be obtained by solving the harmonic excitation in Eq. (5.24):

$$\mathbf{M}\ddot{\mathbf{U}} + \mathbf{K}\mathbf{U} = \mathbf{F}e^{i\omega t} \tag{5.40}$$

directly. This has the advantage that the frequencies and modes of free vibration of the undamped system do not have to be calculated prior to the response analysis. Assuming that the steady state response is harmonic with frequency ω gives

$$[\mathbf{K} - \omega^2\mathbf{M}]\mathbf{U} = \mathbf{F}e^{i\omega t} \tag{5.41}$$

The solution of this equation is

$$\mathbf{U} = [\mathbf{K} - \omega^2\mathbf{M}]^{-1}\mathbf{F}e^{i\omega t} \tag{5.42}$$

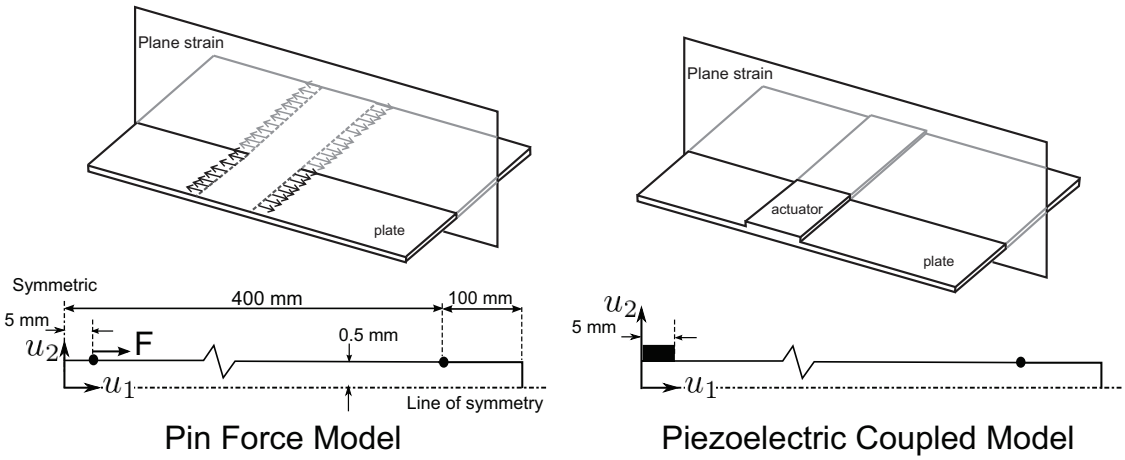

Figure 5.6 Illustration of the pin force model and the coupled piezoelectric model used in the present study.

In this section, we will explore the effect of the PZT thickness, and compare it with the pin force model with equivalent loading as illustrated in Fig. 5.6. The material properties used in the analysis is listed in table 5.1. The plate section and the actuator are both assumed to be in the plane strain, purely elastic materials with no losses for both the plate and the actuator was assumed. The plate was loaded symmetrically by pin forces with the line of symmetry that divides the plate thickness into two equal halves.

The equivalent pin force loading to was computed according to [Banks *et al.*, 1996]:

$$F = \frac{-E_{pzt}h_{pzt}d_{31}}{1-\nu_{pzt}}v_{pzt} \tag{5.43}$$

where E_{pzt} and ν_{pzt} are the elastic modulus and Poisson's ration of the piezoceramic material, respectively, d_{31} the coupling coefficient, h_{pzt} is the thickness, and v_{pzt} is the applied voltage. The mesh used for the forced response were one element ($p = 6$) per thickness of the plate and piezoelectric, and 1 mm long in the length direction.

The forced frequency response using pin forces is shown in Figs. 5.7(a) and 5.7(b) in the u_1 direction since the symmetric loading makes the steady state displacement dominant in the u_1 direction. Figures 5.8(a) and 5.8(b) show the results of the harmonic forced response at the same point in the u_1 direction for 10 V electric excitation for a 0.5 mm thickness piezoceramic element.

The loading was symmetrically applied by two identical piezoceramic elements on the upper and lower surface of the plate.

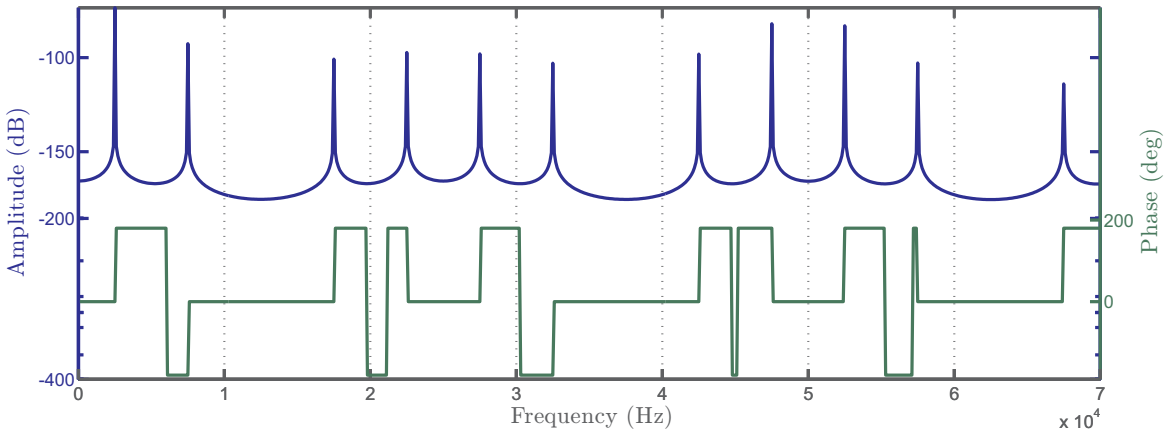

(a) Frequency Response of u_1 at 400 mm distance pin force model, for frequency range 100 Hz-70 kHz

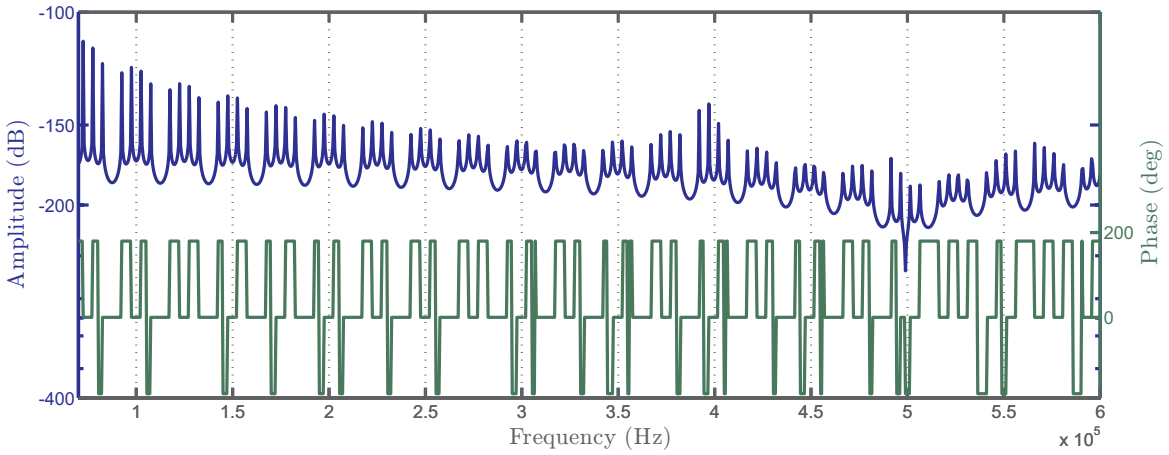

(b) Frequency Response of u_1 at 400 mm distance pin force model, for frequency range 70 kHz-600 kHz

Figure 5.7 Frequency Response of u_1 at 400 mm distance from the plate center, pin force model, and separation of forces was 10 mm.

In Figs. 5.10(a) and 5.10(b) a comparison between the two predicted frequency response to both pin force and a coupled PZT element with 0.5 mm thickness. The shift in resonance frequencies toward higher frequency for the case of the PZT coupled plate may be attributed to the change in modal behavior due to the presence of the PZT. The effect is purely mechanical due to the change in the mechanical normal modes of vibration. To test this hypothesis, a normal mode analysis for the range shown in figure is performed and the results of the modal analysis for the same mesh

that was used for the harmonic response analysis is listed in Table 5.2. Showing that the mere mechanical coupling of the PZT is enough to make this shift in resonance frequencies.

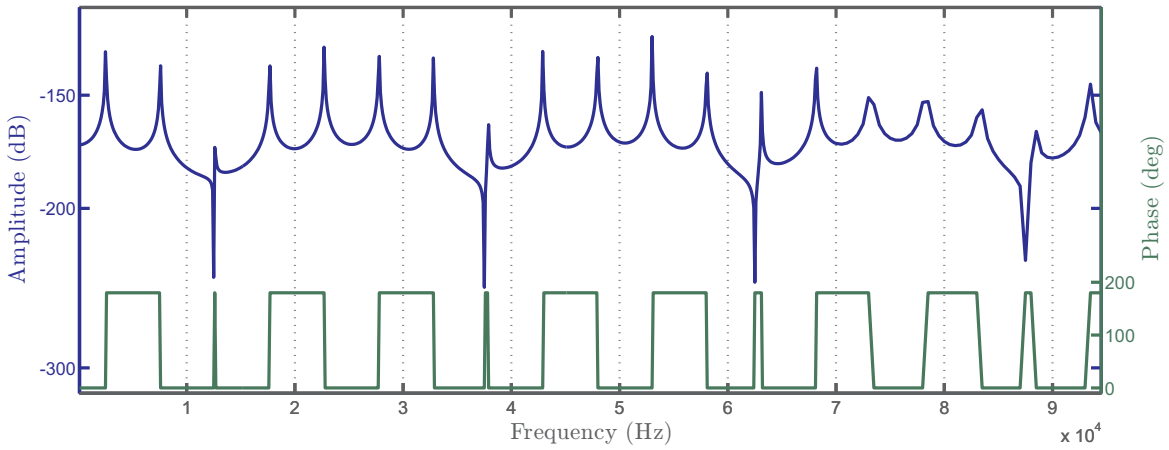

(a) Frequency Response of u_1 at 400 mm distance from the PZT actuator center, for frequency range 100Hz-94.5 kHz

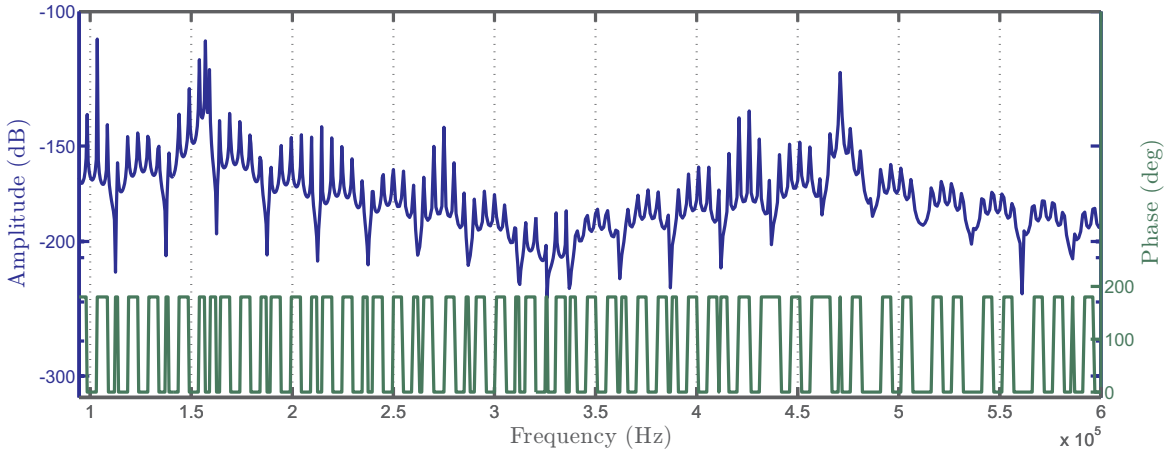

(b) Frequency Response of u_1 at 400 mm distance from the PZT actuator center, for frequency range 94.5 kHz-600 kHz

Figure 5.8 Frequency Response of u_1 at 400 mm distance from the PZT actuator center, PZT thickness is 0.5 mm, and the diameter of the actuator was 10 mm.

Table 5.2 Normal modes frequencies for the range 16600-76000 Hz

Mode	Pin Force (Hz)	PZT Coupled (Hz)	Mode	Pin Force (Hz)	PZT Coupled (Hz)
1	17500	17584	7	47500	47717
2	22500	22607	8	52500	52736
3	27500	27631	9	57500	57755
4	32500	32653	10	62499	62772
5	37500	37675	11	67499	67788
6	42500	42696	12	72498	72802

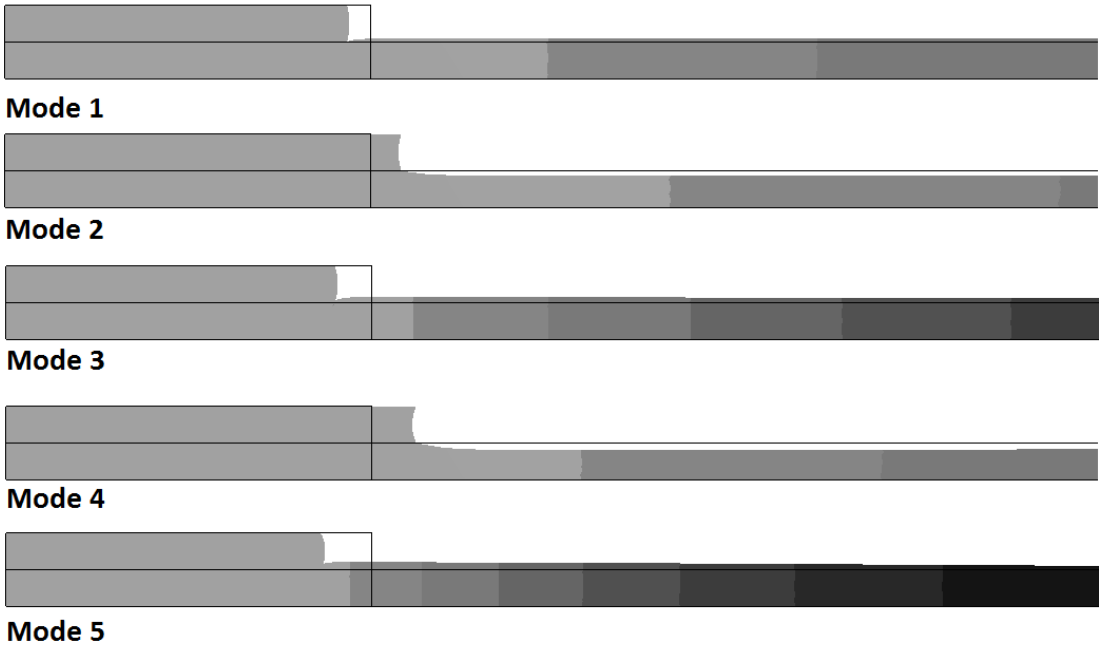

Figure 5.9 The first five Mode shapes in the frequency range 16.6-76 kHz. Considering the symmetry half the domain in both x_1 and x_3 is only plotted.

Figure 5.9 plots the first five free modes with symmetric placement of the actuator.

Table 5.3 Normal modes frequencies for the range 76000-285000 Hz

Mode	Pin Force (Hz)	PZT Coupled (Hz)	Mode	Pin Force (Hz)	PZT Coupled (Hz)
1	77498	77814	22	1.82E+05	1.82E+05
2	82497	82824	23	1.87E+05	1.87E+05
3	87496	87832	24	1.92E+05	1.91E+05
4	92495	92837	25	1.97E+05	1.96E+05
5	97494	97839	26	2.02E+05	2.01E+05
6	1.02E+05	1.03E+05	27	2.07E+05	2.06E+05
7	1.07E+05	1.08E+05	28	2.12E+05	2.11E+05
8	1.12E+05	1.13E+05	29	2.17E+05	2.16E+05
9	1.17E+05	1.18E+05	30	2.22E+05	2.21E+05
10	1.22E+05	1.23E+05	31	2.27E+05	2.26E+05
11	1.27E+05	1.28E+05	32	2.32E+05	2.31E+05
12	1.32E+05	1.33E+05	33	2.37E+05	2.36E+05
13	1.37E+05	1.38E+05	34	2.42E+05	2.41E+05
14	1.42E+05	1.43E+05	35	2.47E+05	2.46E+05
15	1.47E+05	1.48E+05	36	2.52E+05	2.51E+05
16	1.52E+05	1.52E+05	37	2.57E+05	2.56E+05
17	1.57E+05	1.57E+05	38	2.62E+05	2.61E+05
18	1.62E+05	1.62E+05	39	2.67E+05	2.66E+05
19	1.67E+05	1.67E+05	40	2.72E+05	2.70E+05
20	1.72E+05	1.72E+05	41	2.77E+05	2.75E+05
21	1.77E+05	1.77E+05	42	2.82E+05	2.80E+05

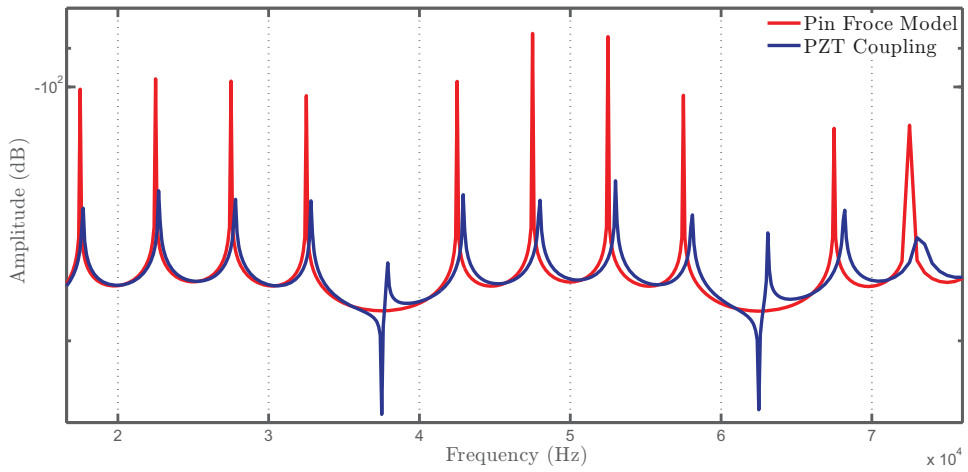

(a) Frequency Response of u_1 at 400 mm distance from the PZT actuator center, for frequency range 16.6 kHz-76 kHz

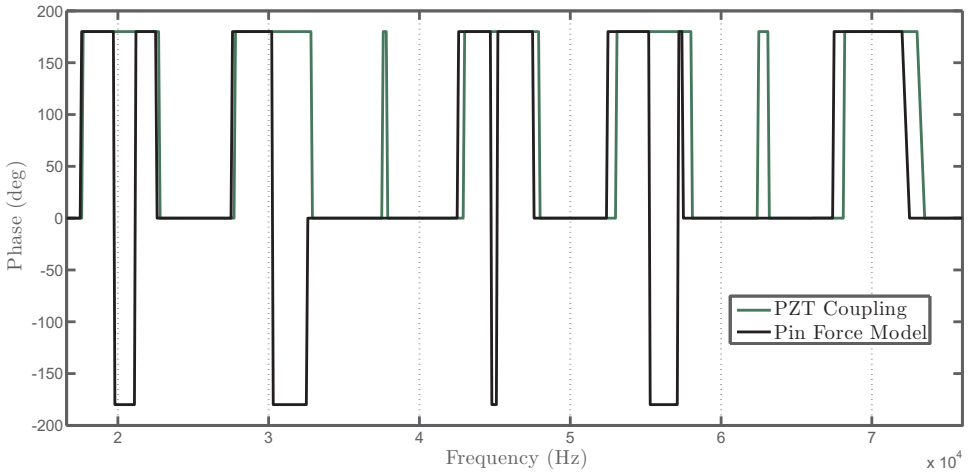

(b) Phase Response of u_1 at 400 mm distance from the PZT actuator center, for frequency range 16.6 kHz-76 kHz

Figure 5.10 Comparison of Pin Force model frequency response and the PZT coupled plate.

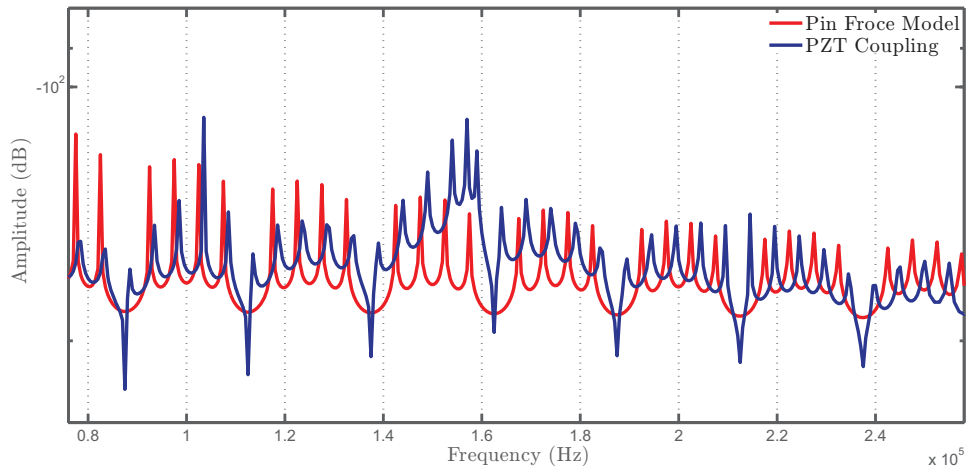

(a) Frequency Response of u_1 at 400 mm distance from the PZT actuator center, for frequency range 76 kHz-285 kHz

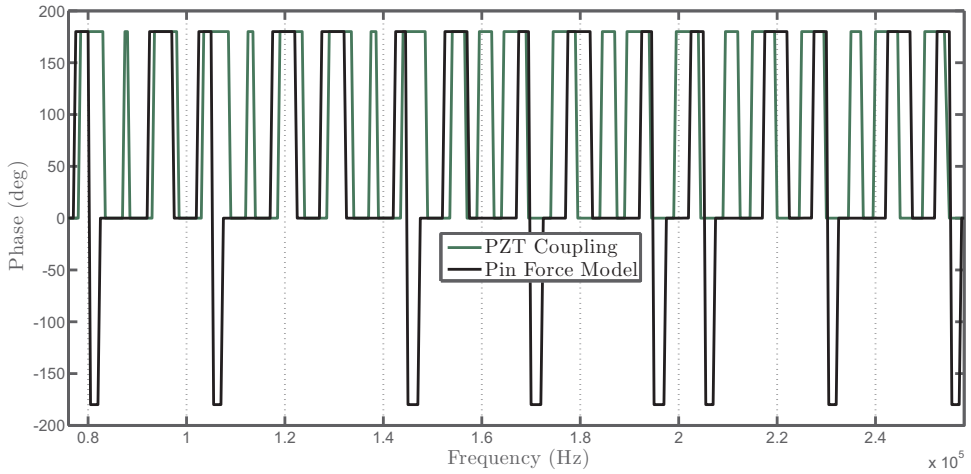

(b) Phase Response of u_1 at 400 mm distance from the PZT actuator center, for frequency range 76 kHz-285 kHz

Figure 5.11 Comparison of Pin Force model frequency response and the PZT coupled plate.

5.3.2 Simulation results

For the modal amplitude extraction, the harmonic displacement components was recorded on both the upper u_x^U, u_y^U and lower surface u_x^L, u_y^L of the plate at the same x value, then this is followed by inverting the matrix of coefficients in the Lamb waves displacement expressions in

Eqs. (4.15).

$$\begin{pmatrix} B \\ \mathbf{C} \\ A \\ \mathbf{D} \end{pmatrix} = \begin{pmatrix} ik_{S0}\cos(\frac{h}{2}\alpha_{S0}) & i\beta_{S0}\cos(\frac{h}{2}\beta_{S0}) & ik_{A0}\sin(\frac{h}{2}\alpha_{A0}) & -i\beta_{A0}\sin(\frac{h}{2}\beta_{A0}) \\ ik_{S0}\cos(-\frac{h}{2}\alpha_{S0}) & i\beta_{S0}\cos(-\frac{h}{2}\beta_{S0}) & ik_{A0}\sin(-\frac{h}{2}\alpha_{A0}) & -i\beta_{A0}\sin(-\frac{h}{2}\beta_{A0}) \\ \alpha_{S0}\sin(\frac{h}{2}\alpha_{S0}) & k_{S0}\sin(\frac{h}{2}\beta_{S0}) & \alpha_{A0}\cos(\frac{h}{2}\alpha_{A0}) & k_{A0}\cos(\frac{h}{2}\beta_{A0}) \\ \alpha_{S0}\sin(-\frac{h}{2}\alpha_{S0}) & k_{S0}\sin(-\frac{h}{2}\beta_{S0}) & \alpha_{A0}\cos(-\frac{h}{2}\alpha_{A0}) & k_{A0}\cos(-\frac{h}{2}\beta_{A0}) \end{pmatrix}^{-1} \begin{pmatrix} u_x^U \\ u_x^L \\ u_y^U \\ u_y^L \end{pmatrix} \quad (5.44)$$

The analysis was done for a 1 m long plate with the same properties as listed in Table 5.1, the mesh used was based on the results of the last chapter with 6 points per wavelength and polynomial degree 8 spectral element, and two elements per the thickness of the plate. The PZT thickness was varied through three values, 0.5 mm, 0.75 mm and 1 mm. The frequency range (50 kHz-800 kHz) was swept with 25 kHz steps. The loading was not symmetrical, only one PZT was bonded to the upper surface of the plate and the harmonic displacement responses were extracted at 580 mm away from the center of a 10 mm long PZT.

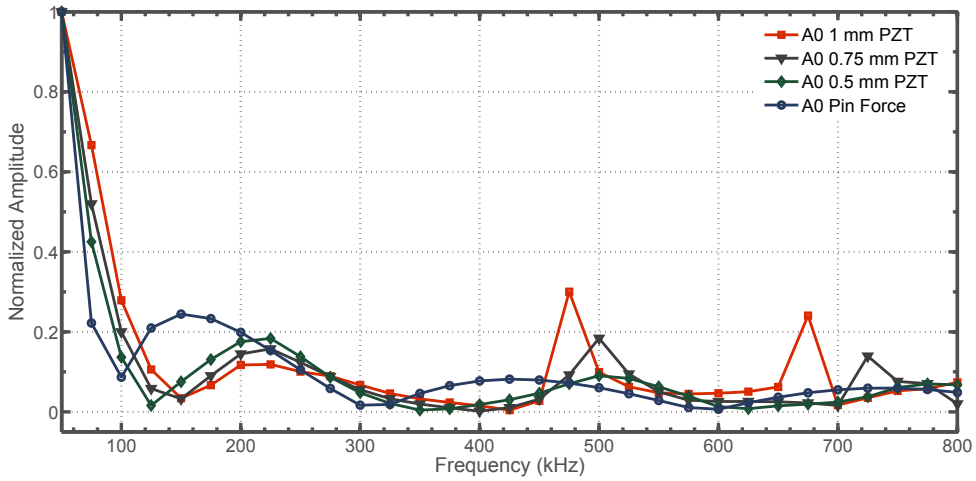

Figure 5.12 A comparison of the different A0 modal amplitudes with varying thickness of the actuator PZT element.

Figure 5.12 shows the normalized displacement amplitudes of the A0 at a distance 580 mm from the center of the plate. Figure 5.14 shows the normalized S0 amplitudes, the normalization was done for each thickness separately, so the ratio between the S0 and A0 amplitudes are preserved.

The main observed effect of increasing the thickness of the PZT element, is the appearance of new resonance like peaks when comparing the strongly coupled PZT with the pin force model.

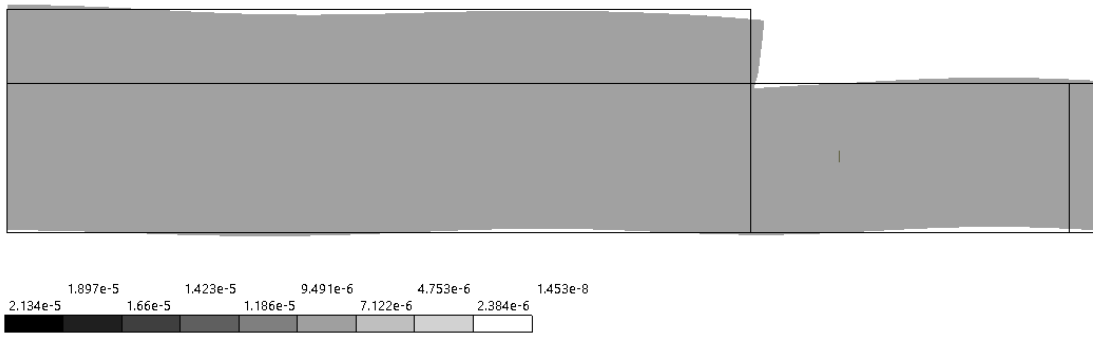

(a) 0.5 mm Thick PZT - 475 kHz

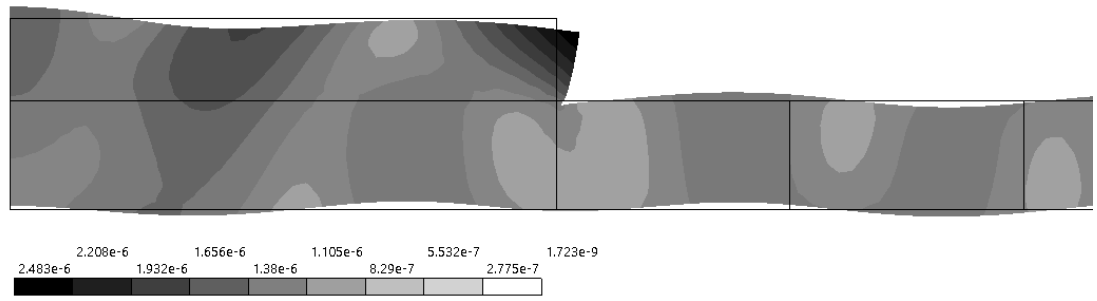

(b) 0.75 mm Thick PZT - 475 kHz

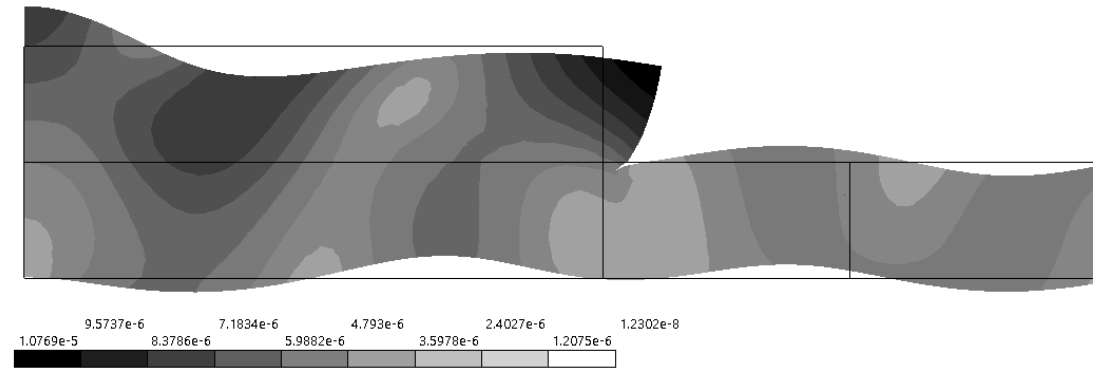

(c) 1 mm Thick PZT - 475 kHz

Figure 5.13 Mode Shapes at 475 kHz for the three thickness values of actuator. Considering the symmetry half the domain in x_1 direction is only plotted.

Figure 5.13 shows the shapes of the actuator and the attached plate at 475 kHz for the different thicknesses of the actuator plotted with visually with the same scale. The variation of the actuation mode is reflected in the different contour values and the their distribution across the domains. The 1 mm thick clearly, have a higher amplitude excitation, with a higher energy transfer to the

plate. This supports the interpretation that the frequency peak observed in Fig.5.12 is attributed to the resonance behavior of the actuator.

For A0 mode plotted in Fig. 5.12 the first maximum amplitude of the pin force model occurs at 150 kHz, while for the three PZT thicknesses they are collocated, it occurs at 225 kHz. A similar shift toward higher frequencies are also observable at second maximum frequency, 425 kHz for pin force, 500 kHz for 0.5 mm PZT and 0.75 mm PZT, while the shift is smaller with respect to frequency for the 1 mm PZT where the maximum is located at 475 kHz. The amplitude also gets more resonance like as the thickness of the actuator PZT increases. Similar behavior is noticed at the third peak located at 725 kHz for 0.75 mm Thick PZT and 625 kHz for the 1 mm thick PZT, while no similar peak is evident for the 0.5 mm thick PZT.

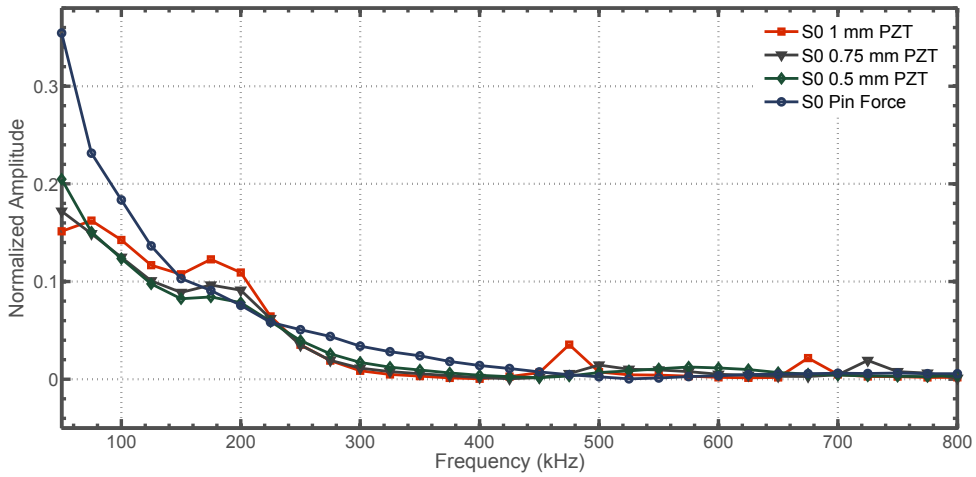

Figure 5.14 A comparison of the different S0 Modal amplitudes with varying thickness of the actuator PZT element.

Figure 5.14 plots the amplitudes of S0 mode for the same results. The amplitudes were normalized with respect to the maximum of the associated A0 mode. The first noticeable observation is the appearance of peaking behavior at 175 kHz that is totally absent from the pin force amplitude, and as the thickness of the PZT increases the amplitude of that peak increases.

Similar behavior are witnessed at other peak frequencies, with a trend to getting sharper in a resonance like manner as the PZT thickness increases as could be observed at 475 kHz for 1 mm PZT, and 500 kHz for 0.75 mm PZT.

As the thickness of the PZT increases from the 0 mm (pin force) to the 1 mm there is a change in both the number and location of maxima with respect to the frequency. This type of curve is

typically used in mode tuning for a specific mode. The idea is to find the frequency corresponding to the maximum amplitude of a specific mode, and use that frequency for SHM purposes.

The shown change in behavior when considering the strongly coupled PZT actuator indicates a change in the mode of actuation as well as a contribution coming form the extra stiffening of the plate by the presence of the ceramic PZT itself. In order to test this hypothesis, a similar frequency sweep were run for the plate with the existing ceramic PZT but without the electric degrees of freedom and with the actuation as pin force. The thickness of the ceramic was 0.75 mm. The results of the pin force actuation with and without the ceramic PZT (mechanical only) is shown in Fig. 5.15.

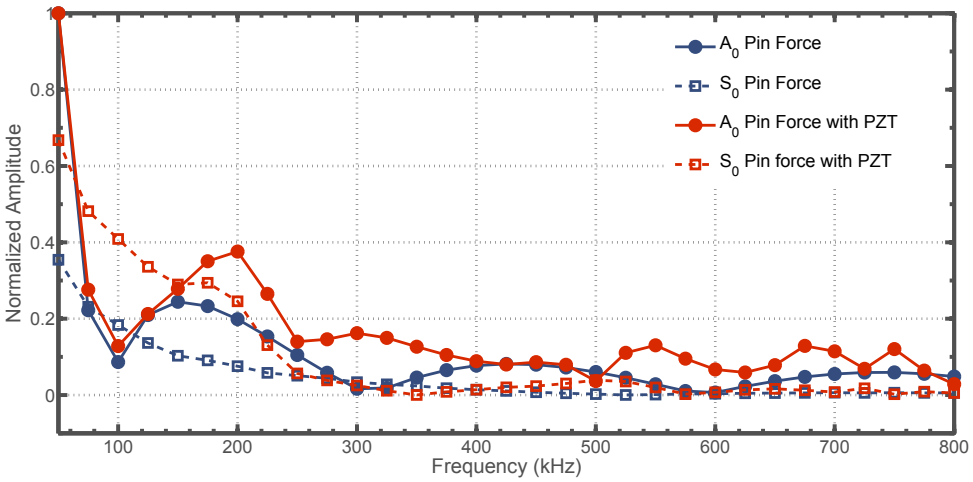

Figure 5.15 The mechanical coupling effect on the pin force mode tuning curves

Considering the A0 alone in Fig. 5.15, it may be observed that there is a shift of the maximum amplitude located at 150 kHz for the pin force toward a higher frequency (200 kHz) only due to the existence of the ceramic stiffener (PZT element) when considered only mechanically coupled and the electrical degrees of freedom are not considered. Another noticeable resonance like peaks at 550 kHz, 675 kHz, and 750 kHz are completely absent for the Pin force loading. As for the S0 amplitudes, the most salient observation is the start of peak in amplitude at 175 kHz, while for the pin force model the amplitude decrease smoothly as would be predicted theoretically. A similar peak is noticed at 500 kHz, while the comparable peak in amplitude for the pin force model is located at 425 kHz. So an important contribution to both the shift in maxima and the appearance of new resonance like peaks could be due to mechanical coupling alone, which are typically ignored for simplification reasons in analytical modeling of the actuation.

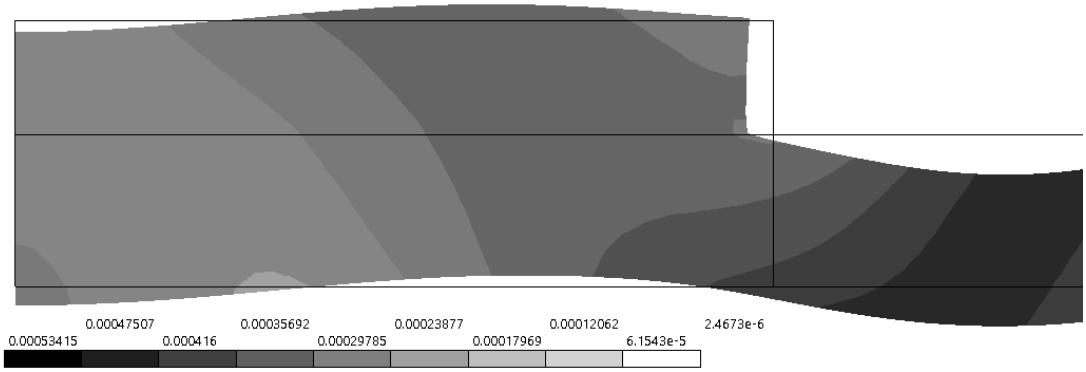

(a) Pin force model with 0.75 mm Thick PZT mechanically coupled only- no electrical degree of Freedom

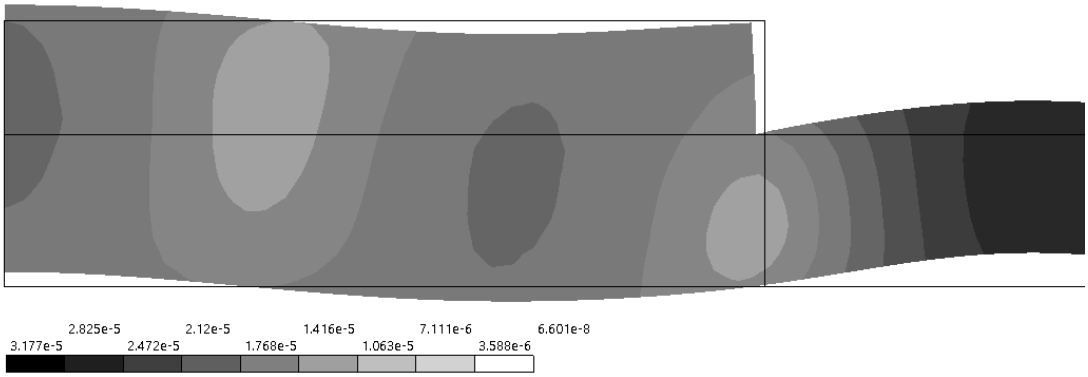

(b) 0.75 mm Thick PZT fully coupled

Figure 5.16 Mode Shapes at 200 kHz for the pin force model with and without the mechanical coupling of the actuator. Considering the symmetry in x_1 direction half the domain is only plotted.

Figure 5.16 shows the actuator modes at 200 kHz for both the pin force model with mechanically coupled PZT ceramic, and the fully coupled piezoelectric actuator.

In order to quantify the change in the mode of actuation, shear stress distribution are extracted at different frequencies at the interface between the PZT and the plate.

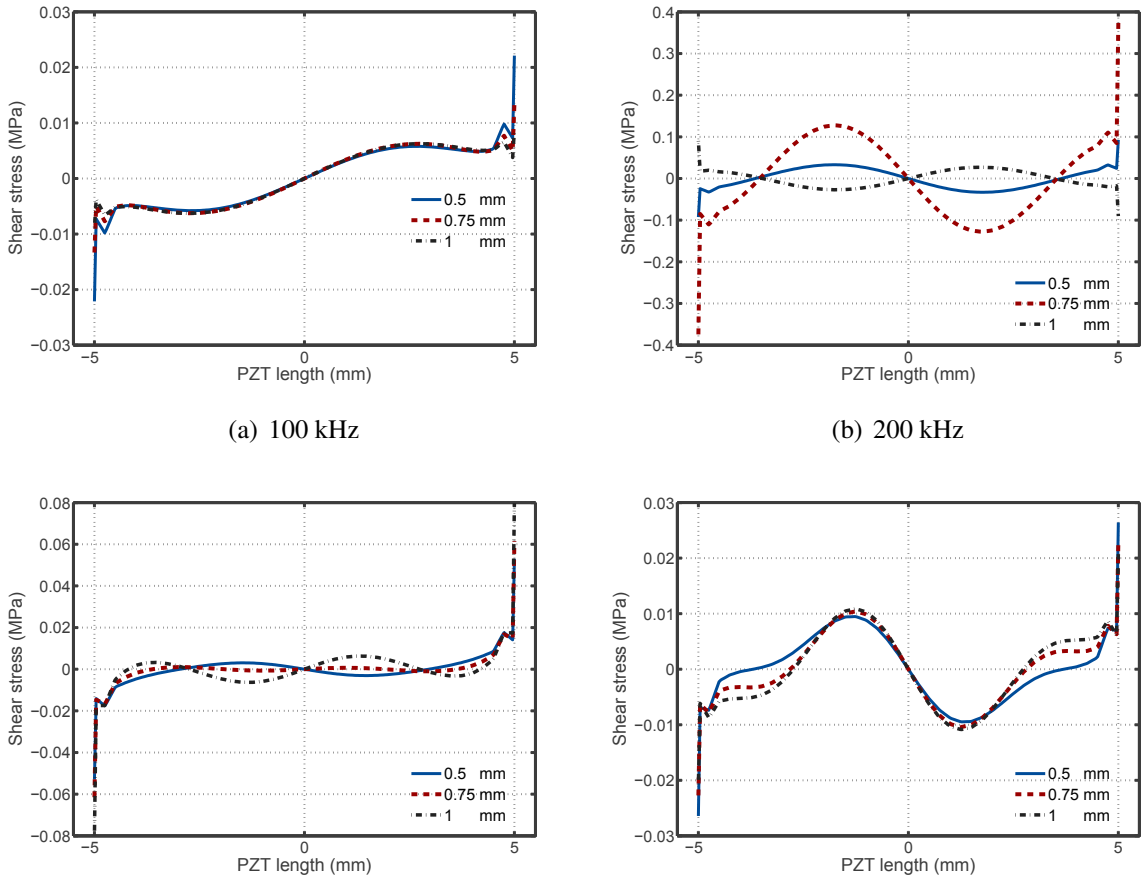

(a) 100 kHz

(b) 200 kHz

(c) 300 kHz

(d) 400 kHz

Figure 5.17 Shear stress distribution at the interface of an ideally bonded PZT with the aluminum plate at various frequencies, with the three PZT thicknesses studied.

Figure 5.17 shows the shear stress distribution at the interface between the plate and the PZT element, extracted form the SEM simulations, with the three thicknesses studied for different frequencies. The change in the overall trend as the frequency increases reflects the changes in actuation mode. The first observation is that as frequency of excitation increases, the shear stress distribution changes from sharp localization at the edges of the PZT and almost constant low value under the PZT at low frequency (100 kHz) to a more periodic variation with increasing number of cycles as the frequency increases (200kHz). The actuation mode is witnessing a more abrupt change between frequency 300 kHz and 400 kHz, probably due to electromechanical resonance. This reinforces the hypothesized change in mode of actuation as being one of the two major reasons for the mode tuning shifts when compared to the pin force model and the appearance of the resonance like energy transfer and accordingly the change in the energy partitioning between the two excited fundamental modes of Lamb wave propagation.

In Fig. 5.17(b), the shear stress at the PZT-plate interface is plotted for the three different values of the PZT thickness used in the present parametric study. The frequency is relevant to the mode tuning curve for the S0 mode where there is a salient discrepancy between the pin force tuning curve and the fully coupled PZT analysis shown in Fig. 5.14. The changes in the shear stress pattern reveals the inadequacy of the quasi-static assumptions underlying the pin force model. Even with a similar shear distribution, the traction forces could barely be considered localized at the edges of the PZT. The periodic shape with one cycle per length of the PZT is apparent. The amplitude of the period changes with the thickness but the overall patterns remains the same under the three thicknesses.

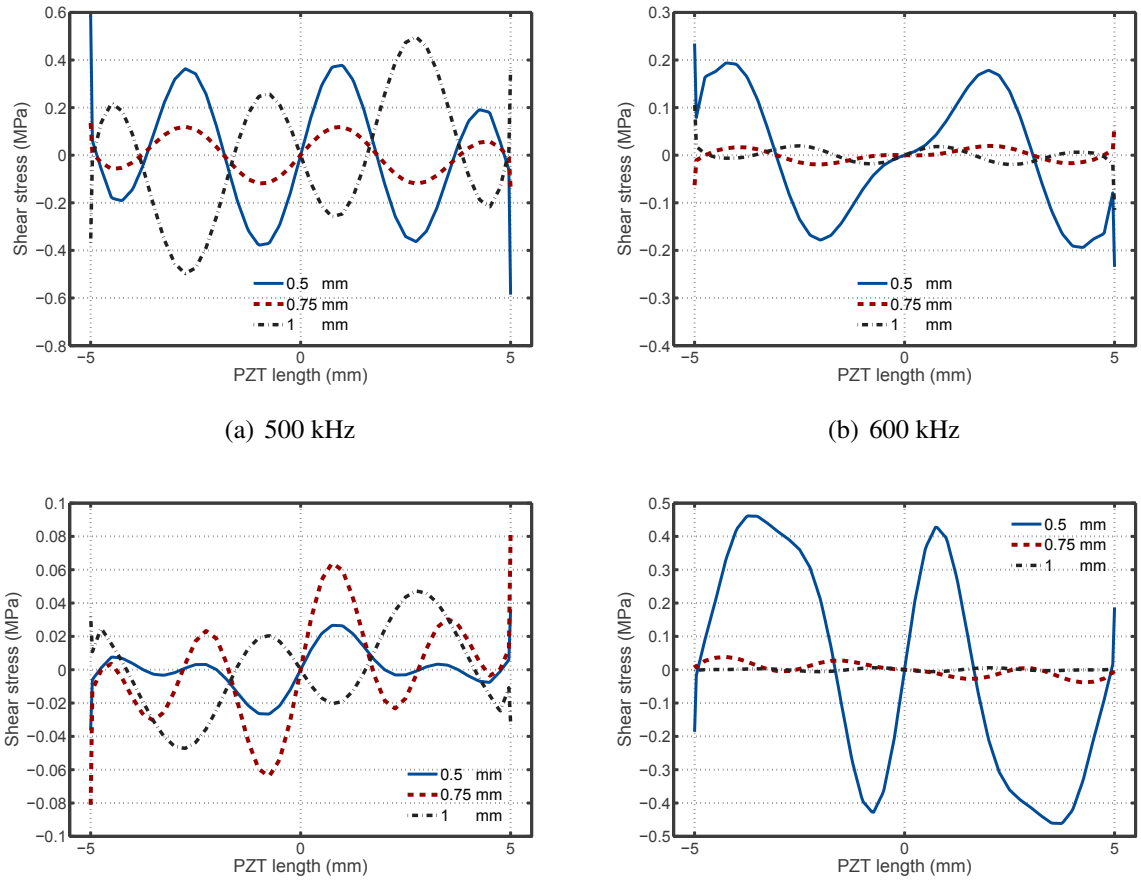

(a) 500 kHz

(b) 600 kHz

(c) 700 kHz

(d) 800 kHz

Figure 5.18 Shear stress distribution at the interface of an ideally bonded PZT with the aluminum plate at various frequencies, with the three PZT thicknesses studied.

Figure 5.18 shows the shear stress distribution at higher frequency range. The number of cycles in the periodic behavior is increased when compared with the frequency range plotted in Fig. 5.17. At 500 kHz plotted in Fig. 5.18(a) the 0.5 mm PZT reveals resonance like behavior, similarly at

700 kHz shown in Fig.5.18(c) the 0.75 mm and 1 mm thick PZT show a large increase in the amplitude of the shear stress as compared to the 0.5 mm PZT at the same frequency. The location of the peaks in amplitude in the shear stress could provide a fair approximation of the effective length of the PZT actuator which could improve the results of the simplified models.

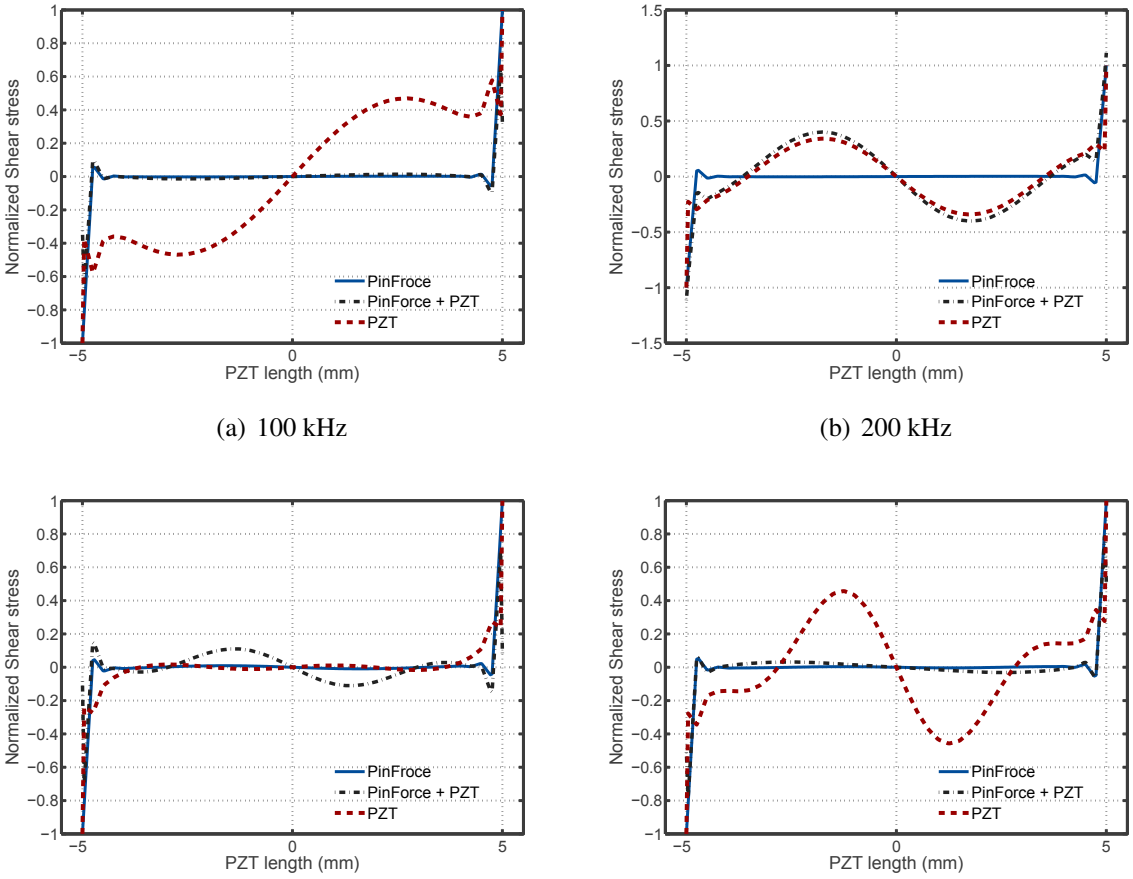

(a) 100 kHz

(b) 200 kHz

(c) 300 kHz

(d) 400 kHz

Figure 5.19 Shear stress distribution due to pin forces applied at the edges of the PZT, and the mechanically cpoupled 0.75 mm PZT thick element considered as ceramic only (Pin Force + PZT) and at the interface of an ideally bonded PZT 0.75 mm thick with the aluminum plate at various frequencies.

In order to separate the effect of the mechanical coupling from the electromechanical full coupling Fig. 5.19 plots the shear stress distribution under the 0.75 mm PZT thick actuator, the corresponding shear stress induced in the plate by pin forces alone, and the shear stress under a ceramic PZT element mechanically coupled to the plate with pin forces as actuator. At 100 kHz, as shown in Fig. 5.19(a), the effect of the pin force and the inclusion of the PZT ceramic on the shear stress is barely distinguishable, while the electromechanical coupling as shown for

the 0.75 mm thick actuator changes the pattern of the shear stress completely. In Fig. 5.19(b) the shear stress at 200 kHz under the mechanically coupled PZT departs from that of the pin force and tends to be more like the electromechanically coupled PZT induced shear stress. A convergence toward the pin force for both electromechanical and pure mechanical coupled PZT is witnessed at frequency 300 kHz as shown in Fig. 5.19(c). from 400 kHz upward the three shear stress distributions are completely different, and as could be seen from Fig. 5.20 the differences gets more pronounced as the frequency increases.

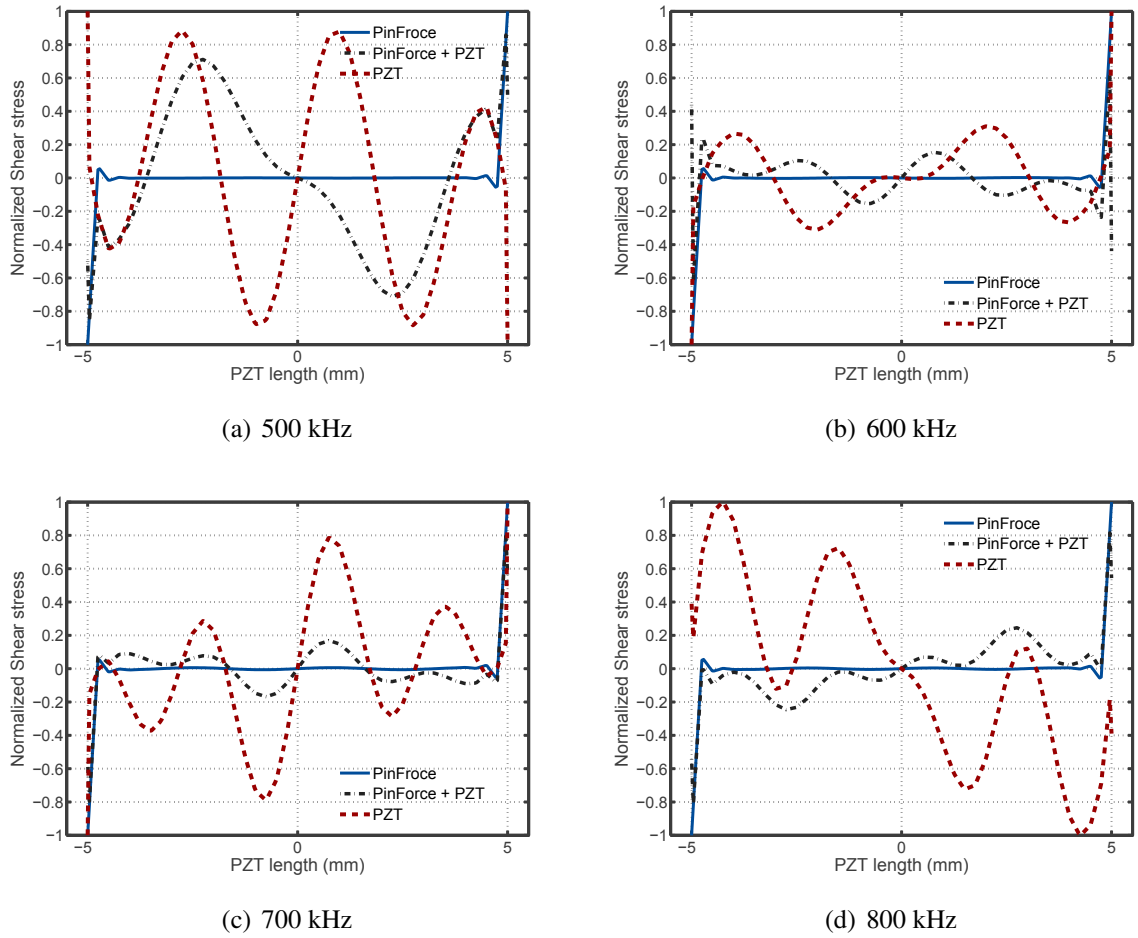

(a) 500 kHz

(b) 600 kHz

(c) 700 kHz

(d) 800 kHz

Figure 5.20 Shear stress distribution due to pure pin forces (PinForce), and same pin forces applied at the edges of a mechanically coupled 0.75 mm PZT thick element considered as ceramic only (PinForce + PZT) and at the interface of an ideally bonded PZT 0.75 mm thick with the aluminum plate at various frequencies.

So, to sum up, the discrepancy between the theoretical pin force mode tuning curves and the real mode tuning curves observed experimentally in literature can be seen in terms of two different effects: the shift on frequency toward a higher frequency, and the appearance of resonance like

peaks at some frequencies not typically predicted by the theoretical model. So, in order to test the limits of the simplifying assumptions underlying the theoretical propagation model, we run an analysis of the ideally bonded PZT, and the conclusion was that the effect of the ideally bonded PZT element can be decomposed into two effects: the first is the change induced only by the mechanical effect of the PZT bonding on the eigenvalues and eigenfrequencies of the PZT plate assembly, this means that the energy imparted into the assembly will partition with respect to the frequency in a different manner from that of the pin force model with traction free surface between the pin forces and also the resonances of the PZT could be attributed to the full electromechanical coupling. The second effect is the change that happens in the mode of actuation, exemplified by the changes in the shear stress experienced by the plate, this in turn will affect the energy partition between the Lamb modes which is reflected in a change in the displacement amplitudes associated with those modes as the thickness of the actuator changes.

The limitations of the present parametric study is that it did not include the material damping effects of the aluminum which may be frequency dependent.

5.4 Adhesive layer effect

In the next two sections, the results of a parametric study of the effect of the adhesive layer thickness and material on the mode tuning behavior as well as the induced shear stresses are reported and discussed.

5.4.1 The effect of adhesive layer thickness

The analysis was done for the same material properties listed in Table 5.1. The adhesive layer thickness was changed from 25 μm, 50 μm and 100 μm with a shear modulus of 2 GPa. The actuator thickness held constant for all the thicknesses at 0.5 mm. The measured displacement amplitudes were recorded at 580 mm distance from the center of a 10 mm PZT element similar to the case shown in Fig. 5.6. The mesh used for the thickness was one element per thickness and 10 elements of $p = 6$ per length like the PZT actuator.

Figure 5.21 shows the effect of the change in the adhesive layer thickness on the mode tuning curve of the A0 mode. The normalization was done for the S0 and A0 using the maximum value of the A0. Till 400 kHz the adhesive layer is likely to have a negligible effect on the mode tuning behavior with the exception of narrow frequency band (125kHz-200kHz) where the effect of the presence of the adhesive layer is manifested in a shift of the A0 amplitude local minimum toward higher frequency when compared with the case of ideal bonding (depicted as 0

μm thickness). The difference between the ideally bonded 0.5 mm PZT and the adhesive layer is starting to be revealed more as the frequency increases, by 500 kHz, the 100 μm thick adhesive layer witness a sudden spike of resonance like nature, probably could be attributed to the change in the eigenfrequency due to the mechanical coupling of the adhesive layer. That was followed but what looks like a damped anti-resonance drop in amplitude at 525 kHz. As the thickness of the adhesive layer increases from 25 μm to 100 μm, the maximum located around 500 kHz changes from a more gradual maximization to an abrupt resonance like spike. Similar behavior could be observed as well for the amplitude of the S0 mode plotted in Fig. 5.22.

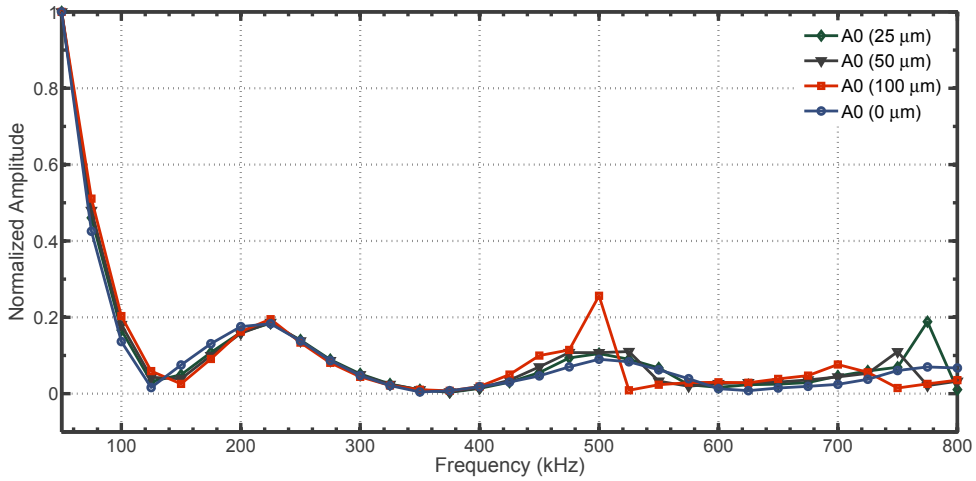

Figure 5.21 The A0 mode tuning curve of adhesive layer thickness effect.

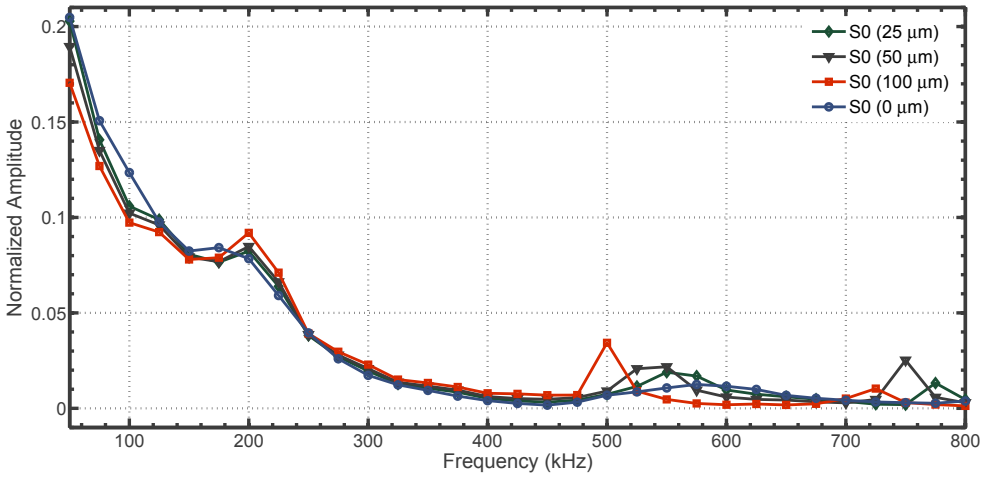

Figure 5.22 The S0 mode tuning curve of adhesive layer thickness effect.

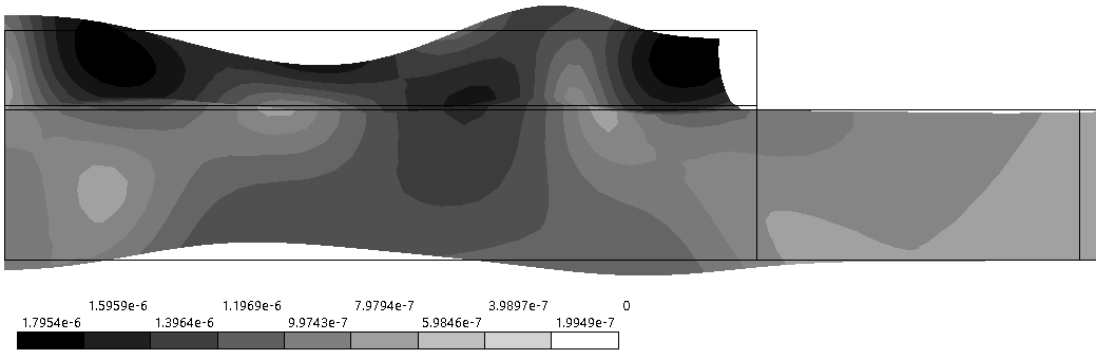

(a) 25 µmm, 2 GPa

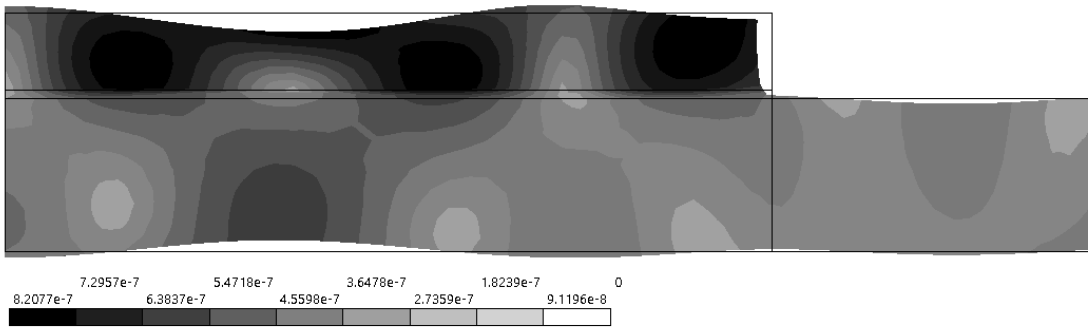

(b) 50 µmm, 2 GPa

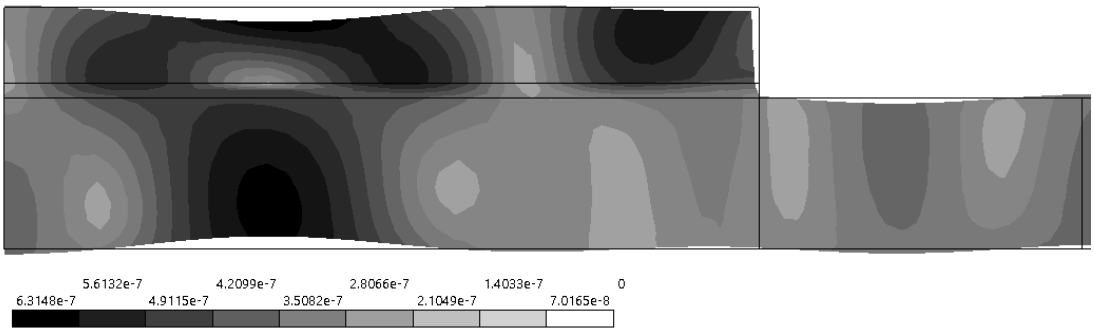

(c) 100 µmm, 2 GPa

Figure 5.23 Mode shapes of the three thickness values of the bonding layer with 0.75 mm thick PZT actuator at 800 kHz.

Figure 5.23 shows the actuation modes at 800 kHz, with the three values of the bonding layer thickness. In Fig. 5.22, the adhesive layer tend to shift the location of the maxima toward higher frequencies, as well as the adhesive layer gets thicker it tends to increase the amplitude of the S0 at the respective frequency. for example taking a close look at 200 kHz, the maximum of

the S0 amplitude for the 100 μm attains a normalized value of 0.085 while for the 50 μm thick adhesive layer the local maximum is located at the same frequency but at a slightly smaller normalized value. All the local maxima of the three adhesive layer thicknesses are located at the same frequency of 200 kHz which is shifted with respect to 175 kHz where the local maximum of the ideally bonded 0.5 mm PZT actuator is located.

In the remaining of this section, a study of the effect of the adhesive layer presence and thickness on the changes in the actuation mode is presented.

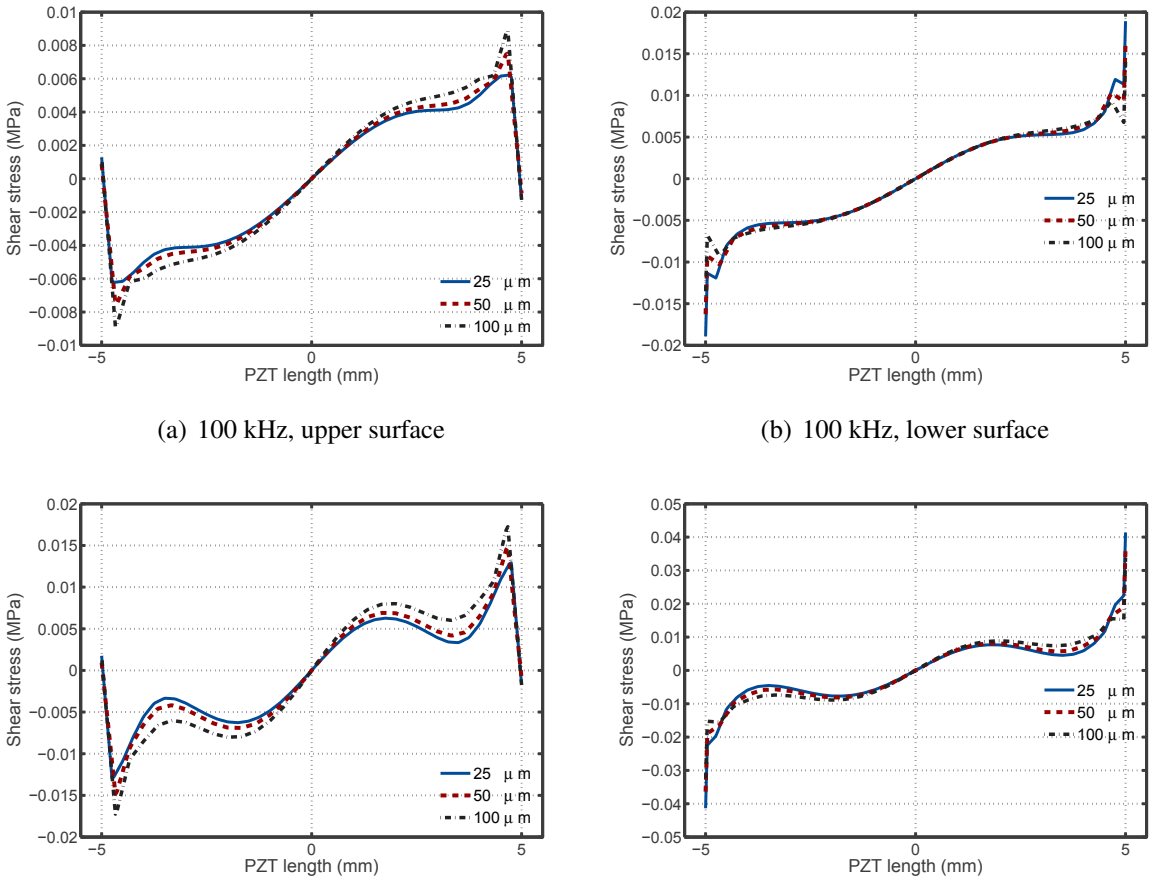

(a) 100 kHz, upper surface

(b) 100 kHz, lower surface

(c) 200 kHz, upper surface

(d) 200 kHz, lower surface

Figure 5.24 Shear stress distribution at the upper and lower interfaces of the adhesive (2 GPa shear modulus) bonding the PZT with the aluminum plate at various frequencies, with the three adhesive layer thicknesses studied.

The mode of actuation is quantified in terms of the shear stress distribution extracted at both the upper and lower interfaces of the adhesive layer. The reason of this differentiation between the upper and lower surface is to reveal if the variation through the thickness have a discernible effect on the mode of actuation, since all the theoretical models are assuming that both the actuator and

the adhesive layer are one dimensional in nature *i.e.* the variation of the shear stress assumed to be solely dependent on the x direction as depicted in Fig. 2.17(b).

Figures 5.24 to 5.27 show the distribution of the shear stress under the PZT at the interface between the PZT element and the adhesive layer (referred to in the figure as upper surface), and between the adhesive layer and the plate (lower surface), respectively.

There are two salient observations, the first is that the variation in the actuation mode is comparable to the case of ideal bonding. The shear stress distribution tend to cluster into groups of similar patterns, originating in variations in actuation mode with the frequency similar to the case of the ideal bonding. The shear lag effect is observed when comparing the upper shear stress distribution with the lower one. The stress distribution at the same frequency is smoothed when going from the upper to the lower surface.

Figure 5.24(a), and 5.24(b) shows almost the same pattern. When comparing the lower surface shear stress distribution with the ideal bonding case, the localization of the loading at the edges are more spread and diffused which is conformal with what is expected from the classical shear lag effect. The other noticeable effect is the change of sign at the edges between the upper and lower surface of the adhesive layer. This change in sign may be attributed to the weak satisfaction of the zero shear stress at the edges of the upper surface while in the lower edge there is a continuity of displacement between the adhesive layer and the plate. This observation seems to be valid for all the frequency range studied, where similar change of signs are observed at frequency 200 kHz as depicted in Fig. 5.24(c) and 5.24(d).

Fig. 5.25 shows the shear stress distribution at 300 kHz and 400 kHz, the sharp changes at the edges of the upper surface of the adhesive layer are smoothed out when transfered through the adhesive layer in the lower surface. This change with thickness are more apparent at thicker adhesive layers than at thinner ones, as could be seen for the case of 100 μm thick adhesive layer when compared with 25 μm.

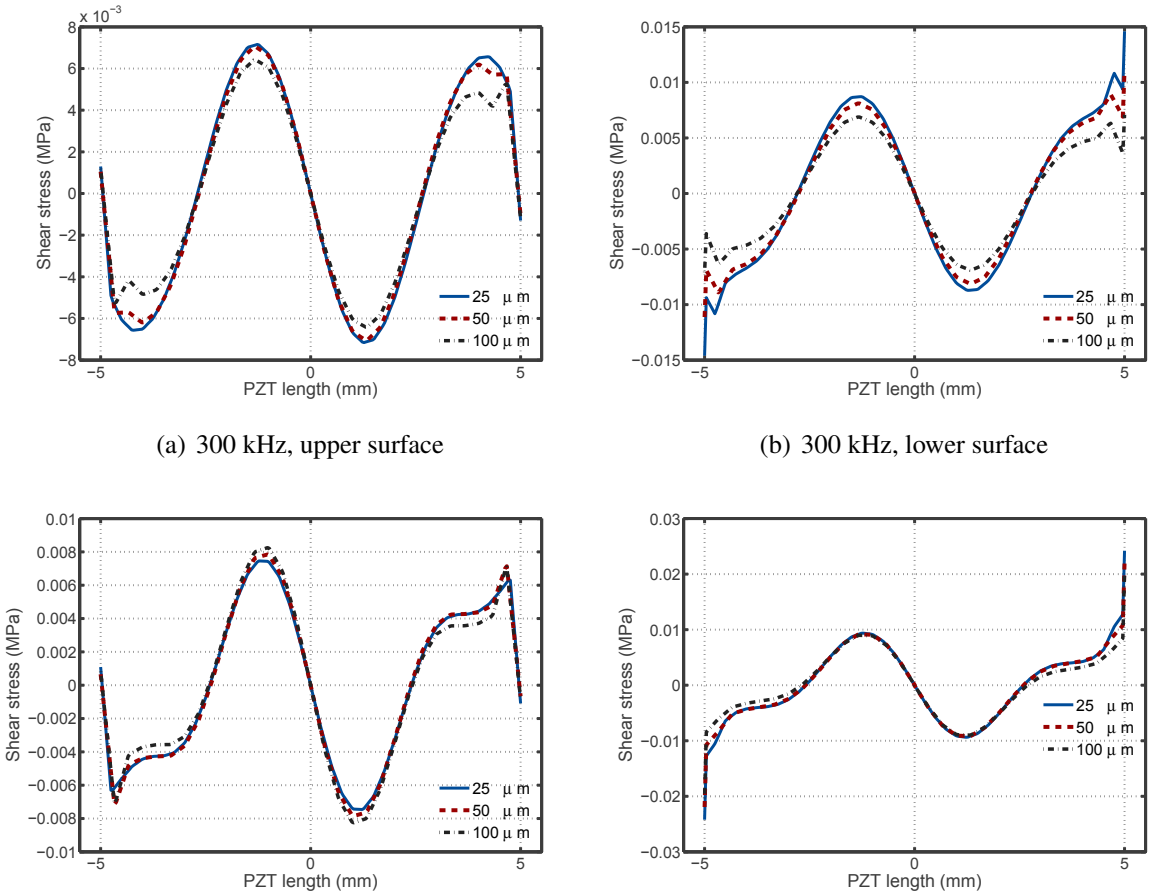

(a) 300 kHz, upper surface

(b) 300 kHz, lower surface

(c) 400 kHz, upper surface

(d) 400 kHz, lower surface

Figure 5.25 Shear stress distribution at the upper and lower interfaces of the adhesive (2 GPa shear modulus) bonding the PZT with the aluminum plate at various frequencies, with the three adhesive layer thicknesses studied.

There are two noticeable effects of the adhesive layer: the thicker the adhesive layer the sharper the changes from a smooth cyclic pattern in inside the actuation zone to localized loading at the edges. This is manifested in Fig. 5.25(a) and 5.25(c) when comparing the sharp transitions near the edges of the adhesive layer for the 100 μm, 50 μm and 25 μm. The other effect, is the effect of the thickness on the smoothening of the shear distribution, where the thicker adhesive layer have more effect on the smoothening of the whole shear stress distribution when comparing the upper to the lower surface as could be deduced form comparing the Fig. 5.25(b) and 5.25(d).

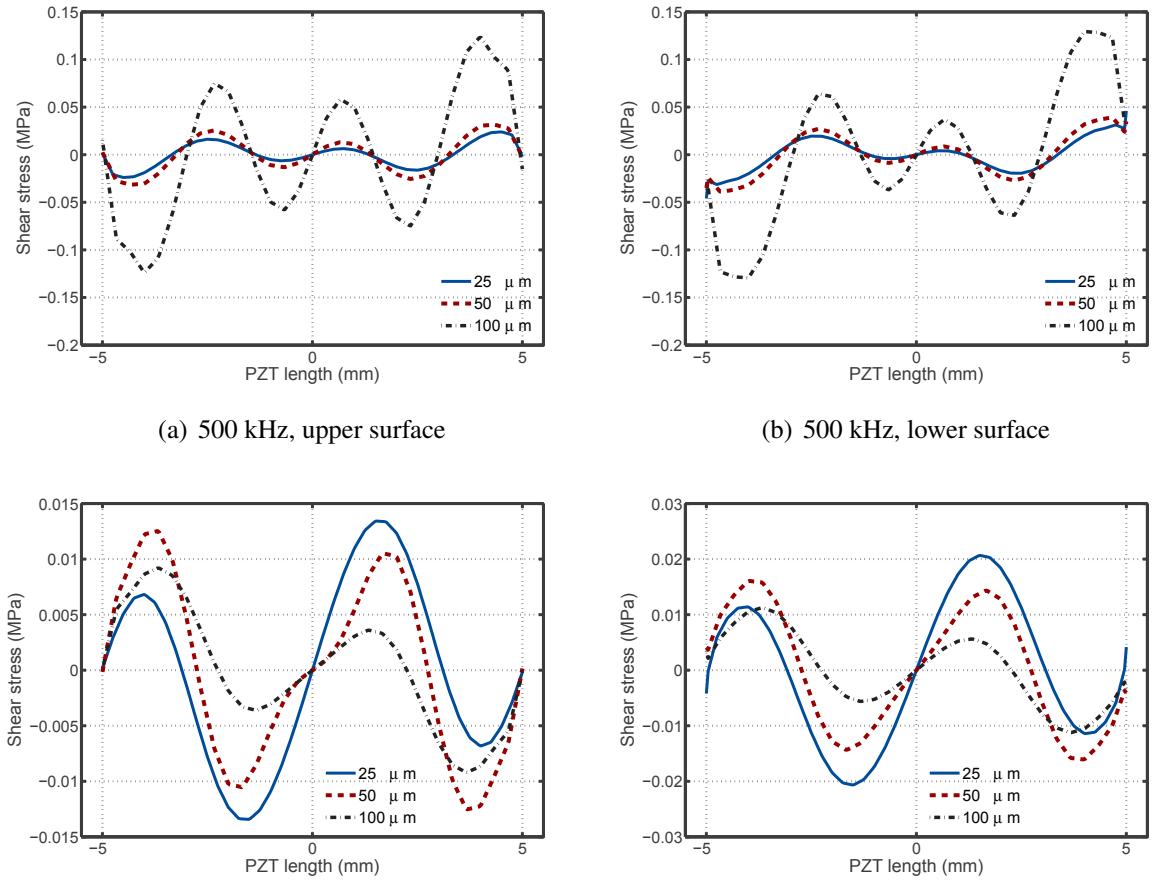

(a) 500 kHz, upper surface

(b) 500 kHz, lower surface

(c) 600 kHz, upper surface

(d) 600 kHz, lower surface

Figure 5.26 Shear stress distribution at the upper and lower interfaces of the adhesive (2 GPa shear modulus) bonding the PZT with the aluminum plate at various frequencies, with the three adhesive layer thicknesses studied.

Figure 5.26 shows a new emerging pattern at frequencies 500 and 600 kHz, the interaction of the resonances of the PZT actuator and the resonance of the adhesive layer itself. Recalling that the actuator for all the three thicknesses of the adhesive layer was 0.5 mm thick, comparing Fig. 5.26(b) with Fig. 5.18(a) the number of cycles are the same, but the amplitude of the shear stress fluctuation is affected strongly with the thickness of the adhesive layer, where for adhesive layer with 100 µm thickness presumably poses a large effect through interaction between the two resonances. Similar interaction could be observed for the 25 µm thick adhesive layer at frequency 600 kHz depicted in Fig. 5.26(c). Going from the upper surface to the lower surface, the smothening effect of the adhesive layer persists as well as the change in sign at the edges of the adhesive layer lower surface with respect to the signs at the edges of the upper surface.

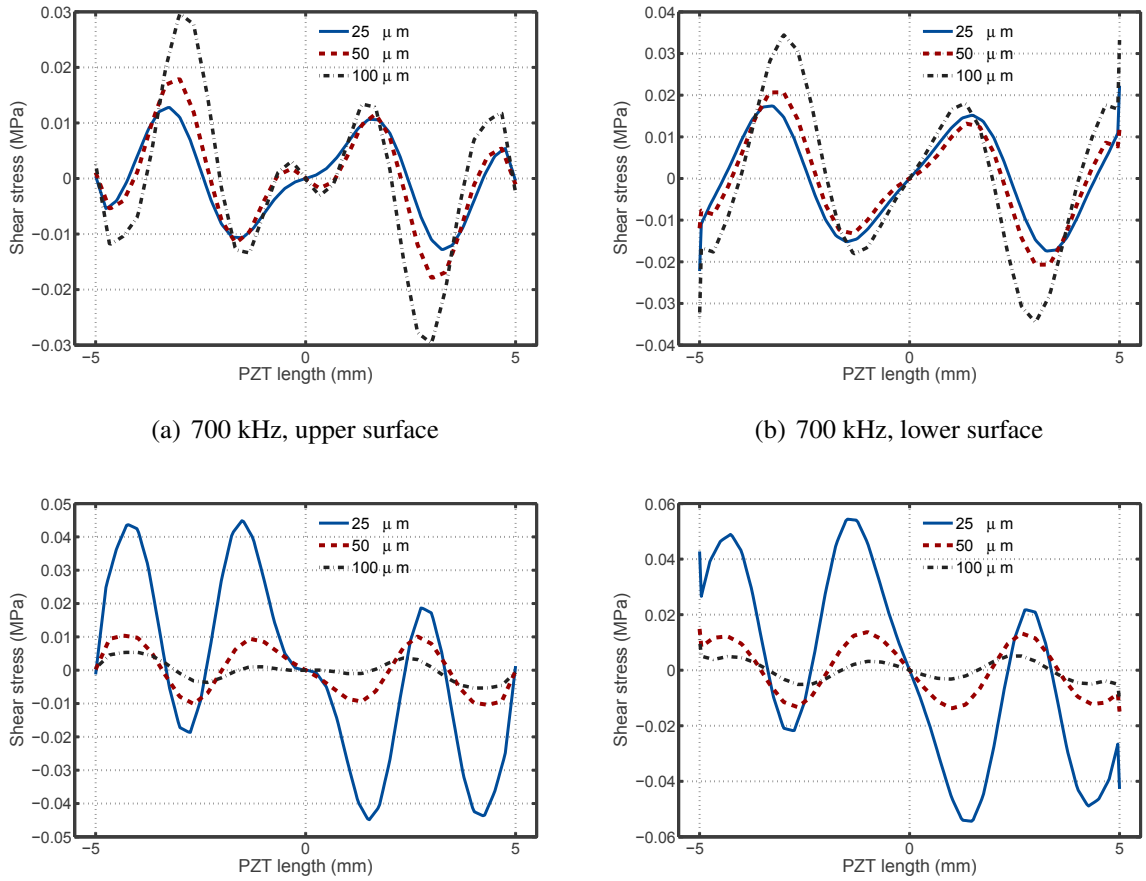

(a) 700 kHz, upper surface

(b) 700 kHz, lower surface

(c) 800 kHz, upper surface

(d) 800 kHz, lower surface

Figure 5.27 Shear stress distribution at the upper and lower interfaces of the adhesive (2 GPa shear modulus) bonding the PZT with the aluminum plate at various frequencies, with the three adhesive layer thicknesses studied.

While the same overall trends persist at the higher frequencies depicted in Fig. 5.27, *i.e.* the changes are smoothed and the sharp fluctuations in the frequency range 700-800 kHz are smoothed out while being transferred through the adhesive layer to the plate. There is new effect of the presence of the adhesive layer when comparing Fig. 5.27(a) with the ideally bonded case depicted in Fig 5.18(c), whereas the number of cycles in the shear stress remains the same the amplitude seems to be modulated somehow, having lower amplitudes at the central region than near the edges, and this effect seems to be amplified by when the shear stress in transfered into the lower surface, to the extent that almost the central cycle is lost from the shear stress distribution at thickness 25 and 50 μm. This can be tentatively understood as an interaction of two mode shapes, one of the PZT and the other of the adhesive layer with slightly shifted location of zeros *i.e.* interference of the two mode shapes with a phase shift.

5.4.2 The effect of adhesive layer material

Figure 5.28 shows the effect of the shear modulus of the adhesive layer on the modal amplitude at the same location (580 mm away from the center of actuator). The thickness of the adhesive layer was fixed at 25 μm.

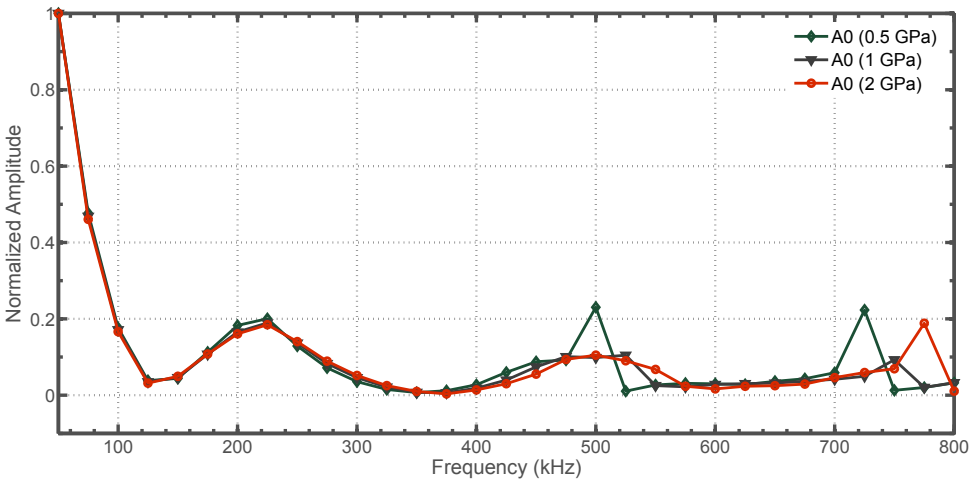

Figure 5.28 The A0 mode tuning curve of adhesive layer shear modulus effect.

The resonance like peaks at 500 kHz for the 0.5 GPa adhesive layer, is a demonstration of the duality effect that the stiffness and the thickness plays. Since in appears at the same frequency of the the thick adhesive layer 100 μm in Fig. 5.21, this could be understood in terms of the formulation of the shear lag solution, where in Eq. (2.6) the ratio G_b/h_b is responsible for this duality effect *i.e.* increasing the stiffness is equivalent to decreasing the thickness and vice versa. Despite the fact that the theoretical shear lag solution is based on a lot of simplifying assumptions and does not capture the resonances of the assembly nor the frequency shift effect due to the complicated loading caused by the full coupling, it is still capable of shedding a light on this observation which seems to remain valid even when taking the full coupling into consideration.

Figure 5.29 shows the mode shapes at the 500 kHz for the three different thicknesses of the bonding layer. For 0.5 μmm thick the wavelength of the actuator is clearly different than the the two non resonant modes.

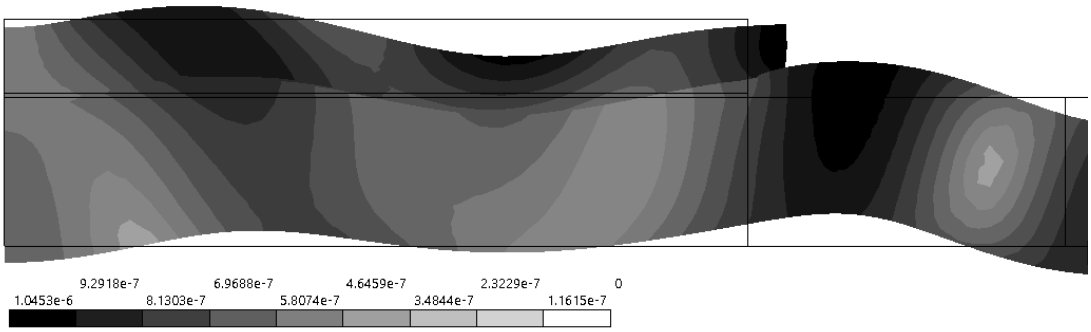

(a) 25 μmm, 2 GPa

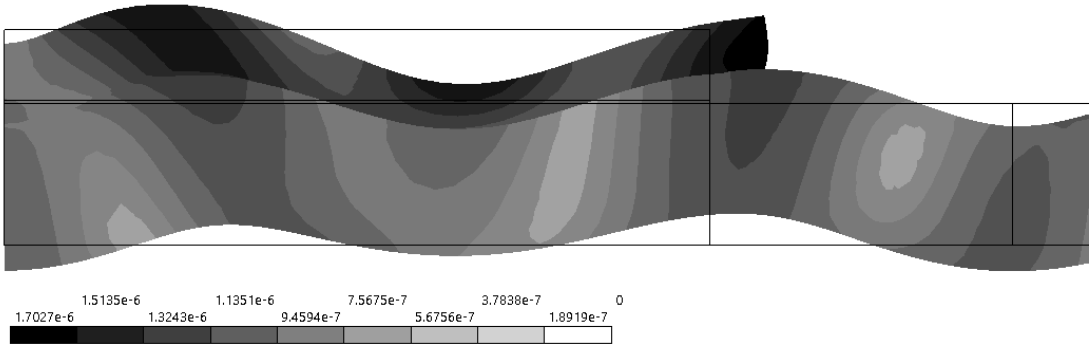

(b) 25 μmm, 1 GPa

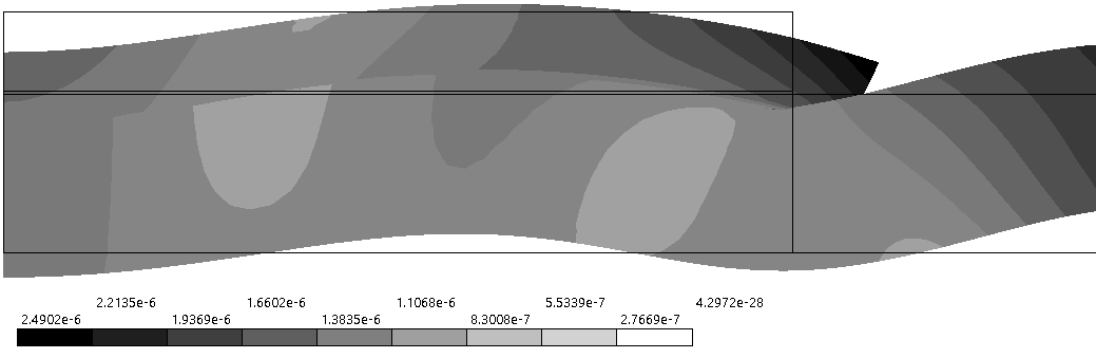

(c) 25 μmm, 0.5 GPa

Figure 5.29 Mode shapes of the three shear modulus values of the bonding layer with 0.75 mm thick PZT actuator at 500 kHz.

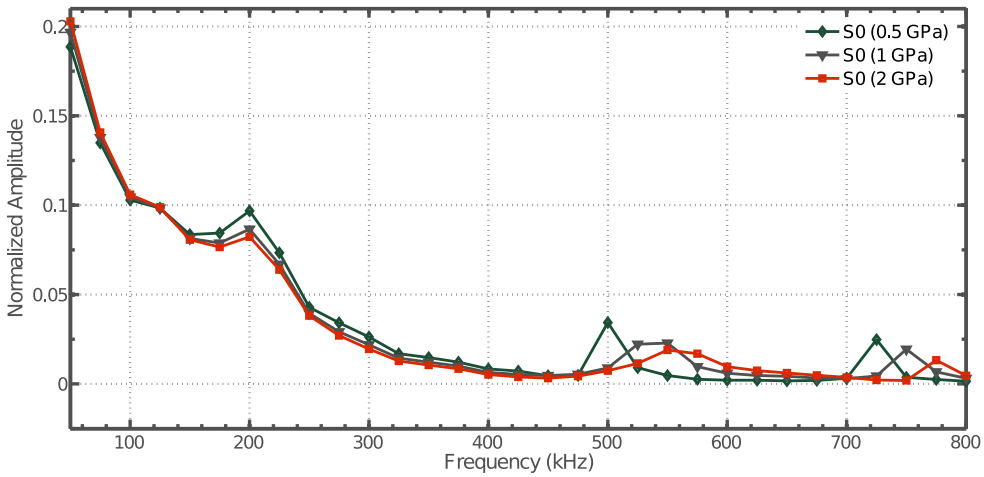

Figure 5.30 The S0 mode tuning curve of adhesive layer shear modulus effect.

In Fig. 5.30, the normalized amplitudes of the S0 displacement are plotted, and when compared with Fig. 5.28 the effect of the shear modulus of the adhesive layer is more pronounced on S0 mode than A0 mode. This could be understood in terms of the change in the repartition parameter in the modified shear lag solution introduced by [Yu *et al.*, 2010], and shown in Fig. 2.17(d).

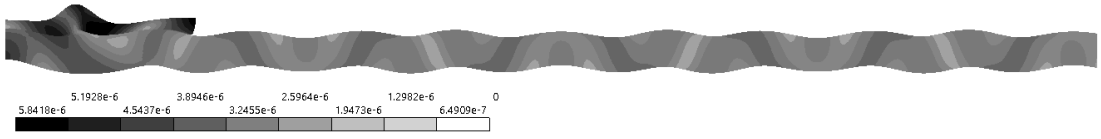

(a) 0.5 GPa, 725 kHz

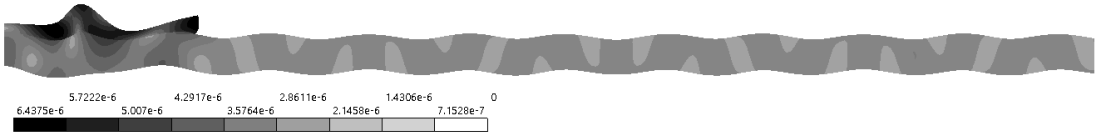

(b) 2 GPa, 775 kHz

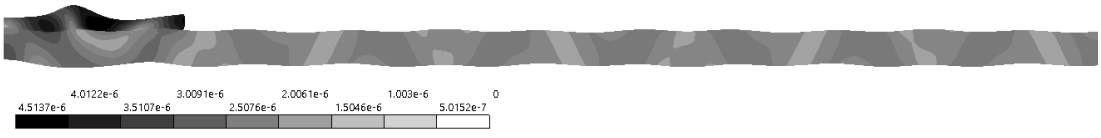

(c) 1 GPa, 750 kHz

Figure 5.31 Mode shapes at three resonating frequencies for the different shear moduli bonding layer.

The sensitivity of the different modal amplitudes to the excitation is dependent on the frequency. Also, the author would hypothesize that the different modes respond differently to the what might look minor variations in the shear stress distribution, as the ones that could be caused by the change in the shear modulus of the adhesive layer. A similar effect for the earlier called "duality effect" between the thickness and the shear modulus of the adhesive layer is manifested at 200 kHz. The stiffer the adhesive layer the more it approaches the similar effect of thinning the adhesive layer.

Figure 5.31 shows the mode shapes at the three resonant like frequencies for the different shear moduli of bonding layer material. The similarity between the modes are evident, supporting the hypothesis that there is a maximum transfer of energy between the actuator and the substructure. In Fig. 5.32 to Fig. 5.34, the shear stress at the upper and lower interfaces of the adhesive layer are plotted. The effect of the presence of the adhesive layer is in accordance with the intuitive understanding that the shear lag solution provide. The localized and sharp changes are smoothed out. By smoothing out we refer to two actions: the fluctuation is reduced *i.e.* the difference between the maximum and minimum is reduced, which is more apparent in Fig. 5.33, the second action is that the originally localized and sharp jumps in shear stress are made more gradual when they are sensed by the plate, and spread over a longer distance at the lower surface in comparison with the upper surface.

It is not surprising that the shear stresses at frequencies 100, 200 and 300 kHz in Fig. 5.32 are similar to the shear stresses plotted in Fig. 5.24 and Fig. 5.25 at the same frequencies since the values of the shear modulus in this parametric study were specifically chosen to preserve G_b/h_b ratio in order to test the limits of the generalization of the duality effect.

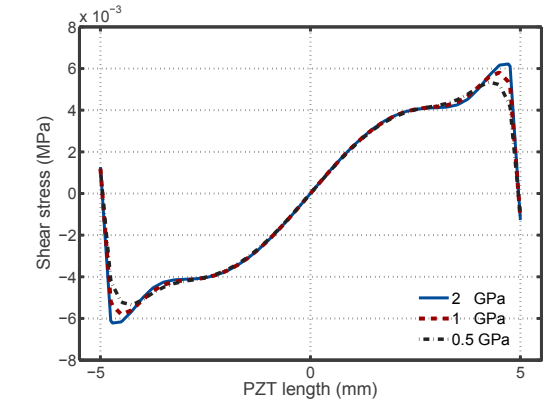

(a) 100 kHz, upper surface

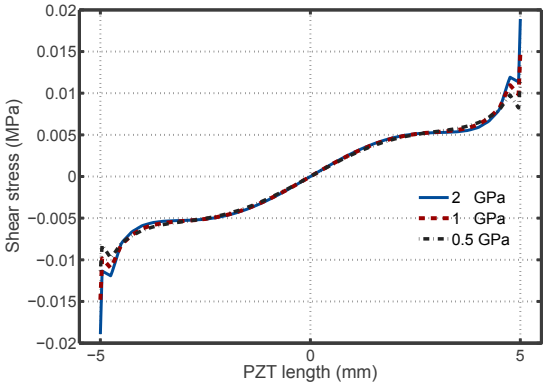

(b) 100 kHz, lower surface

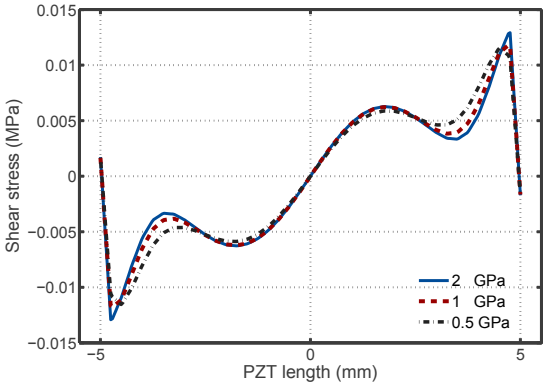

(c) 200 kHz, upper surface

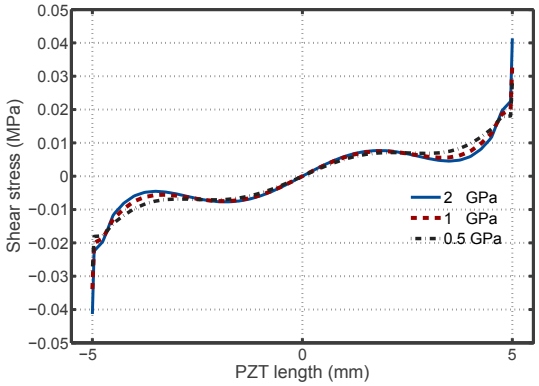

(d) 200 kHz, lower surface

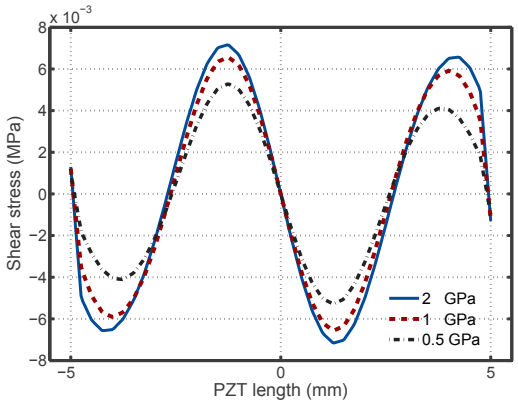

(e) 300 kHz, upper surface

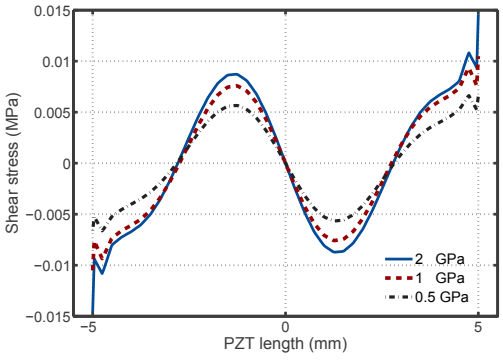

(f) 300 kHz, lower surface

Figure 5.32 Shear stress distribution at the upper and lower interfaces of the adhesive (25 μm thick) bonding the PZT with the aluminum plate at frequency range 100-300 kHz, with the three adhesive layer shear moduli studied.

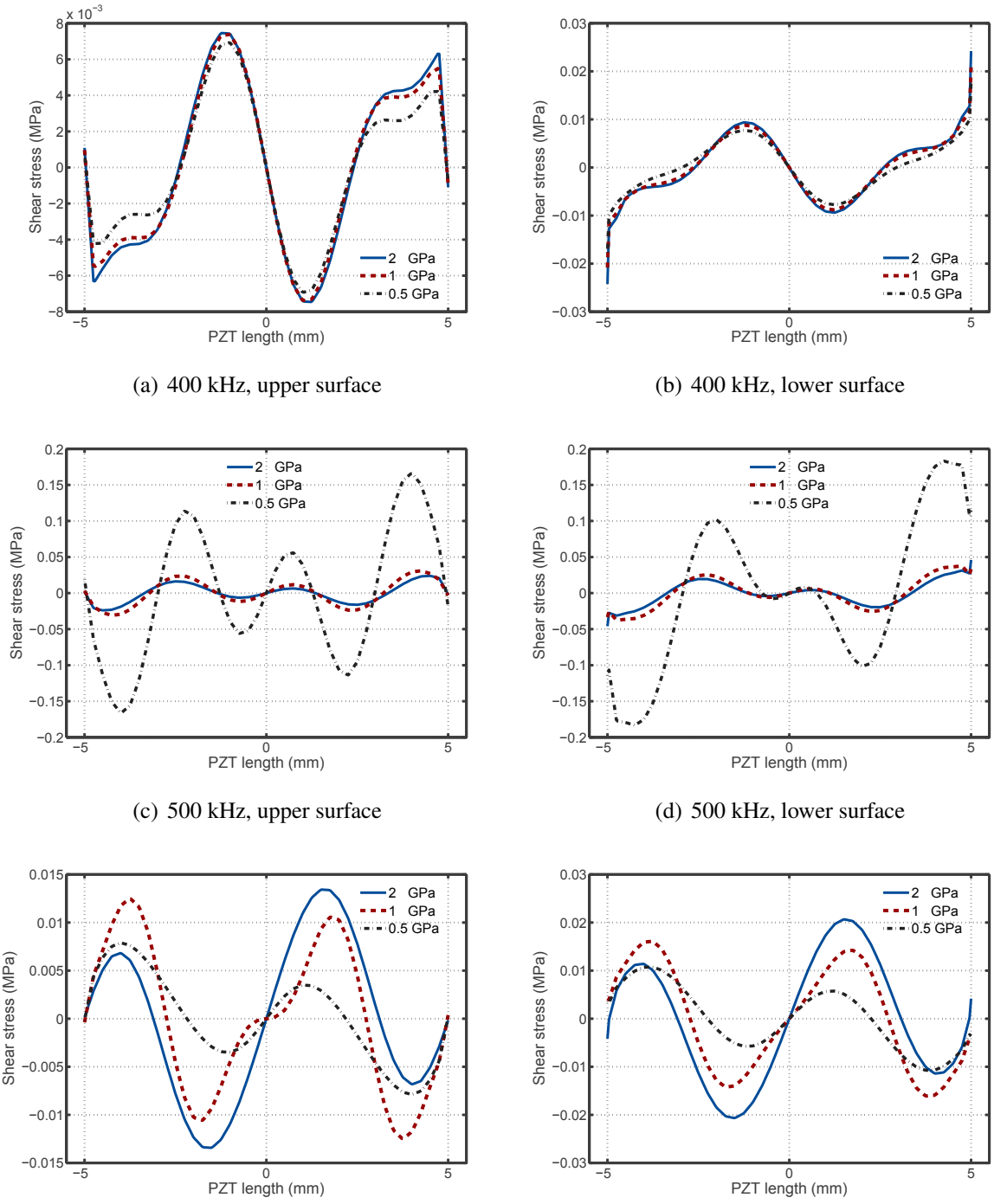

(a) 400 kHz, upper surface

(b) 400 kHz, lower surface

(c) 500 kHz, upper surface

(d) 500 kHz, lower surface

(e) 600 kHz, upper surface

(f) 600 kHz, lower surface

Figure 5.33 Shear stress distribution at the upper and lower interfaces of the adhesive (25 µm thick) bonding the PZT with the aluminum plate at frequency range 400-600 kHz, with the three adhesive layer shear moduli studied.

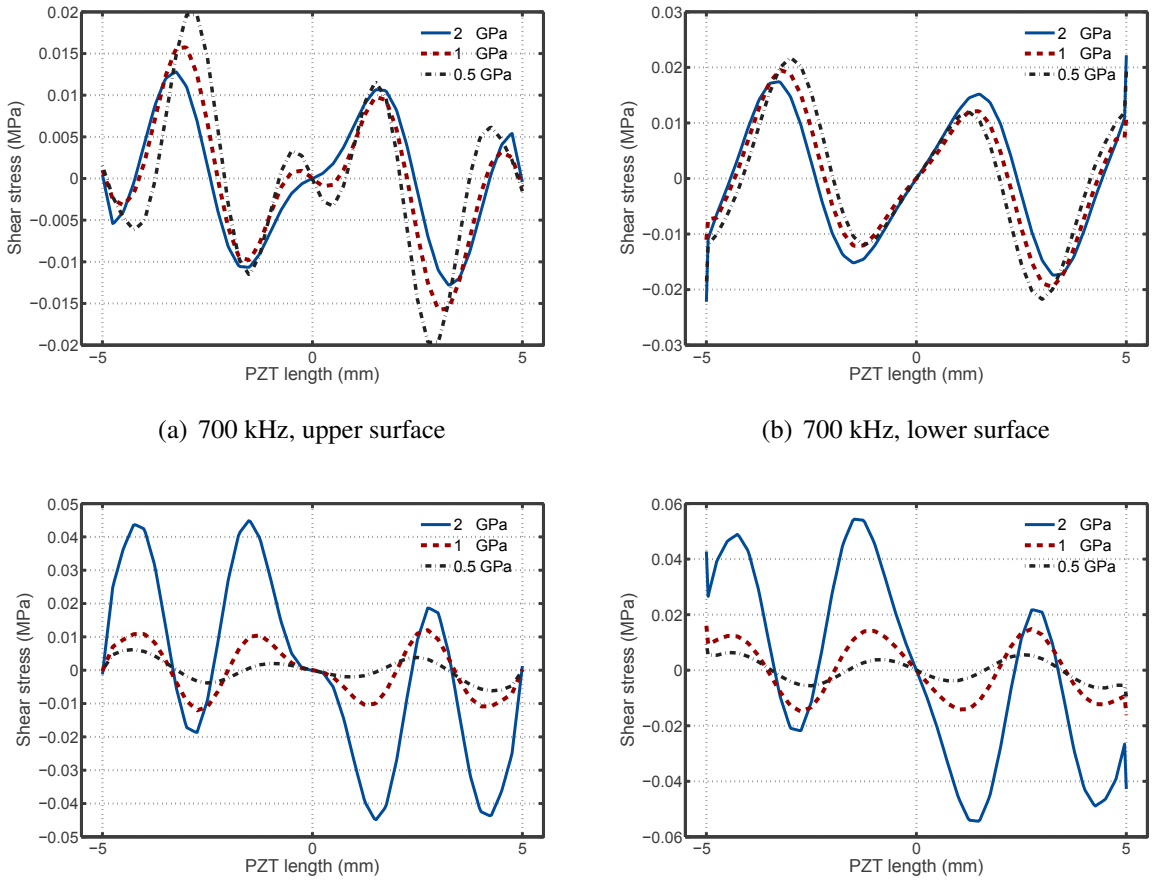

(a) 700 kHz, upper surface

(b) 700 kHz, lower surface

(c) 800 kHz, upper surface

(d) 800 kHz, lower surface

Figure 5.34 Shear stress distribution at the upper and lower interfaces of the adhesive (25 μm thick) bonding the PZT with the aluminum plate at frequencies 700 and 800 kHz, with the three adhesive layer shear moduli studied.

The duality effect seems to break at frequency 400 kHz as could be deduced when comparing Fig. 5.25(d) with Fig. 5.33(b), this may be attributed to the different interaction between the resonance of the adhesive layer due the change in material properties and the interaction of the resonance of different geometries of the adhesive layer with the rest of the assembly.

From Fig. 5.33 and 5.34, it could be concluded that the effect of changing the material properties are more pronounced than changing the adhesive layer thickness. The changes in the shear stress going from 0.5 GPa to 2 GPa is larger than those associated with thickness changes with the same G_b/h_b ratio. Which lead to the conclusion that designing the material properties of the adhesive layer in order to control the mode tuning is a more effective approach than the thickness considering the thickness variation.

The limitation of the present results, is that they did not include the viscous damping or the viscoelastic properties of the adhesive layer, which might be a pertinent feature of the adhesive materials typically used in bonding the PZT elements.

5.5 Experimental verification

In this section, we conclude with an experimental verification of the time domain simulation of two case studies. Recalling the discrete system of equation 5.24 after the static condensation:

$$\mathbf{M\ddot{u}} + (\mathbf{K}_{uu} - \mathbf{K}_{u\phi}\mathbf{K}_{\phi\phi}^{-1}\mathbf{K}_{u\phi}^{\mathrm{T}})\mathbf{u} = -\mathbf{K}_{\phi\phi}^{-1}\mathbf{f_e} \quad \rightarrow \quad \mathbf{MU} + \mathbf{KU} = \mathbf{F} \tag{5.45}$$

Explicit time integration was done using Hilber-Hughes-Taylor Method [Hughes, 1987], with $\alpha = 0.5$:

$$\mathbf{M\ddot{U}}_{n+1} + (1+\alpha)\mathbf{KU}_{n+1} - \alpha\mathbf{KU}_n = \mathbf{F}(t_{n+\alpha}) \tag{5.46}$$

where the time step is determined based on the appropriate CFL number from the results of the previous chapter.

5.5.1 Case study 1

In this case study, a pitch and catch experiment was conducted using a rectangular aluminum plate 1.54 mm thick, 700 mm long and 70 mm wide. The plate was milled to produce a square notch of 0.8 mm length, in the middle of the plate length, as shown in Fig. 5.35(a). Three identical piezoceramic patches (BM500, Sensor Technology Ltd.) were mounted on the upper surface of the plate on the same side of the notch. Each extends over the whole width of the plate, 7 mm wide, 0.4 mm thick. The actuator was bonded at the left edge of the plate using a rapid epoxy, as well as the two sensors shown in Fig. 5.35(b). In order to suppress the reflections from the top and bottom edges of the plate, to approximate as much as possible a two dimensional setting, a damping paste was attached to the top and bottom edges of the plate.

The voltage amplitude of the exciting signal was 10 V and the excitation signal was a 3.5 cycles sinusoid modulated by a Hanning window, the center frequency of the excitation signal was varied from 250 kHz to 500 kHz, with a step size of 50 kHz. The exciting waveform was generated using an HP 33120A signal generator with a sampling frequency of 15 MHz, and a delay 20 μs to be able to window out safely the signal in further analysis. The acquisition of experimental signals is performed using a LabVIEW interface with a high impedance National Instruments PCI-5105 12 bits acquisition board. The recorded signal length was 1 ms and the sampling

frequency is fixed at 60 MHz. Typically, each measurement was averaged 400 times with a pause of 400 ms between each measurement in order to increase the signal to noise ratio.

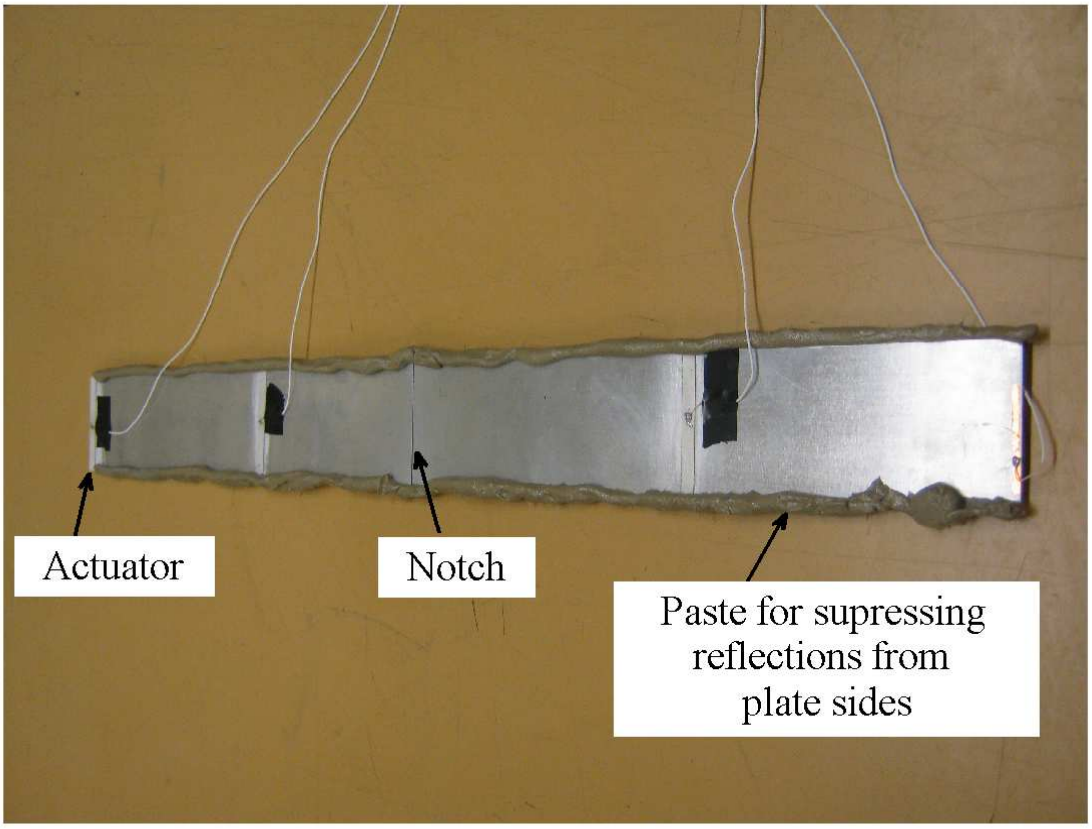

(a)

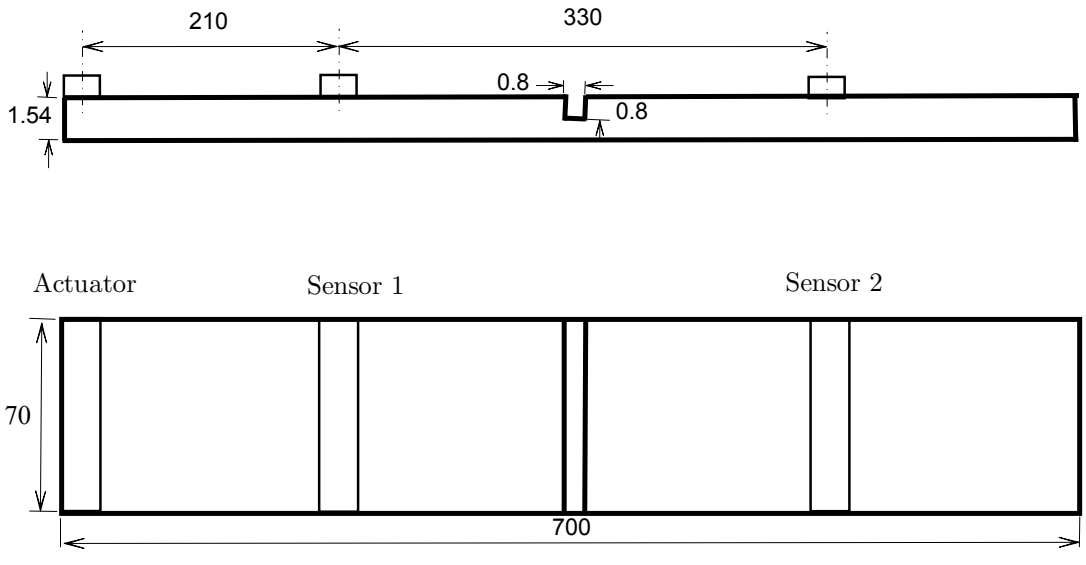

(b)

Figure 5.35 The experimental setup for case study 1.

Figure 5.36 shows the isolated fundamental modes S_0, and A_0 simulated interaction with the notch. The excitation was implemented through symmetric and anti-symmetric application of nodal forces at the edge. The time dependence of the nodal forces are 3.5 cycles modulated by a Hanning window, with central frequency 250 kHz. The plotted values are for the longitudinal displacement recorded at equally spaced points along the length of the plate, and rescaled for clear visualization.

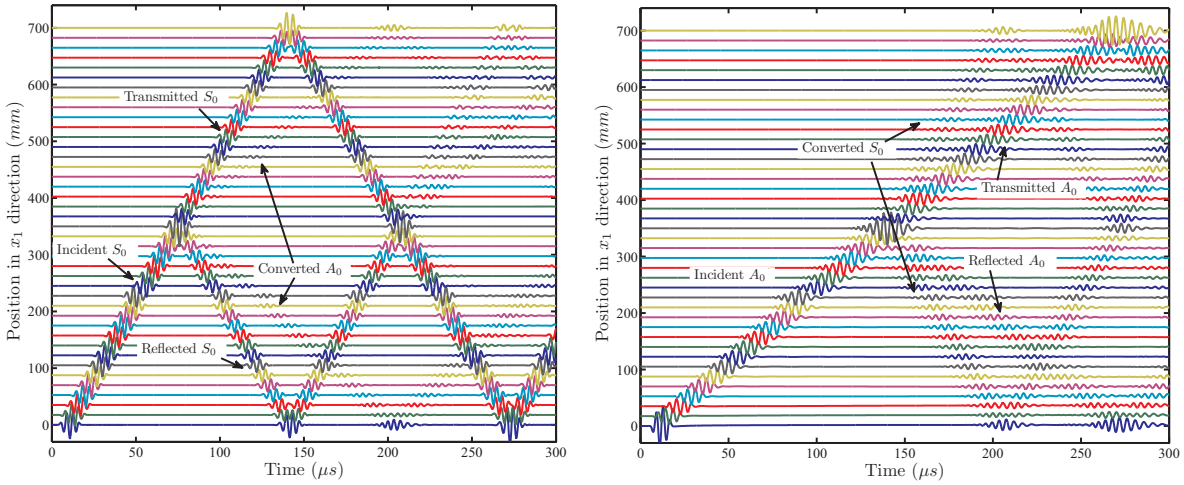

(a) S_0 interaction with the notch.

(b) A_0 interaction with the notch.

Figure 5.36 Isolated fundamental modes interaction with the notch, using nodal forces excitation (250 kHz, 3.5 cycles).

Each of the incident fundamental modes, incident with respect to the notch, experience reflection and transmission, as well as mode conversion on impingement on the notch. In what follows, the converted mode term will be used to identify both the transmitted converted mode (in the propagation direction) and the reflected converted mode, where the distinction is clear from the position of the sensor.

In all of the simulations presented, a polynomial degree of eight was used, with two elements per minimum wavelength in the longitudinal direction, and one element per notch, which provide 17 points per plate thickness. The results of the comparison between the SEM results and experimental signals are shown in Fig. 5.37, for the signal acquired at the 210 mm distant sensor. The simulated output signal was calculated as proportional to the difference between the longitudinal strain at the two edges of the sensor (strain approximation). Since the attenuation of the signal was not included in the model, both of the simulated and experimental results were normalized separately before comparison.

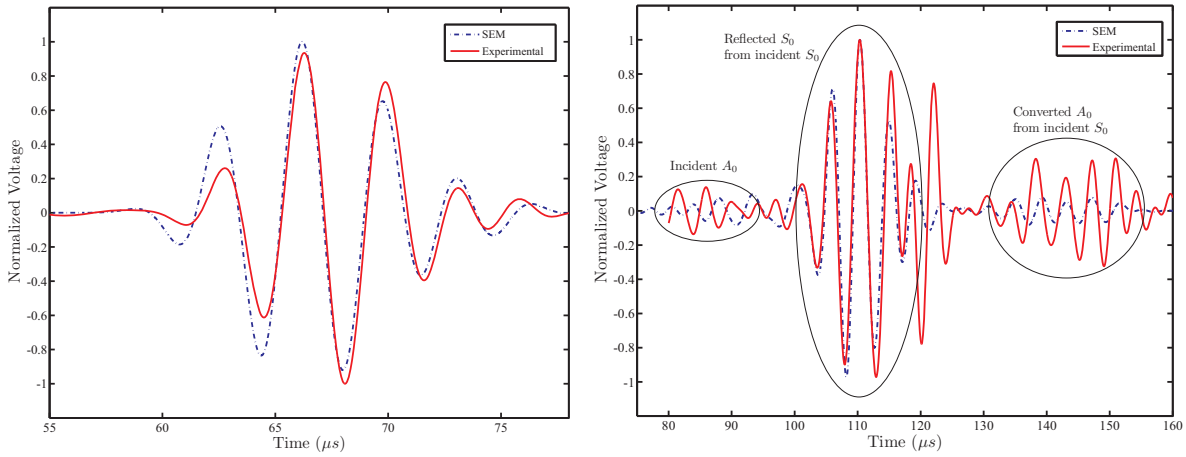

(a) Incident S_0 mode. (b) Interaction of S_0 mode with the notch.

Figure 5.37 A comparison between the SEM and experimental normalized signals, for sensor 1, 210 mm distant from the excitation edge, at a center excitation frequency of 250 kHz.

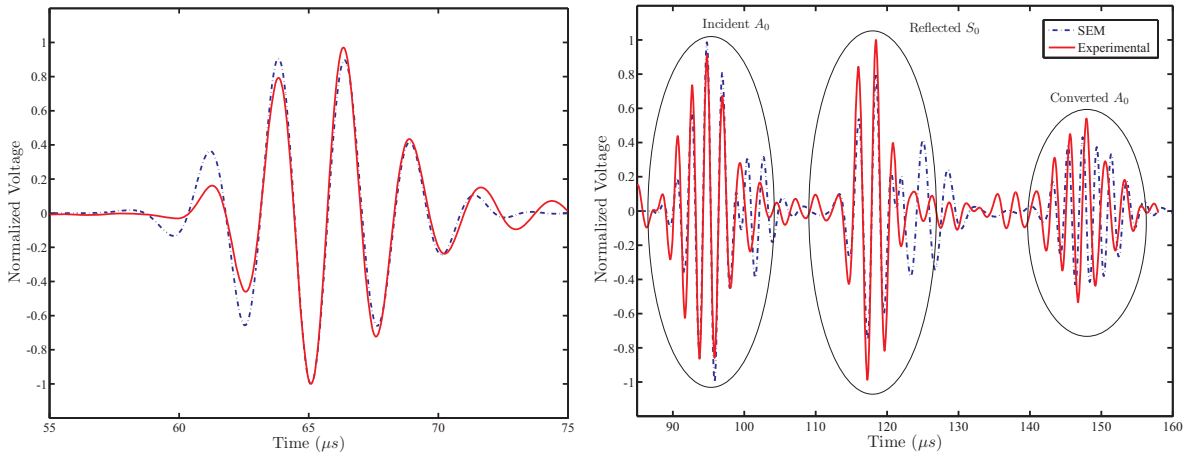

(a) Incident S_0 mode. (b) Interaction of S_0 mode with the notch.

Figure 5.38 A comparison between the SEM and experimental normalized signals, for sensor 1, 210 mm distant from the excitation edge, at a center excitation frequency of 450 kHz.

The incident S_0 is well simulated by the strain approximation as could be seen from the good agreement between the SEM results and the experimental signal depicted in Fig. 5.37(a) for an excitation center frequency of 250 kHz. The difference between the simulated waveform associated with the A_0 mode shown in Fig. 5.37(b), and the experimental signal could be attributed to the inaccuracy of the approximation used to simulate the sensor response. Since A_0 is dominated by out-of-plane displacement u_3, as compared with the S_0 mode which is dominated

by longitudinal displacement u_1. Figure 5.38, shows similar results for the 450 kHz excitation center frequency, with higher amplitude of the A_0 mode as shown in Fig. 5.38(b).

5.5.2 Case study 2

Figure 5.39 shows the experimental setup, consisting of relatively complex thin walled structure, with an L shaped horizontal stiffener, adhesively bonded to the plate by epoxy, the structure was made of aluminum (6066-T6) plate, and instrumented with two circular PZT elements, with flipped electrodes, placed symmetrically on the two sides of the L shape stiffener. The material properties used in the simulation and dimensions of the setup are listed in Table 5.4.

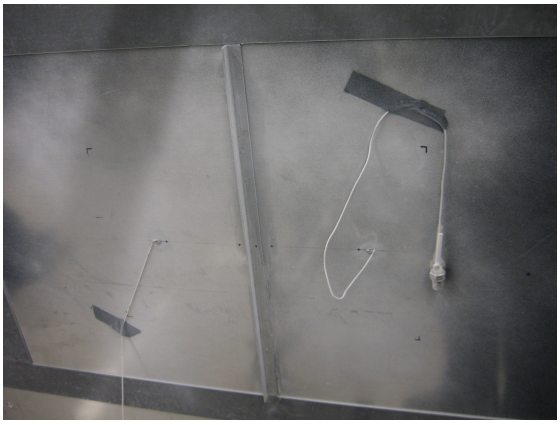

Figure 5.39 Experimental setup for case study 2.

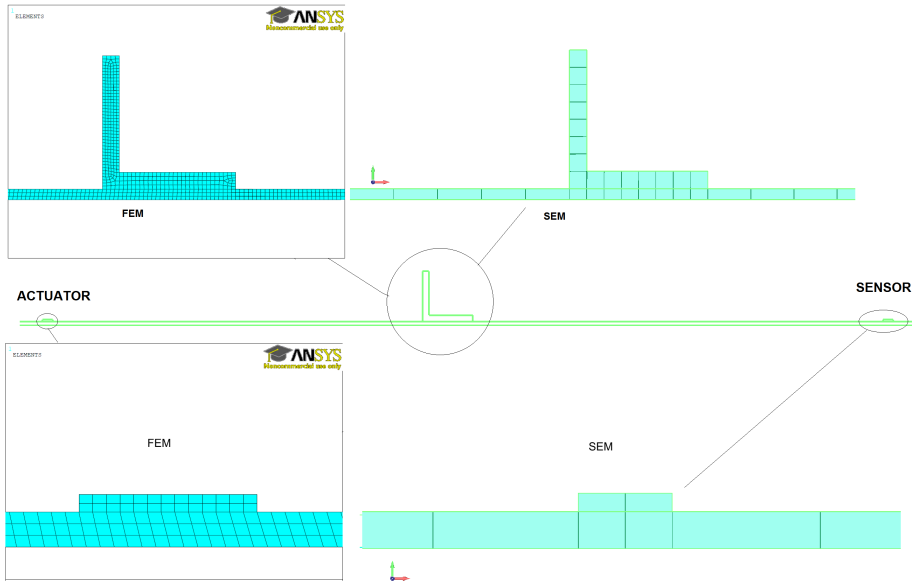

Figure 5.40 The two dimensional model both for the FEM, and the SEM, the mesh sizes were determined based on the resolution criteria for 200 kHz excitation frequency.

A damping tape was bonded along the boundaries of the region of interest to minimize the reflection from the boundaries. Figure 5.40 shows the two dimensional idealization of the cross section passing through the line connection between the two PZT elements. The measurements, as well as the numerical simulations were done at three frequencies, 100 kHz, 200 kHz, and 450 kHz.

Table 5.4 Properties of the aluminium plate and piezoceramics.

Component	Property	Value
Plate (Al 6066-T6)	Length	0.894 m
	Width	0.894 m
	Thickness	0.001 m
	Young's modulus	68.94 GPa
	Density	2712.59 kg/m^3
	Poisson's ratio	0.33
Stiffner (Al 2024)	Length	0.35 m
	Dimensions	0.01265 × 0.01265 m
	Thickness	0.0016 m
	Young's modulus	37.10 GPa
	Density	2767.90 kg/m^3
	Poisson's ratio	0.33
PZT Element	Diameter	0.0051 m
	Thickness	0.0005 m
	Inter-elements spacing (center to center)	0.21 m
	Density	7800 kg/m^3
	Piezoelectric type	PIC255 (Physik Intsrumente, Inc.)
	d_{31} = -180 $\times 10^{-12}$ (C/N)	d_{33} = 400 $\times 10^{-12}$ (C/N)
	d_{15} = 550 $\times 10^{-12}$ (C/N)	ϵ_{11} = 1650 $\times \epsilon_o$ (F/m)
	ϵ_{22} = 1650 $\times \epsilon_o$ (F/m)	ϵ_{33} = 1750 $\times \epsilon_o$ (F/m)
	C_{11} = 6.2112 $\times 10^{10}$ (N/m^2)	C_{12} = 1.576 $\times 10^{10}$ (N/m^2)
	C_{13} = 2.562 $\times 10^{10}$ (N/m^2)	C_{33} = 4.8309 $\times 10^{10}$ (N/m^2)
	C_{55}	2.5641 $\times 10^{10}$ (N/m^2)

A HP 33120A generator with a sampling frequency of 4 MHz and amplified by a voltage amplifier (Musilab UA-8400) is used to send 5.5 cycles modulated sinusoidal bursts to the left piezoceramic. Signal acquisition at the other piezoceramic is performed using a LabVIEW interface with a

high-impedance National Instruments PCI-5105 12 bits acquisition board. The recorded signal length is 1 ms and the sampling frequency is fixed at 60 MHz. All measurements are averaged 100 times. The actuators and sensors are made from PIC 255 piezoceramic from Physik Instrumente.

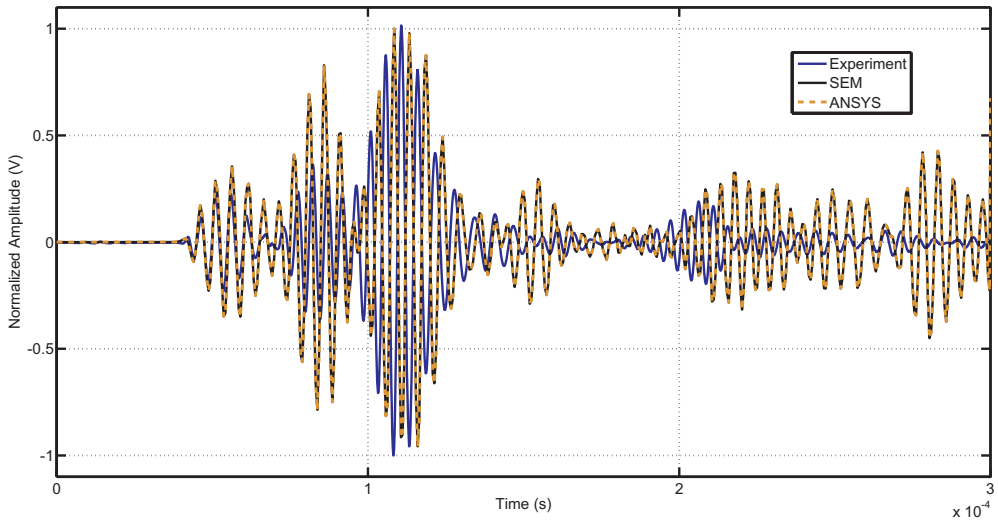

(a) 200 kHz

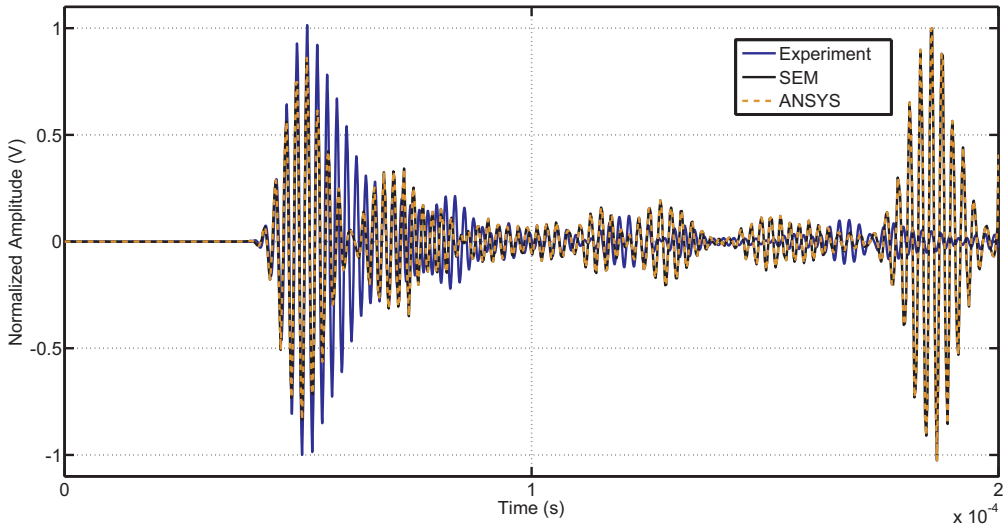

(b) 450 kHz

Figure 5.41 Time trace of the sensor signal, the simulated sensor signal using ANSYS, and the SEM code at (a) 200 kHz, and (b) 450 kHz

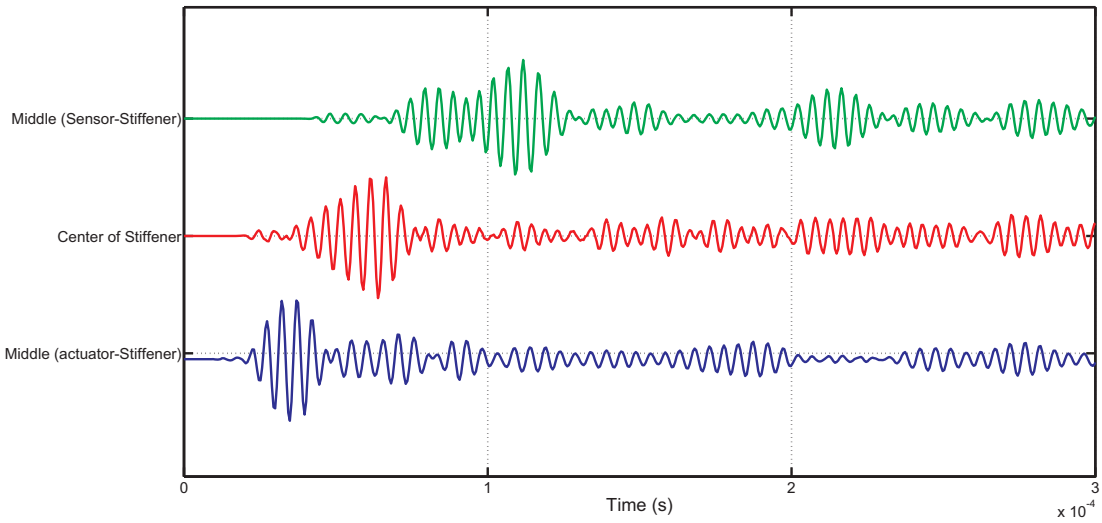

(a) 200 kHz

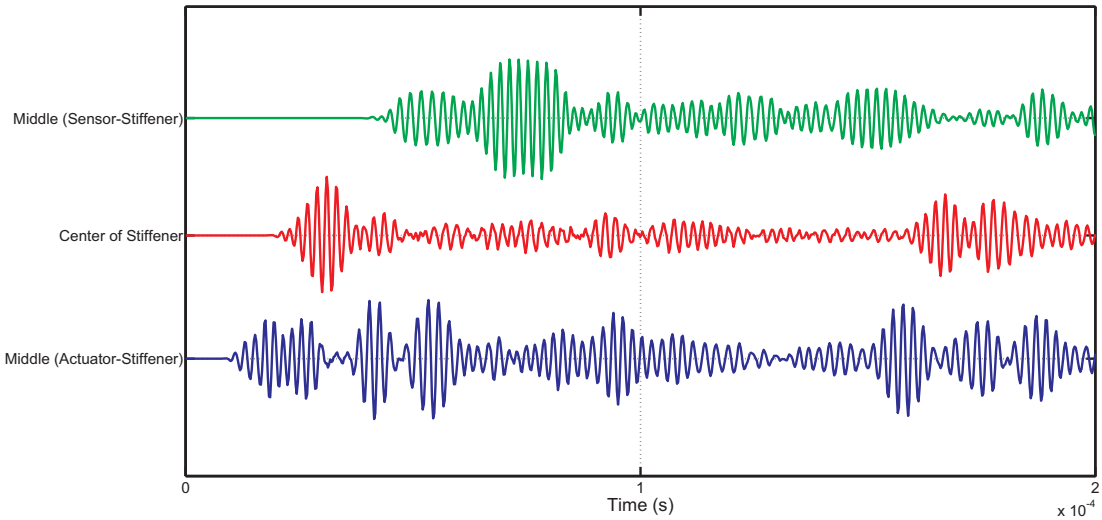

(b) 450 kHz

Figure 5.42 The simulation results of the Y component of the particle velocity, at three different locations surrounding the stiffener, at (a) 200 kHz and (b) 450 kHz.

In order to illustrate the computational effectiveness of the SEM, the same case was simulated using both classical FEM with the commercial FE software ANSYS, and the with SEM. The results of the experimental measurements, and the numerical simulation of the sensor signal for the two frequencies used in the present study are depicted in Figs. 5.41 and 5.42. The SEM and ANSYS results are in prefect agreement. The differences between the experimental and numerical results may be due to the geometrical simplification (the curvature of the stiffener was

not modeled) and to the presence of the bonding layer at the PZT element and the plate interface as well as at the interface between the stiffener and the plate which for the sake of simplicity was not included in the simulation.

In order to illustrate the interaction with the stiffener, the vertical component of the numerical simulation of the particle velocity is plotted at three locations in Fig. 5.42 the middle point between the actuator and L stiffener, the center of the stiffener, and the middle point between the stiffener and the sensor. The trend of interaction at the two frequencies are similar, with a noticeable amplification of the signal at 450 kHz excitation frequency, which could be attributed to the small wave interaction with the stiffener as a rigid body vibration at 200 kHz, since the wavelength is much larger than the width of the stiffener. While at 450 kHz, a higher energy level is imparted into the stiffener.

The CPU time, and the used resources in terms of the mesh size for both ANSYS and the SEM code is shown in Table 5.5 for the two different frequencies that were used in the present study. A reduction in time in the order of 50 % was achieved, without loss of accuracy.

Table 5.5 A comparison of the computational cost between FEM (ANSYS) and SEM code.

Method	Frequency (kHz)	Number of elements	computation time (min)
SEM	200	845	14
FEM		9123	32
SEM	450	1520	32
FEM		45132	54

5.6 Conclusion

As far as the limits of the applicability of the pin force idealization, the pin force model can only provide qualitative estimation about the actuation mechanism for low frequency cases, which needs to be calibrated by either numerical simulation or experimental testing, and piezoelectric resonance effects cannot be captured in the model. The results presented in this chapter and their discussions may be summarized into three main categories:

1. The shift with respect to frequency which is observed when considering the fully coupled PZT-plate problem and is also observed with the inclusion of the adhesive layer in the fully coupled model. Based on what was reported in [Gopalakrishnan *et al.*, 2011] and shown in Fig. 2.16 this form of shift could be attributed to changes in the traction spatial distribution at the interface, even if the mechanical coupling was excluded. But what Sec. 5.3.1 have

preliminarily showed is that even when the full traction loading from a fully coupled PZT is taken into consideration there is a slight shift in the natural frequencies due to the existence of the ceramic material *i.e.* mechanical coupling effect of the PZT.

2. The salient presence of the resonance of the PZT and its effect on the mode tuning curves. This effect is only present for the numerical simulation of the fully coupled system. It is has not been reproduced by any of the results of the reviewed analytical models, because of the simplifying assumptions of the analytical models, typically the geometry of the actuator is translated into traction condition at the interface with complete decoupling of the actuator.

3. The changes induced by the adhesive layer, is playing a very important role in changing the mode tuning curves. This is demonstrated in terms of the changes that the presence of the adhesive layer causes on the shear stress as sensed by the plate. This effects are qualitatively in accordance with the classical shear lag model, *i.e.* the presence of the adhesive layer smooths the fluctuation, and spreads the localized loading over a longer distance. Another aspect that remains valid from the classical shear lag solution is the duality between the thickness and the shear modulus of the adhesive layer. Reducing the thickness will induce a similar effect of increasing the shear modulus; this may be true at certain frequencies till the complicated resonances of the assembly elements (plate, PZT and adhesive layer) and their interactions take place.

Despite the shortcomings of today's analytical models, they remain the best available signposts for understanding the complicated phenomena associated with the PZT excitation of Lamb waves. They may provide an understanding, but when it comes to designing real SHM systems they will only provide guidelines that may not be sufficient or even may be erroneously misguiding when an accurate determination of the optimum excitation frequencies is needed. So, at the conclusion, any attempt to optimize the actuator for mode selectivity should take into consideration the whole actuator substructure assembly. This may limit the generality of the idea of producing a general mode selective actuator. The current paradigm in SHM design should be changing toward a specific tailoring of the actuator and sensor systems with the host structure, and with a more focus on certain areas to be detected.

CHAPTER 6

Conclusions

> Mathematics is a logical method ... Mathematical propositions express no thoughts. In life it is never a mathematical proposition which we need, but we use mathematical propositions only in order to infer from propositions which do not belong to mathematics to others which equally do not belong to mathematics.
>
> LUDWIG WITTGENSTEIN (1889-51)

The design requirements of a guided waves SHM system pose certain challenges to numerical simulation. In the second chapter it was demonstrated that the numerical dispersion is the major challenge confronting numerical simulation of high frequency elastic waves in general, moreover becomes more challenging in the case of guided waves propagation; this is due to the presence of the inherent physical dispersion in the simulated waves. Numerical dispersion is a complicated phenomenon, because it emanates from the accumulation (superposition) of the approximation errors which in turn are dependent on the both the spatial and temporal discretization, while the classical convergence criteria treats approximation errors as random and have no preferred tendency. The CFL analysis provided a corner step toward the understanding of this discretization effects and the nature of its accumulative superposition. The need to distinguish between the physical dispersion inherent in the simulated guided waves propagation and the discretization induced dispersion justify the work for the quantification of the numerical dispersion. Since the major contributer to the approximation error in high order interpolation is the Runge phenomena, minimizing these errors are expected to increase the accuracy of the approximation. The pseudospectral approximations provide a remedy to this problem, but lacks the geometrical flexibility provided by the finite element method and typically needed for simulating real world structures. The spectral element combines the best of both worlds, the geometrical flexibility to a certain extent, and the high accuracy or what is usually referred to as the exponential convergence behavior.

In the spectral element and as demonstrated in the third chapter, the specific distribution of nodes within the high order element overcome the Runge phenomenon associated with high order

interpolation at equispaced nodes. The choice of Legendre distribution influence directly the elemental shape functions and leads to diagonal mass matrices when combined with the corresponding Lobatto quadrature, thus reducing not only the number of nodes needed to accurately simulate the propagation but also the computational efforts needed for inverting the system. The accuracy of the spectral element approximation was demonstrated for the rod elements, for three different approximate theories of increasing complexity. This fact is manifested in the decrease of the numerical dispersion error at the same $\frac{h}{\lambda}$ with increasing polynomial order, which is a general observation for all the cases studied. It is worth noting that one of the conclusions from that chapter is that not just the number of mesh nodes sampling the wavelength that controls the accuracy, but also the distribution of those nodes in the sampled wavelength. For the case of higher order derivatives, normally encountered in the more complex engineering theories, the FEM, needs a special treatment to satisfy the continuity requirements, *e.g.* Hermite polynomials for beam elements. In the case of the spectral element, it is a straightforward extension of the concept of the differentiation matrices.

In this work we proposed a new concept, dubbed as conflict of order, and by which we meant the conflict between orders of both temporal and spatial discretization since generally the direct time integration used is low order while the spatial approximation is high order. The author proposed that this conflict could become more beneficial than normally expected, since the error goes back to zero at fewer grid points. This may be only valid for the simple geometries, but still a point that is worth exploration.

The conflict between orders of both temporal and spatial discretization, a previously observed phenomena in rod elements, is also observed for the case of the spectral element developed for the unbounded two dimensional elastic wave propagation in the forth chapter, *i.e.* the change of the trend of the error from underestimating the phase and group velocity in the harmonic case, to overestimation induced by the low order temporal discretization. This phenomenon could also become more beneficial than normally believed, since the error goes back to zero at fewer grid points, but the fact that there at two propagating wave simultaneously might limit the applicability of this kind of targeting zero error at few grid points.

In the forth chapter we utilized the fact that Lamb waves are plane waves in analyzing for the first time the numerical dispersion of Lamb waves propagation using the same technique of Rayleigh quotient. This analysis resulted in the discovery of the absence of the conflict of order phenomenon. The other interesting conclusion is that in the case of Lamb waves simulation, the numerical dispersion errors are less sensitive to the CFL numbers than the unbounded non dispersive elastic strain waves, suggesting that spectral element is the perfect candidate for simulating the Lamb waves in both the frequency and the time domain efficiently.

Also in the fourth chapter, the first order shear theory dispersion was studied and the conclusion was that the accuracy of the first order shear deformation as an approximate theory for the Lamb fundamental antisymmetric mode is very poor. But this inaccuracy emanates from the nature of the mathematical assumptions, not from the spectral element implementation. The analysis results in a beneficial demonstration of the absence of the shear locking behavior for the spectral element (when using polynomial orders > 3), and the complete absence of the numerical anisotropy for the first order shear deformation theory.

In all the cases of numerical dispersion analysis, the effect of numerical dispersion on the group velocity is larger by an order of magnitude than its effect on the phase velocity, thus it makes a more accurate measure to choose the mesh parameters and time step based on the errors induced in group velocity.

The generality of using Rayleigh quotient in the numerical dispersion analysis suggests a new interpretation: it could be viewed as a test for the efficiency of the sampling of an assumed displacement continuous field at a certain number and locations of discrete points. This interpretation opens a new way of application of this numerical dispersion analysis technique as a systematic approach that could lead to adaptive meshing approach.

The fifth chapter contains the application of the spectral element to the design of SHM systems, the piezoelectric element for PZT patch excitation of Lamb waves are studied in detail. The main limitations of the existing actuation analytical models are illuminated, and the time domain simulation was verified experimentally for two case studies.

As far as the limits of the applicability of the pin force idealization, the pin force model can only provide qualitative estimation about the actuation mechanism for low frequency cases, which needs to be calibrated by either numerical simulation or experimental testing, and piezoelectric resonance effects cannot be captured in the pin force model. The major conclusions are:

- The shift of the maxima and minima of S0 and A0 amplitudes toward higher frequencies is observed when considering the fully coupled PZT-plate problem with and without the adhesive layer. In the literature their is an abundant misconception that this shift is due to the adhesive layer. The results demonstrate otherwise.
- The salient presence of the resonance of the PZT and its effect on the mode tuning curves. This effect is only clear when simulating the fully coupled system. It has not been captured by any of the analytical models reviewed.
- The changes caused by the adhesive layer plays a very important role in changing the mode tuning curves. This is understood in terms of the changes it causes in the shear stress acting on the plate. This effects are qualitatively in accordance with the classical

shear lag model, *i.e.* the presence of the adhesive layer smooths the fluctuation, and spreads the localized loading over a longer distance. Another aspect that remains valid from the classical shear lag solution is the duality between the thickness and the shear modulus of the adhesive layer.

So, at the end, we suggest that any attempt to optimize the actuator for mode selectivity should take into consideration the whole actuator substructure assembly. This may limit the generality of the idea of producing a general mode selective actuator. The current paradigm in SHM design should be changing toward a specific tailoring of the actuator and sensor systems with the host structure, and with a better focus on certain areas to be detected.

Future Work

— The developed numerical dispersion technique is not limited to the SEM or Cartesian meshes. Extending the present study to both structured and unstructured meshes could enable an adaptive accuracy measure for complex geometries.

— Test the possibility of using the numerical dispersion technique as an adaptive convergence technique for complex meshes that does not have an exact solution.

— Extend the PZT full coupling model to the axisymmetric (2.5 dimensional models) and 3D dimensional model to account for the full spectrum of electromechanical resonance.

Conclusions

L'exigence de la conception d'un système SHM ondes guidées pose plusieurs défis de simulation numérique. Dans le deuxième chapitre, il a été démontré que la dispersion numérique est le principal défi auquel fait face la simulation numérique à haute fréquence des ondes élastiques en général. Celle-ci devient en outre plus difficile dans le cas de la propagation des ondes guidées; cela est dû à la présence de la dispersion physique inhérente dans les ondes simulées. La dispersion numérique est un phénomène complexe, car elle émane de l'accumulation (superposition) des erreurs d'approximation qui à leur tour dépendent de la discrétisation spatiale et temporelle, tandis que les critères de convergence classiques traitent les erreurs d'approximation comme aléatoire. L'analyse de la CFL fournit un outil important pour la compréhension des effets de discrétisation et la nature de leur superposition. La nécessité de faire la distinction entre la dispersion physique inhérente à la propagation de l'onde simulée et la dispersion induite par la discrétisation justifie le travail pour la quantification de la dispersion numérique. Puisque la plus grande contribution à l'erreur d'approximation en interpolation d'ordre élevé est le phénomène de Runge, en minimisant cette erreur on peut s'attendre à augmenter l'exactitude de l'approximation. Les approximations pseudospectrales fournissent une solution à ce problème, mais n'offrent pas la flexibilité géométrique fournie par la méthode des éléments finis et généralement nécessaire pour simuler les structures du monde réel. L'élément spectral combine le meilleur des deux mondes, la flexibilité géométrique dans une certaine mesure, et la grande précision ou ce qui est généralement dénommé le comportement de convergence exponentielle.

Dans l'élément spectral, et comme l'a démontré le troisième chapitre, la distribution spécifique des noeuds dans l'élément d'ordre élevé permet de surmonter le phénomène de Runge associé avec interpolation d'ordre élevé àă noeuds équidistants. Le choix de la distribution de Legendre directement dans les fonctions de formes élémentaires conduit à des matrices de masse diagonale lorsqu'il est combiné avec la quadrature de Lobatto correspondante, ce qui réduit non seulement le nombre de noeuds nécessaires pour simuler avec précision la propagation mais aussi les efforts de calcul nécessaires pour inverser le système. La précision de l'approximation par éléments spectraux a été démontrée pour les éléments en forme de tige, pour trois différentes théories approximatives de complexité croissante. Cet effet se manifeste par la diminution de l'erreur de dispersion numérique pour un même ratio $\frac{h}{\lambda}$ avec l'augmentation de l'ordre polynomial, qui est une observation générale pour tous les cas étudiés. Il est intéressant de noter que l'une des conclusions de ce chapitre est que non seulement le nombre de noeuds du maillage d'échantillonnage de la longueur d'onde contrôle l'exactitude, mais aussi la distribution de ces

noeuds dans la longueur d'onde échantillonnée. Pour le cas des dérivées d'ordre supérieur, normalement rencontrées dans les théries d'ingénierie les plus complexes, le FEM, a besoin d'un traitement spécial pour satisfaire aux exigences de continuité, *e.g.* polynômes d'Hermite pour les éléments de faisceau. Dans le cas de l'élément spectral, il s'agit d'un simple prolongement de la notion de matrices de différenciation.

Dans ce travail, nous avons proposé un nouveau concept, baptisé conflit d'ordre, et par lequel nous voulions faire ressortir le conflit entre les ordres de discrétisation temporelle et spatiale puisque généralement l'intégration temporelle directe utilisée est d'ordre faible alors que l'ordre d'approximation spatial est élevé. L'auteur a proposé que ce conflit pourrait devenir plus avantageux qu'on ne le croit généralement, puisque l'erreur tend vers zéro à un nombre réduit de points du maillage. Cette observation est peut-être uniquement valable pour les géométries simples, mais c'est un point qui mérite exploration.

Le conflit entre les ordres de discrétisation temporelle et spatiale, un phénomène déjàă observé dans les éléments de tige, est également observé pour le cas de l'élément spectral développé pour le cas de propagation des ondes élastiques dans un milieu non-borné dans le chapitre quatre, *i.e.* le changement de la tendance de l'erreur d'une sous-estimation de la vitesse de groupe et de phase dans le cas harmonique, à une sur-estimation induite par l'ordre faible de discrétisation temporelle. Ce phénomène pourrait aussi devenir plus avantageux qu'on ne le croit généralement, puisque l'erreur tend vers zéro à un nombre réduit de points du maillage, mais le fait qu'il y ait deux ondes se propageant simultanément peut limiter l'application de ce type de mise à zéro de l'erreur à quelques points du maillage.

Dans le quatrième chapitre, nous avons utilisé le fait que ondes de Lamb sont des ondes planes dans l'analyse, pour la première fois, de la dispersion numérique de la propagation des ondes de Lamb utilisant la technique du quotient de Rayleigh. Cette analyse a abouti à la découverte de l'absence du phénomène de conflit d'ordre. L'autre conclusion intéressante est que, dans le cas de la simulation des ondes de Lamb, les erreurs de dispersion numériques sont moins sensibles aux valeurs de la CFL que dans le cas de l apropagation des ondes élastiques non-bornées, ce qui suggère que l'élément spectral est le candidat idéal pour simuler les ondes de Lamb dans le domaine fréquentiel et le domaine temporel de manière efficace.

Toujours dans le quatrième chapitre, la dispersion de la théorie de déformation du cisaillement de premier ordre a été étudiée et la conclusion était que la précision de la théorie de déformation du cisaillement de premier ordre utilisée comme approximation pour le mode de Lamb anti-symétrique fondamental est très faible. Mais cette imprécision émane de la nature des hypothèses mathématiques, pas de la mise en oeuvre des éléments spectraux. Les résultats d'analyse per-

mettent de démontrer l'absence du comportement de vérouillage en cisaillement de l'élément spectral (lors de l'utilisation des polynômes d'ordre > 3), et l'absence complète de l'anisotropie numérique pour la théorie de déformation de cisaillement de premier ordre.

Dans tous les cas d'analyse de la dispersion numérique, l'effet de dispersion numérique sur la vitesse de groupe est plus grand d'un ordre de grandeur que l'effet sur la vitesse de phase, ce qui rend plus approprié de choisir les paramètres de maillage et de pas de temps sur la base de les erreurs induites dans la vitesse de groupe.

La généralité de l'utilisation du quotient de Rayleigh dans l'analyse de la dispersion numérique propose une nouvelle interprétation: il pourrait être considéré comme un test pour l'efficacité de l'échantillonnage d'un champ de déplacement continu sur un certain nombre de points à différentes positions discrètes. Cette interprétation ouvre une nouvelle voie de l'application de cette technique d'analyse de la dispersion numérique comme une approche systématique qui pourrait conduire à une approche de maillage adaptatif.

Le cinquième chapitre contient l'application de l'élément spectral à la conception de systèmes SHM; l'élément piézoélectrique PZT utilisé pour l'excitation des ondes de Lamb est étudié en détails. Les principales limitations des modèles existants pour l'analyse de l'excitation sont soulignées, et la simulation dans le domaine temporel a été validée expérimentalement pour deux cas d'étude.

En ce qui concerne les limites de l'applicabilité du modèle idéalisé d'excitation piézoélectrique par forces ponctuelles, le modèle de forces ponctuelles ne peut fournir qu'une estimation qualitative sur le mécanisme d'excitation aux basses fréquences. Ce modèle doit être calibré, soit par simulation numérique, soit par des essais expérimentaux. Les effets de résonance piézoélectrique ne peuvent pas être capturés dans le modèle des forces ponctuelles. Les principales conclusions sont les suivantes:

— Le décalage des maxima et des minima d'amplitude des modes S0 et A0 vers des fréquences plus élevées est observé en considérant le problème du PZT complètement couplé avec la plaque avec et sans la couche d'adhésif. Dans la littérature, il existe une fausse conception que ce décalage est causé par la couche d'adhésif, mais les résultats obtenus montrent que ce n'est pas le cas.

— La présence marquée de la résonance du PZT et son effet sur les courbes d'ajustement modal. Cet effet est seulement apparent lors de la simulation avec le modèle complètement couplé. Il n'a été capturé par aucun des modèles analytiques considérés dans ce travail.

— Les changements provoqués par la couche d'adhésif jouent un rôle très important dans l'évolution des courbes d'ajustement modal. Ceci est peut être interprété en termes

des changements qu'elle provoque dans la contrainte de cisaillement agissant sur la plaque. Ces effets sont qualitativement en accord avec le modèle classique de décalage de cisaillement (*shear-lag*), *i.e.* la présence de la couche d'adhésif lisse la fluctuation, et étend la contrainte de cisaillement localisée sur une distance plus longue. Un autre aspect qui reste valable dans le modèle classique de décalage de cisaillement est la dualité entre l'épaisseur et le module de cisaillement de la couche d'adhésif.

Ainsi, à la fin, nous suggèrons que toute tentative visant à optimiser l'actionneur pour une sélectivité modale devrait prendre en consideration l'ensemble de la sous-structure actionneur. Cela peut limiter la généralité de l'idée de produire un actionneur sélectif pour un ensemble d'applications. Le paradigme actuel dans la conception SHM doit évoluer vers une adaptation spécifique des systèmes d'actionneurs et de capteurs sur la structure d'accueil, avec une plus grande attention sur certaines régions qui doivent être surveillées.

Les travaux à venir

— La technique de dispersion numérique développée n'est pas limitée à la SEM ou maillages cartésiens. Extension de la présente étude à deux mailles structurées et non structurées pourrait permettre une mesure de la précision d'adaptation pour des géométries complexes.

— Test de la possibilité d'utiliser la technique de dispersion numérique comme une technique de convergence adaptative pour les maillages complexes qui ne présente pas une solution exacte.

— Étendre le modèle de couplage complet PZT à la révolution (2,5 modèles dimensionnels) et un modèle tridimensionnel 3D pour tenir compte de la gamme complète de résonance électromécanique.

APPENDIX A

Mathematical definitions

A.1 Norms and seminorms

The norm of a function or vector is a measure of the size of the function or vector. Norms are real positive numbers defined on some space X. Norms, denoted by $\|.\|_X$, have the following properties:

1. $\|u\|_X \geq 0$
2. $\|u\|_X = 0$ iff $u = 0$
3. $\|\alpha u\|_X = |\alpha| \|u\|_X$
4. $\|u + v\|_X \leq \|u\|_X + \|v\|_X$

The most commonly used norms in the numerical discretization analysis are the energy norm $\|u\|_E$ which is the square root of the strain energy stored in the elastic domain, for one dimensional domain this is given as

$$\|u\|_E = \sqrt{U(u)} = \sqrt{\frac{1}{2} \int_a^b (\partial_x u)^2 \, dx} \tag{A.1}$$

the maximum norm defined as:

$$\|u\|_{max} = \text{Max}|u(x)| \tag{A.2}$$

and the L_2 norm defined as:

$$\|u\|_{L_2} = \sqrt{\int_a^b u^2 \, dx} \tag{A.3}$$

Seminorms satisfy properties 1, 3 and 4 of norms but do not satisfy property 2. Instead of property 2 seminorms have the property

$$\|u\|_X = 0 \qquad u \in \bar{X} \subset X, \qquad u \neq 0$$

The relative error of u_n, a numerical approximation to u, is defined according to space X as:

$$(e_r)_X = \frac{\|u - u_n\|_X}{\|u\|_X} \tag{A.4}$$

A.2 Convergence

A sequence of functions $u_n \in X$ $(n = 1, 2, \ldots)$ converges in the space X to the function $u \in X$ if for every $\epsilon > 0$ there is a number n_ϵ such that for any $n > n_\epsilon$ the following relationship holds:

$$\|u - u_n\|_X < \epsilon \tag{A.5}$$

A.3 Legendre polynomials

The Legendre polynomials $Pn(x)$ are solutions of the Legendre differential equation for $n = 0, 1, 2, \ldots$:

$$(1 - x^2)y'' - 2xy' + n(1 + n)y = 0, \qquad -1 \leq x \geq 1 \tag{A.6}$$

The first three polynomials are

$$P_0(x) = 0 \tag{A.7}$$

$$P_1(x) = 1 \tag{A.8}$$

$$P_2(x) = \frac{1}{2}(3x^2 - 1) \tag{A.9}$$

Legendre polynomials can be generated from the recursion formula:

$$P_{n+1} = \frac{(2n + 1)xP_n(x) - nP_{n-1}}{n + 1}, \qquad n = 1, 2, \ldots \tag{A.10}$$

and Legendre polynomials satisfy the following relationship:

$$(2n + 1)P_n(x) = P'_{n+1}(x) - P'_{n-1}(x), \qquad n = 1, 2, \ldots \tag{A.11}$$

Legendre polynomials satisfy the following orthogonality property:

$$\int_{-1}^{+1} P_i(x)P_j(x)\,dx = \frac{2\delta_{ij}}{2i + 1} \tag{A.12}$$

All roots of Legendre polynomials are located in the interval $-1 < x < +1$.

A.4 Numerical quadrature

In one dimension the domain of integration is the standard element $-1 < x < +1$. An integral expression on the standard element is approximated by a sum:

$$\int_{-1}^{+1} f(\xi)\,d\xi \approx \sum_{i=1}^{n} w_i f(\xi_i) + R_n \tag{A.13}$$

where w_i are the weights,ξ_i are the abscissas and R_n is the error term which depends on the smoothness of the integrand.

A.4.1 Gauss quadrature

In Gaussian quadrature the abscissa ξ_i is the ith zero of Legendre polynomial P_n. The weights are computed from:

$$w_i = \frac{2}{(1-\xi_i^2)[P_n'(\xi_i)]^2} \tag{A.14}$$

The error term is:

$$R_n = \frac{2^{2n+1}(n!)^4}{(2n+1)[(2n)!]^3} f^{(2n)}(\xi) \tag{A.15}$$

where $f^{(2n)}$ is the $2n$th derivative of f. It can be seen from the error term that if $f(\xi)$ is a polynomial of degree p and Gaussian quadrature is used, then the integral will be exact (up to round-off errors) provided that $n \geq (p+1)/2$.

A.4.2 Gauss Lobatto quadrature

In the Gauss Lobatto quadrature the abscissas are as follows: $x_1 = -1, x_n = 1$ and for $i = 2, 3, \ldots, n-1$ the $(i-1)$th zero of $P_{n-1}'(x)$ where $P_{n-1}(x)$ is the $(n-1)$th Legendre polynomial. The weights are:

$$w_i = \begin{cases} \frac{2}{n(n-1)} & i = 0 \;\&\; n \\ \frac{2}{n(n-1)[P_{n-1}(\xi_i)]^2} & i = 2, 3, \ldots, (n-1) \end{cases} \tag{A.16}$$

The error term is

$$R_n = \frac{-n(n-1)^3 2^{2n-1}[(n-1)!]^4}{(2n-1)[(2n-2)!]^3} f^{(2n-2)}(\xi) \tag{A.17}$$

from which it follows that if $f(\xi)$ is a polynomial of degree p and Gauss Lobatto quadrature is used, then the integral will be exact (up to round-off errors) provided that $n \geq (p+3)/2$.

APPENDIX B

Weak form derivations

The strong form is the combination of the partial differential equation(s) governing the physical phenomena and the boundary conditions, and the set of initial conditions.

B.1 Strong form of IBV elastodynamic problem

The strong form of the initial boundary value (IBV) problem of Elastodynamics could be stated briefly as:

Momentum Conservation Equations

$$\begin{aligned}
&\rho\ddot{u}_i - \partial_i\sigma_{ij} = f_i(t) && \forall \quad \mathbf{x} \in \Omega;\\
&u_i(\mathbf{x},0) = 0,\ \dot{u}_i(\mathbf{x},0) = 0 && \forall \quad \mathbf{x} \in \Omega;\\
&u_i(\mathbf{x},t) = g_i(\mathbf{x},t) && \forall \quad \mathbf{x} \in \Gamma_g;\\
&\sigma_{ij}\,n_i = h_i && \forall \quad \mathbf{x} \in \Gamma_t;
\end{aligned}$$

Constitutive Equations

$$\sigma_{ij} = c_{ijkl}\epsilon_{kl}$$

$$\epsilon_{ij} = \frac{1}{2}(\partial_j u_i + \partial_i u_j)$$

Where the physical domain Ω, is bounded by $\Gamma = \Gamma_g \cup \Gamma_t$ & $\Gamma_g \cap \Gamma_t = \phi$; where at Γ_g the essential boundary condition is specified, and at Γ_t the natural boundary condition is specified, and the initial conditions are homogeneous. The strong form is complemented by the constitutive equations; where c_{ijkl} is the 4th order elasticity tensor elements.

B.2 Weak form of IBV elastodynamic problem

The weak form of the IBV elastodynamic problem is obtained via a Galerkin scheme, by multiplying the strong form by a test vector $\mathbf{v}$.

$$(\mathbf{v}, \rho\ddot{\mathbf{u}}) + a(\mathbf{v},\mathbf{u}) = (\mathbf{v},\mathbf{f}) + (\mathbf{v},\mathbf{h})_\Gamma$$

where

$$\begin{aligned}
a(\mathbf{v},\mathbf{u}) &= \int_\Omega \partial_j \mathrm{v}_i c_{ijkl}\partial_l u_k \, d\Omega\\
(\mathbf{v},\mathbf{f}) &= \int_\Omega \mathrm{v}_i f_i \, d\Omega\\
(\mathbf{v},\mathbf{h})_\Gamma &= \sum_{i=1}^{n_{sd}} \left(\int_{\Gamma_{h_i}} \mathrm{v}_i h_i \, d\Gamma \right)
\end{aligned}$$

B.3 One dimensional theories

B.3.1 Classical theory

We start by stating the strong form formulation,

$$\rho A\ddot{u} - EA\partial_x^2 u = 0 \tag{B.1}$$

Boundary conditions

$$\text{Free}: \quad \partial_x u(x,t) \mid_{x=0,l} = 0 \tag{B.2}$$
$$\text{Fixed}: \quad u(x,t) \mid_{x=0,l} = 0 \tag{B.3}$$

Initial Conditions

$$u(x,0) = 0 \quad \& \quad \dot{u}(x,0) = 0 \tag{B.4}$$

The first step to get the weak formulation is to multiply Equation (B.1) with a time-independent test function $\mathrm{v}(x)$. This function must be H^1 function for second order differential equation, where H^1 is the set of functions that are, together with their first derivative, square integrable (*i.e.* continuous and well-behaved function) over the domain. Integrating the equation over the spatial domain leads to

$$\rho \int_0^l \ddot{u}\mathrm{v}\, dx - E \int_0^l \mathrm{v}\partial_x^2 u\, dx = 0 \tag{B.5}$$

Integrating by parts the second term on left side,

$$\rho \int_0^l \ddot{u}\mathrm{v}\, dx - E(\mathrm{v}\partial_x u) \mid_0^l + E \int_0^l \partial_x \mathrm{v}\partial_x u\, dx = 0 \tag{B.6}$$

After substituting the natural boundary condition (Free ends), we obtain the weak form as

$$\rho \int_0^l \ddot{u}\mathrm{v}\, dx + E \int_0^l \partial_x \mathrm{v}\partial_x u\, dx = 0 \tag{B.7}$$

B.3.2 Rayleigh Love theory

We start by stating the strong form formulation,

$$\rho A\ddot{u} - EA\partial_x^2 u - \rho\nu^2 I_p \partial_x^2 \ddot{u} = 0 \tag{B.8}$$

Boundary conditions

$$\text{Free}: \quad AE\partial_x u(x,t) + \rho\nu^2 I_p \partial_x \ddot{u}(x,t) \mid_{x=0,l} = 0 \tag{B.9}$$
$$\text{Fixed}: \quad u(x,t) \mid_{x=0,l} = 0 \tag{B.10}$$

Initial Conditions

$$u(x,0) = 0 \quad \& \quad \dot{u}(x,0) = 0 \tag{B.11}$$

similar to the previous procedure, we multiply all sides of the equation (B.8) with a test function $\mathrm{v}(x)$, and integrate

$$\rho \int_0^l \ddot{u}\mathrm{v}\, dx - E \int_0^l \partial_x^2 u\mathrm{v}\, dx - \rho\nu^2 I_n \int_0^l \partial_x^2 \ddot{u}\mathrm{v}\, dx = 0 \tag{B.12}$$

where $I_n = I_p/A$, then integrating by parts and rearranging

$$\rho \int_0^l \ddot{u}\mathrm{v}\, dx + \rho\nu^2 I_n \int_0^l \partial_x \ddot{u}\partial_x \mathrm{v}\, dx + E \int_0^l \partial_x u \partial_x \mathrm{v}\, dx - \mathrm{v}(E\partial_x u + \rho\nu^2 I_n \partial_x \ddot{u}) \mid_0^l = 0 \tag{B.13}$$

which after substituting the free boundary condition gives the weak form

$$\rho \int_0^l \ddot{u}\mathrm{v}\, dx + \rho\nu^2 I_n \int_0^l \partial_x \ddot{u}\partial_x \mathrm{v}\, dx + E \int_0^l \partial_x u \partial_x \mathrm{v}\, dx = 0 \tag{B.14}$$

B.3.3 Rayleigh Bishop theory

We start by stating the strong form formulation,

$$\rho A\ddot{u} - EA\partial_x^2 u - \rho\nu^2 I_p \partial_x^2 \ddot{u} + \mu\nu^2 I_p \partial_x^4 u = 0 \tag{B.15}$$

Boundary conditions

$$\text{Free}: \quad AE\partial_x u(x,t) + \rho\nu^2 I_p \partial_x \ddot{u}(x,t) - \mu\nu^2 I_p \partial_x^3 u(x,t) \mid_{x=0,l} = 0 \ \& \ \partial_x^2 u(x,t) \mid_{x=0,l} = 0 \tag{B.16}$$

$$\text{Fixed}: \quad u(x,t) \mid_{x=0,l} = 0 \quad \& \quad \partial_x u(x,t) \mid_{x=0,l} = 0 \tag{B.17}$$

Initial conditions

$$u(x,0) = 0 \quad \& \quad \dot{u}(x,0) = 0 \tag{B.18}$$

Due to the presence of 4th order spatial derivatives, the test function $\mathrm{v}(x)$ should belong to H^2 set of functions (*i.e.* , $\int_0^l (\partial_x^2 \mathrm{v})^2\, dx < \infty$). Since the first three terms are identical to Rayleigh Love theory, the only additional term (4th order derivative) is then integrated by parts twice to yield after rearrangement

$$\rho \int_0^l \ddot{u}\mathrm{v}\, dx + \rho\nu^2 I_n \int_0^l \partial_x \ddot{u}\partial_x \mathrm{v}\, dx + E \int_0^l \partial_x u \partial_x \mathrm{v}\, dx + \mu\nu^2 I_n \int_0^l \partial_x^2 u \partial_x^2 \mathrm{v}\, dx$$
$$- \left[\mathrm{v}(E\partial_x u + \rho\nu^2 I_n \partial_x \ddot{u} + \mu\nu^2 I_n \partial_x^3 u) + \mu\nu^2 I_n \partial_x^2 u \partial_x \mathrm{v}\right] \mid_0^l = 0$$

which after substituting the free boundary condition gives the weak form

$$\rho \int_0^l \ddot{u}\mathrm{v}\, dx + \rho v^2 I_n \int_0^l \partial_x \ddot{u} \partial_x \mathrm{v}\, dx + E \int_0^l \partial_x u \partial_x \mathrm{v}\, dx + \mu v^2 I_n \int_0^l \partial_x^2 u \partial_x^2 \mathrm{v}\, dx = 0 \tag{B.19}$$

B.3.4 Mindlin-Herrmann theory

We start by stating the strong form formulation,

$$\rho A \ddot{u}_0 - (\lambda + 2\mu) A \partial_x^2 u_0 - 2\lambda A \partial_x w_1 = 0 \tag{B.20a}$$
$$\rho I_p \ddot{w}_1 + 2\lambda A \partial_x u_0 - \mu I_p \partial_x^2 w_1 + 4A(\lambda + \mu) w_1 = 0 \tag{B.20b}$$

Boundary conditions

$$\text{Free :} \quad (\lambda + 2\mu)\partial_x u_0(x,t) + 2\lambda w_1(x,t) \mid_{x=0,l} = 0 \;\&\; \partial_x w_1(x,t) \mid_{x=0,l} = 0 \tag{B.21}$$
$$\text{Fixed :} \quad u_0(x,t) \mid_{x=0,l} = 0 \quad \& \quad w_1(x,t) \mid_{x=0,l} = 0 \tag{B.22}$$

Initial conditions

$$u_0(x,0) = 0 \quad \& \quad \dot{u}_0(x,0) = 0$$
$$w_1(x,0) = 0 \quad \& \quad \dot{w}_1(x,0) = 0 \tag{B.23a}$$

Here we assume two test functions v_1 and v_2. Then multiply equation (B.20) by v_1, and integrate over the length:

$$\rho \int_0^l \ddot{u}_0 \mathrm{v}_1\, dx - (\lambda + 2\mu) \int_0^l \partial_x^2 u_0 \mathrm{v}_1\, dx - 2\lambda \int_0^l \partial_x w_1 \mathrm{v}_1\, dx$$

And Integrating by parts all the terms

$$\rho \int_0^l \ddot{u}\mathrm{v}_1\, dx + (\lambda + 2\mu) \int_0^l \partial_x u_0 \partial_x \mathrm{v}_1\, dx + 2\lambda \int_0^l w_1 \partial_x \mathrm{v}_1\, dx - ((\lambda + 2\mu)\mathrm{v}_1 \partial_x u_0 + 2\lambda \mathrm{v}_1 w_1) \mid_0^1 = 0 \tag{B.24}$$

Similarly for equation (B.20), after dividing all terms by A, and multiplying by test function v_2, and integrating over the length:

$$\rho \mathrm{R}^2 \int_0^l \ddot{w}_1 \mathrm{v}_2\, dx - \mathrm{R}^2 \mu \int_0^l \partial_x^2 w_1 \mathrm{v}_2\, dx + 4\lambda \int_0^l \mathrm{v}_2 w\, dx = 0 \tag{B.25}$$

And integrating by parts:

$$\rho \mathrm{R}^2 \int_0^l \ddot{w}_1 \mathrm{v}_2 \, dx + 4\lambda \int_0^l \mathrm{v}_2 \partial_x u_1 \, dx + 8(\lambda+\mu) \int_0^l \mathrm{v}_2 w_1 \, dx + \int_0^l \partial_x w_1 \partial_x \mathrm{v}_2 \, dx - \partial_x w_1 \mathrm{v}_2 \, |_0^l = 0 \quad \text{(B.26)}$$

Which after the substitution of the natural boundary condition, leads to the following weak form:

$$\rho \int_0^l \ddot{u} \mathrm{v}_1 \, dx + (\lambda + 2\mu) \int_0^l \partial_x u_0 \partial_x \mathrm{v}_1 \, dx + 2\lambda \int_0^l w_1 \partial_x \mathrm{v}_1 \, dx = 0 \quad \text{(B.27a)}$$

$$\rho \mathrm{R}^2 \int_0^l \ddot{w}_1 \mathrm{v}_2 \, dx + 4\lambda \int_0^l \mathrm{v}_2 \partial_x u_1 \, dx + 8(\lambda+\mu) \int_0^l \mathrm{v}_2 w_1 \, dx + \int_0^l \partial_x w_1 \partial_x \mathrm{v}_2 \, dx = 0 \quad \text{(B.27b)}$$

B.4 Two dimensional theories

In this section we list the well known two dimensional weak form for the elastic wave equation in plane strain setting. As for the first order shear deformation theory, we refer the reader to [Reddy, 2002], where we followed the same derivation for the spectral element development.

B.4.1 Elastic wave equation

$$(c_l^2 - c_t^2) \nabla (\nabla \cdot \mathbf{u}) - c_t^2 \nabla \cdot \nabla \mathbf{u} = \ddot{\mathbf{u}} \quad \text{(B.28)}$$

We will assume that the medium is isotropic, homogeneous, unbounded, and source free. Taking a dot product of equation (B.28) with a vector test function, integrating over the domain, and using the divergence theorem, we obtain the weak form of the elastic wave equation, given by

$$(c_l^2 - c_t^2) \int_\Omega (\nabla \cdot \mathbf{u})(\nabla \cdot \mathbf{v}) \, dxdy + c_t^2 \int_\Omega \nabla \mathbf{u} : \nabla \mathbf{v} \, dxdy \quad \text{(B.29)}$$

where $\mathbf{v}$ is a sufficiently smooth test function and the double dot product is defined as $\mathbf{A} : \mathbf{B} = \sum_1^n \sum_1^n A_{ij} B_{ij}$ for $\mathbf{A}, \mathbf{B} \in \mathfrak{R}^{\mathbf{n} \times \mathbf{n}}$.

B.5 Piezoelectric element

The starting point is by multiplying Eq. (5.15b) by a test function $\mathbf{w} = (w_1\ w_3)^{\mathrm{T}}$ and integrating parts and using Green's theorem we obtain:

$$\int_{\Omega_p} \mathbf{w}^{\mathrm{T}} \rho_p \ddot{\mathbf{u}}_p \, d\Omega = \int_{\Omega_p} \mathbf{w}^{\mathrm{T}} \boldsymbol{\mathcal{B}}^{\mathrm{T}} (\mathbf{c}^E \boldsymbol{\mathcal{B}} \mathbf{u}_p + \mathbf{e}^{\mathrm{T}} \boldsymbol{\nabla} \phi) \, d\Omega \tag{B.30a}$$

$$= \oint_{\partial\Omega_p} \mathbf{w}^{\mathrm{T}} \mathbf{n}_p^{\mathrm{T}} (\mathbf{c}^E \boldsymbol{\mathcal{B}} \mathbf{u}_p + \mathbf{e}^{\mathrm{T}} \boldsymbol{\nabla} \phi) \, d\partial - \int_{\Omega_p} (\boldsymbol{\mathcal{B}} \mathbf{w})^{\mathrm{T}} (\mathbf{c}^E \boldsymbol{\mathcal{B}} \mathbf{u}_p + \mathbf{e}^{\mathrm{T}} \boldsymbol{\nabla} \phi) \, d\Omega$$

$$= \int_{\partial\Omega_p - \partial_g} \mathbf{w}^{\mathrm{T}} \mathbf{n}^{\mathrm{T}} (\mathbf{c}^E \boldsymbol{\mathcal{B}} \mathbf{u}_p + \mathbf{e}^{\mathrm{T}} \boldsymbol{\nabla} \phi) \, d\partial + \int_{\partial_g} \mathbf{w}^{\mathrm{T}} \mathbf{n}_p^{\mathrm{T}} (\mathbf{c}^E \boldsymbol{\mathcal{B}} \mathbf{u}_p + \mathbf{e}^{\mathrm{T}} \boldsymbol{\nabla} \phi) \, d\partial$$

$$- \int_{\Omega_p} (\boldsymbol{\mathcal{B}} \mathbf{w})^{\mathrm{T}} (\mathbf{c}^E \boldsymbol{\mathcal{B}} \mathbf{u}_p + \mathbf{e}^{\mathrm{T}} \boldsymbol{\nabla} \phi) \, d\Omega$$

$$= \int_{\partial_g} \mathbf{w}^{\mathrm{T}} \mathbf{n}_p^{\mathrm{T}} (\mathbf{c}^E \boldsymbol{\mathcal{B}} \mathbf{u}_p + \mathbf{e}^{\mathrm{T}} \boldsymbol{\nabla} \phi) \, d\partial - \int_{\Omega_p} (\boldsymbol{\mathcal{B}} \mathbf{w})^{\mathrm{T}} (\mathbf{c}^E \boldsymbol{\mathcal{B}} \mathbf{u}_p + \mathbf{e}^{\mathrm{T}} \boldsymbol{\nabla} \phi) \, d\Omega \tag{B.30b}$$

Where by the first part of the contour integral over $\partial\Omega_p - \partial_g$ vanishes by virtue of Eq. (5.15d), and the only remaining part is the second integral representing the traction continuity at the interface ∂_g. For Eq. (5.15c), the same procedure yields:

$$\int_{\Omega_s} \mathbf{w}^{\mathrm{T}} \rho_s \ddot{\mathbf{u}}_s \, d\Omega = \int_{\Omega_s} \mathbf{w}^{\mathrm{T}} \boldsymbol{\mathcal{B}}^{\mathrm{T}} \mathbf{c}_s \boldsymbol{\mathcal{B}} \mathbf{u}_s \, d\Omega \tag{B.31a}$$

$$= \oint_{\partial\Omega_s} \mathbf{w}^{\mathrm{T}} \mathbf{n}_s^{\mathrm{T}} \mathbf{c}_s \boldsymbol{\mathcal{B}} \mathbf{u}_s \, d\partial - \int_{\Omega_s} (\boldsymbol{\mathcal{B}} \mathbf{w})^{\mathrm{T}} \mathbf{c}_s \boldsymbol{\mathcal{B}} \mathbf{u}_s \, d\Omega$$

$$= \int_{\partial\Omega_s - \partial_g} \mathbf{w}^{\mathrm{T}} \mathbf{n}_s^{\mathrm{T}} \mathbf{c}_s \boldsymbol{\mathcal{B}} \mathbf{u}_s \, d\partial + \int_{\partial_g} \mathbf{w}^{\mathrm{T}} \mathbf{n}_s^{\mathrm{T}} \mathbf{c}_s \boldsymbol{\mathcal{B}} \mathbf{u}_s \, d\partial - \int_{\Omega_s} (\boldsymbol{\mathcal{B}} \mathbf{w})^{\mathrm{T}} \mathbf{c}_s \boldsymbol{\mathcal{B}} \mathbf{u}_s \, d\Omega$$

$$= \int_{\partial_g} \mathbf{w}^{\mathrm{T}} \mathbf{n}_p^{\mathrm{T}} \mathbf{c}_s \boldsymbol{\mathcal{B}} \mathbf{u}_s \, d\partial - \int_{\Omega_s} (\boldsymbol{\mathcal{B}} \mathbf{w})^{\mathrm{T}} \mathbf{c}_s \boldsymbol{\mathcal{B}} \mathbf{u}_s \, d\Omega \tag{B.31b}$$

Summing up the two integrals and using the continuity conditions at the interface, we arrive at the following weak form for the displacement field:

$$\int_{\Omega_s} \mathbf{w}^{\mathrm{T}} \rho_s \ddot{\mathbf{u}}_s \, d\Omega + \int_{\Omega_p} \mathbf{w}^{\mathrm{T}} \rho_p \ddot{\mathbf{u}}_p \, d\Omega + \int_{\Omega_s} (\boldsymbol{\mathcal{B}} \mathbf{w})^{\mathrm{T}} \mathbf{c}_s \boldsymbol{\mathcal{B}} \mathbf{u}_s \, d\Omega + \int_{\Omega_p} (\boldsymbol{\mathcal{B}} \mathbf{w})^{\mathrm{T}} (\mathbf{c}^E \boldsymbol{\mathcal{B}} \mathbf{u}_p + \mathbf{e}^{\mathrm{T}} \boldsymbol{\nabla} \phi) \, d\Omega = 0 \tag{B.32}$$

As for Eq. (5.15c), we use a scalar test function v, and perform the same procedure of multiplication followed by integration by parts and application of Green's theorem and substituting the homogeneous Neumann boundary condition to obtain:

$$\int_{\Omega_p} v \boldsymbol{\nabla}^{\mathrm{T}} (\mathbf{e} \boldsymbol{\mathcal{B}} \mathbf{u}_p - \boldsymbol{\varepsilon}^S \boldsymbol{\nabla} \phi) \, d\Omega = \oint_{\partial\Omega_p} v \mathbf{n}_p^{\mathrm{T}} (\mathbf{e} \boldsymbol{\mathcal{B}} \mathbf{u}_p - \boldsymbol{\varepsilon}^S \boldsymbol{\nabla} \phi) \, d\partial - \int_{\Omega_p} (\boldsymbol{\nabla} v)^{\mathrm{T}} (\mathbf{e} \boldsymbol{\mathcal{B}} \mathbf{u}_p - \boldsymbol{\varepsilon}^S \boldsymbol{\nabla} \phi) \, d\Omega$$

$$= \int_{\Omega_p} (\boldsymbol{\nabla} v)^{\mathrm{T}} (\mathbf{e} \boldsymbol{\mathcal{B}} \mathbf{u}_p - \boldsymbol{\varepsilon}^S \boldsymbol{\nabla} \phi) \, d\Omega = 0 \tag{B.33}$$

APPENDIX C

MATLAB functions

In this appendix a list of some of the MATLAB functions used in the current thesis are presented with some demonstration of the covered elementary processes of differentiation and integration on regular and irregular domains.

C.1 Spectral element generation utilities

`GenPlate`: Generates a structure that hold the material properties.

```
function plate = GenPlate(name, c_L, c_T, rho, thick)

% plate = GenPlate(name, c_L, c_T, rho, thick)
% INNPUT:  name   is the material name          string
%          c_L    is the longitudinal Velcity   km/s
%          c_T    is the shear wave velocity    km/s
%          rho    is the elastic Constant       kg/m^3
%          thick  is the plate thickness in     m
   c_ll   = c_L*1e3;           % unit conversion
   c_tt   = c_T*1e3;           % unit conversion
   Rho    = rho;
   mu     = Rho*c_tt^2;
   lambda = Rho*c_ll^2 -2*mu;
   plate.name      = name;
   plate.rho       = Rho ;     % kg/m^3
   plate.h         = thick/2;  % m
   plate.lambda    = lambda;   % Pa
   plate.mu        = mu;       % Pa
   plate.LongVel   = c_ll;     % m/s
   plate.ShearVel  = c_tt;     % m/s
   plate.elast     = (plate.mu*(3*plate.lambda+2*plate.mu))/...
                     (plate.lambda+plate.mu);
   plate.nu        = plate.lambda/(2*(plate.lambda+plate.mu));
```

`legendpf`: Returns Legendre polynomial of order n at $x \in [-1, 1]$.

```
% [p]=LEGENDPF(x, n)

% INNPUT:   x, vector of points of evaluation
%           n, the dgree of Legnedre polynomial P_n
% OUTPUT:   p, vector of length(x)

function [p] = legendpf(x, n)
    m=length(x);
    if m==1
        p=0;
```

```
        if n==0
            p=1;
        else
            p1=1;  p2=x(1);  p3=p2;
            for k =1:n-1
                p3=((2*k+1)*x(1)*p2-k*p1)/(k+1);
                p1=p2;
                p2=p3;
            end
            p=p3;
        end

    else
        %x=x(:);
        p=zeros(m,1);
        if n==0
            p=ones(m,1);
        else
            p1=ones(m,1);  p2=x;  p3=p2;
            for k =1:n-1
                p3=((2*k+1)*x.*p2-k*p1)/(k+1);
                p1=p2;
                p2=p3;
            end
            p=p3;
        end
    end
    return
```

`legendld`: Returns differentiation matrix based on LGL nodes(x) Which is the derivative of Lagrange characteristic polynomials.

```
% [d]=LEGENDLD(x)
% INNPUT:   x, vector of LGL nodes.
% OUTPUT:   d, matrix of l'_{i} arranged in columns
%

function [d] = legendld(x)
    np=length(x);
    d=zeros(np);
    n=np-1;
    for j =1:np
        lnxj = legendpf(x(j),n);
        for i = 1:np
            if i ~= j
                lnxi = legendpf(x(i),n);
                d(i,j) = lnxi/((x(i)-x(j))*lnxj);
            end
        end
    end
    d(1,1) = -0.25*n*np;
    d(np,np) = -d (1,1);

    return
```

`jacopip`: Evaluates Jacobi polynomial, return $P(n, n-1, n-2)$ and $P'(n, n-1, n-2)$.

```
% [p,pd] = jacopip(x,alpha,beta, n)
% Input:    x = scalar or vector of length (m)
%           n =  polynomial degree
%           alpha, beta= parameters of Jacobi polynomial
%
% Output:   p(m,3) =  [Pn(x),   P(n-1)(x),  P(n-2)(x) ];
%           pd(m,3) = [(P'n(x), P'(n-1)(x), P'(n-2)(x)];
%

function [pa, pda] = jacobip(x,alpha,beta,n)
    apb=alpha+beta; ab2=alpha^2-beta^2;
    nn=length(x);
    if nn==1
        pa=zeros(1,1); pda=zeros(1,1);
        % x is a scalar
        p =1;   pd=0;
        p1=0;  pd1=0;
        p2=0;  pd2=0;
        if n == 0
            return
        elseif n==1
            p1 = p; p2=p1;
            p  = (alpha-beta+(apb+2)*x(1))*0.5;
            pd1 = pd; pd2=pd1;
            pd = 0.5*(apb+2);
        else
            p1 = p; p2=p1;
            p  = (alpha-beta+(apb+2)*x(1))*0.5;
            pd1 = pd; pd2=pd1;
            pd = 0.5*(apb+2);
            for k = 1:n-1
                k1=k+1; k2=k*2; k2ab=k2+alpha+beta;
                k2ab1=k2ab+1; k2ab2=k2ab1+1;
                p2=p1; p1=p;
                pd2=pd1; pd1=pd;
                a1 = 2*k1*(k1+apb)*k2ab;
                a21 = k2ab1*ab2;
                a22 = k2ab2*k2ab1*k2ab;
                a3=2*(k+alpha)*(k+beta)*k2ab2;
                p = ((a21+a22*x(1))*p1-a3*p2)/a1;
                pd= (a22*p1+(a21+a22*x(1))...
                    *pd1-a3*pd2)/a1;
            end
        end
        pa = p; pda = pd;
    else
        m=nn;
        pa=[ones(m,1),zeros(m,1),zeros(m,1)];
        pda=zeros(m,3);
        if n == 0
```

```
            return
        elseif n==1
            pa(:,2) = pa(:,1); pa(:,3)=pa(:,2);
            pa(:,1) = (alpha-beta+(apb+2)*x)*0.5;
            pda(:,2) = pda(:,1); pda(:,3)=pda(:,2);
            pda(:,1) = 0.5*(apb+2);
        else
            pa(:,2) = pa(:,1); pa(:,3)=pa(:,2);
            pa(:,1) = (alpha-beta+(apb+2)*x)*0.5;
            pda(:,2) = pda(:,1); pda(:,3)=pda(:,2);
            pda(:,1) = 0.5*(apb+2);
            for k = 1:n-1
                k2=k*2; k2ab=k2+alpha+beta;
                pa(:,3)=pa(:,2); pa(:,2)=pa(:,1);
                pda(:,3)=pda(:,2); pda(:,2)=pda(:,1);
                a1 = 2*(k+1)*(k+apb+1)*k2ab;
                a21 = (k2ab+1)*ab2;
                a22 = (k2ab+2)*(k2ab+1)*k2ab;
                a3=2*(k+alpha)*(k+beta)*(k2ab+2);
                pa(:,1) = ((a21+a22*x).*pa(:,2)...
                          -a3*pa(:,3))/a1;
                pda(:,1)= (a22*pa(:,2)+(a21+a22*x).*...
                          pda(:,2)-a3*pda(:,3))/a1;
            end
        end
    end
    return
```

`lglwx`: Returns the np weigths (w) and the nodes (x) of the Legendre Gauss-Lobatto quadrature formula in the interval [a,b]. When a, and b are left unspecified, it returns the np weights (w) and nodes (x) of Legendre Gauss-Lobatto quadrature formula in the standard interval [-1,1]. When no output is requested it returns x.

```
% [w, x]=LGLWX(np, a, b)
% [w, x]=LGLWX(np)
% INPUT:    np, number of nodes
%           a, b, extrema of the interval(default value [-1,1])
%
% Output:   x = LGL nodes
%           w = LGL weights
%

function [w, x] = lglwx(np,a,b)
    if np <= 1
        error('The number of the quad nodes should be greater than 1');
    end

    if np==2
        x=[-1;1];w=[1;1];
    else
        x=zeros(np,1);
        w=zeros(np,1);
        n=np-1;
```

```
        x(1)=-1;x(np)=1;
        x1=roots(n-1,1,1);
        x(2:n)=x1;
        coef=2/(n*np);
        w=coef./(legendpf(x,n).^2);
    end

    if nargin ==3
        bma=(b-a)*.5;
        bpa=(b+a)*.5;
        x=bma*x+bpa;
        w=w*bma;
    end
    if nargout<2
        w=x;
    end
    function [x]=roots(n, alpha, beta)
        x=zeros(n,1);

        x0=cos(pi/(2*n));
        tol=1.e-16; kmax=15;
        for j=1:n
            diff=tol+1;kiter=0;
            while kiter <=kmax && diff>=tol
                [p,pd]=jacobip(x0, alpha, beta, n);
                ss=sum(1./(x0-x(1:j-1)));
                x1=x0-p/(pd-ss*p);
                diff=abs(x1-x0);
                kiter=kiter+1;
                x0=x1;
            end
            x0=5.d-1*(x1+cos((2*(j+1)-1)*pi/(2*n)));
            x(j)=x1;
        end
        x=sort(x);
    end

end
```

`Derivative`: Computes the partial derivatives of a 2D function $f(x,y)$ using the Galerkin method over irregular domains.

```
function [dfdx, dfdy] = Derivative(f, coordinates, ngll)
    XY = shape(coordinates, ngll);
    xx = squeeze(XY(1, :,:));
    yy = squeeze(XY(2, :,:));
    [~, xgll] = lglwx(ngll,-1,1);
    dershape = dshape(ngll, xgll);
    jac  = SE_Jacobian_e(coordinates, ngll, dershape);
    jaci = SE_InverseJacobian_e(jac, ngll);
    H    = legendld(xgll);
    dUz_dxi  = f(xx,yy)*H';
    dUz_deta = H*f(xx,yy);
    dxi_dx  = squeeze(jaci(1,1,:,:))';
```

```
    dxi_dy  = squeeze(jaci(1,2,:,:))';
    deta_dy = squeeze(jaci(2,2,:,:))';
    deta_dx = squeeze(jaci(2,1,:,:))';
    dfdx = (dUz_dxi.*dxi_dx + dUz_deta.*deta_dx);
    dfdy = (dUz_dxi.*dxi_dy + dUz_deta.*deta_dy);
end
```

`shape`: Computes the inverse mapping from the reference domain to the physical domain.

```
function mappedCoors = shape(Coorg, ngll)
    [~, xgll] = lglwx(ngll, -1, 1);
    for i = 1:ngll
        eta = xgll(i);
        for j = 1:6
            xi = xgll(j);
            mappedCoors(:,i,j) = map(xi, eta, Coorg);
        end
    end
    function X = map(xi, eta, Coord)
        shapeFuns = [0.25*(1-xi)*(1-eta) 0.25*(1+xi)*(1-eta)...
                     0.25*(1+xi)*(1+eta) 0.25*(1-xi)*(1+eta)];
        X = shapeFuns*Coord;
    end
end
```

`dshape`: Computes the derivative of the sub-parametric low order shape functions at each Legendre node.

```
function sem_dshape = dshape(ngll, xgll)
    sem_dshape = zeros(4,2,ngll, ngll);
    for j = 1:ngll
        eta = xgll(j);
        for i = 1:ngll
            xi = xgll(i);
            sem_dshape(:,:,i,j) = getdershape(xi,eta);
        end
    end
end
function dershape = getdershape(s,t)
    sp = s + 1;
    sm = s - 1;
    tp = t + 1;
    tm = t - 1;
    dershape(1,1) = 0.25 * tm;
    dershape(2,1) = - 0.25 * tm;
    dershape(3,1) =  0.25 * tp;
    dershape(4,1) = - 0.25 * tp;
    dershape(1,2) = 0.25 * sm;
    dershape(2,2) = - 0.25 * sp;
    dershape(3,2) =  0.25 * sp;
    dershape(4,2) = - 0.25 * sm;
end
```

SE_Jacobian_e: Computes the Jacobian matrix of the sub-parametric low order shape functions at each Legendre node.

```
function jac = SE_Jacobian_e(coorg, ngll, dshape)

    jac= zeros(2,2,ngll,ngll);

    for j = 1:ngll
        for i = 1:ngll
            jac(:,:,i,j) = coorg'*dshape(:,:,i,j);
        end
    end
```

SE_InverseJacobian_e: Computes the inverse of the Jacobian matrix of the sub-parametric low order shape functions at each Legendre node.

```
function jaci = SE_InverseJacobian_e(jac, ngll)

    jaci= zeros(2,2,ngll,ngll);

    for j = 1:ngll
        for i = 1:ngll
            jaci(:,:,i,j) = invert2(jac(:,:,i,j));
        end
    end

end

function B = invert2(A)

    B = zeros(2,2);
    determinant = A(1,1)*A(2,2) - A(1,2)*A(2,1);

    B(1,1) =   A(2,2);
    B(2,1) = - A(2,1);
    B(1,2) = - A(1,2);
    B(2,2) =   A(1,1);

    B = B/determinant;
end
```

C.2 Examples

C.2.1 Construction of differentiation matrices

We will show an example of constructing a differentiation matrix on a rectangular element. First we construct the standard interval, and nodes.

```
>> [wgll, xgll]= lglwx(6);
>> H            = legendld(xgll);
```

and after constructing the standard differentiation matrix `H`, we define a rectangular domain, then we map the coordinates of the Legendre nodes into the physical domain:

```
>> coordinates = [0 0; 0.8 0; 0.8 1.5; 0 1.5];
>> XY = shape(coordinates, 6);
>> xx = squeeze(XY(1,:,:));
>> yy = squeeze(XY(2,:,:));
```

Then we define the following anonymous function:

```
>> f = @(x,y) x.^2+y.^3;
```

Then evaluating the function at the nodes (in physical domain),

```
>> fun = f(xx,yy);
```

We then construct the partial derivative operator with respect to x, and y. Which is referred to into the body of the thesis as H_x, and H_y respectively.

```
>> DuDy = (1/0.75)*kron(eye(6), H);
>> DuDx = (1/0.4)*kron(H,eye(6));
```

Where by virtue of the properties of the tensor product the flattening of the function matrix into a vector, follows directly the column convention of Matlab. The choice of points of the rectangular element as shown in Fig. C.1 in the order specified facilitates the computation of the inverse of the Jacobian.

$$\mathbf{J}^{-1} = \begin{pmatrix} \frac{1}{0.5\Delta x} & 0 \\ 0 & \frac{1}{0.5\Delta y} \end{pmatrix} \tag{C.1}$$

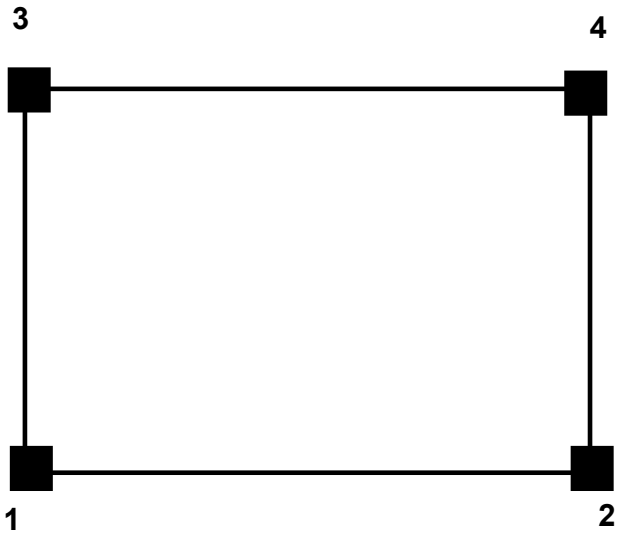

Figure C.1 Rectangular Element

C.2.2 Differentiation on an irregular domain

As a way of illustrating the effectiveness with which the spectral differentiation accurately represents the partial derivatives of a 2D function, $f(x, y) = x^2 + y^3$:

```
>> f = @(x,y) x.^2+y.^3;
```

which have partial derivatives, $\partial_x f = 2x$ and $\partial_y f = 3y^2$; So if we define an irregular sub-domain with the following corner coordinates:

```
>> coordinates = [0 0; 0.8 0.5; 0.6 1; 0.1 0.75];
```

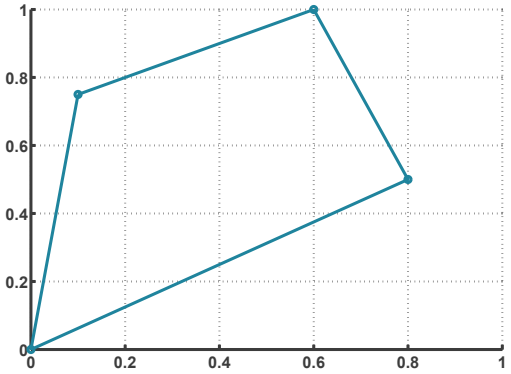

Figure C.2 Irregular Sub-domain for 2D function $f(x, y)$

So, now we can evaluate the partial derivatives over that domain using the function `Derivative`

```
>> [dfdx, dfdy]=Derivative(f, coordinates, 6);
```

and comparing the exact values of the derivatives at the Legendre nodes:

```
>> XY = shape(coordinates, 6);
>> xx = squeeze(XY(1, :,:));
>> yy = squeeze(XY(2, :,:));
>> df_dx = @(x,y) 2*x;
>> norm(df_dx(xx, yy) - dfdx, inf)
ans =
     1.526556658859590e-14
```

Similarly for the $\partial_y f$

```
>> df_dy = @(x,y) 3*y.^2;
>> norm(df_dy(xx, yy) - dfdy, inf)
ans =
     1.398881011027697e-14
```

For the purpose of FEM and SEM, in order to facilitate the assembly of global matrices; we need a matrix column version of the differentiation matrix in physical coordinates like H_x, H_y, for that reason we constructed the following function

```
function [DDx,DDy, dfdx, dfdy] = Derivative_flat(f, coordinates, ngll)
    A = 1:ngll:ngll.^2;
    B = repmat(1:ngll, 1, ngll);

    XY = shape(coordinates, ngll);
    xx = squeeze(XY(1,:,:));
    yy = squeeze(XY(2,:,:));
    [~, xgll] = lglwx_mex(ngll,-1,1);
    dershape  = dshape(ngll, xgll);
    jac  = SE_Jacobian_e(coordinates, ngll, dershape);
    jaci = SE_InverseJacobian_e(jac, ngll);
    dxi_dx  = squeeze(jaci(1,1,:,:))';
    dxi_dy  = squeeze(jaci(1,2,:,:))';
    deta_dy = squeeze(jaci(2,2,:,:))';
    deta_dx = squeeze(jaci(2,1,:,:))';

    H        = legendld_mex(xgll);
    DuDxidx  = kron(H, eye(ngll));
    DuDxidy  = DuDxidx;
    DuDetadx = kron(eye(ngll), H);
    DuDetady = DuDetadx;
%% Construct the flat diff matrices
% dUz_dxi  = f(xx,yy)*H'; DuDxidx = dUz_dxi.*dxi_dx
% dUz_dxi  = f(xx,yy)*H'; DuDxidy = dUz_dxi.*dxi_dy
    for j = 1:ngll
        for i = 1:ngll
            Temp = DuDxidx((j-1)*ngll+1:j*ngll, (i-1)*ngll+1: i*ngll);
            DuDxidx((j-1)*ngll+1:j*ngll, (i-1)*ngll+1: i*ngll) ...
                 = diag(diag(Temp).*dxi_dx(:,j));
            Temp = DuDxidy((j-1)*ngll+1:j*ngll, (i-1)*ngll+1: i*ngll);
            DuDxidy((j-1)*ngll+1:j*ngll, (i-1)*ngll+1: i*ngll) ...
                 = diag(diag(Temp).*dxi_dy(:,j));
        end
    end
% dUz_deta = H*f(xx,yy) => kron(eye(ngll), H); DuDetadx = dUz_deta.*deta_dx
% dUz_deta = H*f(xx,yy) => kron(eye(ngll), H); DuDetady = dUz_deta.*deta_dy
    for i = 1:ngll
        Temp = repmat(deta_dx(:,i), 1, ngll);
        DuDetadx((i-1)*ngll + 1 : i*ngll, (i-1)*ngll + 1 : i*ngll) ...
             = Temp.*DuDetadx((i-1)*ngll + 1 : i*ngll, (i-1)*ngll + 1 : i*
                ngll);
        Temp = repmat(deta_dy(:,i), 1, ngll);
        DuDetady((i-1)*ngll + 1 : i*ngll, (i-1)*ngll + 1 : i*ngll) ...
             = Temp.*DuDetady((i-1)*ngll + 1 : i*ngll, (i-1)*ngll + 1 : i*
                ngll);
    end

%% Compute The derivatives
% dfdx =(dUz_dxi.*dxi_dx + dUz_deta.*deta_dx);
% dfdy = (dUz_dxi.*dxi_dy + dUz_deta.*deta_dy);
    DDx = DuDxidx+DuDetadx;
    func = f(xx, yy);
    dfdx = DDx*func(:);
```

```
52      DDy = DuDxidy+DuDetady;
53      dfdy = DDy*func(:);
```

where `DDx`, and `DDy`, are H_x, and H_y.

C.2.3 Quadrature

Now for the integration, it is straight forward in the case we evaluate the matrix of function in its original form as a matrix `fun`.

```
>> wgll2 = wgll * wgll' ;
>> det = 0.75*0.4;
>> sum(sum(wgll2.*fun)).*det
ans =
     1.268500000000001e+00
```

where the integration is equal to the exact value. For the case of unfolded matrix, which is more appropriate for the case of spectral element formulations we can perform the integration of the derivatives as follows:

```
>> W = wgll2(:);
>> W = diag(W);
>> det = 0.75*0.4;
>> sum(W*DuDx*fun(:)).*det
ans =
     9.600000000000003e-01
```

which is equal to the exact value of the integral $\int_0^{0.8}\int_0^{1.5} \partial_x f(x,y)\,dxdy$. Similarly for the $\partial_y f(x,y)$, we have:

```
>> sum(W*DuDy*fun(:)).*det
ans =
     2.700000000000001e+00
```

REFERENCES

Achenbach, J. D. (1973). *Wave Propagation in Elastic Solids*. North Holland.

Achenbach, J. D. (2009). Structural health monitoring - what is the prescription? *Mechanics Research Communications*, volume 36, pp. 137–42.

Adams, D. E. (2007). *Health Monitoring of Structural Materials and Components Methods with Applications*. John Wiley & Sons.

Agostini, V., Delsanto, P. P., Genesio, I. and Olivero, D. (2003). Simulation of Lamb wave propagation for the characterization of complex structures. *IEEE Trans Ultr Ferr Freq Contr*, volume 50, number 4, pp. 441–48.

Ahmad, Z. and Gabbert, U. (2012). Simulation of lamb wave reflections at plate edges using the semi-analytical finite element method. *Ultrasonics*, volume 52, pp. 815–820.

Ahmad, Z. A. B., Vivar-Perez, J. M. and Gabbert, U. (2013). Semi-analytical finite element method for modeling of lamb wave propagation. *CEAS Aeronaut J*, volume 4, number 1, pp. 21–33.

Alleyne, D. and Cawley, P. (1990). A 2-dimensional fourier transform method for the quantitative measurement of lamb modes. *Ultrasonics Symposium. Proceedings IEEE*, volume 2, pp. 1143–46.

Alleyne, D. and Cawley, P. (1991). A two-dimensional fourier transform method for measurement of propagating multimode signals. *Journal of Acoustical Socity of America*, volume 89, number 3, pp. 1159–68.

Alleyne, D. N. and Cawley, P. (1992). The interaction of Lamb waves with defects. *IEEE Trans Ultr Ferr Freq Contr*, volume 39, number 3, pp. 381–97.

Ambroziński, L. (2013). Beamforming of guided waves. In Stepinski, T., Uhl, T. and Staszewski, W., *Advanced structural damage detection: from theory to engineering applications*, chapter 7. Wiley, pp. 177–212.

ANSI/IEEE (1987). Standard 176, IEEE standard on piezoelectricity. The Institute of Electrical and Electronics Engineers, Inc.

Ansys Inc. (2011). *Ansys 14.0 user manual*.

Babuška and Suri, M. (1994). The p and h-p versions of the finite element method, basic principles and properties. *SIAM Review*, volume 36, pp. 578–632.

Babuška, Szabó, B. and Katz, I. (1981). The p-version of the finite element method. *SIAM Journal of Numerical Analysis*, volume 18, pp. 515–545.

Babuška, I., Ihlenburg, F., Paik, E. T. and Sauter, S. A. (1995). A generalized finite element method for solving the helmholtz equation in two dimensions with minimal pollution. *Computer methods in applied mechanics and engineering*, volume 128, pp. 325–59.

Balageas, D. (2006). Introduction to structural health monitoring. In Balageas, D., Fritzen, C.-P. and Güemes, A., *Structural Health Monitoring*, chapter 1. ISTE Ltd, pp. 13–44.

Balasubramanyamy, R., Quinneyz, D., Challisy, R. E. and Toddy, C. P. D. (1996). A finite-difference simulation of ultrasonic Lamb waves in metal sheets with experimental verification. *J Phys D: Appl Phys*, volume 29, pp. 147–55.

Ballandras, S., Lardat, R., Wilm, M., Pastureaud, T., Reinhardt, A., Champavert, N., Steichen, W., Daniau, W., Laude, V., Armati, R. and Martin, G. (2009). A mixed finite element/boundary element approach to simulate complex guided elastic wave periodic transducers. *Journal Of Applied Physics*, volume 105, p. 014911.

Banerjee, J. R. (1997). Dynamic stiffness formulation for structural elements: A general approach. *Computers and Structures*, volume 63, number 1, pp. 101–3.

Banks, H., Smith, R. and Wang, Y. (1996). *Smart Material Structures: Modeling, Estimation and Control*. Masson/John Wiley, Paris/Chichester.

Basabe, J. D. D. and Sen, M. K. (2007). Grid dispersion and stability criteria of some common finite-element methods for acoustic and elastic wave equations. *Geophysics*, volume 72, number 6, pp. T81–T95.

Bathe, K.-J. (1996). *Finite Element Procedures*.

Bayliss, A. and Turkel, E. (1980). Radiation boundary conditions for wave-like equations. *Commun. Pure Appl. Math.*, volume 33, pp. 707–25.

Benmeddour, F., Treysséde, F. and Laguerre, L. (2011). Numerical modeling of guided wave interaction with non-axisymmetric cracks in elastic cylinders. *International Journal of Solids and Structures*, volume 48, pp. 764–774.

Berenger, J. (1994). A perfectly matched layer for the absorption of electromagnetic waves. *Journal of Computational Physics*, volume 114, pp. 185–200.

Beskos, D. E. and Narayanan, G. V. (1983). Dynamic response of frameworks by numerical laplace transform. *Computational Methods Applied Mechanics Engineering*, volume 37, pp. 289–307.

Bettess, P. (1992). *Infinite Elements*. Penshaw Press.

Boller, C. (2012). Structural health monitoring - an introduction and definitions. In Boller, C., Chang, F.-K. and Fujino, Y., *Encyclopedia of structural health monitroing*, chapter 1. John Wiley and Sons, pp. 1–23.

Boyd, J. P. and Ong, J. R. (2009). Exponentially-convergent strategies for defeating the runge phenomenon for the approximation of non-periodic functions, part i: Single-interval schemes. *Commun. Comput. Phys.*, volume 5, number 2-4, pp. 484–97.

Brillouin, L. (1946). *Wave Propagation in Periodic Structures*, 1st edition. McGraw Hill, NY.

Brillouin, L. (1960). *Wave Propagation and Group Velocity*. Academic Press.

Canuto, C., Hussaini, M. Y., Quarteroni, A. and Zang, T. A. (2007). *Spectral Methods: Evolution to Complex Geometries and Applications to Fluid Dynamics*, *volume 2*. Springer.

Carcione, J. M. (1991). Domain decomposition for wave propagation problems. *J Sci Comp*, volume 6, number 4, pp. 453–72.

Carcione, J. M. (1994). Boundary conditions for wave propagation problems. *Finite Elem Anal Desig*, volume 16, number 3, pp. 317–27.

Carcione, J. M. (1996). A 2D Chebyshev differential operator for the elastic wave equation. *Comput Methods Appl Mech Engng*, volume 130, pp. 33–45.

Carrera, E., Brischetto, S. and Nali, P. (2011). *Plates and Shells for Smart Structures: Classical and Advanced Theories for Modeling and Analysis*.

Casadei, F., Rimoli, J. J. and Ruzzene, M. (2014). Multiscale finite element analysis of elastic waves cattering from localized defects. *Finite Elements in Analysis and Design*, volume 88, pp. 1–15.

Chaljub, E., Komatitsch, D., Vilotte, J.-P., Capdeville, Y., Valette, B. and Festa, G. (2007). Spectral element analysis in seismology. In Wu, R.-S. and Maupin, V., *Advances in Wave Propagation in Heterogeneous Media*, Advances in Geophysics, *volume 48*. Elsevier - Academic Press, pp. 365–419.

Cho, Y. and Rose, J. (2000). An elastodynamic hybrid boundary element study for elastic guided wave interactions with a surface breaking defect. *International Journal of Solids and Structures*, volume 37, pp. 4103–24.

Cho, Y. and Rose, J. L. (1996). A boundary element solution for a mode conversion study on the edge reflection of lamb waves. *Journal of Accoustical Society of America*, pp. 2097–109.

Clayton, R. and Engquist, B. (1977). Absorbing boundary conditions for acoustic and elastic wave equations. *Bulletien of Seismological Society of America*, volume 67, number 6, pp. 1529–40.

Cohen, G. (2002). *Higher-order numerical methods for transient wave equations*. ScientificComputation, Springer-Verlag.

Collino, F. and Tsogka, C. (2001). Application of the perfectly matched absorbing layer model to the linear elastodynamic problem in anisotropic heterogeneous media. *Geophysics*, volume 66, number 1, pp. 294–307.

Courant, R., Friedrichs, K. and Lewy, H. (1967). On the partial difference equations of mathematical physics. *IBM Journal*, volume 11, pp. 215–34.

Crawley, E. and Anderson, E. (1990). Detailed models of piezoceramic actuation of beams. *Journal of Intelligent Material Systems and Structures*, volume 1, number 1, pp. 4–25.

Crawley, E. F. and de Luis, J. (1987). Use of piezoelectric actuators as elements of intelligent structures. *AIAA J*, volume 25, pp. 1373–85.

Crocombe, A. D. and Ashcroft, I. A. (2008). *Modeling of Adhesively Bonded Joints*, chapter Simple Lap Joint Geometry. Springer, pp. 3–24.

Dablain, M. (1986). The application of higher order differencing to the scalar wave equation. *Geophysics*, volume 51, pp. 54–66.

Dauksher, W. and Emery, A. (2000). The solution of elastostatic and elastodynamic problems with Chebyshev spectral finite elements. *Computer methods in applied mechanics and Engineering*, volume 188, pp. 217–33.

Dauksher, W. and Emery, A. F. (1996). The use of spectral methods in predicting the reflection and transmission of ultrasonic signals through flaws. In Thompson, D. and Chimenti, D., *Review of Progress in Quantitative Non-destructive Evaluation*, *volume 15*. Plenum Press, NY, pp. 97–104.

Dauksher, W. and Emery A. F. (1997). Accuracy of modeling the acoustic wave equation with Chebyshev spectral finite elements. *Finite Elements in Analysis and Design*, volume 26, pp. 115–28.

Delsanto, P. P., Schechter, R. S., Chaskelis, H. H., Mignogna, R. B. and Kline, R. B. (1994). Connection machine simulation of ultrasonic wave propagation in materials II: The two-dimensional case. *Wave Motion*, volume 20, pp. 295–314.

Delsanto, P. P., Schechter, R. S. and Mignogna, R. B. (1997). Connection machine simulation of ultrasonic wave propagation in materials III: The three-dimensional case. *Wave Motion*, volume 26, pp. 329–39.

Delsanto, P. P., Whitcombe, T., Chaskelis, H. H. and Mignogna, R. B. (1992). Connection machine simulation of ultrasonic wave propagation in materials I: the one-dimensional case. *Wave Motion*, volume 16, pp. 65–80.

Desceliers, C., Soize, C., Grimal, Q., Haiat, G. and Naili, S. (2008). A time-domain method to solve transient elastic wave propagation in a multilayer medium with a hybrid spectral-finite element space approximation. *Wave Motion*, volume 45, number 4, pp. 383–99.

Dimitriadis, E. K., Fuller, C. R. and Rogers, C. A. (1991). Piezoelectric actuators for distributed vibration excitation of thin plates. *ASME J Vibr Acoust*, volume 113, pp. 100–07.

Ditri, J. J. and Rajana, K. (1997). An experimental study of the angular dependence of Lamb wave excitation amplitudes. *J Soun Vibr*, volume 204, number 5, pp. 755–68.

Dosh, J. J., Inman, D. J. and Garcia, E. (1992). Self-sensing piezoelectric actuator for collocated control. *Journal of Intelligent Materials, Systems and Structures*, volume 3, pp. 166–85.

Doyle, J. F. (1989). *Wave Propagation in Structures: Spectral Analysis Using Fast Fourier Transforms*. Springer.

Drozdz, M. (2008). *Efficient Finite Element modelling of ultrasound waves in elastic media*. Ph.D. thesis, Mechanical Engineering Department, Imperial College, London.

Drozdz, M., Lowe, M. J. S., Skelton, E. and Craster, R. V. (2007). Modeling bulk and guided wave propagation in unbounded elastic media using absorbing layers in commercial fe packages. In Thompson, D. O. and Chimenti, D. E., *Review of progress in quantitative non destructive evaluation*, AIP Conference Proceedings. volume 26. pp. 87–94.

Drozdz, M., Moreau, L., M. Castaings, M. J. S. L. and Cawley, P. (2006). Efficient numerical modelling of absorbing regions for boundaries of guided waves problems. In Thompson, D. O. and Chimenti, D. E., *Review of progress in quantitative non destructive evaluation*, AIP Conference Proceedings.

Engquist, B. and Madja, A. (1979). Radiation boundary conditions for acoustic and elastic calculation. *Commun. Pure Appl. Math.*, volume 32, pp. 313–57.

Epperson, J. F. (1987). On the runge example. *Amer. Math. Monthly*, volume 1994, pp. 329–41.

Farrar, C. R. and Lieven, N. A. J. (2007). Damage prognosis: the future of structural health monitoring. *Phil Trans R Soc A*, volume 365, pp. 623–32.

Farrar, C. R. and Worden, K. (2007). An introduction to structural health monitoring. *Phil Trans R Soc A*, volume 365, pp. 303–15.

Fish, J. and Belytschko, T. (2007). *A First Course in Finite Elements*. John Wiley & Sons.

Fornberg, B. (1996). *A Practical Guide to Pseudospectral Methods*. Cambridge University Press.

Funaro, D. (1992). *Polynomial Approximation of Differential Equations*. Springer Verlag.

Furumural, T. and Takenaka, H. (1996). 2.5-D modelling of elastic waves using the pseudospectral method. *Geophys J Int*, volume 124, pp. 820–32.

Giurgiutiu, V. (2005). Tuned lamb wave excitation and detection with piezoelectric wafer active sensors for structural health monitoring. *J Int Mat Syst Str*, volume 16, pp. 291–305.

Giurgiutiu, V. (2008). *Structural Health Monitoring with Piezoelectric Wafer Active Sensors*. Elsevier Academic Press.

Giurgiutiu, V. and Bao, J. (2002). Embedded-ultrasonics structural radar for the nondestructive evaluation of thin-wall structures. In *Proceedings of 2002 ASME International Mechanical Engineering Congress*, ASME. pp. #IMECE2002–39017.

Glushkov, E., Glushkova, N., Kvasha, O. and Lammering, R. (2010). Selective lamb mode excitation by piezoelectric coaxial ring actuators. *Smart Materials and Structures*, volume 19.

Glushkov, E., Glushkova, N., Kvasha, O. and Seemann, W. (2007). Integral equation based modeling of the interaction between piezoelectric patch actuators and an elastic substrate. *Smart Materials and Structures*, volume 16, pp. 650–664.

Glushkov, E., Glushkova, N., Lammering, R., Eremin, A. and Neumann, M. (2011). Lamb wave excitation and propagation in elastic plates with surface obstacles: proper choice of central frequencies. *Smart Materials and Structures*, volume 20.

Gopalakrishnan, S., Chakraborty, A. and Mahapatra, D. R. (2008). *Spectral Finite Element Method: Wave Propagation, Diagnostics and Control in Anisotropic and Inhomogeneous Structures*. Springer.

Gopalakrishnan, S., Ruzzene, M. and Hanagud, S. (2011). *Computational Techniques for Structural Health Monitoring*. Springer Series in Reliability Engineering, Springer.

Graff, K. F. (1991). *Wave Motion in Elastic Solids*. Dover Publications.

Grondel, S., Paget, C., Delebarre, C., Assaad, J. and Levin, K. (2002). Design of optimal configuration for generating A0 Lamb mode in a composite plate using piezoceramic transducers. *J Acoust Soc Am*, volume 112, pp. 84–90.

Ha, S. and Chang, F.-K. (2010). Optimizing a spectral element for modeling PZT-induced Lamb wave propagation in thin plates. *Smart Materials and Structures*, volume 19, number 1, p. 015015.

Hochstenbach, M. and van der Vorst, H. (2003). Alternatives to the rayleigh quotient for the quadratic eigenvalue problem. *SIAM Journal on Scientific Computing*, volume 25, number 2, pp. 591–603.

Hughes, T. J. R. (1987). *The Finite Element Method: Linear Static and Dynamic Finite Element Analysis*. Prentice-Hall International, Englewood Cliffs, NJ.

Huston, D. (2011). *Structural sensing, health monitoring, and performance evaluation*. CRC Press.

Idesman, A. V., Schmidt, M. and Foley, J. R. (2010). Accurate finite element modeling of linear elastodynamics problems with the reduced dispersion error. *Computational Mechanics*, volume 47, number 5, pp. 555–572.

Idesman, A. V., Schmidt, M. and Sierakowski, R. L. (2008). A new explicit predictor multicorrector high-order accurate method for linear elastodynamics. *Journal of Sound and Vibration*, volume 310, number 1-2, pp. 217–229.

Igawa, H., Komatsu, K., Yamaguchi, I. and Kasai, T. (2004). Wave propagation analysis of frame structures using the spectral element method. *J Sound Vibr*, volume 277, pp. 1071–81.

Israeli, M. and Orszag, S. (1981). Approximation of radiation boundary conditions. *Journal of Computational Physics*, volume 41, pp. 115–35.

Jensen, M. (1996). High convergence order finite elements with lumped mass matrix. *International Journal of Numerical Methods and Engineering*, volume 39, pp. 1879–1888.

Kaltenbacher, M. (2007). *Numerical Simulation of Mechatronic Sensors and Actuators*, 2nd edition. Springer.

Karniadakis, G. E. and Sherwin, S. J. (2005). *Spectral/hp Element Methods for CFD*, 2nd edition. Oxford University Press.

Katzir, S. (2006). *The Beginnings Of Piezoelectricity A Study In Mundane Physics*, Boston studies in philosophy of science, *volume 246*. Springer.

Ke, W., Castaings, M. and Bacon, C. (2009). 3d finite element simulations of an air-coupled ultrasonic ndt system. *NDT&E International*, volume 42, pp. 524–533.

Kelly, C. T. (1995). *Iterative Methods for Linear and Nonlinear Equations*. SIAM.

Kessler, S. S. (2002). *Piezoelectric-Based In-Situ Damage Detection of Composite Materials for Structural Health Monitoring Systems*. Ph.D. thesis, Department of Aeronautics and Astronautics, Massachusetts Institute of Technology, Cambridge, MA, USA.

Kim, J., Varadan, V. V. and Varadan, V. K. (1997). Finite element modelling of structures including piezoelectric active devices. *Int J Num Meth Engng*, volume 40, pp. 817–32.

Kim, Y., Ha, S. and Chang, F.-K. (2008). Time-domain spectral element method for built-in piezoelectric-actuator-induced Lamb wave propagation analysis. *AIAA Journal*, volume 46, number 3, pp. 591–600.

Komatitsch, D., Barnes, C. and Tromp, J. (2000). Simulation of anisotropic wave propagation based upon a spectral element method. *Geophysics*, volume 65, pp. 1251–60.

Komatitsch, D. and Tromp, J. (1999). Introduction to the spectral-element method for 3-D seismic wave propagation. *Geophys J Int*, volume 139, number 3, pp. 806–22.

Komatitsch, D. and Tromp, J. (2003). A perfectly matched layer absorbing boundary condition for the second-order seismic wave equation. *Geophys J Int*, volume 154, pp. 146–53.

Komatitsch, D., Tsuboi, S. and Tromp, J. (2005). The spectral-element method in seismology. In Levander, A. and Nolet, G., *Seismic Earth: Array Analysis of Broadband Seismograms*, Geophysical Monograph, *volume 157*. American Geophysical Union, Washington DC, USA, pp. 205–228.

Komatitsch, D. and Vilotte, J. P. (1998). The spectral element method: An efficient tool to simulate the seismic response of 2D and 3D geological structures. *Bull Seismol Soc Am*, volume 88, number 2, pp. 368–92.

Komatitsch, D., Vilotte, J. P., Rossana, V., Castillo-Cvarrubias, J. M. and Sánchez-sesma, F. J. (1999). The spectral element method for elastic wave equations-application to 2D and 3D seismic problems. *Int J Numer Meth Engng*, volume 45, pp. 1139–64.

Krenk, S. (2001). Dispersion-corrected explicit integration of the wave equation. *Comput Methods Appl Mech Eng*, volume 191, pp. 975–987.

Kroening, M., Berthold, A. and Meyendorf, N. (2005). Sensor modules for structural health monitoring and reliability of components. In *Advanced Sensor Technologies for Nondestructive Evaluation and Structural Health Monitoring, SPIE 5770.*

Kudela, P., Krawczuka, M. and Ostachowicza, W. (2007a). Wave propagation modelling in 1D structures using spectral finite elements. *J Sound Vibr*, volume 300, pp. 88–100.

Kudela, P., Zak, A., Krawczuka, M. and Ostachowicz, W. (2007b). Modelling of wave propagation in composite plates using the time domain spectral element method. *J Sound Vibr*, volume 302, pp. 728–45.

Lamb, H. (1917). On waves in an elastic plate. *Proc R Soc A*, volume 93, pp. 114–28.

Lee, B. C. and Staszewski, W. J. (2003a). Modelling of Lamb waves for damage detection in metallic structures, part I: wave propagation. *Smart Mater Struct*, volume 12, pp. 804–14.

Lee, B. C. and Staszewski, W. J. (2003b). Modelling of Lamb waves for damage detection in metallic structures, part II: wave interactions with damage. *Smart Mater Struct*, volume 12, pp. 815–24.

Lee, B. C. and Staszewski, W. J. (2007a). Lamb wave propagation modelling for damage detection: Part I. two-dimensional analysis. *Smart Mater Struct*, volume 16, pp. 249–59.

Lee, B. C. and Staszewski, W. J. (2007b). Lamb wave propagation modelling for damage detection: Part II. damage monitoring strategy. *Smart Mater Struct*, volume 16, pp. 260–74.

Lee, U. (2009). *Spectral Element Method in Structural Dynamics*. John Wiley & Sons.

Lin, M. W. and Rogers, C. A. (1993). Actuation response of a beam structure with induced strain actuators. *Adaptive Struct. Mater. Sys.*, volume 35, pp. 129–139.

Liu, G. and Quek, J. (2003a). A non-reflecting boundary for analysing wave propagation using the finite element method. *Finite Elements in Analysis and Design*, volume 39, pp. 403–17.

Liu, G. R. and Quek, S. S. (2003b). *The Finite Element Method: A Practical Course*. Butterworth-Heinemann.

Lowe, M. J. S. (1992). *Plate Waves for The NDT of Diffusion Bonded Titanium*. Ph.D. thesis, Imperial College of Science, Technology and Medicine University of London.

Lowe, M. J. S. (1995). Matrix techniques for modeling ultrasonic waves in multilayered media. *IEEE Trans Ultr Ferr Freq Contr*, volume 42, pp. 525–42.

Lowe, M. J. S., Cawley, P., Kao, J.-Y. and Diligent, O. (2002). The low frequency reflection characteristics of the fundamental antisymmetric Lamb wave a_0 from a rectangular notch in a plate. *J Acoust Soc Am*, volume 112, number 6, pp. 2612–22.

Lowe, M. J. S. and Diligent, O. (2002). The low frequency reflection characteristics of the s_0 Lamb wave from a rectangular notch in a plate. *J Acoust Soc Am*, volume 111, number 1, pp. 64–74.

Lua, Y., Yea, L., Sub, Z. and Yanga, C. (2008). Quantitative assessment of through-thickness crack size based on lamb wave scattering in aluminium plates. *NDT&E International*, volume 41, pp. 59–68.

Lysmer, J. and Kuhlemeyer, R. (1969). Finite dynamic model for in!nite media. *J. Eng. Mech. Div. ASCE*, volume 95, pp. 859–77.

Maday, Y. and Rønquist, E. M. (1990). Optimal error analysis of spectral methods with emphasis on non-constant coefficients and deformed geomtries. *Comp Meth Appl Mech Engng*, volume 80, pp. 91–115.

Mańka, M., Rosiek, M. and Martowicz, A. (2013). Piezocomposite transducers for guided waves. In Stepinski, T., Uhl, T. and Staszewski, W., *Advanced structural damage detection: from theory to engineering applications*, chapter 9. Wiley, pp. 109–39.

Martowicz, A., Packo, P., Staszewski, W. and Uhl, T. (2012). Modelling of nonlinear vibro-acoustic wave interaction in cracked aluminium plates using local interaction simulation

approach. In *Proceedings of 6th European Congress on Computational Methods in Applied Sciences and Engineering (ECCOMAS 2012)*, University of Vienna.

Mazzotti, M., Bartoli, I., Marzani, A. and Viola, E. (2013). A boundary element formulation for the computation of damped guided waves. In *AIP Conf. Proc.* volume 1511. p. 113.

Mohamed, R. and Masson, P. (2010a). A parametric study of piezoceramic thickness effect on the generation of fundamental lamb modes. In *Proc. of SPIE*.

Mohamed, R. and Masson, P. (2010b). A time domain spectral element model for piezoelectric excitation of lamb waves in isotropic plates. In *Proc. SPIE 7650, Health Monitoring of Structural and Biological Systems*. p. 76502G.

Mohamed, R. and Masson, P. (2011). A time domain spectral element for coupled piezoelectric actuator/sensor with complex thin-walled assembly structures. In *International Workshop On Structural Health Monitoring*.

Mori, N., Biwa, S. and Hayashi, T. (2013). Reflection and transmission of lamb waves at an imperfect joint of plates. *JOURNAL OF APPLIED PHYSICS*, volume 113, number 074901.

Moser, F., Jacobs, L. J. and Qu, J. (1999). Modeling elastic wave propagation in waveguides with the finite element method. *NDT & E International*, volume 32, number 4, pp. 225–234.

Moulin, E., Assaad, J., Delebarre, C., Grondel, S. and Balageas, D. (2000a). Modeling of integrated Lamb waves generation systems using a coupled finite element normal modes expansion method. *Ultrasonics*, volume 38, pp. 522–26.

Moulin, E., Assaad, J., Delebarre, C. and Osmont, D. (2000b). Modeling of Lamb waves generated by integrated transducers in composite plates using a coupled finite element-normal modes expansion method. *J Acoust Soc Am*, volume 107, number 1, pp. 85–94.

Mulder, W. A. (1999). Spurious modes in finite element discretizations of the wave equation may not be all that bad. *Applied Numerical Mathematics*, volume 30, pp. 425–445.

Mullen, R. and Belytschko, T. (1982). Dispersion analysis of finite element semidiscretizations of the two-dimensional wave equation. *International Journal for Numerical Methods and Engineering*, volume 18, pp. 11–29.

Nieuwenhuis, J., Neumann, J., Greve, D. W. and Oppenheim, I. (2005a). Generation and detection of guided waves using PZT wafer transducers. *IEEE Trans Ultrason Ferroelectr Freq Control*, volume 52, pp. 2103–11.

Nieuwenhuis, J. H., Neumann, J. J., Greve, D. W. and Oppenheim, I. J. (2005b). Simulation and testing of transducers for lamb wave generation. In *IMAC-XXIII Conference on Structural Dynamics, Society for Experimental Mechanics, Orlando*.

P, P., T, U. and WJ, S. (2010). Coupled thermo-mechanical simulations of lamb waves propagation in structures with damage. In *18th International Congress on Sound and Vibration*.

Paćko, P. (2013). Numerical simulation of elastic wave propagation. In Stepinski, T., Uhl, T. and Staszewski, W., *Advanced structural damage detection: from theory to engineering applications*, chapter 2. Wiley, pp. 17–56.

Packo, P., Bielak, T., Spencer, A. B., Staszewski, W. J., Uhl, T. and Worden, K. (2012). Lamb wave propagation modelling and simulation using parallel processing architecture and graphical cards. *Smart Materials and Structures*, volume 21, pp. 1–13.

Packo, P. and Uhl, T. (2011). Multiscale approach to structure damage modelling. *Journal of Theoretical and Applied Mechanics*, volume 49, number 1, pp. 243–264.

Pao, Y.-H. and Mindlin, R. D. (1960). Dispersion of flexural waves in an elastic, circular cylinder. *Journal of Applied Mechanics*, volume 27, pp. 513–520.

Patera, A. T. (1984). A spectral element method for fluid dynamics: laminar flow in a channel expansion. *J Comput Phys*, volume 54, pp. 468–88.

Pavlakovic, B. and Lowe, M. (2003). *Disperse User's Manual*. Non-Destructive Testing Laboratory, Imperial College.

Peng, H., Meng, G. and Li, F. (2009). Modeling of wave propagation in plate structures using three-dimensional spectral element method for damage detection. *J Sound Vibr*, volume 320, pp. 942–54.

Peng, H., Ye, L., Meng, G., Mustapha, S. and Li, F. (2010). Concise analysis of wave propagation using the spectral element method and identification of delamination in cf/ep composite beams. *Smart Materials and Structures*, volume 19, number 8, p. 085018.

pzflex (2005). Finite element modeling for ultrasonic applications.

Qi, Q. and Geers, T. L. (1994). Evaluation of the perfectly matched layer for computational acoustics. *J. Comput. Phys.*, volume 139, pp. 166–83.

Raghavan, A. and Cesnik, C. E. S. (2005a). Finite-dimensional piezoelectric transducer modeling for guided wave based structural health monitoring. *Smart Mater Struct*, volume 14, pp. 1448–61.

Raghavan, A. and Cesnik, C. E. S. (2005b). Lamb wave based structural health monitoring. In Inman, D. J., Farrar, C. R., Lopes, V. and Steffen, V., *Damage Prognosis for Aerospace, Civil and Mechanical Systems*, chapter 11. John Wiley & Sons Ltd, pp. 235–258.

Reddy, J. (2002). *Energy Principles and Variational Methods In Applied Mechanics*, 2nd edition. Wiley and Sons.

Rokhlin, S. (1980). Diffraction of lamb wave by a finite crack in an elastic layer. *Journal of Acoustical Socity of America*, volume 67, pp. 1157–165.

Rokhlin, S. (1981). Resonance phenomena of lamb waves scattering by a finite crack in a solid layer. *Journal of Acoustical Socity of America*, volume 69, pp. 922–28.

Rose, J., Pelts, S. and Cho, Y. (2000). Modeling of flaw sizing potential with guided waves. *Journal of Nondestructive Evaluation*, volume 19, pp. 55–66.

Rose, J. and Zhao, X. (2001). Anomaly through-wall depth measurement potential with shear horizontal guided waves. *Materials Evaluation*, volume 59, pp. 1234–1238.

Rose, J. L. (2003). Dispersion curves in guided wave testing. *Material Evaluation*, volume 61, number 1, pp. 20–22.

Rose, J. L. (2004). *Ultrasonic Waves in Solid Media*. Cambridge University Press.

Rose, J. L., Pelts, S. P. and Quarry, M. J. (1998). A comb transducer model for guided wave NDE. *Ultrasonics*, volume 36, pp. 163–69.

Royer, D. and Dieulesaint, E. (2000). *Elastic Waves in Solids I: Free and Guided Propagation*. Springer Verlag.

Sadler, J. and Maev, R. G. (2007). Experimental and theoretical basis of Lamb waves and their applications in material sciences. *Can J Phys*, volume 85, pp. 707–31.

Salas, K. I. and Cesnik, C. (2010). Design and characterization of a variable-length piezocomposite transducer for structural health monitoring. *Journal of Intelligent Material Systems and Structures*, volume 21, pp. 249–360.

Schulte, R. T., Fritzen, C.-P. and Moll, J. (2010). Spectral element modelling of wave propagation in isotropic and anisotropic shell-structures including different types of damage. *IOP Conference Series: Materials Science and Engineering*, volume 10, pp. 12–65.

Seco, F. and Jiménez, A. R. (2012). Modelling the generation and propagation of ultrasonic signals in cylindrical waveguides. In *Ultrasonic waves*. Intech Open Access Publisher, pp. 1–28.

Seemann, W., Ekhlakov, A., Glushkov, E., Glushkova, N. and Kvasha, O. (2007). The modeling of piezoelectrically excited waves in beams and layered substructures. *Journal of Sound and Vibration*, volume 301, pp. 1007–22.

Semblat, J. and Brioist, J. (2000). Efficiency of higher order finite elements for the analysis of seismic wave propagation. *Journal of Sound and Vibration*, volume 231, number 2, pp. 460–467.

Seriani, G. and Oliveira, S. (2008). Dispersion analysis of spectral element methods for elastic wave propagation. *Wave Motion*, volume 45, number 6, pp. 729–744.

Sohn, H., Farrar, C. R., Hemez, F. M., Shunk, D. D., Stinemates, D. W. and Nadler, B. R. (2004). *A review of structural health monitoring literature: 1996-2001* (Technical Report LA-13976-MS). Los Alamos National Laboratory.

Sohn, H. and Lee, S. J. (2010). Lamb wave tuning curve calibration for surface-bonded piezoelectric transducers. *Smart Mater. Struct.*, volume 19, pp. 7–15.

Sprague, M. and Geers, T. (2007). Legendre spectral finite elements for structural dynamics analysis. *Communications In Numerical Methods In Engineering*, , number April, pp. 1–13.

Stacey, R. (1988). Improved transparent boundary formulations for the elastic wave equation. *Bulletien of Seismological Society of America*, volume 87, number 6, pp. 2089–97.

Staszewski, W. J., Boller, C., Gronde, S., Biemans, C., Brien, E., Delebarre, C. and Tomlinson, G. R. (2004). Damage detection using stress and ultrasonic waves. In Staszewski, W. J., Boller,

C. and Tomlinson, G. R., *Health Monitoring of Aerospace Structures*. John Wiley & Sons, pp. 125–162.

Stephen, N. G. (1997). Mindlin plate theory: Best shear coefficient and higher spectra validity. *Journal of Sound and Vibration*, volume 202, number 4, pp. 539–553.

Strang, G. and Fix, G. J. (1988). *An analysis of the finite element method*. Wellesley-Cambridge Press.

Su, Z. and Ye, L. (2009). *Identification of Damage Using Lamb Waves From Fundamentals to Applications*. Springer-Verlag.

Su, Z., Ye, L. and Lu, Y. (2006). Guided Lamb waves for identification of damage in composite structures: A review. *J Sound Vibr*, volume 295, pp. 753–80.

Sundararaman, S. and Adams, D. E. (2008). Modeling guided waves for damage identification in isotropic and orthotropic plates using a local interaction simulation approach. *J Acous Vibr*, volume July 2008, p. online.

Szabó, B. and Babŭska, I. (2011). *Introduction to Finite Element Analysis: Formulation, Verification and Validation*. John Wiley & Sons, Ltd.

Sze, K. E. and Pan, Y. S. (1999). Hybrid finite element models for piezoelectric materials. *J Sound Vibr*, volume 226, number 3, pp. 519–47.

Thompson, L. L. and Pinsky, P. M. (1994). Complex wavenumber fourier analysis of the p-version finite element method. *Computational Mechanics*, volume 13, number 4, pp. 255–275.

Trefethen, L. N. (2011). *Trefethen's Index Cards: Forty Years of Notes About People, Words and Mathematics*. World Scientific.

Trefethen, N. L. (1982). Group velocity and finite difference schemes. *SIAM Review*, volume 24, number 2, pp. 113–136.

Trefethen, N. L. (2001). *Spectral Methods in Matlab*. SIAM.

Tromp, J., Komatitsch, D. and Qinya, L. (2008). Spectral-element and adjoint methods in seismology. *Commun Comput Phys*, volume 3, number 1, pp. 1–32.

Uchino, K. (2013). *Applications of ATILA FEM software to smart materials: Case studies in designing devices*, chapter Overview of the ATILA finite element method (FEM) software code, Woodhead Publishing Series in Electronic and Optical Materials, *volume 31*. Woodhead Publishing Limited, pp. 3–24.

Vallen (2009). *Vallen Dispersion software*. Vallen Systeme GmbH.

Viktorov, I. A. (1967). *Rayleigh and Lamb Waves: Physical Theory and Applications*. Plenum Press.

Virieux, J. (1986). P-SV wave propagation in heterogeneous media: velocity-stress finite-difference method. *Geophysics*, volume 51, pp. 889–901.

Wang, C., Reddy, J. and Lee, K. (2000). *Shear Deformable Beams And Plates Relationships With Classical Solutions*. ELSEVIER Science Ltd.

Wang, X. D. and Meguid, S. A. (2000). On the electroelastic behavior of a thin piezoelectric actuator attached to an infinite host structure. *S. A. Int. J. Solids Struct.*, volume 37, pp. 3231–3251.

Witkowski, W., Rucka, M., Chróścielewski, J. and Wilde, K. (2012). On some properties of 2D spectral finite elements in problems of wave propagation. *Finite Elements in Analysis and Design*, volume 55, pp. 31–41.

Worlton, D. C. (1957). Ultrasonic testing with Lamb waves. *Non-Destructive Testing*, volume 15, pp. 218–22.

Yu, L., Bottai-Santoni, G. and Giurgiutiu, V. (2010). Shear lag solution for tuning ultrasonic piezoelectric wafer active sensors with applications to lamb wave array imaging. *International Journal of Engineering Science*, volume 48, pp. 848–861.

Yu, L. and Giurgiutiu, V. (2008). In situ 2-D piezoelectric wafer active sensors arrays for guided wave damage detection. *Ultrasonics*, volume 48, pp. 117–34.

Zak, A. (2009). A novel formulation of a spectral plate element for wave propagation in isotropic structures. *Finite Elements in Analysis and Design*, volume 45, number 10, pp. 650–658.

Zak, A. and Krawczuk, M. (2011). Certain numerical issues of wave propagation modelling in rods by the spectral finite element method. *Finite Elements in Analysis and Design*, volume 47, number 9, pp. 1036–1046.

Zak, A. A., Krawczuk, M. and Ostachowicz, W. (2006). Propagation of in-plane elastic waves in a composite panel. *Finite Elements in Analysis and Design*, volume 43, number 2, pp. 145–154.

Zhang, J. Q., Zhang, B. N. and Fan, J. H. (2003a). A coupled electromechanical analysis of a piezoelectric layer bonded to an elastic substrate: Part i, development of governing equations. *Int. J. Solids Struct.*, volume 40, pp. 6781–6797.

Zhang, J. Q., Zhang, B. N. and Fan, J. H. (2003b). A coupled electromechanical analysis of a piezoelectric layer bonded to an elastic substrate: Part ii, numerical solution and applications. *Int. J. Solids Struct.*, volume 40, pp. 66799–6612.

Zhao, X. and Rose, J. L. (2003). Boundary element modeling for defect characterization potential in a wave guide. *International Journal of Solids and Structures*, volume 40, pp. 2645–58.

Zhu, W. and Rose, J. L. (1999). Lamb wave generation and reception with time-delay periodic linear arrays: A BEM simulation and experimental study. *ieee transactions on ultrasonics, ferroelectrics, and frequency control*, volume 46, number 3.

Zienkiewicz, O. and Taylor, R. (2005). *The Finite Element Method for Solid and Structural Mechanics*.

Zienkiewicz, O., Taylor, R. and Zhu, J. (2005). *The finite element method: its basis and fundamentals*.

Zingg, D. W. (2000). Comparison of high-accuracy finite-difference methods for linear wave propagation. *SIAM J Sci Comput*, volume 22, number 2, pp. 476–502.

Zyserman, F. and Gauzellino, P. (2005). Dispersion analysis of a nonconforming finite element method for the three-dimensional scalar and elastic wave equations. *Finite elements in analysis and design*, pp. 1309–1326.

Zyserman, F. I., Gauzellino, P. M. and Santos, J. E. (2003). dispersion analysis of a non-conforming finite element method for the Helmholtz equation. *International Journal for Numerical Methods in Engineering*, volume 58, pp. 1381–1395.